INVESTIGATION ON LITHIUM ION CONDUCTIVITY AND CHARACTERIZATION OF PMMA–PVC BASED POLYMER ELECTROLYTES INCORPORATING IONIC LIQUID AND NANO–FILLER

By

LIEW CHIAM WEN

A thesis submitted to the Department of Bioscience and Chemistry,
Faculty of Engineering and Science,
Universiti Tunku Abdul Rahman,
in partial fulfillment of the requirements for the degree of
Master of Science in
April 2011

ABSTRACT

INVESTIGATION ON LITHIUM ION CONDUCTIVITY AND CHARACTERIZATION OF PMMA–PVC BASED POLYMER ELECTROLYTES INCORPORATING IONIC LIQUID AND NANO–FILLER

Liew Chiam Wen

There are four polymer electrolyte systems in this project. First and second polymeric systems are known as screening steps. Poly(methyl methacrylate) (PMMA) and poly(vinyl chloride) (PVC) were used as host polymers with lithium bis(trifluoromethanesulfonyl) imide (LiTFSI) as doping salt. Additives such as 1–butyl–3–methylimidazolium bis(trifluoromethylsulfonyl imide) (BmImTFSI) ionic liquid and nano–sized inorganic reinforcement filler, fumed silica (SiO_2) were employed. All the polymer electrolytes are prepared by means of solution casting technique. PMMA (70 wt%) and PVC (30 wt%) is the most compatible ratio in the first system. The highest ionic conductivity of 1.60×10^{-8} Scm^{-1} was achieved at ambient temperature. Upon addition of 30 wt% of LiTFSI (second system), a maximum room temperature ionic conductivity of 1.11×10^{-6} Scm^{-1} was achieved. The ambient temperature– ionic conductivity of gel polymer electrolytes increased to a maximum value of 1.64×10^{-4} Scm^{-1} upon addition of 60 wt% BmImTFSI. For further enhancement of conductivity, SiO_2 was incorporated as filler and the highest ionic conductivity obtained at ambient temperature was 4.11 $mScm^{-1}$ with 8 wt% of SiO_2. The ionic conductivities of all of the samples increased with increasing temperature due to the polymer expansion effect. Arrhenius behavior of

samples was determined from the plots. The dielectric behavior was analyzed using dielectric permittivity and dielectric modulus of the samples. In addition, horizontal attenuated total reflectance–Fourier Transform infrared (HATR-FTIR) spectroscopy indicated the complexation of the materials in the polymer electrolytes based on the changes in shift, changes in intensity, changes in shape and formation of new peaks. X–ray diffraction (XRD) studies implied the higher degree of amorphous nature of the polymer electrolytes by reducing the intensity of characteristic peaks. The morphology of the samples was also explored by scanning electron microscopy (SEM). Agglomeration occurs if the materials are in excess. In the images, the higher porosity disclosed the higher amount of ionic transportation in the polymer matrix. Entrapments of ionic liquid into the polymer matrix were further verified through the images. Wavy type appearance also divulged the gel–like appearance of polymer electrolytes. Excellent thermal properties of samples were proven in differential scanning calorimetry (DSC) studies. Thermogravimetric analyses (TGA) indicated that the samples are stable up to 200 °C and were greatly preferred in lithium batteries as its operating temperature is normally in the range of 40–70 °C. Rheological studies revealed the viscosity of samples and their elastic properties through oscillation and rotational test.

ACKNOWLEDGEMENTS

Firstly, I would like to take this opportunity to express my greatest gratitude to my supervisors, Dr. Ramesh T. Subramaniam and Dr. Rajkumar Durairaj for their guidance throughout this project stint. Besides, they act as model for me through his effort, diligence, patience, wisdom and tenacity despite failure and hurdle. In addition, they have guided, advised and encouraged me when I faced obstacles in the project. I really appreciate their efforts and guidances during this research period.

Gratitude also goes to UTAR and Malaysia Toray Science Foundation (MTSF) as this work was supported by the foundation and UTAR Research Fund (UTARRF). It also provides the venue for education and research, instruments, apparatus and facilities. Besides, it provides a good working environment for the completion of this research. Apart from that, I feel very grateful to all the laboratory officers and lab assistants for their assistance and patience throughout this lab work. In addition, I feel very thankful to all of fellow research team mates and coursemates who provided me useful information, views and support when I am facing the problem. I cherish the moments that we work hard together, exchange information, view and idea during the difficult period.

Finally, I would like to extend my deepest appreciation to my dearest family members for their moral support, love and encouragement to persuade my interest in this research.

APPROVAL SHEET

This thesis entitled "**INVESTIGATION ON LITHIUM ION CONDUCTIVITY AND CHARACTERIZATION OF PMMA–PVC BASED POLYMER ELECTROLYTES INCORPORATING IONIC LIQUID AND NANO–FILLER"** was prepared by LIEW CHIAM WEN and submitted as partial fulfillment of the requirements for the degree of Master of Science at Universiti Tunku Abdul Rahman.

Approved by:

_____
(Associate Prof. Dr. Ramesh a/l T. Subramaniam)
Date:……..
Supervisor
Department of Mechanical and Material Engineering
Faculty of Engineering and Science
Universiti Tunku Abdul Rahman

_____
(Associate Prof. Dr. Rajkumar a/l Durairaj)
Date:…….
Co-supervisor
Department of Mechanical and Material Engineering
Faculty of Engineering and Science
Universiti Tunku Abdul Rahman

FACULTY OF ENGINEERING AND SCIENCE
UNIVERSITI TUNKU ABDUL RAHMAN

Date: _____

PERMISSION SHEET

It is hereby certified that **LIEW CHIAM WEN** (ID No: **08UEB08128**) has completed this thesis/dissertation entitled "INVESTIGATION ON LITHIUM ION CONDUCTIVITY AND CHARACTERIZATION OF PMMA–PVC BASED POLYMER ELECTROLYTES INCORPORATING IONIC LIQUID AND NANO–FILLER" under the supervision of Dr. Ramesh a/l T. Subramaniam (Supervisor) from the Department of Mechanical and Material Engineering, Faculty of Engineering and Science, and Dr. Rajkumar a/l Durairaj (Co-Supervisor) from the Department of Mechanical and Material Engineering, Faculty of Engineering and Science.

I hereby give permission to the University to upload softcopy of my thesis in pdf format into UTAR Institutional Repository, which will be made accessible to UTAR community and public.

Yours truly,

_____
(LIEW CHIAM WEN)

DECLARATION

I hereby declare that the dissertation is based on my original work except for quotations and citations which have been duly acknowledged. I also declare that it has not been previously or concurrently submitted for any other degree at UTAR or other institutions.

Name _____

Date _____

TABLE OF CONTENTS

LIST OF TABLES

LIST OF FIGURES

LIST OF ABBREVIATIONS

SPEs	Solid polymer electrolytes
GPEs	Gel polymer electrolytes
CPEs	Composite polymer electrolytes
PMMA	Poly(methyl methacrylate)
PVC	Poly(vinyl chloride)
LiTFSI	Lithium bis(trifluoromethanesulfonyl) imide
BmImTFSI	1–buty–3–methylimidazolium bis(trifluoromethylsulfonyl imide)
SiO_2	Fumed silica
HATR–FTIR	Horizontal attenuated total reflectance–Fourier Transform infrared
XRD	X–ray diffraction
SEM	Scanning electron microscopy
DSC	Differential scanning calorimetry
T_g	Glass transition temperature
T_m	Crystalline melting temperature
T_d	Decomposition temperature
TGA	Thermogravimetric analysis
THF	Tetrahydrofuran
η	Viscosity
σ	Conductivity in S cm^{-1}
R_b	Bulk impedance in Ohm

A	Area of the disc electrodes in cm^2
d	Thickness of the thin film in cm

CHAPTER 1

INTRODUCTION

1.1 Solid Polymer Electrolyte (SPE)

A polymer electrolyte (PE) is defined as a solvent–free system whereby the ionically conducting pathway is generated by dissolving the low lattice energy metal salts in a high molecular weight polar polymer matrix with aprotic solvent. The fundamental of ionic conduction in the polymer electrolytes is the covalent bonding between the polymer backbones with the ionizing groups. Initially, the electron donor group in the polymer forms solvation to the cation component in the dopant salt and then facilitates ion separation, leading to ionic hopping mechanism. Hence, it generates the ionic conductivity. In other words, the ionic conduction of PE arises from rapid segmental motion of polymer matrix combined with strong Lewis–type acid–base interaction between the cation and donor atom (Ganesan *et al*., 2008).

However, the well separated ions might be poor conductors if the ions are immobile and unable for the migration. Therefore, the host polymer must be sufficiently flexible to provide enough space for the migration of these two ions (Gray, 1997a). The solid polymer electrolyte in the lithium–based cells is classified into three major types, namely dry polymer electrolyte or known as solid

polymer electrolyte (SPE), gel polymer electrolyte (GPE) and composite polymer electrolyte (CPE).

SPE serves three principal roles in a lithium rechargeable battery. Firstly, it acts as the electrode separator that insulates the anode from the cathode in the battery which removes the requirement of inclusion of inert porous spacer between the electrolytes and electrodes interface. Besides, it plays the role as medium channel to generate ionic conductivity which ions are transported between the anode and cathode during charging and discharging. This leads to enhancement of energy density in the batteries with formation of thin film. In addition, it works as binders to ensure good electrical contact with electrodes. Thus, high temperature process for conventional liquid electrolytes is eliminated as well (Gray, 1991; Kang, 2004).

1.2 Gel Polymer Electrolyte (GPE)

SPE possesses high mechanical integrity, but it exhibits low ionic conductivity. Therefore, gel polymer electrolyte (GPE), sometimes known as gelionic solid polymer electrolyte is yet to be developed to replace the solid polymer electrolyte because of its inherent characteristics (Stephan *et al*., 2000a). Such features are reduced reactivity, improved safety and high ionic conductivity at room temperature as well as exhibit better shape flexibility and manufacturing (Ahmad *et al*., 2008; Pandey and Hashmi, 2009). GPE is obtained by dissolving

the polymer host along with a metal dopant salt in a polar organic solvent (more commonly known as plasticizer) (Osinska *et al*., 2009; Rajendran *et al*., 2008). An inactive polymeric material is added to give the mechanical stability (Gray, 1997a). In other words, it is an immobilization of a liquid electrolyte in a polymer matrix (Han *et al*., 2002).

Room temperature ionic liquid (RTIL) has received an upsurge of interest to substitute the plasticizer. RTIL is a non–volatile room temperature molten salt which comprised of bulky, asymmetric organic cation and highly delocalized–charge inorganic anions. It remains in a liquid form at ambient temperature as its unique characteristic (Pandey and Hashmi, 2009; Sirisopanaporn *et al*., 2009). Indeed, GPEs must have sufficient mechanical properties to withstand the electrode stack pressure and stresses which caused by dimensional changes so as to remove the use of separator (Ahmad *et al*., 2008).

1.3 Composite Polymer Electrolyte (CPE)

Unfortunately, the dimensional and mechanical stabilities of GPEs are scarce because of the impregnation of a liquid electrolyte into a polymer system and this leads to the softening of the polymer (Stephan *et al*., 2000b; Han *et al*., 2002). This main drawback can be circumvented by adding inorganic reinforcement filler. Composite polymer electrolyte (CPE) was eventually produced. Therefore, CPE is defined as a type of polymer electrolyte which

comprises of inorganic fillers in the polymer matrix (Osinska *et al*., 2009). The composite polymer electrolytes containing ceramic fillers of nanometre grain size are generally termed as nanocomposite polymer electrolytes (NCPEs). These CPEs offer some attractive advantages such as superior interfacial contacts, highly flexible, improve lithium transportation, high ionic conductivity and better thermodynamic stability towards lithium and other alkali metals (Gray, 1997a). Examples of inorganic fillers are alumina (Al_2O_3), fumed silica (SiO_2) and titania (TiO_2).

1.4 Advantages of Polymer Electrolytes

A force had been driven in the development of PE in order to replace conventional liquid electrolytes due to its intrinsic advantages. These features including eliminate the problems of corrosive solvent leakage and harmful gas during operation, easy processability due to elimination of liquid component, suppression of lithium dendrite growth, configured in any shape because of high flexibility of polymer matrix, high automation potential for electrode application and no new technology requirement as well as light in weight (Xu and Ye, 2005; Gray, 1991). Other advantages of PEs are no vapor pressure, ease of handling and manufacturing, wide operating temperature range, low volatility, high energy density and high ionic conductivity at ambient temperature (Baskaran *et al.*, 2007; Rajendran *et al*., 2004). In addition, the electrochemical, structural, thermal,

photochemical and chemical stabilities can be enhanced for PE in comparison to conventional liquid electrolyte (Adebahr *et al*., 2003; Nicotera *et al*., 2006).

1.5 Applications of Polymer Electrolytes

Polymer electrolytes have a wide range of applications in the technology field, ranging from small scale production of commercial secondary lithium ion batteries (also known as the rechargeable batteries) to advanced high energy electrochemical devices, such as chemical sensors, fuel cells, electrochromic windows (ECWs), solid state reference electrode systems, supercapacitors, thermoelectric generators, analog memory devices and solar cells (Gray, 1991; Rajendran *et al*., 2004). As for the commercial promises of lithium rechargeable batteries, there is a wide range of applications which ranges from portable electronic and personal communication devices such as laptop, mobile phone, MP3 player, PDA to hybrid electrical vehicle (EV) and start–light–ignition (SLI) which serves as traction power source for electricity (Gray, 1997a; Ahmad *et al.*, 2005).

1.6 Objectives of Research

In this research, the main objective was to investigate the effect on ionic conductivity of poly(methyl methacrylate) (PMMA)–poly(vinyl chloride) (PVC)

polymer blend electrolytes with lithium dopant salt upon addition of ionic liquid and nano–sized inorganic filler. The aspire of this project was also to study the effect of temperature onto the polymer blend electrolytes and examine the mechanisms pertaining to transport of conducting ions of these polymer blend electrolytes

Besides, it was aimed to study the dielectric behaviour of the polymer blend electrolytes and characterize the morphological, structural and thermal properties of these polymer blend electrolytes. This project was also designed to explore the knowledge of rheological properties of the polymer blend electrolytes. The morphological of polymer blend electrolytes were scrutinized by scanning electron microscopy (SEM), whereas the structural behaviour of these polymer blend electrolytes were characterized by means of x–ray diffractor (XRD) and horizontal attenuated total reflectance–Fourier Transform infrared (HATR–FTIR). On the contrary, the thermal properties of polymer electrolytes were studied by thermogravimetric analysis (TGA) and differential scanning calorimetry (DSC) studies.

CHAPTER 2

LITERATURE REVIEW

2.1 Ionic Conductivity

2.1.1 General Description of Ionic Conductivity

Ionic conductivity is the main aspect to be concerned in the solid polymer electrolytes. Ionic conductivity is defined as ionic transportation under the influence of an external electric field. In general, the ions are being trapped on their lattice sites for most ionic solids (West, 1999a). However, the ions rarely have enough thermal energy to escape from their lattice sites although they vibrate continuously. Ionic conduction, migration, hopping or diffusion is occurred if they are able to escape and move into their adjacent lattice sites. There are two possible mechanisms for the movement of ions through a lattice viz., vacancy mechanism and interstitial mechanism. These mechanisms are sketched in Figure 2.1.

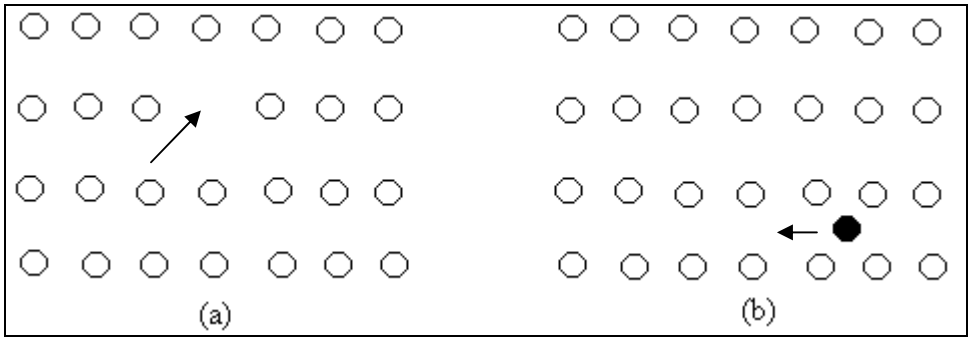

Figure 2.1: Schematic representation of ionic motion by (a) a vacancy mechanism and (b) an interstitial mechanism.

Vacancy mechanism is defined as the hopping mechanism of an ion from its normal position on the lattice to an adjacent equivalent but empty site. In contrast, an interstitial ion jumps or hops to an adjacent equivalent sites and this is called the interstitial mechanism (Smart and Moore, 2005a). As a result, the minimum requirement of an ionic conduction is either the presence of some vacant sites and thus the adjacent ions can hop into the vacancies, leaving their own sites vacant or there are some ions in the interstitial sites which can hop into the adjacent vacant interstitial sites (West, 1999a).

The general expression of ionic conductivity of a homogenous polymer electrolyte is shown as

$$\sigma(T) = \sum_i n_i q_i \mu_i \qquad \text{(Equation 2.1)}$$

where n_i is the number of charge carriers type of i per unit volume, q_i is the charge of ions type of i, and μ_i is the mobility of ions type of i which is a measure of the drift velocity in a constant electric field (Gray, 1991b; Gray, 1997c; Smart and Moore, 2005). These charge carriers include free ion and ion pairs, such as ion aggregates. Based on the equation, the amount and mobility of charge carriers are the main aspects that could affects the ionic conductivity of polymer electrolytes as the charge of the mobile charge carriers are the same and negligible.

2.1.2 Basic Conditions to Generate the Ionic Conductivity

Five basic conditions must be satisfied in order to produce the ionic hopping process:

(a) A large number of the ions of one species should be mobile.

(b) A large number of empty sites should be available for the ionic conduction. This is essentially a corollary of (a) because ions can be mobile only if there are vacant sites available for them to occupy.

(c) The empty and occupied sites should have similar potential energies with a low activation barrier (also known as activation energy) for jumping between the neighboring sites. It is useless to have a large number of available vacant sites if either the mobile ions cannot get into them or if they are too small.

(d) The structure should have a framework, preferably three–dimensional, permeated by open channels through which mobile ions may migrate.

(e) The anion framework should be highly polarizable (West, 1999a).

2.1.3 Aspects to Govern the Ionic Conductivity

Three aspects are investigated to govern the magnitude of the ionic conductivity viz., the degree of crystallinity, salt concentration and temperature. In defect–free solids, there are no atom vacancies and the interstitial sites are completely empty. If the crystal structure of polymer electrolytes were perfect, it would be difficult to visualize the migration of ions through ionic hopping

mechanism. Therefore, the ionic conduction is easier to be generated if the crystal defects are involved. The deterioration of the crystalline portion in the polymer electrolytes will initiate the formation of amorphous phase. Amorphous is a physical state of a polymer where the molecules are in unordered arrangement, whereas the crystalline refers to the situation where polymer molecules are in oriented or aligned arrangement (Malcolm and Stevens, 1999a). Figure 2.2 depicts the schematic diagram of mixed amorphous and crystalline macromolecules in the polymer regions in semi–crystalline polymer structure. A completely amorphous polymer such as atactic polystyrene (PS) and poly(methyl methacrylate) (PMMA) is able to form a stable and flow–restricting entanglements at high molecular weight because of its long, randomly coiled and interpenetrating polymeric chains.

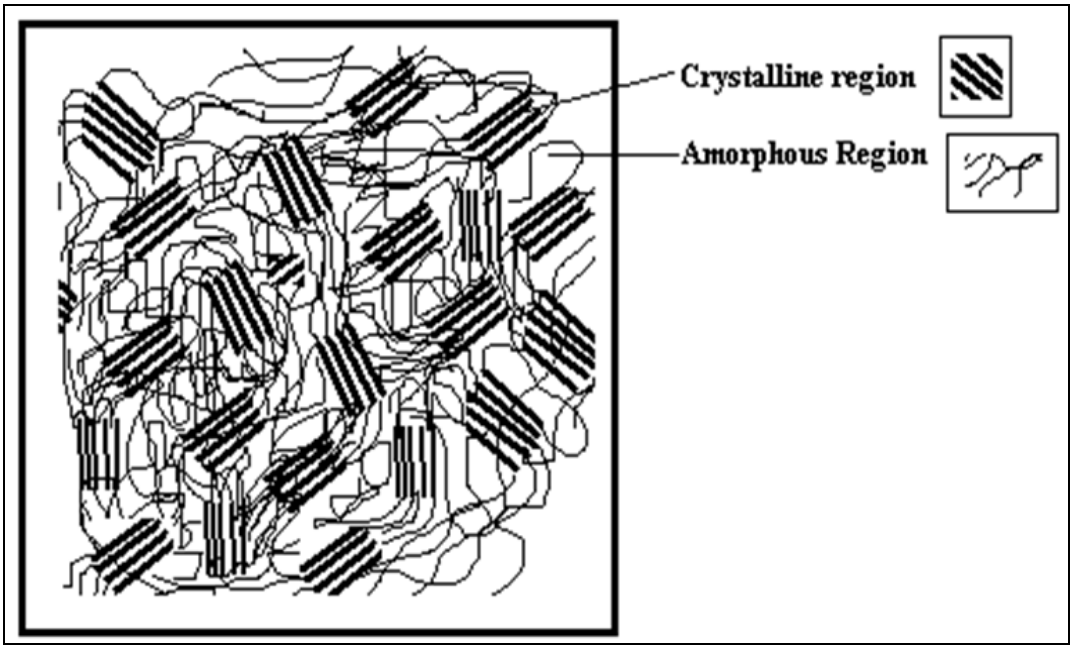

Figure 2.2: Schematic diagram of mixed amorphous and crystalline regions in semi–crystalline polymer structure.

Since the amorphous region is composed of unordered arrangement, thus the molecules within the polymeric chain are not packed tightly in the lattice site. It therefore leads to the higher flexible of the polymeric segment and hence increases the mobility of charge carriers. Moreover, this unordered region creates more empty spaces or voids for ionic hopping. As a consequence, amorphous nature of the polymer electrolytes raises the ionic conductivity.

In principle, at low salt concentration, the ionic conductivity is strongly controlled by number of charge carriers and the mobility of ions is relatively unaffected. However, at high salt concentration, the ionic conductivity is strongly dependent on the mobility of ions and the ionic conduction pathway (Yu *et al*., 2007; Gray, 1991b). The ionic transportation is closely correlated to the relaxation modes of the polymer. This can be observed through the increase in T_g of polymer system as the salt content is increased. In this phenomenon, the segmental mobility is significantly reduced as increases the intra and inter coordination bonds within the polymer chains (Gray, 1991b). Since polymer electrolytes fall apart into charged polyions and oppositely charged counterions, thus all the charges attached to the polymer matrix would repel each other. At low salt concentration, the random coils in the polymer chain expand tremendously due to the repulsion effect of the like charges on the polymer chain. The expansion allows these charges to be as far apart as possible. When the polymer matrix stretches out, it takes up more spaces. Therefore, the availability of vacant sites for ionic conduction is enormously deceased (Braun, 2005a).

However, the ionic conductivity is greatly reduced at high salt concentration due to the decreases in availability of vacant coordinating sites. Another attributor is the formation of ion pairs or ion aggregates. Less mobile charge carriers are produced and then restrained ionic migration. The polymer chains collapse back into the random coils with increasing the salt concentration. It is attributed to the decrease in the range of the intra–molecular Coulombic force. At higher temperature, the ionic hopping is easier to be conducted. It is due to the higher thermal energy of ions at elevated temperature. Hence, the ions will vibrate more vigorously (West, 1999a). The crystalline portion is progressively defected and dissolved in the amorphous phase with increasing the temperature. It thus increases the density of charge carriers (Gray, 1991b).

2.2 Methods to Improve Ionic Conductivity

Investigations on polymer electrolytes have primarily focused on the enhancement of ionic conductivity at ambient temperature. Several techniques have been proposed and developed by researchers to modulate the ionic conductivity such as random and comb–like copolymer of two polymers, polymer blending, mixed salt system and mixed solvent system as well as impregnation of additives such as plasticizers and ceramic inorganic fillers. Polymer blending and inclusion of additives are the routes to increase the ionic conductivity of polymer electrolytes in this project.

2.2.1 Random Copolymerization

The random copolymerization increases the ionic conductivity by providing a more flexible system and thus enhances the ionic motion. The random ethylene oxide–propylene oxide (EO–PO) is synthesized via anionic copolymerization, by using a heterogeneous catalyst system based on aluminium alcoholate grafted on porous silica. However, the dimethyl siloxyl groups were used instead of methylene oxide units to improve the ionic conductivity. A similar random copolymer to amorphous oxymethylene–linked poly(ethylene oxide) has been synthesized. Low glass transition temperature (T_g) of poly(dimethyl siloxane) that is around –123 ^{o}C aids to provide a more flexible polymer chains and thus increases the ionic mobility (Gray, 1997b).

2.2.2 Comb Polymerization

In general, comb polymers contain pendant chain and they are structurally related to grafting copolymers. The comb–branched system consists of low molecular weight of polyether chain grafted to polymer backbone. Thus, it lowers the T_g and then helps to optimize the ionic conductivity by improving the flexibility of polymer chain into the system. As a consequent, the bulk conductivity is increased (Gray, 1997b). According to Kerr (2002), he synthesized polymer electrolyte systems where the polymer structure is a comb branch

polypropylene oxide backbone structure with side chains of varying lengths which contain different ether groups, which are ethylene oxide (EO) or trimethylene oxide (TMO) and LiTFSI served as doping salt. He concluded that there is a dramatic effect of the TMO groups on the T_g values with increasing the concentration of salt and this affects the ionic conductivity at ambient temperature. Ikeda and co–workers synthesized polyether comb polymer, that is poly(ethylene oxide/ MEEGE) and produced the elastic polymer electrolyte films. The degree of crystallinity was decreased with increasing the composition of MEEGE in copolymers, which in accordance with higher ionic conductivity. The introduction of the side chain of MEEGE in the copolymers enhances the flexibility of polymer matrix and hence improves the ion mobility. The highest ionic conductivity of 10^{-4} S cm^{-1} was achieved at room temperature (Ikeda *et al*., 1998).

2.2.3 Mixed Salt System

The conductivity of the mixed salts in polymer electrolyte is higher than single salt electrolyte. It is due to the addition of second salt may prevent the formation of aggregates and clusters. Thus, it increases the mobility of ion carriers (Gray, 1997b). An approach had been done by Arof and Ramesh (2000). In this research, they synthesized poly (vinyl chloride) (PVC)–based polymer electrolytes with lithium trifluoromethanesulfonate ($LiCF_3SO_3$) and lithium tetrafluoroborate ($LiBF_4$) as doping salts. The ionic conductivity is increased by four orders of

magnitude in comparison to single salt system. It is attributed to the increase in the mobility of charge carriers by avoiding the aggregation process.

2.2.4 Mixed Solvent System

On the other hand, the increase of conductivity in binary solvent system is proven by Deepa *et al*. (2002). In this study, poly(methyl methacrylate) (PMMA)–based polymer electrolytes containing lithium perchlorate ($LiClO_4$), with a mixture of solvents of propylene carbonate (PC) and ethylene carbonate (EC) were prepared. The maximum ionic conductivity of 10^{-3} S cm^{-1} was obtained and it was increased by two orders of magnitude as compared to polymer electrolyte system with single solvent. Synergistic effect is the major factor to increase the ionic conductivity in mixed solvent system. In this effect, different physicochemical properties of the individual solvents come into play and contribute to high ionic conductivity. For example, high dielectric constant and low viscosity of EC and low freezing point of PC with good plasticizing characteristics enhance the performance of the polymer electrolytes (Tobishima and Yamaji, 1984).

2.2.5 Polymer Blending

Polymer blend is physical mixtures of two or more different polymers or copolymers that are not linked by covalent bond. A new macromolecular material

with special combinations of properties was prepared. For polymer blends, a first phase adopted to absorb the electrolyte active species, whereas the second phase is tougher and sometimes substantially inert. It is a feasible way to increase the ionic conductivity because it offers the combined advantages of ease of preparation and easy control of physical properties within the definite compositional change (Rajendran *et al*., 2002). Polymer blending is of great interest due to their advantages in properties and processability compared to single component. In industry area, it enhances the processability of high temperature or heat–sensitive thermoplastic in order to improve the impact resistance. Besides, it can reduce the cost of an expensive engineering thermoplastic. The properties of polymer blends depend on the physical and chemical properties of the participating polymers and on the state of the phase, whether it is in homogenous or heterogeneous phase. If two different polymers able to be dissolved successfully in a common solvent, this polymer blends or intermixing of the dissolved polymers will occur due to the fast establishment of the thermodynamic equilibrium (Braun, 2005b).

According to Rajendran *et al*. (2000), the ionic conductivity of PVC–PMMA– $LiAsF_6$–DBP polymer blend electrolytes increases with the concentration of PMMA. Besides, the polymer blend electrolyte containing 20 wt % of $LiClO_4$ exhibits the highest conductivity of 1.76×10^{-3} Scm^{-1} at ambient temperature, which reveals that this polymer blend electrolyte can be a good candidate for lithium rechargeable battery (Baskaran, 2006). Sivakumar, *et al*. (2006) observed that PVA (60 wt %)–PMMA (40 wt %)–$LiBF_4$ complex exhibits the maximum conductivity of 2.8×10^{-5} S cm^{-1} at ambient temperature. It is also higher than the

pure PVA system which has been reported to be 10^{-10} Scm^{-1}. However, the conductivity deceases as PVA content is further increased. It may due to the high PVA content which imparts a high viscosity and thus affects the ionic mobility.

2.2.6 Plasticization

The common additives such as plasticizers and inorganic fillers are the effective and efficient routes to enhance the ionic conductivity. Plasticizer is widely been incorporated in GPE as additive. Plasticizer is generally a low volatile liquid with high dielectric constant such as ethylene carbonate (EC) and propylene carbonate (PC). High salt–solvating power, sufficient mobility of ionic conduction and reduction in crystalline nature of the polymer matrix are the main features of the plasticizer (Rajendran *et al*., 2004; Suthanthiraraj *et al*., 2009). However, upon addition of plasticizer, some limitations are obtained such as low flash point, slow evaporation, decreases in thermal, electrical and electrochemical stabilities. Low performances, for instance, small working voltage range, narrow electrochemical window, high vapor pressure and poor interfacial stability with lithium electrodes are the disadvantages of plasticized–gel polymer electrolytes (Kim *et al*., 2006; Pandey and Hashmi, 2009; Raghavana *et al*., 2009).

Normally, it is composed of low molecular weight of organic compound which has a T_g in the vicinity of –50 °C. The principal function of a plasticizer is to reduce the modulus of polymer at the desired temperature by lowering its T_g.

The increase in concentration of plasticizer causes the transition from the glassy state to rubbery region at progressively lower temperature. In addition, it can occur over a wide range of temperature rather than unplasticized polymer. Besides, it improves the flexibility of polymer chains in the polymer matrix. Moreover, it reduces the viscosity of melting to facilitate the molding or extruding process. In polymer electrolytes, it is used to increase the free volume of polymer and enhances the long–range segmental motion of the polymer molecules in the system. A maximum electrical conductivity of 2.60×10^{-4} S cm^{-1} at 300 K has been observed for 30 wt % of PEG as plasticizer compared to the pure PEO–$NaClO_4$ system of 1.05×10^{-6} S cm^{-1}. This can be explained that the addition of plasticizer enhances the amorphous phase in with concomitant the reduction in the energy barrier. Eventually, it results in a maximum segmental motion of lithium ions (Kuila *et al*., 2007).

2.2.7 Addition of Ionic Liquid

Recently, room temperature ionic liquids (RTILs) (also known as "green solvent") have received an upsurge of interest to overcome those drawbacks of plasticizer. RTIL is a non–volatile room temperature molten salt with a low melting point (<100 °C). It is comprised of bulky, asymmetric organic cation such as ammoniums, phosphoniums, imidazoliums, pyridiniums and highly delocalized–charge inorganic anion, such as triflate (Tf^-), tetrafluoroborate (BF_4^-),

bis(trifluoromethylsulfonyl imide) ($TFSI^-$) and hexaflurophosphate (PF_6^-) (Pandey & Hashmi, 2009).

A lot of literatures had been done on the development of ionic liquid. P. K. Singh and his co–worker had developed the stable and high conducting polymer electrolytes by doping low viscosity 1–ethyl–3–methylimidazolium trifluromethanesulfonate (EmImTFO) into PEO–NaI–I_2 polymer complexes (Singh *et al*., 2009). The overall cell efficiency and photoelectrochemical properties of dye–sensitized solar cell (DSSC) were enhanced upon addition of ionic liquid. Sirisopanaporn *et al.* (2009) had developed freestanding, transparent and flexible gel polymer electrolyte membranes by trapping N–n–butyl–N–ethylpyrrolidinium N,N–bis(trifluoromethane)sulfonamide–lithium N,N–bis(trifluoromethane)sulfonamide (Py_{24}TFSI–LiTFSI) ionic liquid solutions in poly(vinylidene fluoride)–hexafluoropropylene copolymer (PVdF–co–HFP) matrices. The resulting membranes exhibited high room temperature ionic conductivity from 0.34 to 0.94 $mScm^{-1}$. These polymer electrolytes can operate up to 110 °C without degradation and did not showed any IL leakage within 4 months storage time (Sirisopanaporn *et al*., 2009). Another new type of tailor–made polymer electrolytes based on ILs and polymeric ionic liquids (PILs) are proposed by Marcilla and co–workers. These polymer electrolytes showed the ionic conductivity in the range between 10^{-2} and 10^{-5} Scm^{-1} (Marcilla *et al*., 2006).

An effort was done by Shin and co–workers on the development of ionic liquids based polymer electrolytes. They found that the ionic conductivity was

increased by two orders of magnitude upon incorporation of $PYR_{13}TFSI$ onto $P(EO)_{20}LiTFSI$ polymer matrix. The ionic conductivity of ~10^{-4} Scm^{-1} was achieved by adding 100 wt% $PYR_{13}TFSI$ at room temperature (Shin *et al*., 2003). In addition, a new proton conducting polyvinylidenefluoride–co–hexafluoropropylene (PVdF–HFP) copolymer membrane containing 2,3–dimethyl–1–octylimidazolium trifluromethanesulfonylimide (DMOImTFSI) had been synthesized. The maximum ionic conductivity of 2.74 $mScm^{-1}$ was achieved at 130 °C, along with good mechanical stability (Sekhon *et al*., 2006). Poly ionic liquid 1–ethyl 3–(2–methacryloyloxy ethyl) imidazolium iodide (PEMEImI) was synthesized by Yu and co–workers (Yu *et al*., 2007). The ionic conductivity of these gel polymer electrolytes increased with iodide content and the highest ionic conductivity of above 1 $mScm^{-1}$ was achieved at ambient temperature.

2.2.7.1 Advantages of Ionic Liquid

RTIL is a promising candidate due to its wider electrochemical potential window (up to 6V), wider decomposition temperature range, non–toxicity and non–volatility as well as non–flammability (Jiang *et al*., 2006; Cheng *et* al., 2007). Indeed, RTIL possess many inherent and attractive properties such as excellent thermal, chemical and electrochemical stabilities (Reiter *et al*., 2006; Yu *et al*., 2007). Besides, it serves as potential replacement for volatile organic compounds in the chemical industry as it has negligible vapor pressure (Vioux *et al*., 2009). In

addition, it is able to dissolve a wide range of organic, inorganic and organometallic compounds (Vioux *et al*., 2009).

It still remains in liquid form in a wide temperature range and does not coordinate with metal complexes, enzymes and different organic substrates as its unique characteristic (Jain *et al*., 2005). Other intrinsic features are excellent safety performance and relatively high ionic conductivity due to high ion content (Marcilla *et al*., 2006; Sekhon *et al*., 2006). The low viscosity of ionic liquid improves the ionic mobility among the polymer matrix. Doping of ionic liquid produces gel–like polymer electrolyte (GPE), perhaps sticky gel polymer electrolyte. Sticky gel polymer electrolyte has advantage in electrochemical devices designing by providing a good contact between electrolyte and electrode (Reiter *et al*., 2006).

2.2.7.2 Applications of Ionic Liquid

Ionic liquid is a versatile molten salt and has wider applications in scientific and technology fields. It is primarily used as an additive in gel polymer electrolytes. Such gel polymer electrolytes are applied onto electrochemical devices such as dye–sensitized solar cells, electrical supercapacitors, actuators, light–emitting electrochemical cells and lithium batteries (Shin *et al*., 2003; Vioux *et al*., 2009). A new attempt to use ionic liquid in the field of homogeneous catalyst by organometallic complexes has been carried out. It is due to the addition

of ionic liquids has improved the efficiency and selectivity of the catalysts and easy for preparation (Vioux *et al*., 2009).

In addition, the uses of ionic liquids have been keen of interest in inorganic chemistry, especially in metal electrodeposition, "ionothermal" syntheses and sol–gel process. It also serves as drying control chemical additives, catalysts, structure directing agents and solvent as well (Vioux *et al*., 2009). RTILs are well known as "green solvent" and are responsible to protect the environment by reducing the loads on the environment from viewpoint of green chemistry via recycle process. It is therefore designated as alternative recyclable solvent to aprotic and harmful organic solvent. It is also extensively used for liquid–liquid extraction process in organometallic reactions, in biocatalysis, for catalytic cracking of polyethylene and for radical polymerization (Jain *et al*., 2005).

2.2.8 Addition of Inorganic Reinforcement Filler

Typically, the polymer electrolyte is comprised of one or more types of polymer, dopant salt and a variety of additives such as plasticizers and fillers. The main objectives of dispersion of inorganic filler are to alter the properties of the polymer and enhance processability. Generally, the fillers for thermoplastics and thermosets are composed of inert materials. The fillers (also known as reinforcing fillers) are divided into two types which are inorganic and organic. The examples of inorganic fillers include fly ash, calcium carbonate, mica, clay, titania (TiO_2),

fumed silica (SiO_2) and alumina (Al_2O_3), whereas the graphite fibre and aromatic polyamide are the examples for organic fillers. In this research, nano–sized fumed silica was used as inorganic filler.

2.2.8.1 Advantages of Inorganic Filler

The main purpose of dispersion of inorganic filler is to improve the mechanical stability in the polymer electrolyte system. Several intrinsic advantages are possessed by inorganic filer. For instance, mica serves to modify the electrical and heat insulating properties of polymers. Besides, it plays a role to reduce resin costs, enhance processability and dissipate heat in exothermic thermosetting reaction. Other particulate fillers such as graphite, carbon black, aluminium flakes are used to reduce mold shrinkage or to minimize the electrostatic charging. For example, the high amount of carbon fibres can exhibit electromagnetic interference (EMI) shielding for computer applications (Joel, 2003a).

Dispersion of inorganic fillers can also improve the ionic conductivity in a polymer electrolyte. Besides improving the lithium transport properties, the inclusion of ceramic filler has been found to enhance the interfacial stability of polymer electrolytes (Osinska *et al*., 2009). Kim *et al*. (2003) revealed that the addition of TiO_2 filler improves the ionic conductivity and lowers the interfacial resistance in the PMMA and PEGDA polymer blends. The effect supports this idea

which says that the addition of ceramic filler does not impede the mobility of lithium ions in the polymer matrix. The enhancement of ionic conductivity with dispersion of filler is mainly due to the decrease in the crystalline phase of the polymer electrolyte. The same theory can also be observed in the Sharma and Sekhon (2007) review. In this research, the addition of fumed silica on GPEs exhibits higher ionic conductivity than the corresponding conventional liquid electrolytes. They suggested that the aggregation of ions were dissociated as the percentage of fumed silica increases.

2.2.8.2 Developments on the Composite Polymer Electrolytes

Several developments had been accomplished onto the composite polymer electrolytes. Ahmad and co–workers found out that dispersion of 6 wt% of SiO_2 had achieved the maximum ionic conductivity with poly(methyl methacrylate) (PMMA) as host polymer, lithium triflate as salt and propylene carbonate (PC) as plasticizer. These CPEs are homogeneous and exhibit wide electrochemical stability with excellent rheological properties at ambient temperature (Ahmad *et al*., 2006b). Organic–inorganic hybrid membranes based on poly(vinylidene fluoride–co–hexafluoropropylene) (PVdF–HFP)/sulfosuccinic acid (SSA) were fabricated with different nano–sized silica particles. The proton conductivity is increased with SiO_2 loadings. The highest proton conductivity of 10^{-2} Scm^{-1} was achieved. The decrease in the filler size induced to the formation of effective pathway of polymer–filler interface and hence promoted the proton conductivity of

the membranes (Kumar *et al*., 2009).

Composite polymer electrolyte containing methylsisesquioxane (MSQ) filler and 1–butyl–3-methyl–imidazolium-tetrafluoroborate ($BMImBF_4$) ionic liquid in poly(2–hydroxyethyl methacrylate) (PHEMA) polymer matrix had been prepared via free radical polymerization of HEMA macromer (Li *et al*., 2005). In this study, MSQ filler improved the mechanical strength of the polymer matrix and increased ionic conductivity by providing the ion conductive pathway. Saikia and Kumar reported the synthesis of P(VDF–HFP)–PMMA–$LiCF_3SO_3$–(PC+DEC)–SiO_2 composite polymer electrolytes and the maximum ionic conductivity of this polymer electrolyte system is found to be 1x 10^{-3} S cm^{-1} at 303K (Saikia and Kumar, 2005). Ahmad and his fellow workers had developed fumed silica–based composite polymer electrolytes. They discovered that the mechanical and thermal stabilities of these CPEs were enhanced by forming three–dimensionals network via hydrogen bonding among the aggregates (Ahmad *et al*., 2008). According to Xie *et al*. (2004), the effects of fumed silica nanoparticles on the conductivities of the polymer electrolytes at temperature above and below their melting points were examined. The ionic conductivities of polymer electrolytes decreased at temperatures above melting point, whereas it is increased below the melting point (Xie *et al*., 2004).

2.3 Poly(methyl methacrylate) (PMMA)

2.3.1 General Description of PMMA

Poly (methyl methacrylate) (PMMA) (also known as poly(methyl 2-methylpropenoate) is a synthetic amorphous polymer of methyl methacrylate. The common name for PMMA is acrylic glass because it is a member of a family of polymers called acrylates and it is often used as alternative to glass. It is a hard thermoplastic with high light transparency and more impact resistant than glass. The structure of PMMA is illustrated as below.

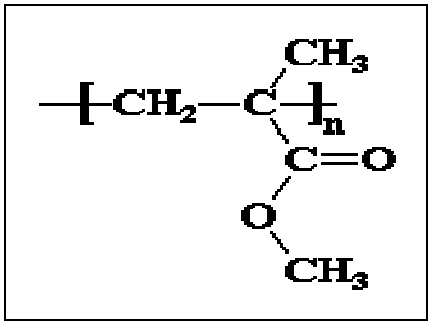

Figure 2.3: Chemical structure of PMMA.

PMMA was polymerized from the monomer methyl methacrylate by free radical initiators such as peroxides and azo compounds via free radical vinyl polymerization and exemplified as below.

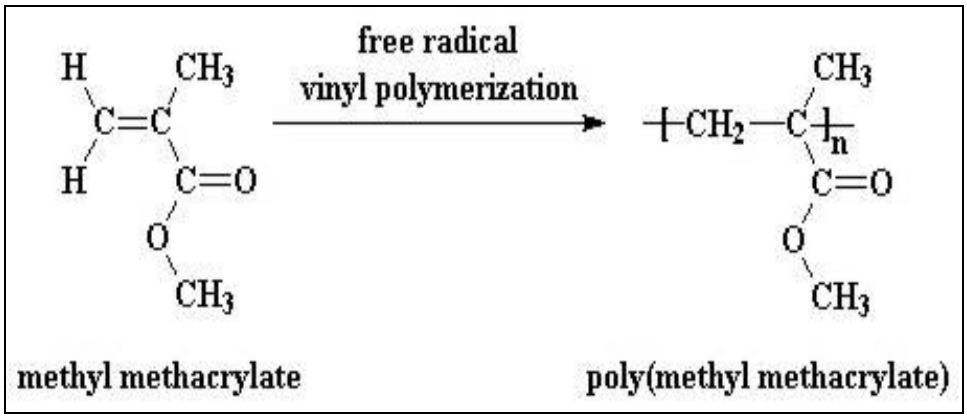

Figure 2.4: Free radical vinyl polymerization of PMMA.

From the figure above, the rigid PMMA was produced due to the substitution of the methyl and methacrylate groups on every carbon of the main carbon backbone chain, providing the steric effects. Various types of anomalous units or different tacticity were produced in the chain during this radical polymerization.

2.3.2 Tacticity of PMMA

Tacticity is one of aspects from stereochemistry that influences T_g. It is a relative arrangement of adjacent chiral centres within the polymer chains. Three stereoregular arrangements are possible to be obtained from PMMA, including isotactic (*iso*–PMMA), syndiotactic (*syn*–PMMA) and atactic (*a*–PMMA) as illustrated in Figure 2.5. The isotatic arrangement occurs when each of the chiral centres has the same configuration, whereas the syndiotactic involving the alternate chiral centres has the same configuration. In contrast, atactic polymer has the random distribution of the substituent groups. The schematic diagram of

different chain structures and arrangement of isotactic PMMA, syndiotactic PMMA and atactic PMMA were shown as below.

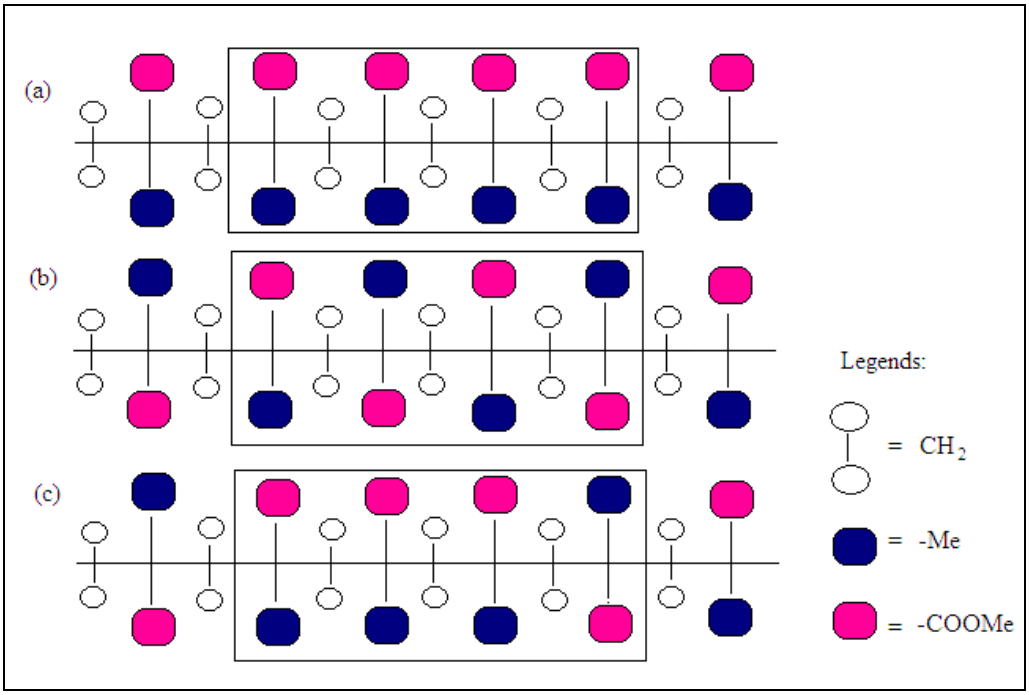

Figure 2.5: Schematic diagram of different chain structures of PMMA where (a) *iso*–PMMA, (b) *syn*–PMMA and (c) *a*–PMMA.

In general, atactic polymers, isotactic and syndiotactic polymers usually are amorphous, semicrystalline and crystalline compounds, respectively. It is due to the ordered structures which are isotactic and syndiotactic are more able to pack into the crystal lattice, whereas the disordered structure is not suitable for packing the lattice. As a result, both isotactic and syndiotactic favor the crystallization and lead to increase in T_g. On the contrary, atactic configuration of polymeric chain inhibits the occurrence of crystallization and results in the amorphous structure due to its random arrangement of the asymmetrical carbon atom.

2.3.3 Reasons to choose PMMA

In the initial study of poly(ethylene oxide) (PEO) with various inorganic lithium salts, PEO showed low ionic conductivity at ambient temperature due to high degree of crystallization (Li *et al*., 2006b). To overcome this obstacle, PMMA was used as it has an amorphous phase and flexible backbone which results high ionic conductivity (Ramesh and Wen, 2009). PMMA is of special interest because it provides a high transparency, good gelatinizing properties, high solvent retention ability and excellent compatibility with the liquid electrolytes (Ahmad *et al*., 2006a; Choi and Park, 2001). In particular, it is easier for handling and processing. Apart from that, it has good outdoor weatherability and good resistance to acid as well as low cost. In addition, it has an excellent environmental stability. Moreover, it has a poor resistance to solvent, thus it can be dissolved easily. PMMA is selected because it has higher surface resistance, compatible with most of the polymers, exhibits good interfacial stability towards the lithium electrodes and high ability to solvate inorganic salts to form complexation between polymer and salt (Choi and Park, 2001; Stephan *et al*., 2002).

2.3.4 Applications of PMMA

The major application of PMMA is in automotive industry, such as rear lamps and light fixtures. Besides, it used as glazing for aircraft and boats, advertisement signs, spectator protection in ice hockey and protective goggles. In

addition, it is used as composite materials for kitchen sinks, basins and bathroom fixtures (Joel, 2003b). It is also used for construction of residential and commercial aquariums.

2.4 Poly(vinyl chloride) (PVC)

2.4.1 General Description of PVC

Apart from PEO, poly(vinyl alcohol) (PVA), poly(acrylonitrile) (PAN), poly(ethyl methacrylate) (PEMA), poly(vinyl chloride) (PVC), poly(vinylidene fluoride) (PVdF) have also been used as polymer host materials. PVC is a thermoplastic polymer where its IUPAC name is poly(chloroethanediyl). It is a vinyl polymer composed of numerous repeating vinyl groups, whereby one of their hydrogen atoms is replaced with a chloride group, as shown as below.

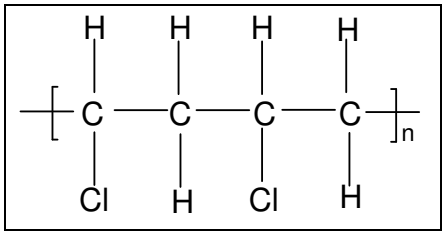

Figure 2.6: Chemical structure of PVC.

PVC is mainly produced by radical polymerization (Endo K, 2002). In this polymerization, it associates the vinyl chloride molecules and thus forms the polymeric chains of macromolecules. However, this radical polymerization of VC results in different tacticity in the chain during polymerization. Again, the tacticity

alters the physical properties and thermal stability of the polymer electrolytes, as discussed in section 2.3.2.

2.4.2 Reasons to Choose PVC

Although the conductivity can be enhanced by introducing PMMA, however, the mechanical strength is reduced. Hence, it exhibits brittle property especially under a loaded force. In this study, PVC was introduced into the polymer blend system to improve the mechanical stability of the polymer electrolytes as it acts as a mechanical stiffener. It can stiffen the polymer backbone through the solvation of inorganic lithium salts by the lone pair electrons at the chlorine atom and also the dipole–dipole interaction between the hydrogen and chlorine atoms (Ramesh and Chai, 2007). PVC is chosen due to its high compatibility with the liquid electrolyte, good ability to form homogeneous hybrid film, commercially available and inexpensive (Li *et al*., 2006). Other unique characteristics are easy processability and well compatible with a large number of plasticizers (Ramesh and Ng, 2009).

2.4.3 Applications of PVC

After polyethylene and polypropylene, PVC is the third most widely produced plastic. The inherent properties of PVC make it suitable for a wide

variety of applications. It is a better choice for most household sewerage pipes and other pipe applications where the corrosion would limit the use of metal as it exhibits biologically and chemically resistant. PVC pipe is the most common PVC product. It has been extensively used as films, sheets and moldings, such as plastic leather and curtain in clothing, lead wire coating, upholstery, tubing, flooring, electrical cable insulation and wallboard as well. Besides, it is widely used in figurines and in inflatable products such as waterbeds, pool toys, and inflatable structures. Even though the scope of the application to electrochemical fields is limited, however, the plasticized PVC has been widely used as membranes in ion selective electrodes. Furthermore, plasticized PVC–based polymer electrolyte systems have been reported to be applicable to lithium and lithium–ion secondary batteries (Uma *et al*., 2005).

2.5 Lithium bis(trifluoromethanesulfonyl) imide (LiTFSI) salt

2.5.1 General Description of LiTFSI

Lithium bis(trifluoromethanesulfonyl) imide (LiTFSI or LiIm) dopant salt is constructed of lithium cation and bis(trifluromethanesulfonyl) imide anion, as shown in the Figure 2.7.

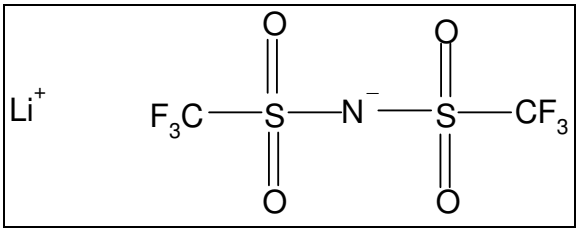

Figure 2.7: Chemical structure of LiTFSI.

As can been seen, the imide anion is stabilized by two trifluoromethanesulfonyl (triflic) groups. The imide anion is very stable due to the delocalization of the formal negative charge. The occurrence of this delocalization is a result of combination of the inductive effect by the electron withdrawing group and the conjugated structure. In other words, the strong electron–withdrawing behavior of triflic groups and the conjugation between triflic group and the lone electron pair on the nitrogen favor the delocalization process of this negative charge. The anion is well delocalized as shown in the figure below (Kang X., 2004).

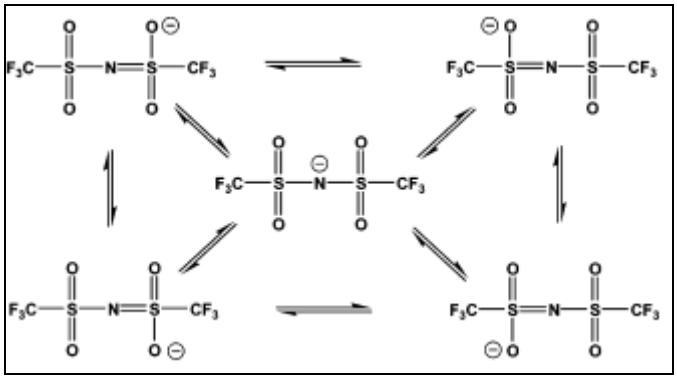

Figure 2.8: Resonance structures of imide (Im) anions.

It is a new designed metal salt to substitute poorly conducting lithium triflate (LiTf), the hazardous $LiClO_4$, the thermally unstable $LiBF_4$ and lithium hexafluorophosphate ($LiPF_6$), and the toxic lithium hexafluoroarsenate ($LiAsF_6$) in lithium battery applications.

2.5.2 Reasons to choose LiTFSI as dopant salt

To further improve the ionic conductivity, the attempt of using lithium bis(trifluoromethanesulfonyl) imide (LiTFSI) had been make because of its large electronegativity and high mechanically flexible anion. In this current study, LiTFSI is used as a salt due to its extensive delocalized electrons in $TFSI^-$ anion which causes a low tendency for coordination with lithium cations by weakening the interactions between alkali metals and nitrogen with the polyether oxygen. Hence, lithium cations are more available for migration and this leads to an increase in ionic conductivity (Ramesh and Lu, 2008). In addition, the attempt of using LiTFSI is because of its non–corrosive behavior towards electrodes and wide electrochemical stability. In addition, it is a safe and promising candidate with excellent thermal stability. It manifests superior thermal properties as it melts at 236 °C without decomposition and does not decompose until 360 °C. Apart from that, this salt can dissociates very well even in low dielectric solvents, although it contains large anion size (Kang X., 2004).

2.6 1–buty–3–methylimidazolium bis(trifluoromethylsulfonyl imide) (BmImTFSI) ionic liquid

As explained in section 2.27, the ionic liquid consists of cations and counteranions. Therefore, the cations and counteranions are the major aspects to concern in the development of ionic liquid as the solubility of ionic liquids is

strongly depending on the nature of cations and counteranions (Jain *et al*., 2005). 1–buty–3–methylimidazolium bis(trifluoromethylsulfonyl imide) (BmImTFSI) ionic liquid is constructed of 1–buty–3–methylimidazolium cation ($BmIm^+$) and bis(trifluoromethylsulfonyl imide) anion ($TFSI^-$), as shown in Figure 2.9.

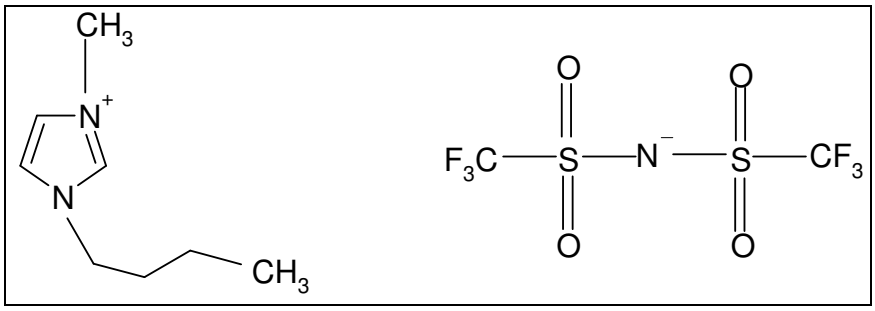

Figure 2.9: Chemical structure of BmImTFSI.

Ionic liquid are commonly composed of various type of cations, for instance, tetraalkylammonium, trialkylsulphonium, tetraalkylphoshonium, 1,3–dialkylimidazolium, N–alkylpyridinium, N,N–dialkylpyrrolidinium, N–alkylthiazolium, N,N–dialkyltriazolium, N,N–dialkyloxazolium, and N,N–dialkylpyrazolium (Jain *et al*., 2005). However, among all the cations, 1,3–dialkylimidazolium (Im) is the appealing cation because of its favorable properties and ease to gather abundant and useful information (Kim *et al*., 2006).

On the contrary, some common anions are employed to form a neutral and stoichiometric ionic liquid such as trifluoromethanesulfonate or triflate ($CF_3SO_3^-$ or Tf^-), tris(trifluoromethylsulfonyl)methide [$C(CF_3SO_2)_3^-$], bis(trifluoromethylsulfonyl imide) [$N(CF_3SO_2)_2^-$ or $TFSI^-$], bis(perfluoroethysulfonyl) imide [$N(C_2F_5SO_2)_2$ or $BETI^-$], tetrafluoroborate (BF_4^-),

hexaflurophosphate (PF_6^-), hexfluoroantimonate (SbF_6^-), zinc(III) chloride ($ZnCl_3^-$), copper(II) chloride ($CuCl_2^-$) and iminodisulfuryl [$N(FSO_2)_2^-$] (Jain *et al*., 2005). However, TFSI anion is chosen because of its bulky structure which enhances the electrochemical stability (Reiter *et al*., 2006). Apart from that, high charge delocalization which occurred across the SO_2–N–SO_2 segment is another reason (Shin *et al*., 2003). Other attribution is high flexibility of this anion by showing two low energy conformations and eventually, accelerating the ionic dissociation. In general, low viscosity of RTILs aids to help in improvement of ionic mobility among the polymer matrix. The viscosity of anions in the 1–alkyl–3–methyl imidazolium–based molten salts decreases in the order: Cl^-> PF_6^-> BF_4^-> $TFSI^-$ (Jain *et al*., 2005). It can therefore be concluded that 1–alkyl–3–methyl imidazolium bis(trifluoromethylsulfonyl imide) ionic liquid is a versatile candidate.

2.7 Fumed Silica (SiO_2)

2.7.1 General Description of SiO_2

Fumed silica is used as inorganic filler in this study. Fumed silica was produced from a continuous flame hydrolysis technique of silicon tetrachloride in a hydrogen–oxygen flame. Two processes are involved in the production of fumed silica. Firstly, silicon tetrachloride ($SiCl_4$) is converted to the gas phase. Then, it reacts with water to yield silica (SiO_2) and hydrochloric acid (HCl), as shown below.

$$SiCl_4 + H_2O \rightarrow SiO_2 + HCl \qquad \text{(Equation 2.2)}$$

The HCl is easily separated out as it remains in the gas phase, while the fumed silica is in solid form. The fumed silica produced is a hydrophilic compound due to the presence of hydroxyl groups on the surface. In addition, the treated grades of fumed silica are produced by reacting fumed silica with organosilicons and they will convert the natural hydrophilic into a hydrophobic behaviour.

The physical gel appearance is obtained through formation of hydrogen bonding and Van der Waals attraction forces as the fumed silica is hydrophilic (Li *et al*., 2006b). In particular, fumed silica has unique properties and it is commonly added to liquids and solids to alter their properties. Since fumed silica has chain–like particle morphology, therefore the chains are then bonded together with surface of hydroxyl group via weak hydrogen bonds, resulting in a three–dimensional network among the aggregates. These three–dimensional networks will trap the liquid molecules and hence increases the viscosity.

There are some applications for fumed silica, including filler for rubbers and plastics, coatings, adhesives and sealants. Besides, it is widely used in the manufacturing of cosmetics, pharmaceuticals, pesticides, inks, batteries and abrasives (The A to Z of materials, 2002).

2.7.2 Advantages of SiO_2

The dispersion of nano–sized SiO_2 does not only enhance the mechanical properties such as modulus, tensile or tear strength and abrasion resistance of the polymer electrolytes, but also increases the ionic conductivity of the CPEs. Nano–sized fumed silica (SiO_2) is a superior candidate as inorganic inert filler because it provides large surface contact area with its branched primary structure. It thus enhances the volume fraction of amorphous proportion of polymer systems and thereby increases the ionic conductivity. Apart from that, the incorporation of SiO_2 improves interfacial stability for the electrolyte in contact with lithium metal via the mechanism and also lithium transportation (Srinivasa *et al*., 1998).

Moreover, it has high ability to tailor the surface functionalities by forming the native surface onto fumed silica, which is silanol (Si–OH) (Ahmad *et al*., 2005; Osinska *et al*., 2009). Besides, it gives rise to flaw by reducing the fracture strength in the polymer chains and thus causes the elongation of failure. In the CPEs, the fumed silica is used as a catalyst support instead of the catalyst (Ahmad *et al*., 2006a). It also leads to a superior thermal stability and has a wide electrochemically stable potential window. Upon addition of fumed silica into the polymer electrolyte, a highly transparent in the visible region of the thin film would be formed.

2.8 Fundamentals of Instruments

Various types of analytical and evaluative methods are available in the polymer field. Several instruments were used to characterize the polymer blend electrolytes. These instruments include impedance spectrometer, horizontal attenuated total reflectance–Fourier Transform Infrared (HATR–FTIR) spectrometer, X–ray diffractometer, scanning electron micrometer, differential scanning calorimeter, thermogravimetric analyzer and rheometer. Impedance spectroscopy was employed to study the ionic conductivity, electrical and dielectric properties of the polymer electrolytes. However, the structural and thermal analyses are of great interest. The structural characterizations of polymer blend electrolytes were also investigated by X–ray diffraction (XRD), scanning electron microscopy (SEM) and HATR–FTIR spectroscopy. On other hand, rheometer is used to envisage the physical properties of the polymer systems, includes elastic properties and viscosity.

2.8.1 AC–Impedance Spectroscopy

Impedance spectroscopy (IS) is a powerful analytical tool to characterize the electrical properties of materials and their interfaces with electronically conducting electrodes. It is also widely been used to envisage the dynamics of bound or mobile charge in the bulk or interfacial regions of any kind of solid or liquid material: ionic, semiconducting, mixed electronic–ionic and even insulator

(dielectric). This spectroscopy is not only well known in determination of ionic conductivity for solid electrolyte; it also extended for other solid dielectrics (Barsoukov & Macdonald, 2005a). It is an extensive method because it involves a simple electrical measurement that can readily be automated. The impedance diagram can be much more informative because it is correlated with complex materials variables, ranging from mass transport, rates of chemical reactions, corrosion and dielectric behavior, to defects of crystalline portion, microstructure, and compositional influences on the conductance of solids. The microscopic parameters such as mobility of charge carriers, concentrations and rates of electron transfer reaction can also be predicted through the characterization in the impedance response. In addition, it has been used to investigate the membrane behavior in living cells as it can estimate the aspects of the performance of chemical sensors and fuel cells. It also serves as an empirical quality control procedure via the interpretation of fundamental electrochemical and electronic processes. The true grain resistance is obtained as it decouples the grain and grain boundary effects (Barsoukov & Macdonald, 2005a).

The principle of the impedancemetry is based on the ability of a medium to pass an alternating electrical or frequency current. It is well functioned by conducting current and measuring the potential difference created by the circulation of this current. AC–impedance study also provides the quantitative information about conductance, capacitance, dielectric coefficient, static properties of the interface and its dynamic change due to adsorption or charge–transfer phenomena. When an electric field is applied across the sample, the polar group

might be activated as dipoles which always interact with the corresponding ions due to the Coulombic electric force. Thus, these dipole moments will rearrange themselves under the influence of the external electric field, depending on the mobility of backbone. So, lithium cations can travel faster along these activated or polarising areas to reach opposite of the electrode and generate current (Selvasekarapandian *et al.*, 2006).

The complex impedance (Z) plot consists of 2 parts, that are real part (Z') and imaginary part (Z'') as shown in Figure 2.10. In the frequency domain, Z' and Z'' are denoted as dispersion and absorption of the spectrum at each excitation, respectively. Basically, $Z = Z' + jZ''$ where j is a constant. Z' is plotted on the x–axis whereas the Z'' is plotted on the y–axis.

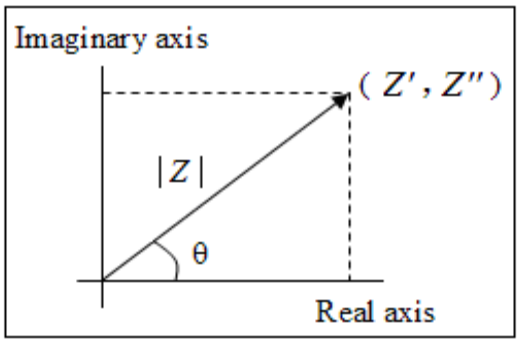

Figure 2.10: Magnitude of impedance (Z) of pseudo straight line.

From the figure above, Z' and Z'' are determined by using equations 2.3 and 2.4 as exemplified as below.

$$Z' = |Z| \cos \theta \qquad \text{(Equation 2.3)}$$

$$Z'' = |Z| \sin \theta \qquad \text{(Equation 2.4)}$$

where θ is the phase of impedance

However, there is a main shortcoming for the complex impedance. From the entire data plot, the indication of frequency is absent. Therefore, it can be concluded that low frequency data are located on the right side of the plot whereas the higher frequency are on the left side (Rajendran *et al*., 2002).

2.8.2 Dielectric Study

Frequency dependence studies of the conductivity and of the dielectric response are useful techniques to obtain the detailed information of ionic conduction mechanism and differences in ion–polymer interactions in polymer electrolytes (Gray, 1991c). Dielectric relaxation study is an approach to investigate the dynamic and relaxation behavior of the electric dipoles in the polymer matrix by studying the electrode polarization effect onto the polymer electrolytes (Gray, 1991c; Rajendran *et al*., 2004). Conductivity relaxation refers as a phenomenon where the time is required to build up the charge carriers at the electrode–electrolyte interface before the electric field changes the direction (Baskaran *et al*., 2006a). The resulting in a net cumulative moment will give rise to a relaxation. The build up of the charge carriers are known as polarization. The polarization disappears when the voltage is removed (West, 1999a).

In general, there are three types of relaxation process in the dielectric study: α' relaxation, α relaxation and β relaxation. α' relaxation depends on the molecular weight and its amplitude is lower than others, ascribing to crystal–disordering mechanism. In contrast, α relaxation is a relaxation in the amorphous phase which emphasizes onto the relationship between the segmental mobility of polymer chains and their strong Arrhenius behavior in temperature dependence study. Empirical Vogel–Tamman–Fulcher (VTF) equation is mainly been used to explain α relaxation by exhibiting a non-linear temperature dependence study. On the contrary, β relaxation is related to the localized motions of the structural units and it has a weaker Arrhenius–type behavior in temperature dependence study (or linear relationship). It is associated with an amorphous transition involving short–range bond rotations (Fernandez *et al*., 2008).

The real part of dielectric relaxation constant (also known as dielectric constant, ε') is the direct measure of stored charge in a material (Kumar and Bhat, 2009), whereas imaginary permittivity of the dielectric relaxation constant (also known as dielectric loss) is a direct measure of dissipation of energy which generated from transportation of charge carriers and polarization effect of charge carriers (Stephan *et al*., 2000b). It is used to study the energetic of relaxations of complex ionic defects (Barsoukov & Macdonald, 2005b). Polymer electrolytes should possess high dielectric strength and low dielectric loss. It is because the low dielectric constant will limit the reduction of the dimensions of the polymer electrolytes. As a result, the existence of strong electric fields will alter and

degrade the device performance. On the other hand, high dielectric constant is able to withstand high voltages without undergoing the degradation (West, 1999a).

2.8.3 Horizontal Attenuated Total Reflectance–Fourier Transform Infrared (HATR–FTIR) Spectroscopy

The main fundamental of FTIR is to determine structural information about a molecule. FTIR brings greater versatility to polymer structural studies. It facilitates the study of such polymer reactions as degradation or cross–linking because the spectra can be scanned, recorded and transformed into a matter of seconds. Besides, it is a qualitative identification of unknown sample. It is accomplished by the comparison. In addition, it allows the spectra to generate the hidden spectra via digital subtraction. A very small size is sufficient to undergo the analysis for highly localized sections of the sample by coupling the FTIR instrument with a microscope. FTIR is also used to study the polymer blends. If the immiscible blend of polymers, the IR spectrum will exhibit a superposition of two homopolymer spectra. Additionally, the interaction which arises from chemical or physical interaction between the homopolymer is also exhibited (Malcolm and Stevens, 1999b).

The main principle of FTIR is based on interferometry which is an optic study. It separate infrared beam of light which serves as light source radiation into two ray beam. Once the beam of infrared is passed through the sample, the molecules absorb infrared radiation and then excited to a higher energy state. Thus,

the energies associated with these vibrations are quantized; within a molecule, only specific vibrational energy levels are allowed. The amount of energy absorbed at each wavelength was recorded. The frequencies which have been absorbed by the sample are determined by detector and the signal is amplified. Hence, IR spectrum was obtained. FTIR spectroscopy is not only applied in the crystalline region of complexation, whereas the complexation in amorphous phase can also be determined (Ramesh and Chai, 2007).

On the contrary, HATR is an internal reflection accessory which can simplify the FTIR analysis of pastes, gels, semi–solids, powders and films. The FTIR spectrum is easily to be collected via this horizontal sampling surface, with minimal sample preparation, in all laboratory environments. HATR used to analyze samples that are too strongly absorbing for conventional transmittance measurements, because HATR is a surface–sampling technique. HATR is supplied with a top plate fitted with a Zinc Selenide (ZnSe) crystal.

2.8.4 X–ray Diffraction (XRD)

XRD is used as fingerprint method to detect the presence of a known compound or phase in a specimen. It is a useful method in the identification of compounds for qualitative analysis. It is also widely been probed to provide a rough check of the purity of sample (Smart and Moore, 2005b). It is an identification of unknown crystalline materials, characterization of crystalline

material and determination of unit cell dimensions. In general, X–ray is an electromagnetic radiation of wavelength ~1 Å (10^{-10}m) and lies between γ–ray and the ultraviolet in the electromagnetic spectrum. A filament, usually tungsten, is electrically heated and thus a beam of electrons are emitted. These electrons are accelerated by a high potential difference (20–50kV) and thus allowed to strike a metal target, often copper (Cu). The incident electrons have sufficient energy to knock out (or ionize) electrons from the innermost K shell ($n=1$) and this in turn creates vacancies. An electron in an outer orbital ($2p$ or $3p$) immediately drops down to occupy the vacant and the energy released appears as radiation, as shown in Figure 2.11. The electrons descending from the L shell ($n=2$ or $2p$) produce K_α lines with a wavelength of 1.5418 Å, whereas the electrons from the M shell ($n=3$ or 3 p) will give rise to K_β lines with wavelength of 1.3922 Å. K_α transition occurs more frequently than K_β transition. K_α line is usually selected and K_β line is filtered out by using a filter made of nickel metal foil. In XRD, monochromatic radiation, which defined as single wavelength or a very narrow range of wavelengths, is required (West 1999b; Smart and Moore, 2005b).

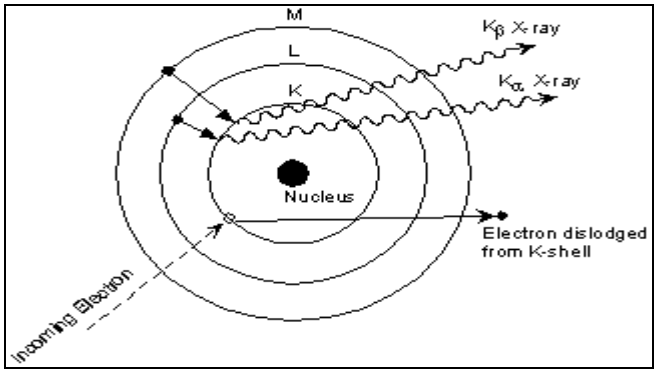

Figure 2.11: Generation of K_α and K_β transitions.

Bragg's law is executed in powder diffraction technique. In this approach, XRD behaves like "reflection" from the planes of atoms within crystal and that only at specific orientations of the crystal with respect to the source and detector are X–rays "reflected" from the planes. Figure 2.12 illustrates the Bragg condition for the reflection of X–rays by a crystal. Two X–rays beams, Ray 1 and Ray 2, are reflected from adjacent plans, where the spacing between the atomic planes occurs over the distance, *d*. Ray 1 reflects off the upper atomic plane at an angle of θ which equal to its incident angle. Similarly, Ray 2 reflects off the lower atomic plane at the same angle θ. However, it has to travel the extra distance *xyz* (or distance of 2a) as compared to Ray 1. For the reflected beams to emerge as a single beam of reasonable intensity, they must reinforce, or arrive in phase with one another. This phenomenon is known as constructive interference. For constructive interference to take place, the path lengths of the interfering beams must differ by an integral number of wavelengths (nλ). The perpendicular distance between pairs of adjacent planes (*d)* and the angle of incidence, or Bragg angle (θ) are related to the distance *xy* by

$$xy = yz = d \sin \theta \qquad \text{(Equation 2.5)}$$

The difference in path length between the two beams is given by:

$$\text{Difference in path length} = xy + yz \qquad \text{(Equation 2.6)}$$

Thus, difference in path length = $2d \sin \theta$

This must be equal to an integral number, *n*, of wavelengths. If the wavelength of the X–rays is λ, then

$$n\lambda = 2d \sin \theta \qquad \text{(Equation 2.7)}$$

This is known as the Bragg equation. At angles of incidence other than Bragg angle, the reflected beams are out of phase and destructive interference or cancellation occurs (West 1999b; Smart and Moore, 2005b).

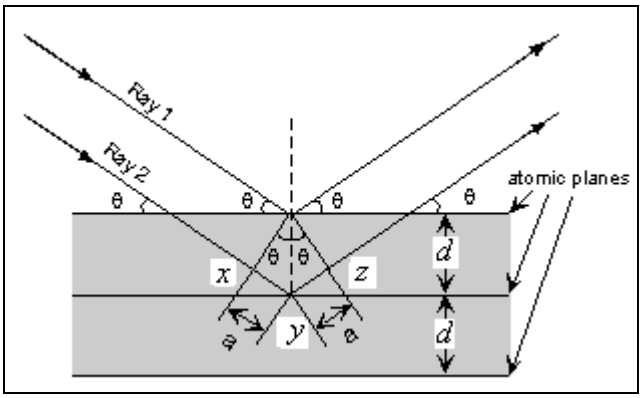

Figure 2.12: Derivation of Bragg's law.

A finely ground crystalline specimen consists of abundant of small crystals, which known as crystallites. These crystallites orient randomly to one another. The sample is placed in the path of a monochromatic X–ray beam, the planes in these crystallites will orient at the correct angle to fulfill the Bragg condition and hence form the diffraction. The diffracted beams make an angle of 2θ with the incident beam. The collection of powder diffraction patterns is performed by automatic diffractometers. A scintillation or CCD detector is used to record the angle and the intensity of diffracted beams, which are plotted as intensity against 2θ (Smart and Moore, 2005b). The increase in the width of the diffraction peak indicates the decrease in the crystallite size.

2.8.5 Scanning Electron Microscopy (SEM)

In the characterization of solid–state compound, scanning electron microscopy (SEM) is widely used to investigate the structure, morphology and crystallite size, to examine the surface defects of crystal, and to determine the distribution of elements (Smart and Moore, 2005b). In this technique, an electron beam is produced by heating the tungsten filament and then focused by magnetic fields in a high vacuum. The vacuum prevents the interaction of the beam with any extraneous particles in the atmosphere. The electrons from this finely focused beam are scanned across the surface of a sample in a series of lines and frames called a raster. At any given moment, the specimen is then bombarded with electrons over a very small area. These electrons may be elastically reflected by the surface of the sample with no loss of energy (backscattered electrons), they may be absorbed and emitted secondary electrons of low energy, they may be absorbed and give rise to the emission of visible light, and they may give rise to electric currents within the specimen. All these effects can be detected and hence given a map of the surface topography of samples (Braun, 2005c; Smart and Moore, 2005b). Some of the samples may need to be coated with gold or graphite to stop charge building up on the surface of the specimen (Smart and Moore, 2005b).

For backscattered electrons, the atomic number of the elements in the sample is used to determine the contrast in the produced image. The image will show the distribution of different chemical phases in the sample. The resolution in

the image is not as good as for secondary electrons because of the emission of these electrons from a depth in the sample. Among all the means, the low–energy secondary electron technique is the most common method. The primary electrons enter a surface of the specimen with an energy of 0.5–30keV and generate many low–energy secondary electrons. The intensity of these secondary electrons is mainly governed by the surface topography of the sample. The image of the sample can thus be constructed by measuring secondary electron intensity as a function of the position of the scanning primary electron beam. High spatial resolution can be obtained because the primary electron beam can be focused to a very small spot (< 10nm).

2.8.6 Differential Scanning Calorimetry (DSC)

Thermal analysis is a technique to investigate the properties of solids as a function of a change in temperature. In this work, the thermal analyses employed are differential scanning calorimetry (DSC) and thermogravimetric analysis (TGA). DSC is a quantitative study of thermal transitions of polymer matrix by heating polymer sample and an inert reference. The reference is either an empty cup or a cup containing an inert material, such as anhydrous alumina. In DSC, the individual heaters are provided to the sample and reference. Then, the energy is supplied to isothermal both of the samples and reference. Hence, the electrical power difference between sample and reference ($d\Delta Q/dt$) is measured. The data are plotted as $d\Delta Q/dt$ on the coordinate against temperature on the abscissa and the

plots are known as thermograms. The major advantage of DSC is the peak areas of thermograms are directly related to enthalpy changes in the sample. Therefore, the data obtained can be used for measurements of heat capacities, heats of fusion and enthalpies of reactions (Malcolm and Stevens, 1999b). In addition, DSC measures the amount of heat released by a sample as the temperature is increased or decreased at a controlled uniform rate (Smart and Moore, 2005b).

The basic principle of DSC depends on the amount of heat needed to flow in to maintain the samples and reference at the same temperature when the samples undergoes some physical transformation such as phase transition. Thus, exothermic and endothermic reactions play a vital role. In general, endothermic reaction is a process that absorbs energy in the form of heat, whereas for the exothermic process, heat will be released. So, the endothermic process such as melting process at which the matrix polymer electrolytes is melted to a liquid form will require more heat flowing into the sample to increase its temperature at the same rate as the reference. On the other hand, the heat required is lesser to raise the temperature of sample if it undergoes an exothermic phase transition such as crystallization from matrix polymer to liquid state. Therefore, both the sample and reference are maintained nearly at the same temperature throughout the experiment. In general, the temperature program for a DSC analysis is designed to ensure temperature of the sample holder increases linearly as a function of time. In conclusion, the DSC plays an important role to determine the glass transition temperature (T_g), crystallization temperature (T_c) and crystalline melting point

(T_m). Other than that, the decomposition temperature (T_d) can also be obtained as well.

T_g is a vital characteristic of the amorphous behavior of a polymer during the transition from solid to liquid (or melt) state. The kinetic energy of the molecules increases if an amorphous polymer is heated. As the polymer retains in the glass–like properties, the mobility of molecules are still restricted even there is a presence of short–range vibrations and rotations. As the temperature is further increased or the polymer matrix is further melted, its glass–like structure will be converted into rubbery state which is soft and elastomeric. This characteristic temperature is known as T_g. At this transition, it is accompanied by more long range molecular motion and thus the degree of rotational freedom increases. As a result, there is more segmental movement among the atoms of the chains. Thus, the space between the atoms will be increased and then results in the increase of the specific volume.

It is less commonly known as second–order transition temperature because it is associated with a change in heat capacity but no latent heat is involved in this process. It depends on the chemical nature of the polymer, on the configuration, on the degree of crystallinity, on the length of the side chains, and on the degree of branching (Braun, 2005c). There are two methods to determine T_g. Firstly, the temperature at which this change in specific volume takes place was determined by dilatometry method. Another method to measure T_g is called calorimerty. It is

based on the enthalpy change of the polymer at the glass transition. In contrast, the modulus (also known as stiffness) decreases appreciably and it is readily detected by using mechanical measurement.

After it reaches above T_g, the molecules start to gain the freedom in motion. Once they reached a particular stage where they have enough freedom of motion, thus they will arrange themselves spontaneously into a crystalline form. At this state, it is known as crystallization temperature (T_c) and the heat is given out. So, it is an exothermic reaction and it results a peak in the DSC thermograms as shown in Figure 2.13. As the polymer is further heated, it will lose the elastometric properties and it melts to a flowable liquid. At this point, the crystalline melting temperature, T_m is reached. In this transition, an endothermic process was undergone. Transitions like crystallization and melting, which do have latent heats, are called as first–order transitions. If the heating is continued, the polymer will be degraded and it is known as decomposition temperature, T_d (Malcolm, 1999b).

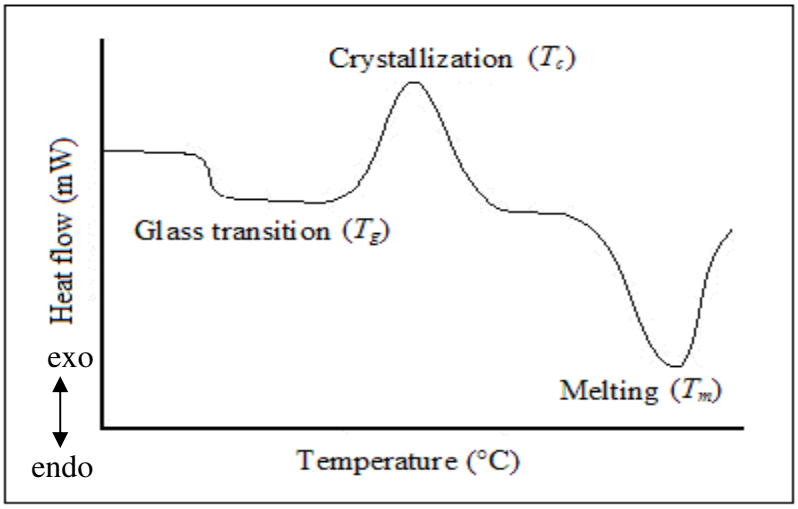

Figure 2.13: A schematic DSC thermogram demonstrating the appearance of several common features, which are glass transition, crystallization and melting process.

2.8.7 Thermogravimetric Analysis (TGA)

TGA is a versatile thermal and primarily used to determine thermal stability and thermal degradation of the samples as a function of change in temperature under inert conditions. In general, the thermal stability is concerned with chemical transformations. The main principle of TGA is to monitor the weight of the samples on a sensitive balance (also known as thermobalance) continuously as the sample temperature is increased under an inert atmosphere or air at a controlled uniform rate. The data were recorded as a thermogram of weight which is in y–axis against sample temperature which is in x–axis. In addition, the TGA is used to characterize the polymer in a copolymer by monitoring the weight loss of a known entity which correlated to percentage of the polymer into the copolymer.

Apart from that, it also used to determine the volatilities of plasticizers and other additives (Malcolm and Stevens, 1999b). TGA does not only capable of determining the weight loss or weight gain of a polymer after heated at high temperature, it can also be used to determine the melting point (T_m) and decomposition temperature (T_d). T_m can be further confirmed with the result obtained from the DSC. At low temperature, the weight loss may results from evaporation of residual solvent and moisture, whereas the decomposition of polymer is the contributor for the weight loss at high temperature. There are several factors affect the TGA curve. The primary factors are heating rate and sample size. Other features such as the particle size of the sample, its morphology, and the gas flow rate can also affect the progress of thermal reaction (Braun, 2005c).

2.8.8 Rheological Studies

As usual, the ionic conductivity is closely related to the viscosity of sample. For instances, low viscosity of sample will produce high ionic conductivity by forming more voids within the polymer matrix. Therefore, the physical properties of samples are also well been studied in order to understand the effect of physical characteristics onto bulk ionic transportation further. In general, all materials can behave as solid or liquid. Solid–like materials flow as liquids under a sustained shear stress at very long time (or equivalently at very low frequency). It can

therefore be concluded that all materials are visco–elastic and it depends on the timescale of deformation.

Rheology study is a well known physical technique to study the flow and deformation properties of materials (Kavanagh and Murphy, 1998). It is composed of two main tests that are rotational test and oscillation test. Rotational test is used to determine to the flow behavior of sample after the stress was applied onto the sample, whereas the viscoelastic behavior is explored by oscillation test. Examples of rotational test are flow curve, viscosity curve and thixotropy which defined as structure recovery. On the other hand, oscillation test are such as amplitude sweep (AS), frequency sweep (FS) and temperature sweep (TS). Amplitude sweep is probed to study the linear visco–elastic (LVE) range of the sample, whereas frequency sweep is the oscillatory equivalent to the rotational flow curve which scrutinizes the long–term structural stability of samples.

Amplitude sweep is designed to measure the visco–elastic properties of samples without the disruption of the internal structures (Ebagninin *et al*., 2009). A sinusoidal stress as a function of the angular frequency (ω) and the stress amplitude (τ_0) is applied on the samples with its responding sinusoidal strain (Durairaj *et al*., 2009). Both applied stress and resultant strain are expressed as below:

$$\tau = \tau_0 \sin(\omega t) \qquad \text{(Equation 2.8)}$$

$$\gamma = \gamma_0 \sin(\omega t + \delta) \qquad \text{(Equation 2.9)}$$

where ω is angular frequency and $\omega=2\pi f$, f being the frequency in Hertz (Hz); t is the time and δ is phase shift. The ratio of the applied shear stress to the maximum strain is known as complex modulus (G^*) and it is a measure of the resistance of a material to deform. The complex modulus is illustrated as

$$G^* = G' + G'' \qquad \text{(Equation 2.10)}$$

where G' is storage modulus and G'' is loss modulus.

The proportion of elastic (solid) properties is determined by storage modulus (G') which defined as a measure of elastic energy. On the contrary, loss modulus (G'') is employed to characterize viscous (liquid) behavior and it is the dissipation of viscous energy. Both storage and loss moduli are given by:

$$G' = \left(\frac{\tau_0}{\gamma_0}\right)\cos\delta = G^*\cos\delta \qquad \text{(Equation 2.11)}$$

$$G'' = \left(\frac{\tau_0}{\gamma_0}\right)\sin\delta = G^*\sin\delta \qquad \text{(Equation 2.12)}$$

where τ_0 is stress amplitude; γ_0 is strain amplitude and δ is the phase angle between the stress and strain (or known as loss angle) within $0<\theta<90°$. In principle, the material is pure elastic system when the resultant stress wave is exactly in

phase with the strain, along with δ=0. On the other hand, when the rate of change of sinusoidal oscillation is a maximum and the strain is becoming to zero, the perfect viscous sample is described if the resultant stress wave is exactly π/2 (or equivalent as 90°) out of phase with the imposed deformation (Kavanagh and Murphy, 1998; Durairaj *et al*., 2009; Ebagninin, 2009).

CHAPTER 3

MATERIAL AND METHODS

3.1 Materials

The host polymers, PMMA with an average molecular weight of 350000 was obtained from Aldrich while high molecular weight of PVC was obtained from Fluka. The inorganic dopant salt, LiTFSI and ionic liquid, BmImTFSI were obtained from Fluka and Sigma–Aldrich, respectively. The nanocomposite inorganic filler, SiO_2 with the particle size 7 nm was obtained from Sigma–Aldrich while the solvent, tetrahydrofuran (THF) AR. grade was obtained from J.T.Baker. All materials were used without further purification. All the polymer blend electrolytes were prepared by solution casting technique.

3.2 Preparation of Polymer Electrolyte

Prior to the preparation of the polymer electrolytes, LiTFSI was dried at 100 °C for 1 hour to eliminate trace amounts of water in the material. There are four polymer blend electrolytes systems in this work, whereby first and second systems are known as preliminary steps. The quantity of materials added was expressed as weight percent (wt %). Appropriate amounts of materials were dissolved in THF. The solution was then stirred continuously for 24 hours on a hot plate (without heating) at room temperature to obtain a homogenous mixture of

polymer system at room temperature. After that, the solution was cast on a glass Petri dish and allowed to evaporate slowly inside a fume hood.

3.2.1 First Polymer Blend Electrolytes System

First polymer blend electrolytes system was employed to figure out the most compatible ratio of PMMA to PVC. Solid polymer electrolytes were formed in this system. The compositions prepared were [xPMMA–(1–x)PVC] where x is 0.1, 0.2, 0.3, 0.4, 0.5, 0.6, 0.7, 0.8 and 0.9, with a fixed amount of LiTFSI. 10 wt% of LiTFSI was fixed. The compositions of PMMA and PVC and their designations were tabulated in table below.

Designations	**Compositions of PMMA: PVC**	
	PMMA (wt %)	**PVC (wt %)**
PE 1	90	10
PE 2	80	20
PE 3	70	30
PE 4	60	40
PE 5	50	50
PE 6	40	60
PE 7	30	70
PE 8	20	80
PE 9	10	90

Table 3.1: Designations of first polymer blend electrolytes system.

3.2.2 Second Polymer Blend Electrolytes System

From first system, 70 wt% of PMMA and 30 wt% of PVC was achieved the highest ionic conductivity. Thus, this ratio is being fixed in this system. In contrast, the most compatible ratio of polymer blends PMMA–PVC to LiTFSI was determined in second polymer blend electrolytes system. Similarly, solid polymer electrolytes were formed. The quantity of LiTFSI salt added into the polymer blends was ranged from 5 wt% to 50 wt%. The weight fractions of polymer blends to LiTFSI and their designations are shown in Table 3.2.

Designations	Compositions of PMMA–PVC : LiTFSI	
	PMMA–PVC (wt %)	LiTFSI (wt %)
SPE 1	95	5
SPE 2	90	10
SPE 3	85	15
SPE 4	80	20
SPE 5	75	25
SPE 6	70	30
SPE 7	65	35
SPE 8	60	40
SPE 9	55	45
SPE 10	50	50

Table 3.2: Designations of second polymer blend electrolytes system.

3.2.3 Third Polymer Blend Electrolytes System

BmImTFSI ionic liquid was further added in third polymer blend electrolytes system, leading to formation of gel polymer electrolytes. The BmImTFSI content dispersed in the polymer electrolytes lies within the range of 10 and 90 wt%. PMMA–PVC (70 wt%) and LiTFSI (30 wt%) were employed as

fixed variables as SPE 6 achieved the maximum ionic conductivity in previous system. Table 3.3 shows the variation of the compositions of polymer blend electrolytes (PMMA–PVC–LiTFSI) and ionic liquid and their designations.

Designations	Compositions of PMMA–PVC–LiTFSI : BmImTFSI	
	PMMA–PVC–LiTFSI (wt %)	BmImTFSI (wt %)
IL 1	90	10
IL 2	80	20
IL 3	70	30
IL 4	60	40
IL 5	50	50
IL 6	40	60
IL 7	30	70
IL 8	20	80
IL 9	10	90

Table 3.3: Designations of third polymer blend electrolytes system.

3.2.4 Fourth Polymer Blend Electrolytes System

Since IL 6 exhibited the highest ionic conductivity, thus the ratio of 40 wt% of PMMA–PVC–LiTFSI to 60 wt% of BmImTFSI is fixed in this system. Nanocomposite polymer electrolytes were formed in fourth system by dispersing nano–sized SiO_2. In this work, addition of 2, 4, 6, 8 and 10 wt % of SiO_2 was investigated and assigned as CPE 1, CPE 2, CPE 3, CPE 4 and CPE 5, respectively, as tabulated as follow:

Designations	Compositions of PMMA–PVC–LiTFSI–BmImTFSI : SiO_2	
	PMMA–PVC–LiTFSI–BmImTFSI (wt %)	SiO_2 (wt %)
CPE 1	98	2
CPE 2	96	4
CPE 3	94	6
CPE 4	92	8
CPE 5	90	10

Table 3.4: Designations of fourth polymer blend electrolytes system.

3.3 Characterizations of Polymer Electrolytes

3.3.1 Impedance Spectroscopy

The prepared samples were subjected to alternating current (AC)–impedance spectroscopy for ionic conductivity studies. The thicknesses of the polymer electrolytes were measured by using a micrometer screw gauge. The parameter of thickness of the polymer electrolytes is very vital because the result may be affected if there is any change of thickness. The measurement of thickness should be repeated a few more times onto the surroundings of the samples in order to obtain an average thickness. It aims to produce a more precise result. The ionic conductivities of the samples were determined, by using HIOKI 3532–50 LCR HiTESTER, over the frequency range of 50 Hz to 1 MHz. Two stainless steel (SS) blocking electrodes were used in this study with the configuration SS/ PE/ SS.

3.3.1.1 Ambient Temperature–Ionic Conductivity and Temperature Dependence–Ionic Conductivity Studies

For ambient temperature–ionic conductivity, the ionic conductivities of the samples were measured at room temperature. On the other hand, the measurements of ionic conductivities of the polymer electrolytes were taken from ambient temperature until 80 °C, for temperature dependence–ionic conductivity studies. The bulk ionic conductivity of polymer electrolytes is determined by using the equation below.

$$\sigma = \frac{\ell}{R_b A} \quad \text{(Equation 3.1)}$$

where ℓ is the thickness (cm); R_b is bulk resistance (Ω) and A is the known surface area (cm^2) of polymer electrolytes. The semicircle fitting was accomplished to obtain R_b value. R_b of the thin electrolytes film was calculated from extrapolation of the semicircular region on Z real axis (Z'), as shown in Appendix A. Besides, Z' and Z imaginary (Z'') axis must be in equal scale because the radius of a circle must be the same.

3.3.1.2 Frequency Dependence–Ionic Conductivity Studies

In this study, the conductivity was expressed as below:

$$\sigma = \frac{G\ell}{A} \quad \text{(Equation 3.2)}$$

where G is the conductance (S) which obtained from impedance spectrometer by choosing this parameter.

3.3.1.3 Dielectric Behavior Studies

The complex dielectric behavior of a polymer electrolyte system was expressed as:

$$\varepsilon^* = \varepsilon' + i\varepsilon'' \quad \text{(Equation 3.3)}$$

$$\left|\varepsilon^*\right| = \sqrt{(\varepsilon')^2 + (\varepsilon'')^2} \quad \text{(Equation 3.4)}$$

where ε' and ε'' are real and imaginary parts of dielectric constant of the polymer electrolyte system. On the contrary, these ε' and ε'' of the dielectric constants were determined as follows:

$$\varepsilon' = \frac{C_p \ell}{\varepsilon_o A} \quad \text{(Equation 3.5)}$$

$$\varepsilon'' = \frac{\sigma}{\omega \varepsilon_o} \quad \text{(Equation 3.6)}$$

where C_p is parallel equivalent static capacitance which obtained from impedance spectrometer by choosing this parameter; ε_o is permittivity in free space (also known as electric constant) which is equal to 8.856×10^{-14} Fcm^{-1}; ω is angular frequency and $\omega = 2\pi f$, f being the frequency in Hertz (Hz).

3.3.1.4 Dielectric Moduli Formalism Studies

The complex dielectric modulus can be determined by the equation below:

$$M^* = M' + iM'' \quad \text{(Equation 3.7)}$$

$$\left|M^*\right| = \sqrt{(M')^2 + (M'')^2} \quad \text{(Equation 3.8)}$$

where M^* is the complex dielectric modulus; M' is real part of dielectric modulus and M'' is imaginary part of dielectric modulus. In contrast, M' and M'' are expressed as below:

$$M' = \frac{\varepsilon'}{[(\varepsilon')^2 + (\varepsilon'')^2]} \quad \text{(Equation 3.9)}$$

$$M'' = \frac{\varepsilon''}{[(\varepsilon')^2 + (\varepsilon'')^2]} \quad \text{(Equation 3.10)}$$

3.3.2 Horizontal Attenuated Total Reflectance–Fourier Transform Infrared (HATR–FTIR)

HATR–FTIR analysis was carried out by using FTIR Spectrometer Spectrum RX1 (Perkin–Elmer) with HATR, an internal reflection accessory, in the wave region between 4000 cm^{-1} and 650 cm^{-1}. The resolution of the spectra obtained at room temperature was 4 cm^{-1} and recorded in the transmittance mode.

3.3.3 X–ray Diffraction (XRD)

The amorphous degree of polymer electrolytes was investigated using XRD. The XRD patterns were recorded on a Siemens D 5000 diffractometer with Cu–K_α radiation (λ=1.54060 Å), over the range of 2θ=5–80° at ambient temperature. Debye–Scherrer equation is used to determine the coherence length as shown as below:

$$L = \frac{0.9\lambda}{\Delta 2\theta_b \cos\theta_b} \quad \text{(Equation 3.11)}$$

where λ is X–ray wavelength; θ_b is glancing angle of the peak; $\Delta 2\theta_b$ is full width at half maximum (FWHM). The peak at $2\theta \approx 18°$ was chosen to determine the coherence length for the polymer electrolytes.

3.3.4 Scanning Electron Microscopy (SEM)

Using Leica's SEM (model S440) at 10kV, the morphology of polymer blends at room temperature was studied. Insulators such as pure PMMA, pure PVC and PMMA–PVC samples were coated with a thin layer of gold to prevent electrostatic charging.

3.3.5 Differential Scanning Calorimetry (DSC)

DSC analysis was carried out, under nitrogen flow rate of 50 ml min^{-1}, using a METTLER TOLEDO Thermal Analyzer which comprised of DSC 823^e as the main unit and STARe software. Samples weighing approximately 2–3 mg were hermetically sealed in a 40µl aluminum crucible and then perforated in order to keep the samples at atmospheric pressure. The samples were heated from 25°C to 105°C to remove any traces of solvent and water. The temperature was then maintained at 105°C for 2 minutes to ensure the complete evaporation. The samples were then cooled rapidly to 25 °C and then reheated to 450°C at a heating rate of 10°C min^{-1}. The final heating scan was used to evaluate the T_g, T_m and T_d. The mid point of endothermic reaction is assigned as T_g. The endothermic peak point of melting and decomposition are assigned as T_m and T_d, respectively.

3.3.6 Thermogravimetric Analysis (TGA)

TGA was carried out using a METTLER TOLEDO Thermal Gravimetric Analyser which comprised of TGA/SDTA851^{e} as the main unit and STARe software. Samples weighing 2–3 mg were placed in a 150µl silica crucible. The samples were then heated from 30°C to 400°C, at a heating rate of 10°C min^{-1}, under nitrogen flow rate of 10 ml min^{-1}.

3.3.7 Rheological Studies

Rheological measurements were performed on Anton–Paar Physica MCR 301 rheometer. The geometry was a cone plate with diameter of 60mm and gap height of 0.056mm. All the rheological measurements were carried out at ambient temperature with fresh sample. All the parameters were in logarithm scale. The sample was sandwiched between stainless steel cone plate geometry and a stationary bottom plate and excessive sample is trimmed thereafter. Solvent trap was used to slow down the evaporation process of solvent in the sample. Before starting the test, about 1 min of rest period was allowed, in order to stabilize the normal forces between the polymer electrolytes and the cone plate.

3.3.7.1 Amplitude Sweep and Oscillatory Stress Sweep

Amplitude and oscillatory stress sweeps studies were examined in a log strain ramp from 0.001 % to 150 % with 5 points per decade at angular frequency of $10s^{-1}$. For time setting, 30 measuring points with 5 seconds duration had been set in the whole measurement.

3.3.7.2 Oscillatory Frequency Sweep

All the data acquisitions for frequency sweep tests were carried out over a frequency range between $0.01s^{-1}$ and $0.1s^{-1}$, with 20 measuring points per 5 seconds duration.

3.3.7.3 Viscosity Test

As the profile of viscosity curves, a fixed shear rate parameter, ranging from $0.1s^{-1}$ to $100s^{-1}$, with 32 measuring points per 5 seconds duration were recorded.

CHAPTER 4

RESULTS AND DISCUSSION OF FIRST POLYMER BLEND ELECTROLYTES SYSTEM

4.1 AC–Impedance Studies

Figure 4.1 shows the typical impedance plot for PE 3 at room temperature. In general, this impedance plot has been divided into two well defined regions: a slanted spike at low frequency and a semicircle portion which reveals the characteristic of a parallel combination of R_b and bulk capacitance of the polymer matrix at high frequency (Venkateswarlu *et al*., 2000). However, the spike is slanted at an angle less than 90°. This phenomenon indicates the non–idealism of capacitance and induces to an establishment of double layer at the blocking electrodes or also known as non–Debye effect. It implies that a constant phase element is appeared at the electrode and polymer electrolyte interface and leads to a formation of double layer at the electrodes. In addition, the angle and the amount of inclination is attributed to the distribution of conductivity relaxation time which defined as the time required to build up charges at the electrode and electrolyte interface before the electric field changes the direction (Baskaran *et al*., 2006a).

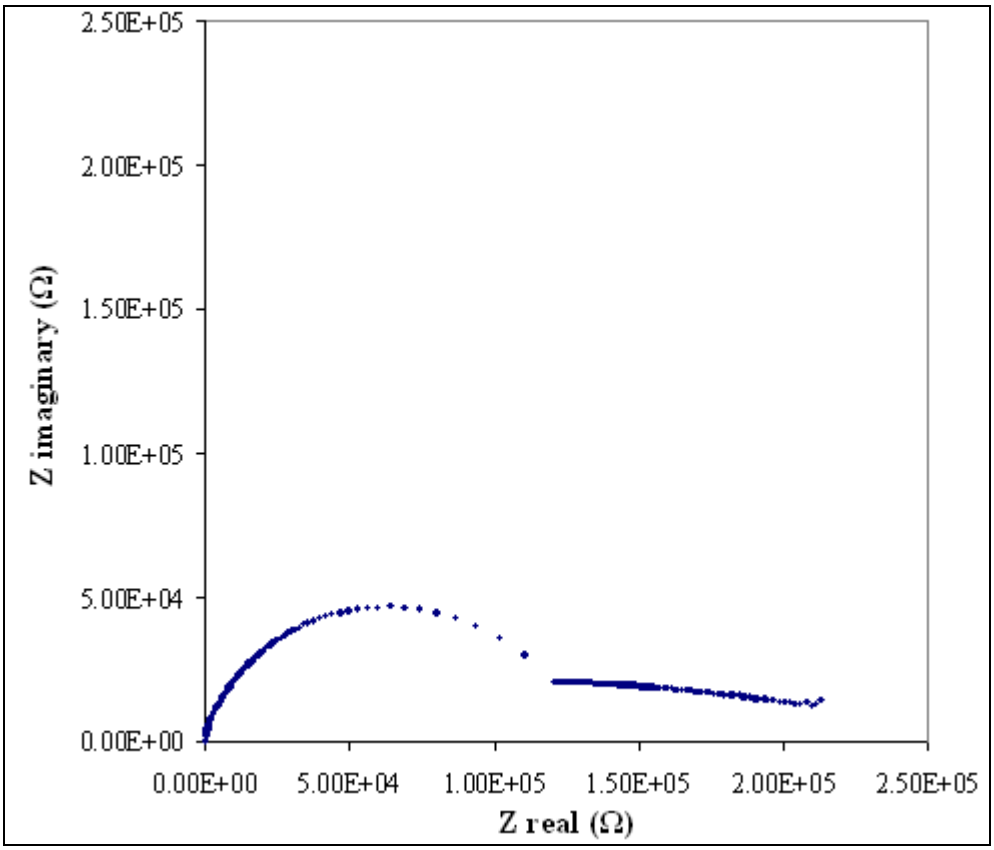

Figure 4.1: Typical Cole–Cole plot for PE 3 at ambient temperature.

4.2 Ambient Temperature–Ionic Conductivity Studies

Figure 4.2 depicts the ionic conductivity of the polymer matrix with different PVC content at ambient temperature. The ionic conductivity of polymer matrix increases with PVC concentration, to an optimum level and then decreases. Initially, the increase in ionic conductivity is due to the long range coulombic forces leading to re–dissociation of solvated ion pairs. Then, more and more number of free mobile charges is produced and these mobile charges are available for segmental transportation in electrolytic conduction. Since the degree of segmental mobility of charge carriers is increased, thus the ionic conductivity is

increased (Fu *et al*., 2003). After 30 wt% of PVC is blended into the system, it exhibits the highest ionic conductivity of $(1.60\pm0.08)\times10^{-8}$ Scm^{-1}as shown in Figure 1. This is because the mobility and concentration of mobile charge has reached an optimum level and induces to this optimum ionic conductivity (Fu *et al*., 2003). Another perception of having the highest ionic conductivity is that the polymer electrolyte had reached the optimum percolation threshold where the formation of percolation pathway will give rise to conductivity behavior of lithium salt in the PE 3 to achieve the maximum limit (Ramesh and Chai, 2007).

As expected, the conductivity decreases as the amount of PVC is increased. It is due to the formation of PVC–rich phase which is a solid–like medium and leads to a hurdle for ion penetration in the electrolytic system. So, the ion must transport via indirect movement along a convoluted pathway restricted to PMMA–rich phase because of such blocking of transport of charges. Therefore, the ionic conductivity of the polymer matrix is decreased (Rajendran *et al*., 2000). Moreover, at the higher concentration of PVC, the re–dissociation of solvated ion pairs is replaced with short range ion–solvent interaction. Although the number of ions dissolved into the polymer matrix increases, the effective number of mobile charges which are available for migration is reduced (Stephan *et al*., 2002)

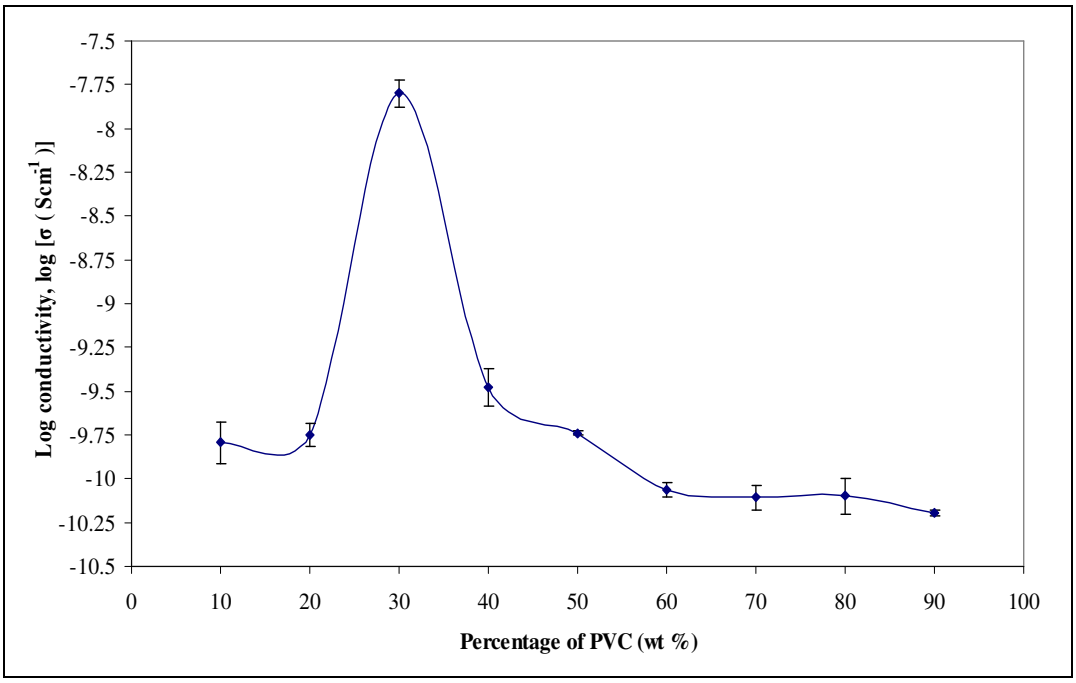

Figure 4.2: Variation of log conductivity, log σ as a function of weight percentage PVC added into PMMA–PVC–LiTFSI based polymer electrolyte at ambient temperature.

4.3 Temperature Dependence–Ionic Conductivity Studies

Figure 4.3 depicts the Arrhenius plot of PE 3, PE 5 and PE 9 which shows that the ionic conductivity increases with temperature. This is attributed to the expansion of polymer matrix. The polymer matrix expands with increase in temperature and then weakens the interaction within the polymer matrix, promoting the decoupling of Li cations from the polymer complex. This assists the mobility of ions. The polymeric chain also acquires faster internal vibrational modes with increasing the temperature, which in turn to increase in mobility of polymer segments by initiating the bond rotation within the polymer matrix. Therefore, it favors the ionic transportation and hence increases the ionic

conductivity (Baskaran, 2006b).

As shown in Figure 4.3, the regression values are close to unity, indicating the presence of Arrhenius behavior. In this rule, the conductivity is expressed as:

$$\sigma = A\exp\left(\frac{-E_a}{kT}\right) \qquad \text{(Equation 4.1)}$$

where A is a constant which is proportional to the amount of charge carriers, E_a is activation energy and k is Boltzmann constant, that is 8.6173×10^{-5} eV K^{-1} and T represents the absolute temperature in K. In general, this theory follows the hopping mechanism which states that the interaction of polar group of the polymeric chain with Li^+ is weaker and hence these charge carriers are decoupled from the segmental motion of polymer matrix. This creates vacant sites in the polymer chain. Therefore, the ions from adjacent sites tend to occupy these neighboring vacant sites and form the coordination with the polymer chain.

Figure 4.3 shows that ionic conductivity of PE 3 is greater than PE 5 and that of PE 5 is greater than PE 9. The amorphous nature of PE 3 increases as the content of PMMA increases in comparison with PE 5 and PE 9. The increase in amorphous region leads to the disorder mode of segmental polymer chain and thus forms more free voids for ionic conduction. This promotes the ion transportation and hence the increase in ionic conductivity (Achari *et al*., 2007). The lower ionic conductivity of the polymer electrolyte is attributed to excessive cross–linking

effect. Higher amount of PVC incorporated in the polymer electrolytes leads to high degree of cross–linking between PMMA and PVC and increases the viscosity by forming entanglements within the polymer chain. As a result, free space for ion transportation is reduced and then impedes the mobility of charge carriers. Consequently, the ionic conductivity is decreased (Kumar *et al*., 2007). The mechanism of cross–linking is discussed further in section 4.10.

The activation energy, E_a, is also determined in this study. As discussed earlier, the Li^+ tends to dissociate from the polymer chain and other Li^+ ions from the surrounding favor to coordinate with the polymer chain with the aid of segmental motion of polymer chain. Energy is required to overcome this reorganization and reformation of the polymer chain with Li^+. This energy is defined as activation energy. As shown in Table 4.1, E_a is inversely proportional to ionic conductivity. This is mainly attributed to the amorphous region in the polymer matrix, which is the prerequisite of the higher ionic conductivity. The degree of amorphous phase leads to the disorderly arrangement of molecules in the polymer matrix which results in a more flexible polymer chain. Therefore, the attractive bonds between the macromolecules become weaker and requiring less energy to break the bond for reorganization and reformation of coordination with Li^+. This enhances the Li^+ diffusivity in the polymer matrix (Kumar *et al*., 2007). Based on the above discussion it can be concluded that the hopping process is favorable with decreasing E_a.

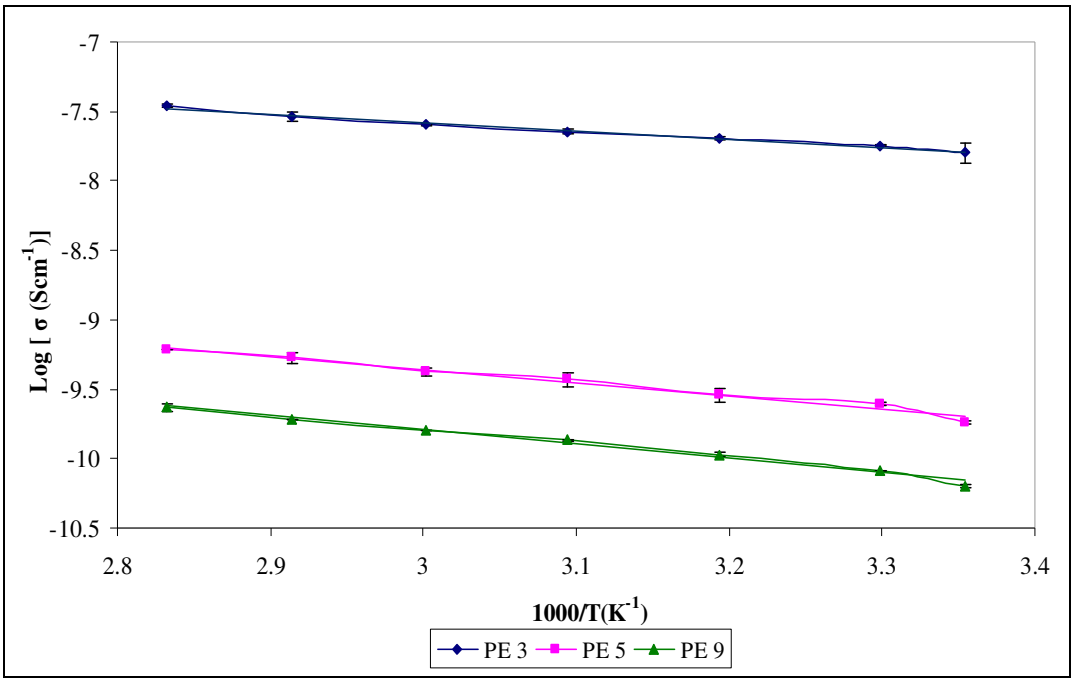

Figure 4.3: Arrhenius plot of ionic conductivity of PE 3, PE 5 and PE 9.

Composition of PMMA and PVC (% wt)		Designations	Activation energy, E_a (eV)
PMMA	PVC		
70	30	PE 3	0. 12021
50	50	PE 5	0. 18724
10	90	PE 9	0. 20393

Table 4.1: Activation energies for polymer blend electrolytes as a function of PVC loadings.

4.4 Frequency Dependence–Ionic Conductivity Studies

In order to understand the relaxation behavior of the polymer electrolytes system, the ionic conductivity as a function of frequency for polymer electrolytes is studied. The variation plot of logarithm of ionic conductivity with corresponding frequency for PE 3 and PE 4 at ambient temperature is shown in Figure 4.4.

According to this figure, the ionic conductivity increases as the frequency is increased. The low frequency dispersion region is attributed to interfacial impedance or space charge polarization. As the frequency decreases, the amount of charge accumulates at the electrode and electrolyte interface increases. As a consequence, the number of mobile ions or charge carriers available for transportation decreases and this leads to a decrease in ionic conductivity. This indicates the presence of non–Debye properties in the polymer electrolytes. In contrast, at higher frequency, the mobility of charge carriers is increased and eventually contributes to higher ionic conductivity with respect to frequency (Ramesh and Arof, 2001a).

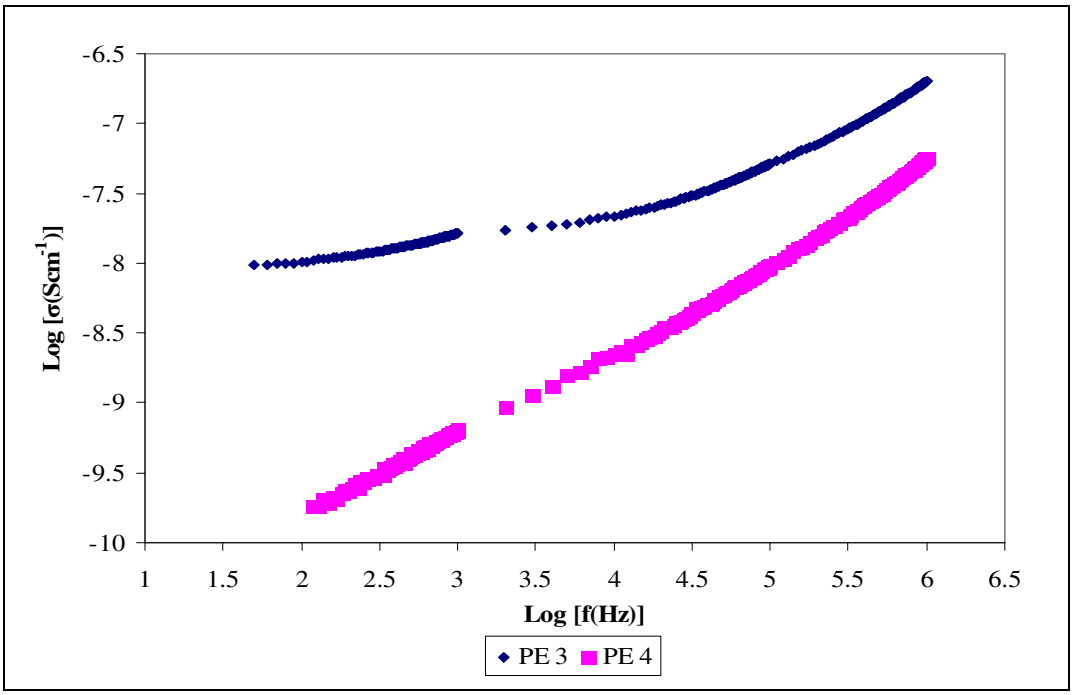

Figure 4.4: Frequency–dependent conductivity at ambient temperature for PE 3 and PE 4.

4.5 Dielectric Relaxation Studies

The dielectric relaxation study is a versatile study used to investigate the behaviour of polymer blends by studying the relaxation behaviour of dipoles of polymer electrolyte (Rajedran *et al*., 2004). In this study, the same frequency range is used for both PE 3 and PE 4 samples. Figures 4.5 and 4.6 illustrate the frequency dependence variation of real (ε') and imaginary permittivity (ε'') of the dielectric relaxation constant for PE 3 and PE 4 polymers electrolytes respectively. As shown in both figures, PE 3 prevails at higher region and this indicates that PE 3 has higher mobile charge carriers for migration compared to PE 4. This eventually contributes to higher ionic conductivity and it has been proven in Figure 4.2.

At low frequency, both real and imaginary parts of dielectric relaxation constants rise sharply. This may be attributed to the electrode polarization effect which may be due to the accumulation of charge at the electrode and electrolyte interface and space charge effects which can normally be observed in ionic glasses. This had further confirmed the presence of non–Debye characteristic in the polymer matrix. In addition, it may also be due to the retention of trace amount of water in the thin film (Goodwin *et al*., 1999). At high frequency, the decreases of ε' and ε'' are mainly attributed to the high occurrence of periodic reversal of the electric field at the interface which reduces the contribution of charge carriers. As a result, it induces the absence of excessive ion diffusion in the direction of the

electric field (Ramesh and Chai, 2007). Thus, the orientation of the dipoles is inhibited, resulting in a decrease in polarization. Since the interaction between dipoles and external electrical field is becoming weaker, hence the values of ε' and ε'' decrease (Ramesh and Ng, 2009).

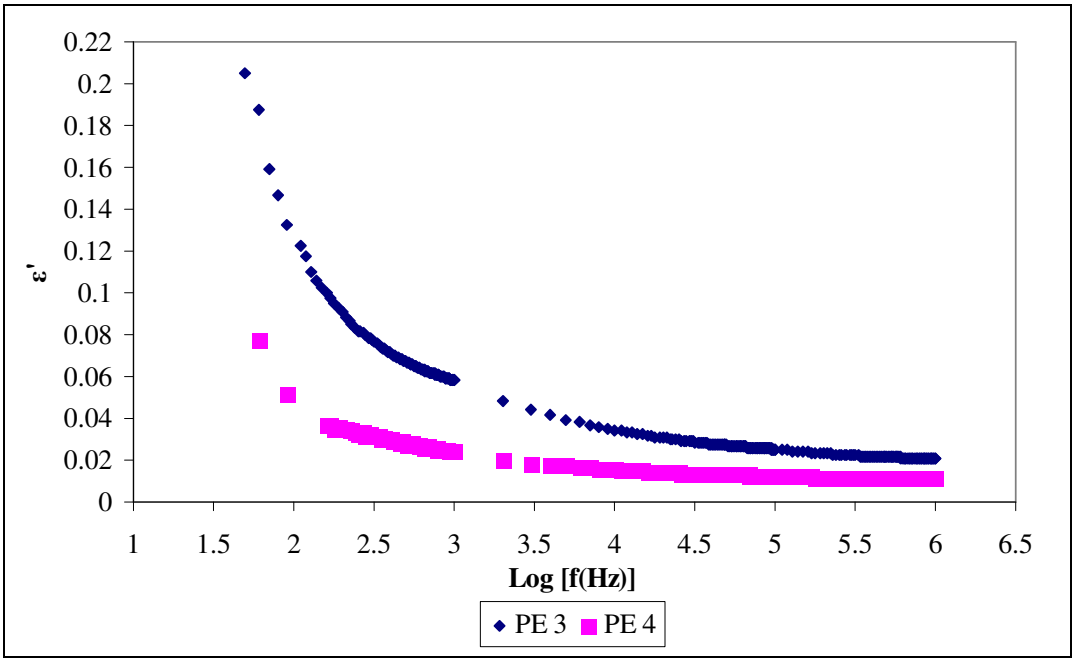

Figure 4.5: Variation of real part of dielectric constant, ε' with respect to frequency for PE 3 and PE 4 at ambient temperature.

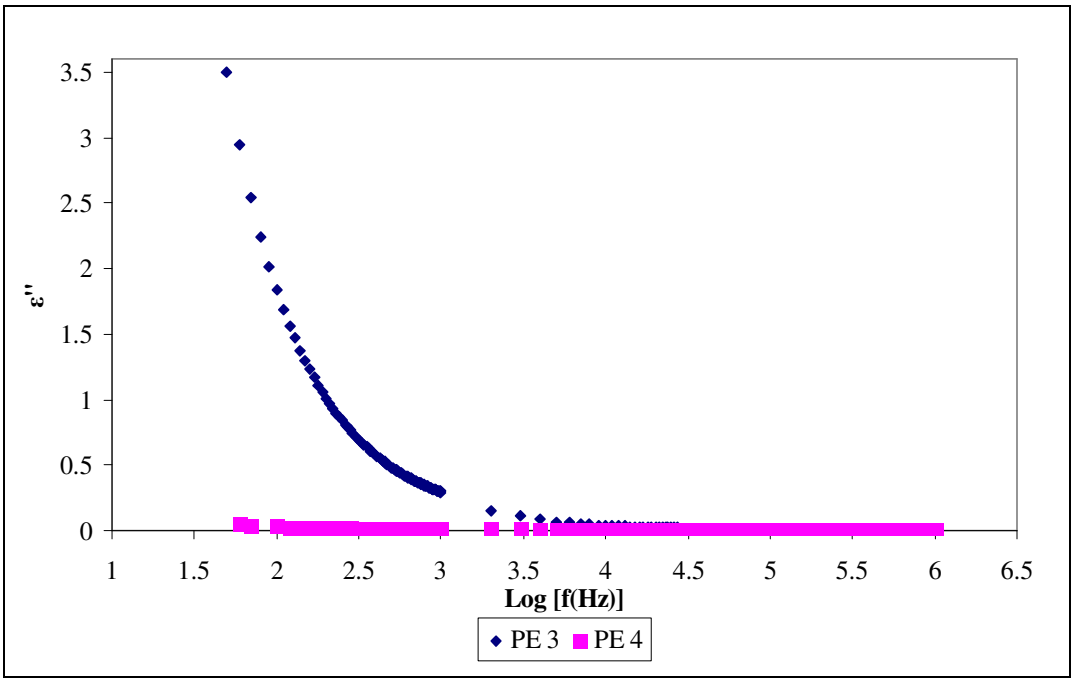

Figure 4.6: Variation of imaginary part of dielectric constant, ε'' with respect to frequency for PE 3 and PE 4 at ambient temperature.

4.6 Dielectric Moduli Studies

The dielectric moduli analysis is a further study to investigate the dielectric behaviour of polymer blends by suppressing the polarization effects of the electrode (Ramesh and Arof, 2001a). The real (M') and imaginary (M'') parts of dielectric moduli as a function of frequency for sample PE 3 and PE 4 are exemplified in Figures 4.7 and 4.8, respectively. In these figures, the appearance of the peaks in the modulus formalism at high frequency reveals that the polymer electrolytes are ionic conductors. It may be due to the existence of bulk effect (Ramesh and Chai, 2007). As shown in Figure 4.7, well–defined dispersion peaks are absent, however, M' is still showing a distinctive increment at high frequency.

The intensity of the peaks decreases as the PVC content increases. This implies that there is a plurality of relaxation mechanism. On the other hand, the value of $M^{'}$ and $M^{''}$ tends to approach to zero at low frequency. This reveals that the contribution of electrode polarization due to the accumulation of charge is insignificant. Apart from that, for PE 3, the presence of long tail at low frequency indicates the association of large capacitance with the electrodes (Ramesh and Arof, 2001a).

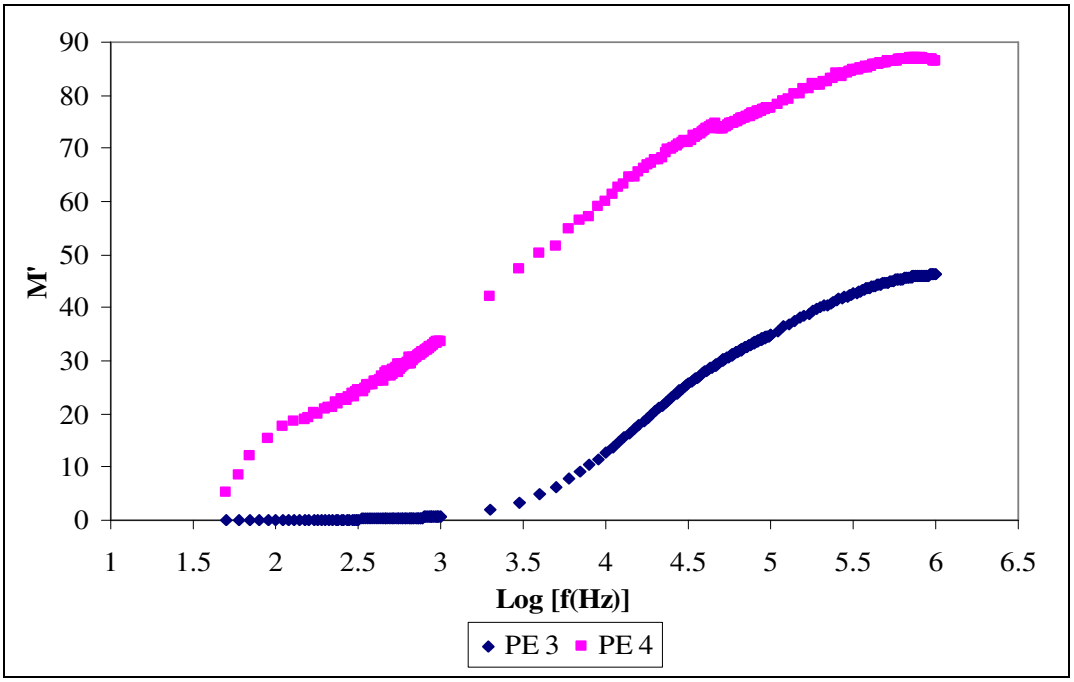

Figure 4.7: Variation of real part of modulus, $M^{'}$ with respect to frequency for PE 3 and PE 4 at ambient temperature.

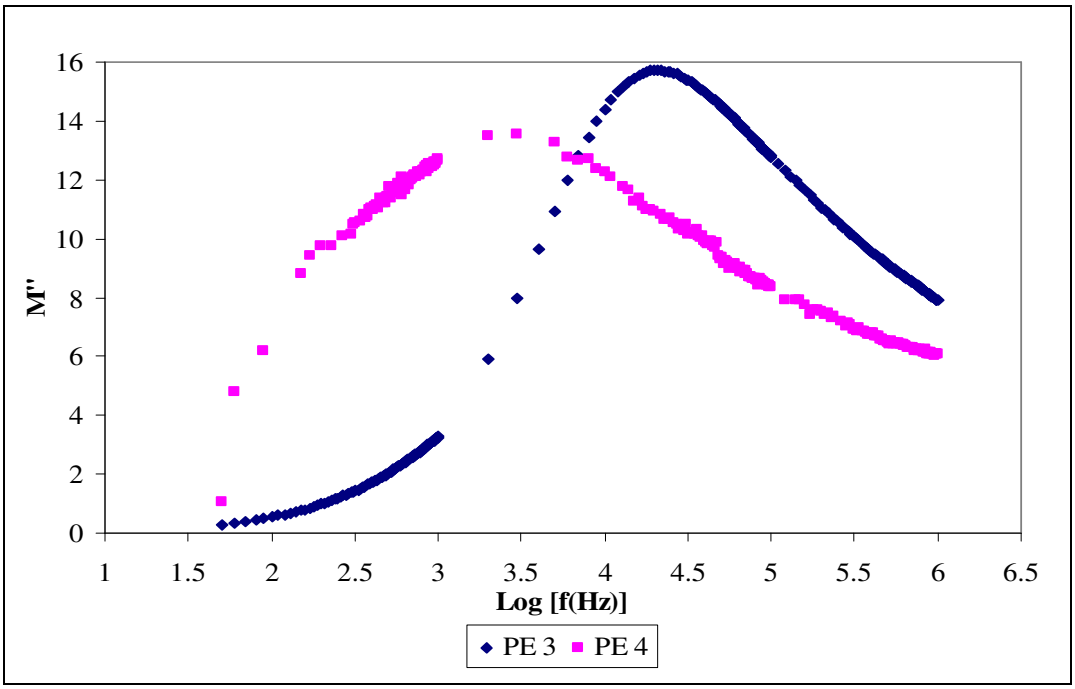

Figure 4.8: Variation of imaginary part of modulus, $M^{"}$ with respect to frequency for PE 3 and PE 4 at ambient temperature.

4.7 HATR–FTIR studies

The HATR–FTIR spectra of pure PMMA, pure PVC and PMMA–PVC are shown in Figure 4.9 (a)–(c). The combination of HATR–FTIR spectra of pure PMMA, pure PVC and PMMA–PVC is shown in Figure 4.10, whereas all the assignments of the vibrational modes are tabulated in Table 4.2. As shown in Figure 4.10, four peaks are disappeared upon addition of pure PVC into pure PMMA compound. These peaks are assigned as trans C–H wagging mode of PVC at 956 cm^{-1}, CH_2 deformation mode of PVC at 1328 cm^{-1}, C–CH_3 stretching mode of PMMA at 1385 cm^{-1} and CH_2 scissoring mode of PMMA at 1484 cm^{-1}, as highlighted in Figure 4.10. These disappearances indicate formation of

complexation between PMMA and PVC. All the characteristic peaks of (PMMA–PVC) exhibit changes in shift, as listed in Table 4.2.

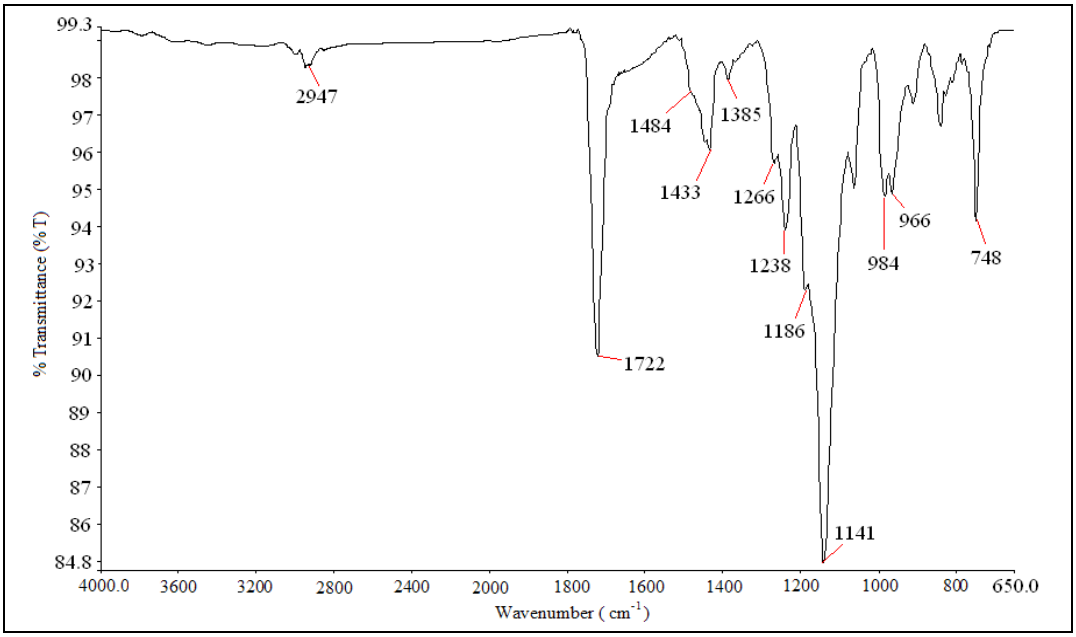

Figure 4.9 (a): HATR–FTIR spectrum of pure PMMA.

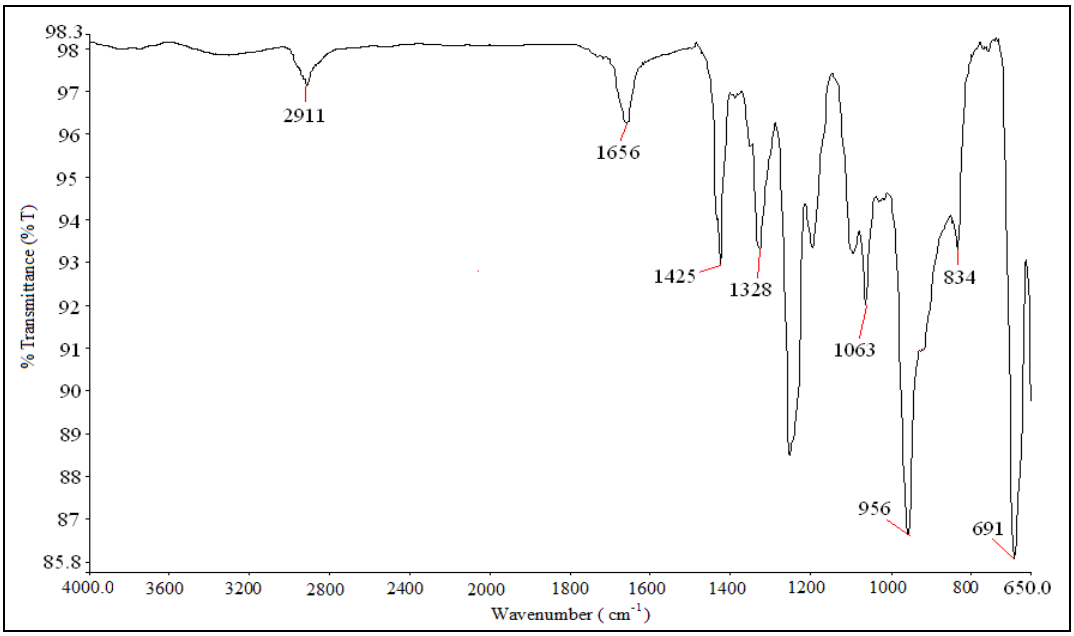

Figure 4.9 (b): HATR–FTIR spectrum of pure PVC.

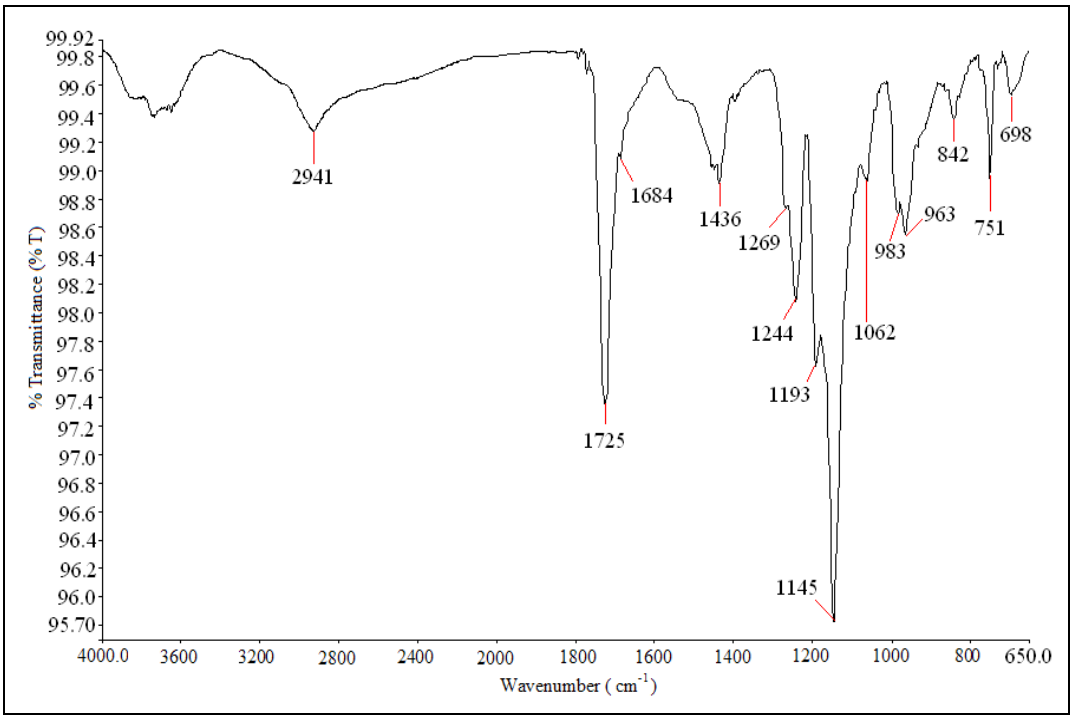

Figure 4.9 (c): HATR–FTIR spectrum of PMMA–PVC.

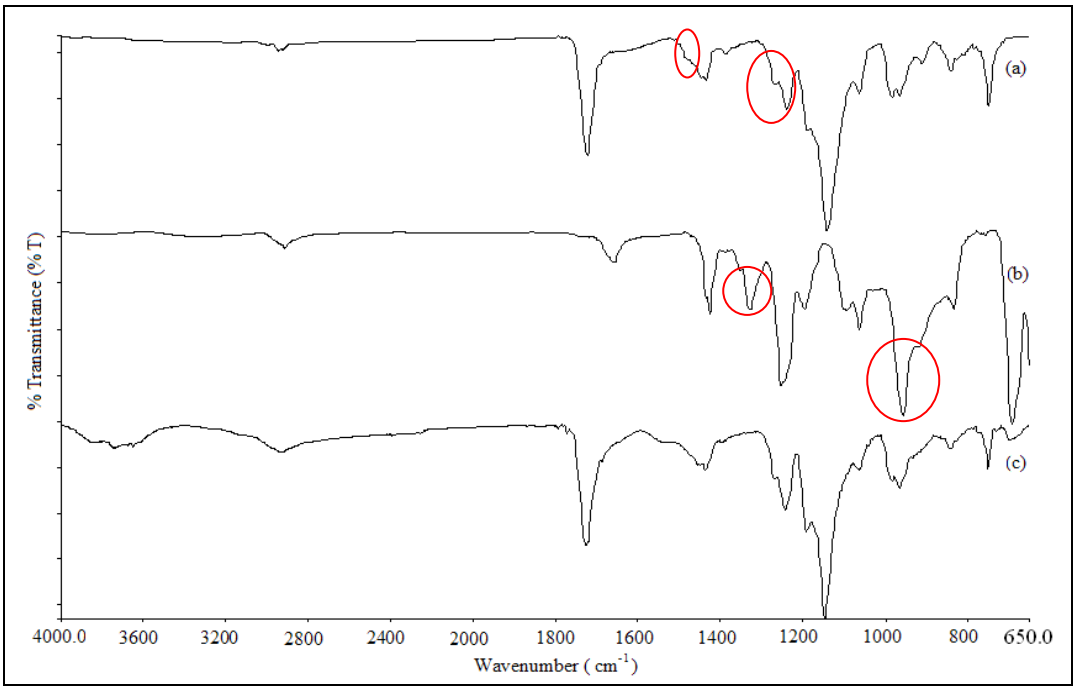

Figure 4.10: Combination of HATR–FTIR spectra of (a) pure PMMA, (b) pure PVC and (c) PMMA–PVC.

Description vibration modes	Wavenumber (cm^{-1})	
	PMMA –PVC	PMMA / PVC
Cis C–H wagging mode of PVC	698	691
CH_2 rocking mode of PMMA	751	748
C–Cl stretching mode of PVC	842	834
Combination of C–O symmetric stretching mode in C–O–C linkage of PMMA and trans C–H wagging mode of PVC	963	966 / 956
CH_2 wagging mode of PMMA	983	984
C–H rocking mode of PVC	1062	1063
C–O asymmetric stretching mode in C–O–C linkage of PMMA	1145	1141
CH_2 twisting mode of PMMA	1193	1186
CH_3 symmetric bending mode of PMMA	1244	1238
C–O–C symmetric stretching mode of PMMA	1269	1266
Combination of CH_3 asymmetric bending mode of PMMA and C–H stretching mode of CH_2 group of PVC	1436	1433 / 1425
C=C stretching mode of PVC	1684	1656
C=O stretching mode of PMMA	1725	1722
CH_3 asymmetric stretching mode of PMMA and PVC	2941	2947 / 2911

Table 4.2: Assignments of vibrational modes of PMMA and PVC in PMMA–PVC polymer blends.

As shown in Figure 4.11, pure PVC shows a sharp peak at 691 cm^{-1} and it is assigned as cis C–H wagging mode of PVC. The characteristic peak is shifted to 698 cm^{-1} by blending with PMMA. On the other hand, the intensity of this characteristic peak reduces from 8.70 % to 0.42 %, in transmittance mode. Upon dispersion of PVC, CH_3 asymmetric stretching mode of pure PMMA at 2947 cm^{-1} is shifted to 2941 cm^{-1}. In term of intensity, the peak becomes broader due to the interaction between PMMA and PVC, leading to an overlapping of CH_3 asymmetric stretching mode of PMMA and PVC.

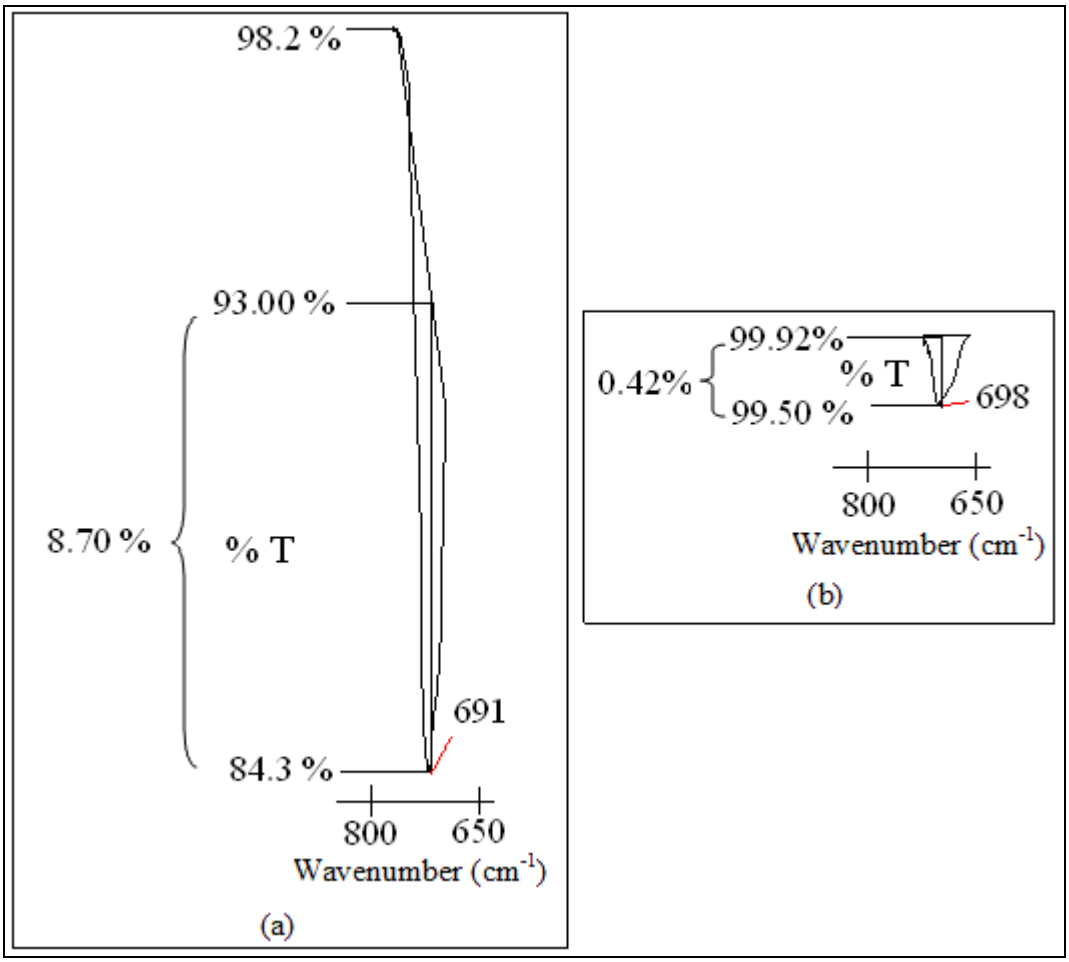

Figure 4.11: The comparison of change in intensity and shift of cis C–H wagging mode of PVC in (a) pure PVC and (b) PMMA–PVC in the HATR–FTIR spectrum.

Apart from the changes in shift, it also demonstrates the change in shape. As shown in Figure 4.12, two weak peaks are changed to a new weak peak with a shoulder. Two apparent peaks are observed in the region of 1000–900 cm^{-1}. For pure PMMA, the first peak is designated as combination of C–O symmetric stretching mode in C–O–C linkage of PMMA and trans C–H wagging mode of PVC at 966 cm^{-1}, whereas CH_2 wagging mode of PMMA is assigned for second peak at 984 cm^{-1}. The first peak is shifted to 963 cm^{-1} due to the overlapping of trans C–H wagging mode of PVC with C–O symmetric stretching mode of PMMA

by adding PVC. This indicates that PMMA is complexed with PVC. On the contrary, the latter weak peak is changed to a shoulder peak and shifted to 983 cm^{-1} by blending with PVC. This is further proven the interaction between PMMA and PVC.

For pure PMMA, the C=O stretching mode of PMMA appears as a sharp peak at 1722 cm^{-1}. However, upon addition of PVC, a new sharp peak at 1725 cm^{-1} with a shoulder at 1684 cm^{-1} is obtained. This shoulder peak is assigned as C=C stretching mode of PVC, revealing the entanglement of PMMA and PVC. Based on the changes in shift, changes in intensity, changes in shape and disappearance of the characteristic peaks, it can be concluded that there is a complexation between PMMA and PVC in the PMMA–PVC polymer system.

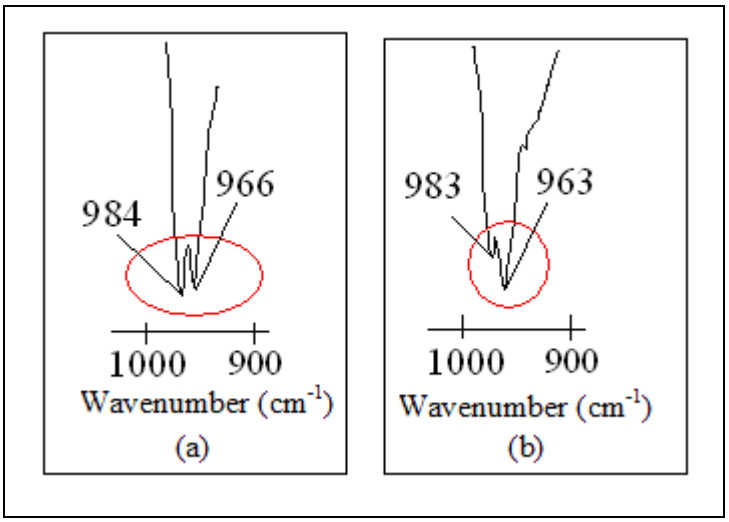

Figure 4.12: The comparison of change in shape of the characteristic peaks within the region of 1000–900 cm^{-1} in (a) pure PMMA and (b) PMMA–PVC.

HATR–FTIR spectrum for pure LiTFSI, PE 3, PE 5 and PE 9 are illustrated in Figures 4.13 (a)–(d), whereas Figure 4.14 shows the combination of the HATR–FTIR spectrum. Table 4.3 depicts the assignments of important bands of PE 3. Since PE 3 achieves the maximum ionic conductivity, thus the HATR–FTIR spectrum of PE 3 is discussed in details. Seven new peaks are formed upon addition of 10 wt% of LiTFSI as highlighted in Figure 4.14. These characteristic peaks are assigned as trans C–H wagging mode of PVC at 923 cm^{-1}, S–N–S asymmetric bonding mode of LiTFSI at 1055 cm^{-1}, C–SO_2–N bonding mode of LiTFSI at 1333 cm^{-1}, SO_2 asymmetric stretching mode of LiTFSI at 1357 cm^{-1}, CH_3 asymmetric stretching mode of PMMA at 1963 cm^{-1} and S–CH_3 bonding mode of LiTFSI at 2827 cm^{-1} and 2996 cm^{-1}. This is suggestive of the formation of complexation between LiTFSI and PMMA–PVC blends.

The disappearance of some characteristics peaks is another way to prove the interactions between LiTFSI and PMMA–PVC blends. For example, a weak peak at 698 cm^{-1} is shown in Figure 4.9 (c). This peak is assigned as cis C–H wagging mode of PVC. However, the peak is disappeared by adding 10 wt% of LiTFSI. In comparing pure LiTFSI spectrum with PE 3 spectrum, it also found out that the peak at 787 cm^{-1} which assigned as combination of C–S and S–N stretching mode of LiTFSI is absent. The same phenomenon is also observed for PMMA. Combination of C–O symmetric stretching mode in C–O–C linkage of PMMA and trans C–H wagging mode of PVC which located at 963 cm^{-1} is also disappeared, by comparing PMMA–PVC spectrum and PE 3 spectrum. These

absences of the characteristic peak divulge the formation of coordination bonding between PMMA, PVC and LiTFSI.

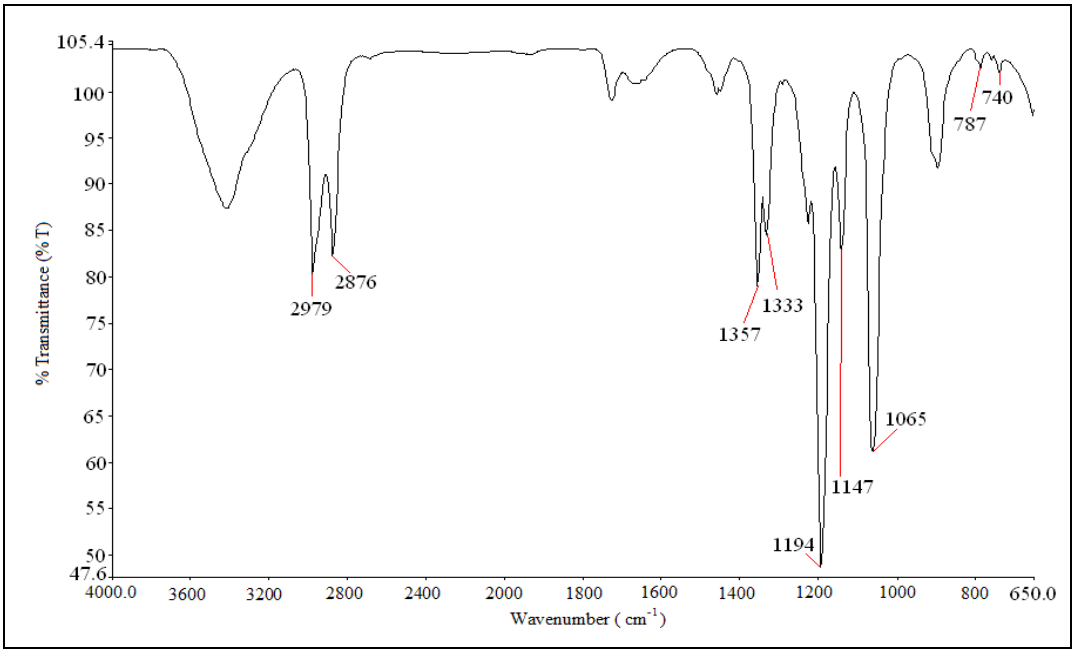

Figure 4.13 (a): HATR–FTIR spectrum of pure LiTFSI.

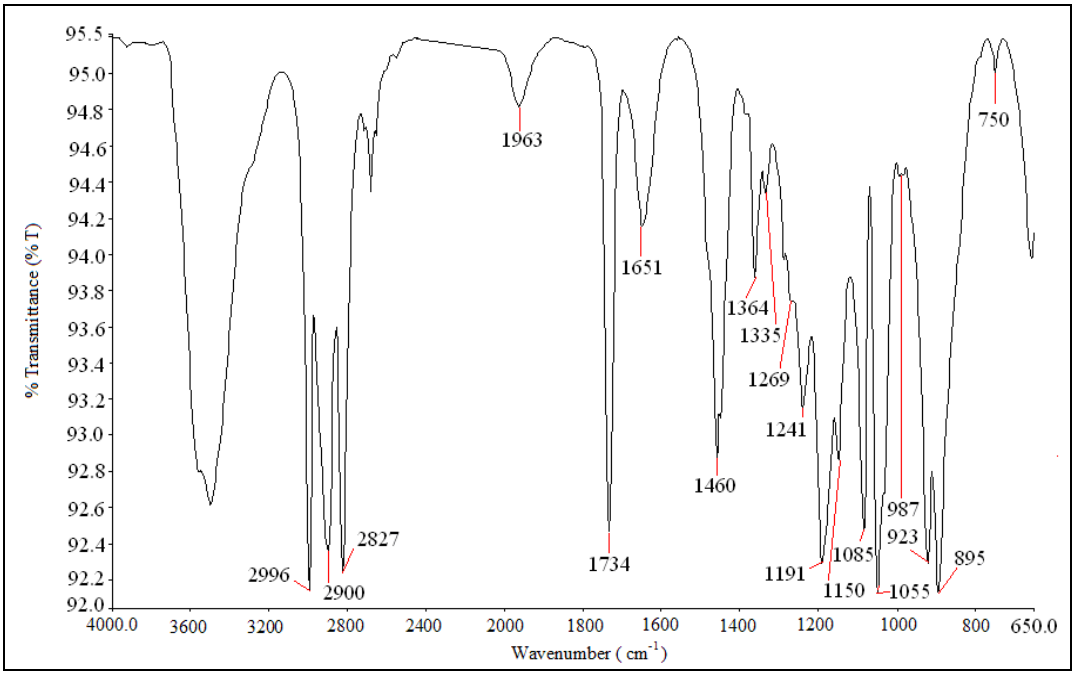

Figure 4.13 (b): HATR–FTIR spectrum of PE 3.

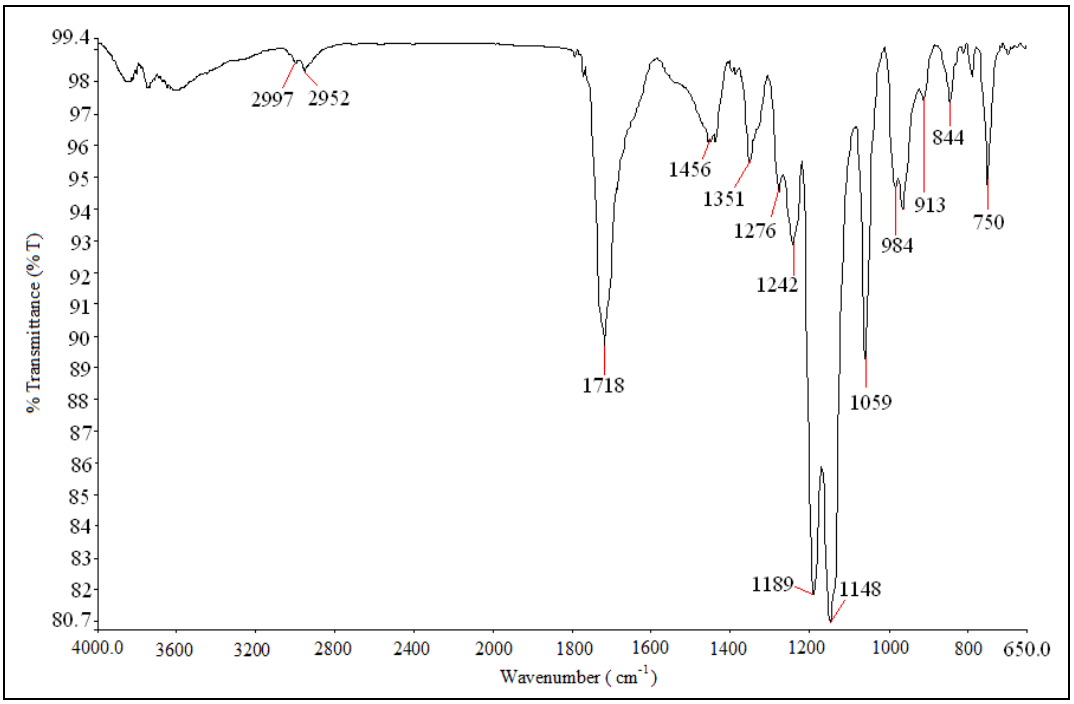

Figure 4.13 (c): HATR–FTIR spectrum of PE 5.

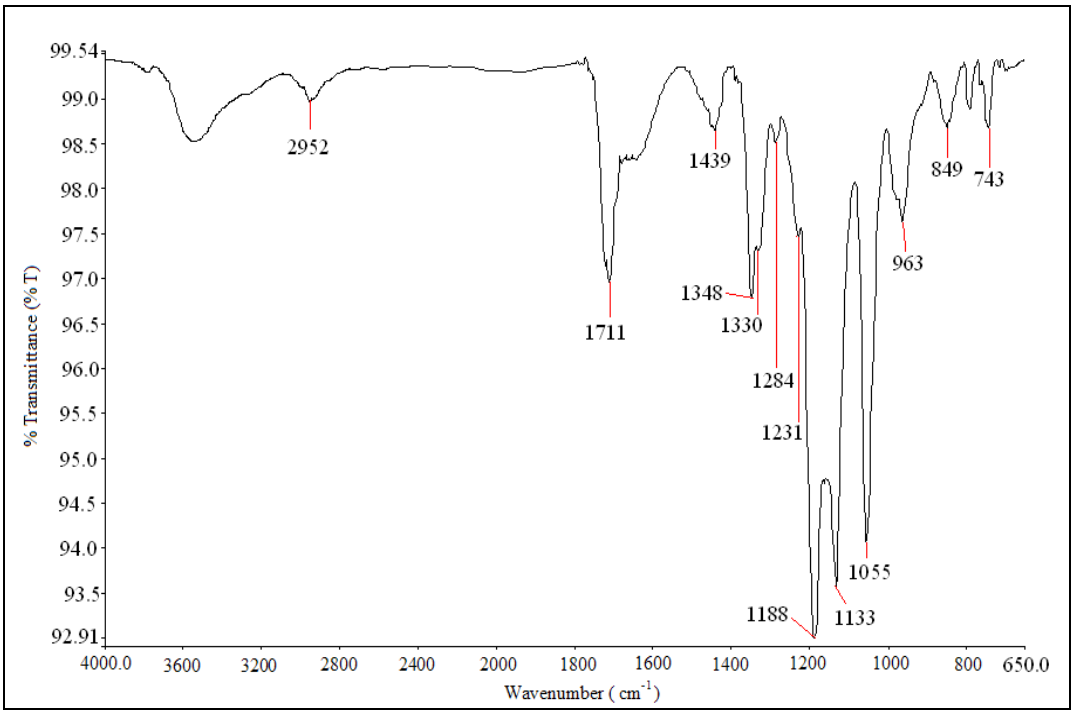

Figure 4.13 (d): HATR–FTIR spectrum of PE 9.

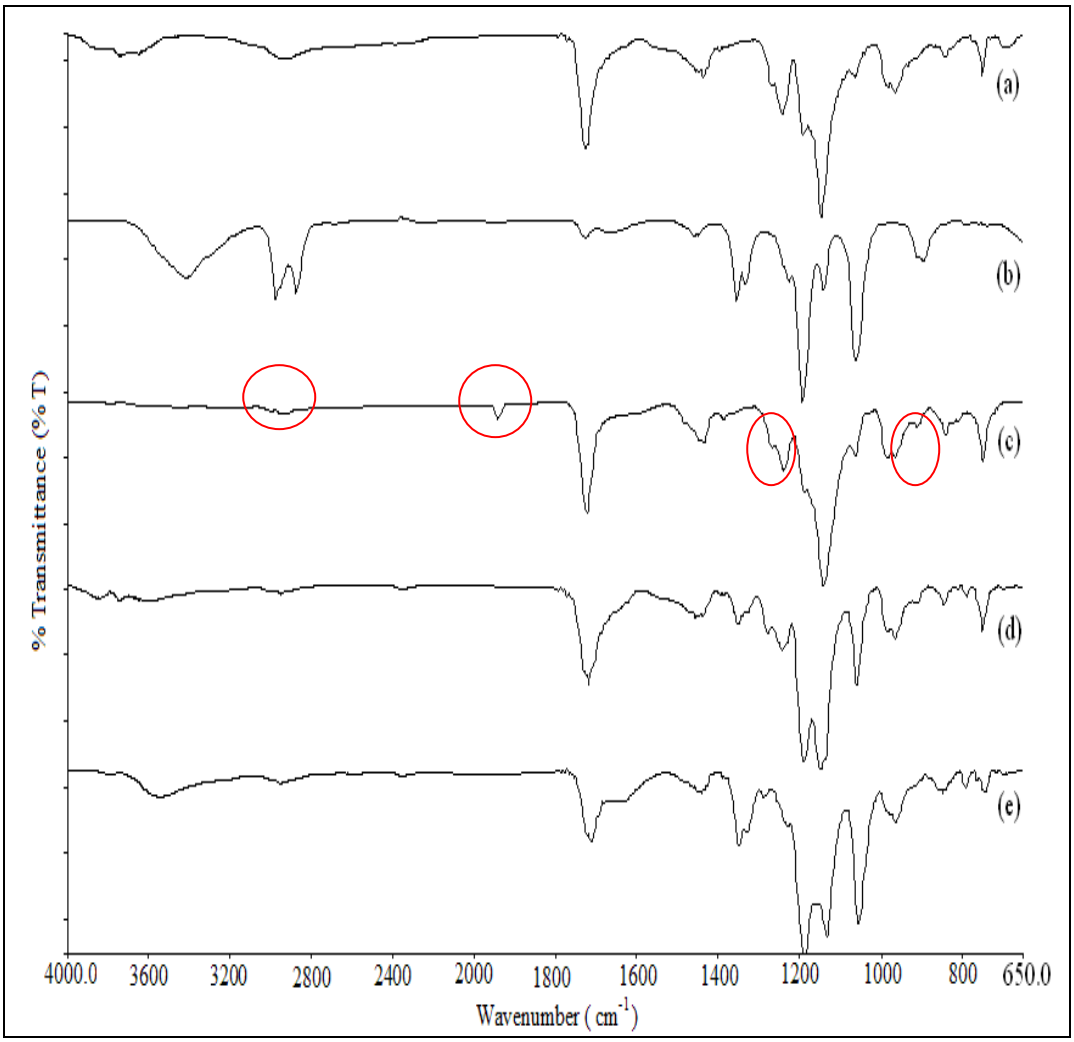

Figure 4.14: Combination of HATR–FTIR spectra of (a) PMMA–PVC, (b) pure LiTFSI, (c) PE 3, (d) PE 5 and (e) PE 9.

Description vibration modes	Wavenumber (cm^{-1})	
	PE 3	PMMA–PVC / LiTFSI
Combination of CH_2 rocking mode of PMMA and S–N stretching of LiTFSI	750	751 / 740
C–Cl stretching mode of PVC	895	842
Combination of C–O symmetric stretching mode in C–O–C linkage of PMMA and trans C–H wagging mode of PVC	923	963
CH_2 wagging mode of PMMA	987	983
S–N–S asymmetric bonding mode of LiTFSI	1055	1065
C–H rocking mode of PVC	1085	1062
Combination of C–O asymmetric stretching mode in C–O–C linkage of PMMA and C–SO_2–N bonding mode of LiTFSI	1150	1145 / 1147
Combination of CH_2 twisting mode of PMMA and CF_3 symmetric stretching mode of LiTFSI	1191	1193 / 1194
CH_3 symmetric bending mode of PMMA	1241	1244
C–O–C symmetric stretching mode of PMMA	1269	1269
C–SO_2–N bonding mode of LiTFSI	1335	1333
SO_2 asymmetric stretching mode of LiTFSI	1364	1357
Combination of CH_3 asymmetric bending mode of PMMA and C–H stretching mode of CH_2 group of PVC	1460	1436
C=C stretching mode of PVC	1651	1684
C=O stretching mode of PMMA	1734	1725
CH_3 asymmetric stretching mode of PMMA	1963	–
S–CH_3 bonding mode of LiTFSI	2827, 2996	2876, 2979
CH_3 asymmetric stretching mode of PMMA and PVC	2900	2941

Table 4.3: Assignments of vibrational modes of PMMA, PVC and LiTFSI in PE 3 polymer blend electrolyte.

All the characteristic peaks undergo the changes in shift; except the characteristic peak at 1269 cm^{-1}. The peak is assigned as C–O–C symmetric stretching mode of PMMA and appeared as a shoulder peak. In order to probe the complexation of PMMA, PVC and LiTFSI, the changes in intensity of characteristic peaks are observed. At 750 cm^{-1}, the weak peak is designated as combination of CH_2 rocking mode of PMMA and S–N stretching of LiTFSI. For

this characteristic peak, the intensity increases from 0.27 % to 0.5 %, in transmittance mode. It may be due to the overlapping of S–N stretching of LiTFSI with the rocking mode. As shown in Figure 4.15, in term of intensity, C=O stretching mode of PMMA at 1734 cm^{-1} increases from 1.90 % to 2.60 %, in transmittance mode. In addition, it exhibits upward shift, from 1725 cm^{-1} to 1734 cm^{-1}. As can be seen, there is a visible change in shape in this figure. For PMMA–PVC, the shoulder peak at 1684 cm^{-1} is assigned as C=C stretching mode of PVC. In contrast, for PE 3, it has been changed to a new peak and shifted to 1651 cm^{-1}, as depicted in Figure 4.15.

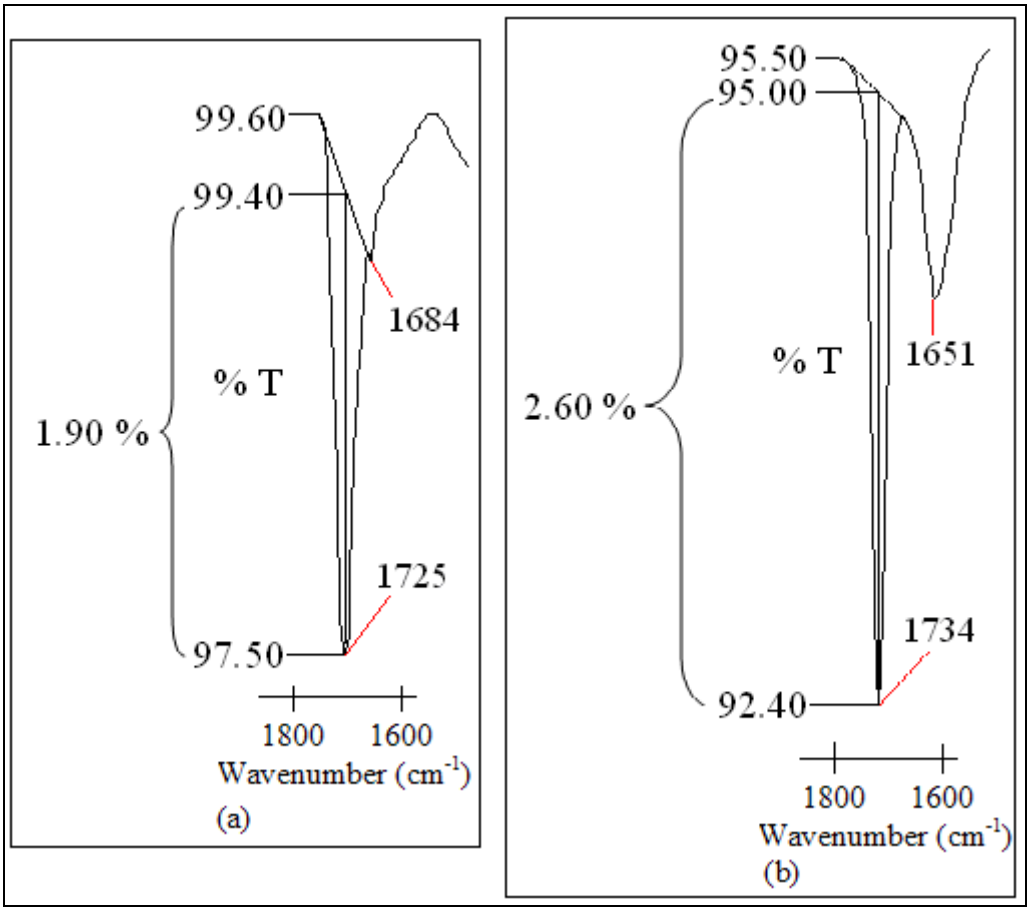

Figure 4.15: The comparison of change in intensity of C=O stretching mode of PMMA in (a) PMMA–PVC and (b) PE 3.

Another evidence to prove the change in shape is shown in Figure 4.16. For PMMA–PVC polymer blends, the vibrational mode of CH_3 asymmetric stretching mode of PMMA and PVC shows a weak peak at 2941 cm^{-1} in the region of 3000–2800 cm^{-1}. However, three peaks are observed in this region upon dispersion of 10 wt% of LiTFSI. CH_3 asymmetric stretching mode of PMMA and PVC shifts downward to 2900 cm^{-1}, whereas two new peaks are observed at 2827 cm^{-1} and 2996 cm^{-1}. These peaks are assigned as S–CH_3 bonding mode of LiTFSI. This reveals the interaction between LiTFSI and PMMA–PVC polymer blends and produces the complexation between lithium conducting salt and polymer blends in the polymer electrolyte system. In addition, a weak peak is observed at 842 cm^{-1} and assigned as C–Cl stretching mode of PVC in PMMA–PVC. However, two medium peaks are obtained by dispersing 10 wt% of LiTFSI in PE 3. As the first peak, C–Cl stretching of PVC is observed at 895 cm^{-1}, whereas combination of C–O symmetric stretching mode in C–O–C linkage of PMMA and trans C–H wagging mode of PVC at 923 cm^{-1} is designated for latter peak.

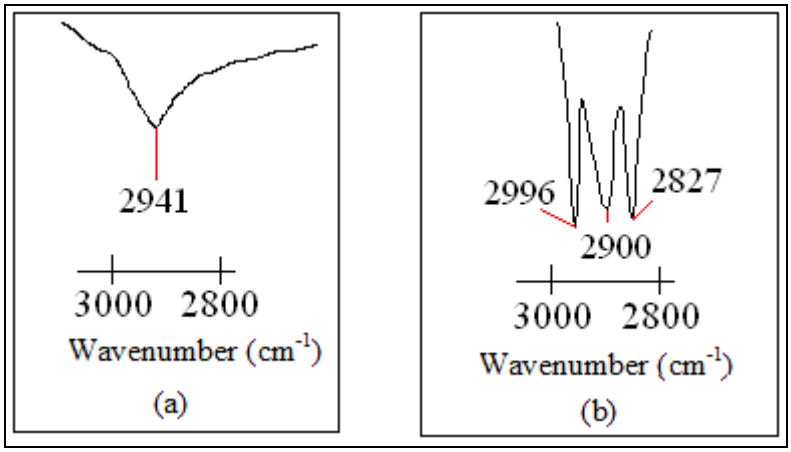

Figure 4.16: The comparison of change in shape of the characteristic peaks in (a) PMMA–PVC and (b) PE 3 within the range of 3000–2800cm^{-1}.

Some of the characteristic peaks are disappeared with increasing PVC content. For both PE 5 and PE 9, CH_3 asymmetric stretching mode of PMMA and C=C stretching mode of PVC at 1651 cm^{-1} and 1963 cm^{-1}, respectively, are absent in comparison to PE 3. In addition, in the region of 3000–2800 cm^{-1}, three weak peaks are changed to two weak peaks for PE 5, revealing the absence of S–CH_3 bonding mode of LiTFSI. On the contrary, for PE 9, there is only a weak peak remains in this region. It further indicates the disappearance of both S–CH_3 bonding modes of LiTFSI. Based on the absence of the characteristic peaks of LiTFSI, this suggests that PVC particles favor to form agglomeration in the polymer matrix rather than form complexation with LiTFSI. For PE 9, the peak which assigned as trans C–H wagging mode of PVC is also disappeared upon addition of PVC.

4.8 XRD studies

Figures 4.17 and 4.18 illustrate the XRD diffractograms of pure PMMA, pure PVC, PMMA–PVC, pure LiTFSI and PMMA–PVC blend–based polymer electrolytes. From Figure 4.17 (a), a broad characteristic peak of PMMA was obtained at angles of 2θ=16.4° with a shoulder at 2θ=22.5° which reveals the amorphous phase of PMMA. The intensity of these characteristic peaks is decreased after the impregnation of PVC. This implies that the addition of PVC disrupted the arrangement in the polymer backbone of PMMA (Baskaran *et al.*, 2006b). The presence of interactions between PMMA and PVC, such as cross–

linking, is attributed to this phenomenon. Complexation of PMMA and PVC occurs with the aid of these interactions and it is further discussed in section 4.10. Apart from the peak intensity of these characteristic peaks, another evidence of complexation is observed. The blending of PMMA with PVC shifts the peaks at 2θ= 16.4° and 2θ= 22.5° to 15.8° and 22.3°, revealing the change in crystallographic organization (Kumar *et al*., 2007).

Figure 4.18 (a) illustrates the sharp intense peaks at 2θ=13.6°, 15.9°, 18.6°, 18.9° and 21.4° and reveals the crystalline character of LiTFSI. These crystalline peaks were disappeared in PMMA–PVC based polymer blend electrolytes. The absence of excess salt indicates that LiTFSI is fully complexed with PMMA and PVC (Rajendran *et al*., 2004). A complete dissolution in the polymer electrolytes leads to a complexation between PMMA, PVC and LiTFSI (Baskaran *et al*., 2006b). Absence of these crystalline peaks in polymer blended electrolytes indicates that the electrolytes are in amorphous region. As shown in Figure 4.18, the characteristic peaks of PMMA–PVC at 2θ= 15.8° and 2θ=22.3° are shifted to 2θ angles of 16.9° and 22.6° for PE 3, to 16.1° and 22.4° for PE 5 and to 16.4° and 22.7° for PE 9. This variation confirms the complexation between PMMA–PVC polymer blends and LiTFSI (Ramesh and Arof, 2001b). The presence of complexation has been further confirmed based on the changes in peak intensity. It can be seen by comparing Figure 4.17 (c) with Figures 4.18 (b), (c) and (d) that the characteristic peak intensity decreases upon incorporation of LiTFSI. It can be inferred from the above comparison that the degree of crystallinity decreases and hence increases the amorphous region in polymer electrolytes which leads to

higher ionic conductivity (Ganesan *et al*., 2008). As discussed in section 4.3, the amorphous behavior increases with PMMA concentration. It has been proved in this study that the intensity of characteristic peak reduces upon the addition of higher PMMA loadings. Comparing the intensity of characteristic peaks of PE 3, PE 5 and PE 9, PE 3 shows the lowest value. It implies the highest amorphous degree of PE 3. This increment in amorphous character improves the ionic transportation in the polymer matrix and induces the highest ionic conductivity. In other words, higher loading of PVC in polymer electrolytes impedes the ion mobility by forming entanglements in the polymer network via cross–linking, thus leading to lower ionic conductivity.

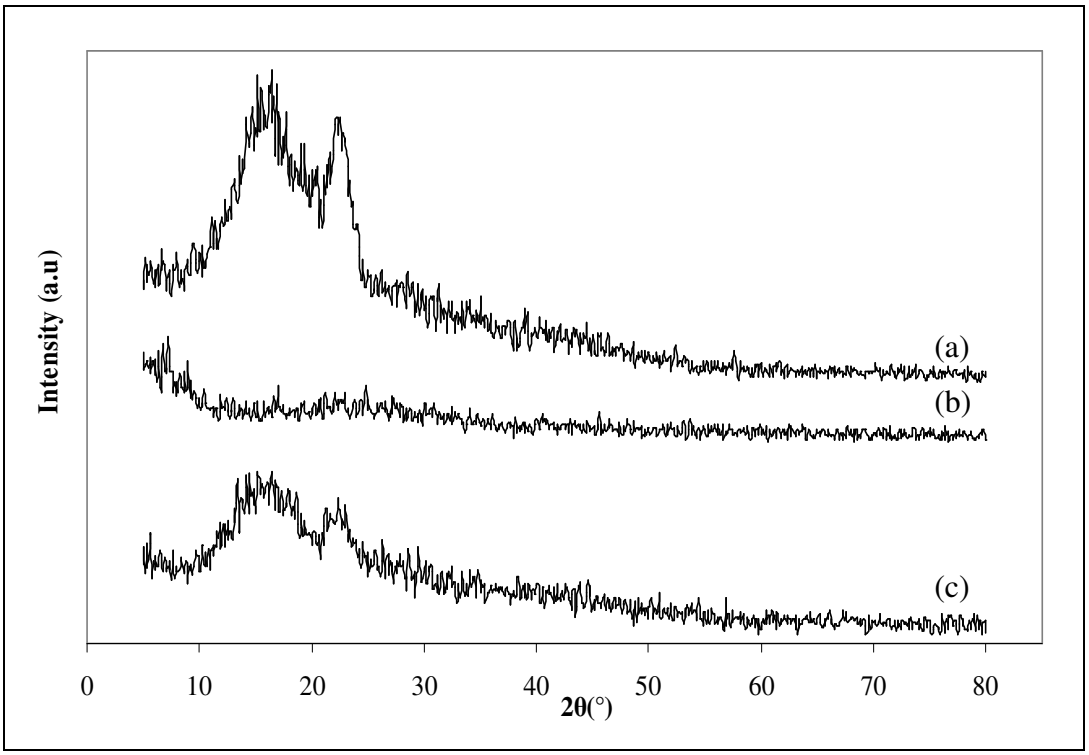

Figure 4.17: XRD patterns of (a) pure PMMA, (b) pure PVC and (c) PMMA–PVC.

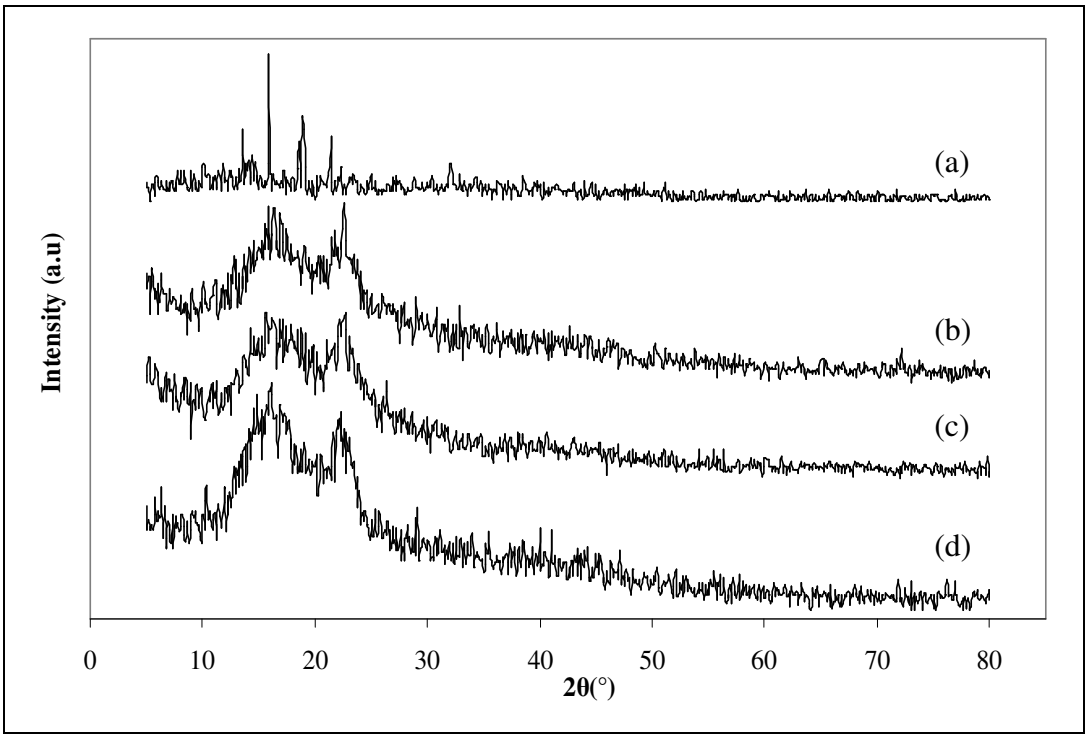

Figure 4.18: XRD patterns of (a) Pure LiTFSI, (b) PE 3, (c) PE 5 and (d) PE 9.

4.9 SEM studies

SEM images of PMMA, PVC and polymer blend electrolytes are shown in Figure 4.19 (a)–(f). Small craters with average pore size of 1 μm and 2 μm have formed on the pure PMMA and PMMA–PVC respectively and this is ascribed to the evaporation of THF solvent during the preparation of thin film (Stephan *et al*., 2000a). From Figure 4.19 (a) it can be observed that the spherical pore size of PMMA is around 15.1 μm. The pore size of PVC is around 7.08 μm which is approximately half that of PMMA. As expected, the pore size increases for PMMA–PVC polymer blends and the average diameter of these particles is 27.9 μm. The tendency of PMMA and PVC to join is revealed by the change in shape

of particles from spherical to rectangular shape. As a result, PMMA is coordinated with PVC and forms complexation. It can be observed by comparing Figures 4.19 (c)–(f) that the pore size of PMMA–PVC much smaller than PMMA–PVC with adulteration of LiTFSI. This suggests the presence of structural reorganizations of polymer chain and leads to Li^+ ion transportation in the polymer matrix.

The effect of variation in ratio of PMMA and PVC is also studied. It can be seen from Figures 4.19 (d)–(f) that PE 3 has a better pore surface distribution than PE 5 and PE 9. It can be inferred that the polymer matrix is in homogenous condition and agglomeration of similar phase of PVC is lesser at high PMMA content. Therefore, phase separation is absent in this polymer electrolyte system. As a result, the charge carriers can be transported quickly and easily without the presence of blocking phase and hence the highest ionic conductivity is observed for PE 3. The highest ionic conductivity is also ascribed to the highest porosity. As observed in Figure 4.19 (d), the porosity of PE 3 is larger than PE 5 and PE 9. It can therefore be proved that these voids promote the migration of ions and enhance the ionic conductivity of polymer electrolytes (Baskaran *et al*., 2007).

As shown in Figure 4.19 (e), spherules with average particles size of 0.4 μm are aggregated. As discussed earlier, the formation of globular agglomeration of similar phase of PVC at high PVC loadings ultimately leads to the formation of phase separation. Eventually, this phase separation hinders the migration of Li^+ in the polymer matrix which in turn reduces the ionic conductivity. Stephan *et al*. (2000) suggests that the higher pore size leads to lesser phase segregation and

forms a more homogeneous polymer electrolytes system. Similar trend is observed for PE 5 and PE 9. The average pore size of PE 5 and PE 9 is 14.5 μm and 10.6 μm respectively. As PMMA loadings decrease, it tends to increase the driving force for phase separation at 90 wt% PVC content. Therefore, ion transportation is less favored in this system and hence the porosity is relatively lesser than PE 5. As a result, lowest ionic conductivity is achieved by PE 9 as discussed in Sections 4.2 and 4.3.

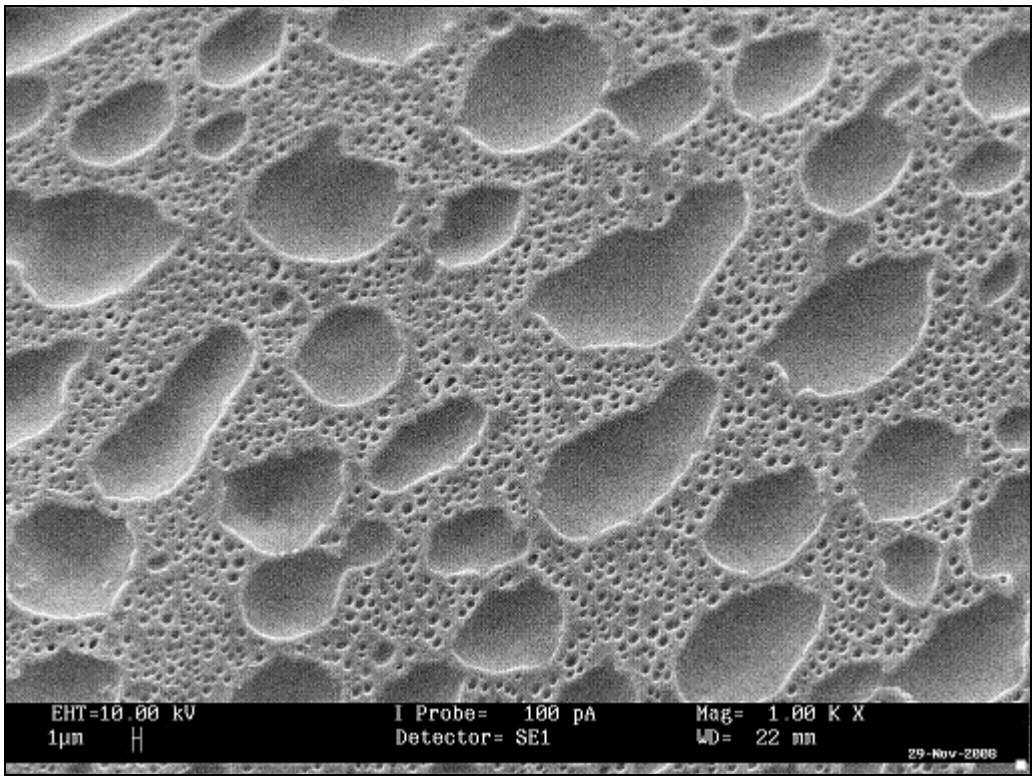

Figure 4.19 (a): SEM image of pure PMMA.

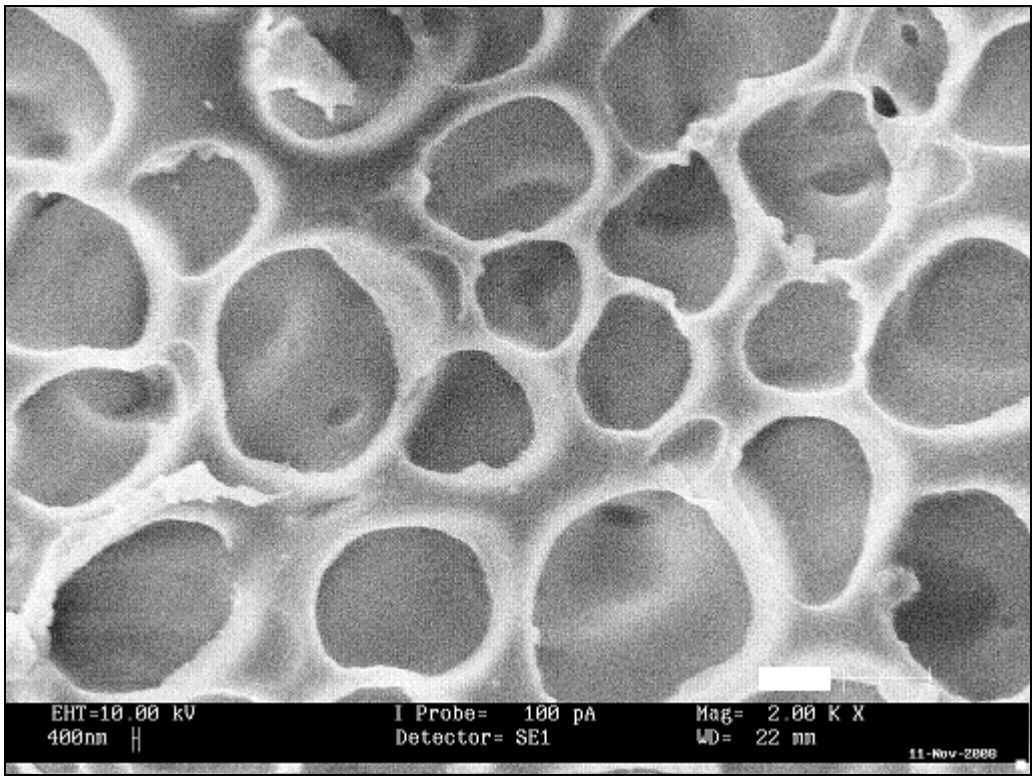

Figure 4.19 (b): SEM image of pure PVC.

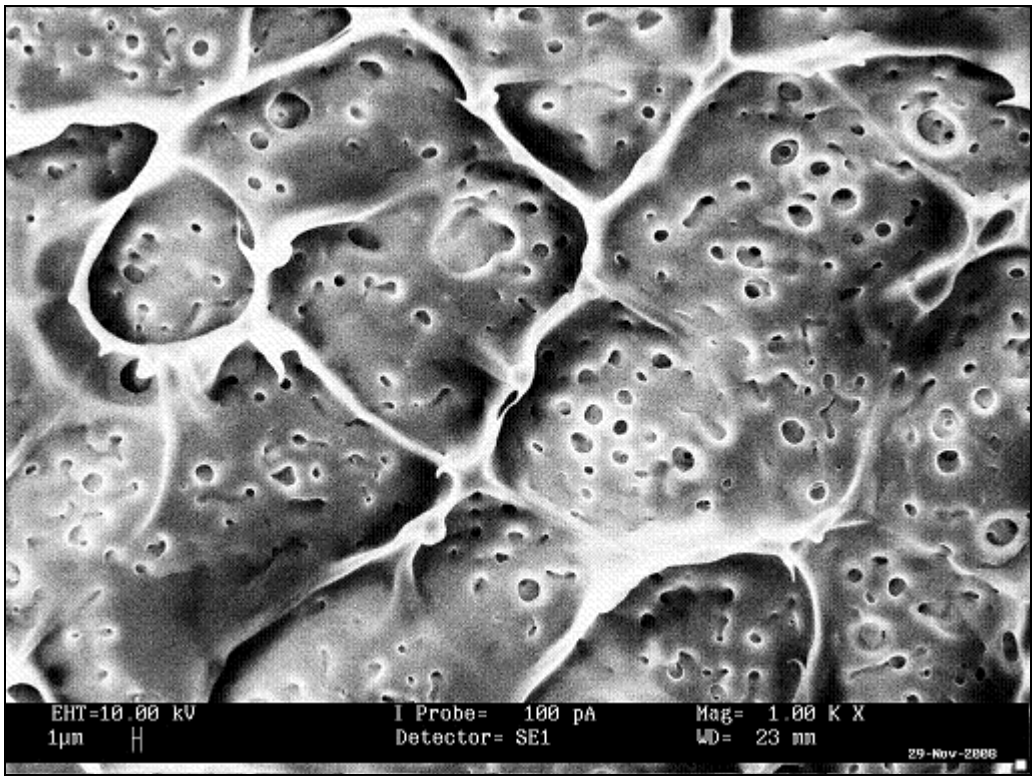

Figure 4.19 (c): SEM image of PMMA–PVC.

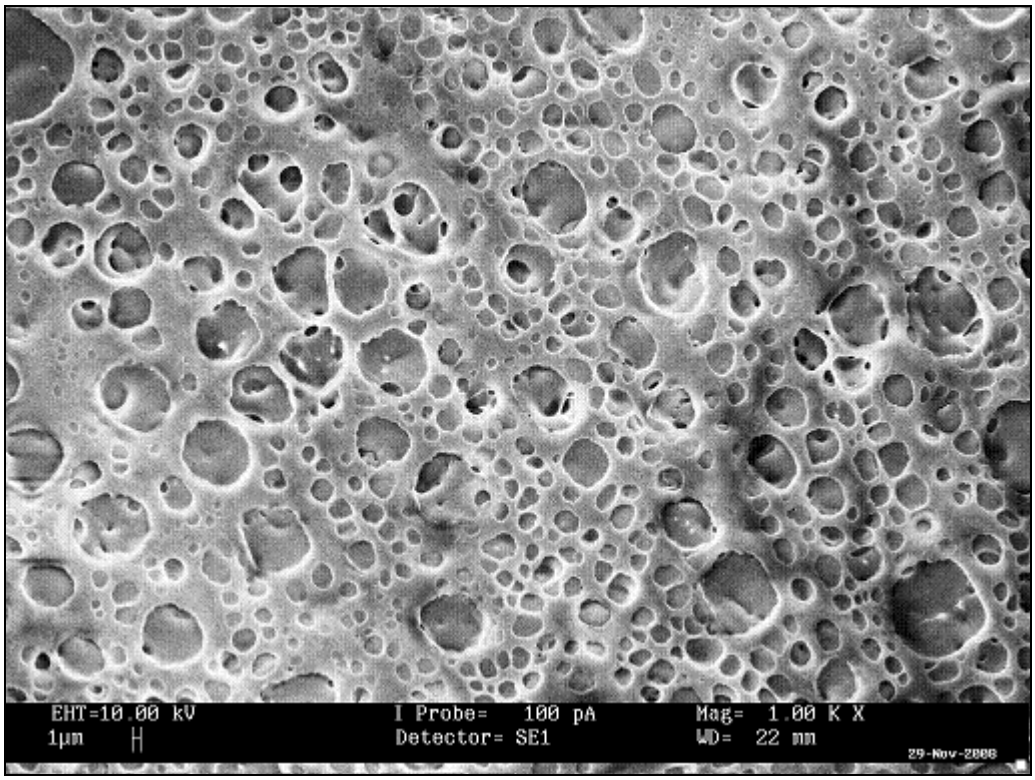

Figure 4.19 (d): SEM image of PE 3.

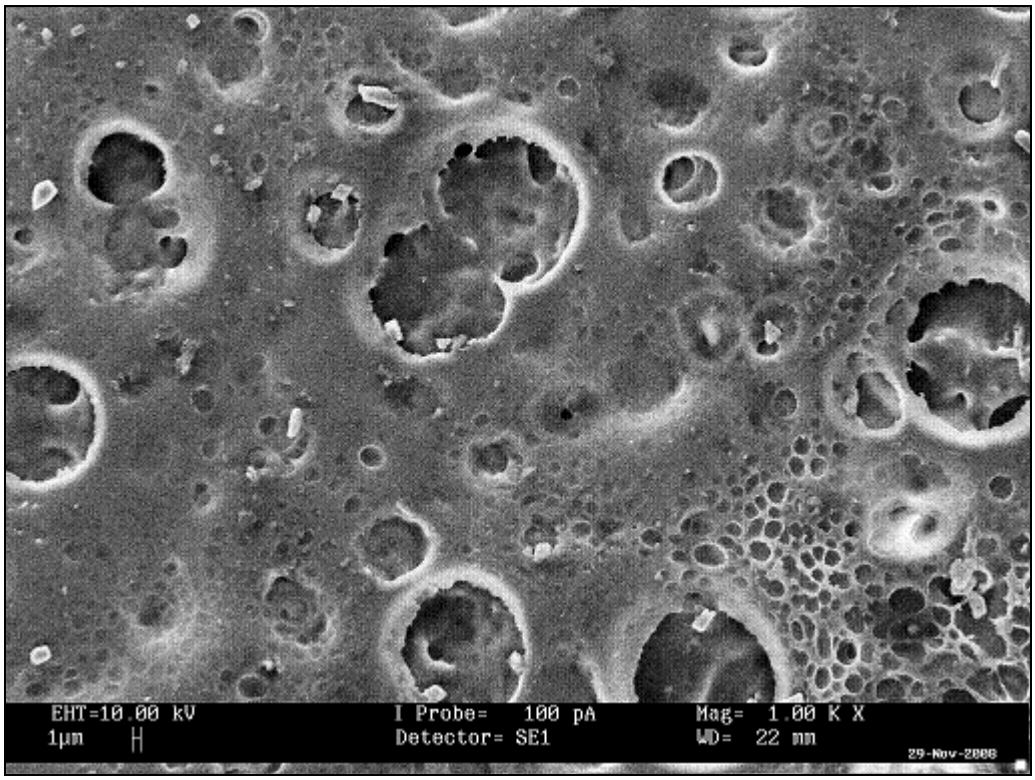

Figure 4.19 (e): SEM image of PE 5.

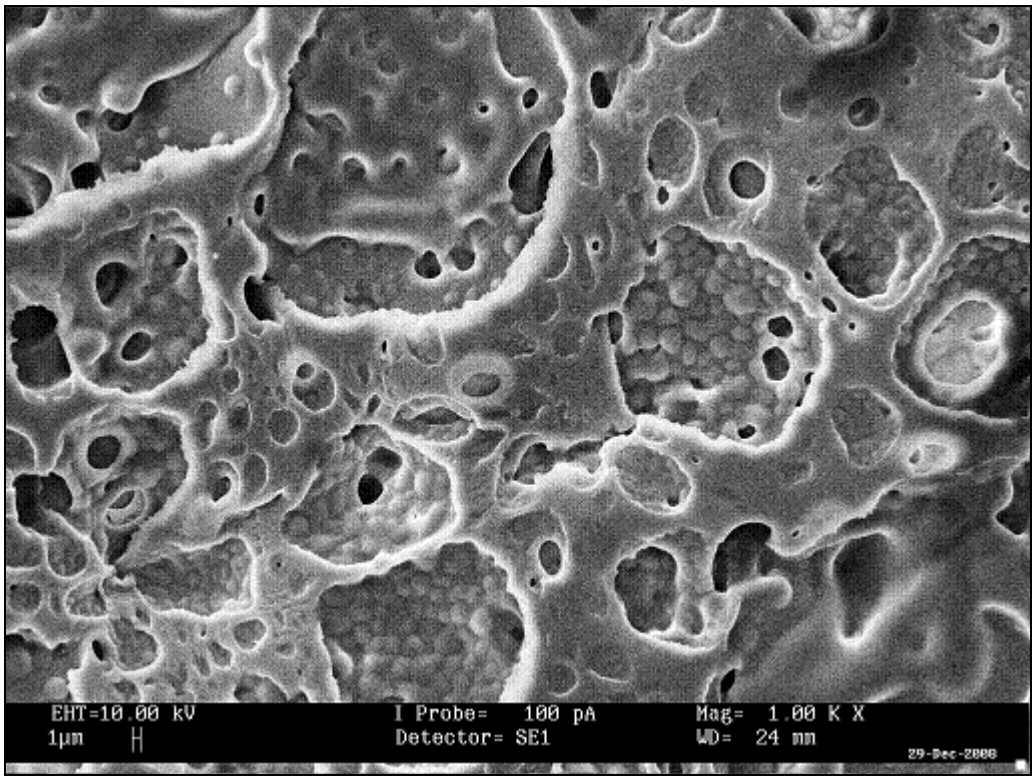

Figure 4.19 (f): SEM image of PE 9.

4.10 DSC studies

The DSC thermograms of pure PMMA, pure PVC, PMMA–PVC and PMMA–PVC blend based polymer electrolytes are shown in Figures 4.20 and 4.21. The DSC measurements are tabulated in Table 4.4. The following trend is observed in all the DSC thermograms. An endothermic reaction, T_g is observed which is then followed by T_m and T_d upon heating the samples further. Apparently, only one T_g is displayed for PMMA–PVC polymer blend and this indicates the homogeneous behavior of the polymer electrolyte (Ahmad *et al*., 2006a). In addition, T_g decreases upon incorporation of PVC due to the interaction

between PMMA and PVC via cross–linking. In contrast, T_m has been found to fall in the range of T_m values of PMMA and PVC as well as T_d values. One distinct endothermic peak T_m is illustrated in Figure 4.20. This broad peak is due to the overlapping of the melting points of PMMA and PVC. Two endothermic peaks are observed thereafter. These peaks are known as decomposition temperature, T_d. The first intense peak is related to the dehydrochlorination of PVC (Ahmad *et al*., 2007), whereas the degradation of unsaturated group of PMMA and the degradation of PVC contribute to second endothermic decomposition peak (Ahmad *et al*., 2006a). According to Figure 4.21, T_g is increased with the addition of LiTFSI. The shift towards higher temperature is due to the Li^+ preferring to interact with electron–rich coordinating groups, such as –O– and carbonyl group via transient cross–linkage bonds. These cross–linkage bonds obstruct the rotation of polymer segments and hence increase the energy barrier to the segmental movement. Eventually, this Li^+–O^- binding reduces the flexibility of polymer backbone (Li *et al*., 2006a; Ramesh and Arof, 2001b).

Moreover, the effect of higher loading of PVC onto DSC analyses is also investigated in order to determine the most compatible ratio of PMMA and PVC polymer blends. As shown in Figure 4.21, a single value for T_g is obtained for PE 3 whereas two values for T_g are obtained for PE 5 and PE 9. T_{g1} and T_{g2} correspond to the T_g values of PVC and PMMA, respectively. It shows the presence of phase separation of PMMA and PVC. This result is in agreement with

the SEM results. This phase separation is mainly due to the slow evaporation of polymer solutions during preparation. The slow increase of polymer concentration up to the solid state induces inhomogeneities in the polymer matrix. This is due to the polymer matrix having sufficient time to separate which in turn promotes the phase segregation (Braun *et al*., 2005a). At high PVC loadings, the agglomeration of similar phase of PVC happens and thus leads to the formation of inhibitors into the polymer segments. Such blocking region reduces the flexibility of polymer chain and contributes to the lower segmental motion of polymeric chain. Eventually, lower ionic conductivity is obtained for PE 5 and PE 9.

Excessive PVC adulteration enhances the dehydrochlorination process, thus promoting the cross–linking between polymer segments. This leads to insufficient flexibility of polymer chain and impedes the ion transportation (Ahmad *et al*., 2007). The detailed mechanism for cross–linking of PMMA and PVC is shown in Figure 4.22. Degrading products such as Cl free radicals and HCl are produced initially upon combustion. For further propagation, these free radicals are favored to react with the methoxyl group of PMMA due to the resonance effect, leading to dehydrochlorination process. At the same time, these radicals abstract hydrogen from PVC and produces HCl. These macroradical products from dehydrochlorination process react with each other and eventually form a cross–linkage between PMMA and PVC as shown in the termination process.

PE 3 shows the lowest T_g compared to PE 5 and PE 9. T_g is defined as the transition of temperature from glassy state to rubbery state. Beyond this transition, a long range molecular motion occurs and thus the degree of rotational freedom increases. As a result, the decrease in T_g helps in the softening of the polymer backbone and improves the segmental movement of polymer chains (Ramesh and Arof, 2001b, Stephan *et al*., 2002). Hence the ions flow more easily throughout the polymer chain. This enhances the ion transportation which achieves the highest ionic conductivity for PE 3. A discrete trend is also illustrated in Figure 4.21. In principle, polymer with higher crystalline region should have a higher melting point and heat of fusion (Yang *et al*., 2008b). As shown in Figure 4.21, T_m increases significantly with increase in the PVC content. Obviously, the heat of fusion also increases upon addition of PVC loadings. PE 3 exhibits lowest T_m and heat of fusion, thus indicating the lowest crystallinity of PE 3 as proven in XRD and SEM studies.

However, T_d are decreased upon further addition of PVC. PE 3 exhibits the highest T_d values, while PE 9 shows the lowest values, as tabulated in Table 4.3. These results suggest that PE 3 has excellent thermal properties than PE 5 and PE 9. It can be concluded from this study that 70 wt% of PMMA blended with 30 wt% PVC is the most compatible ratio. Beyond the decomposition temperature, the heat is maintained well. This indicates the complete decomposition of these polymer blend electrolytes at 450 °C.

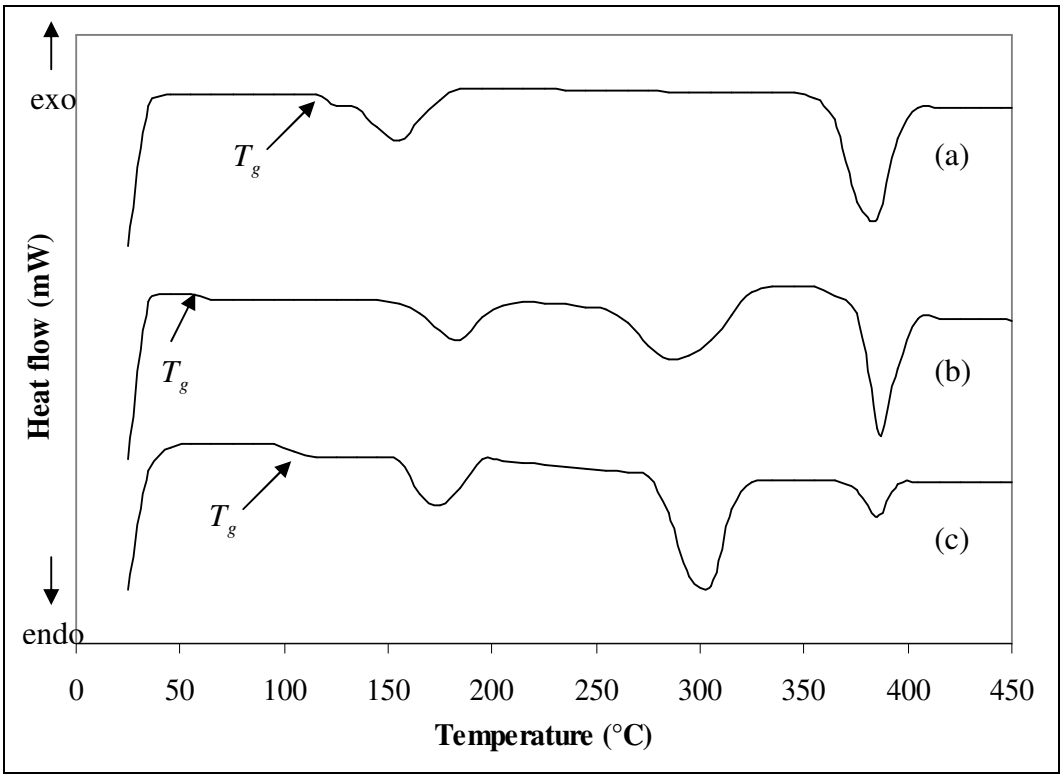

Figure 4.20: DSC thermograms of (a) pure PMMA, (b) pure PVC and (c) PMMA–PVC.

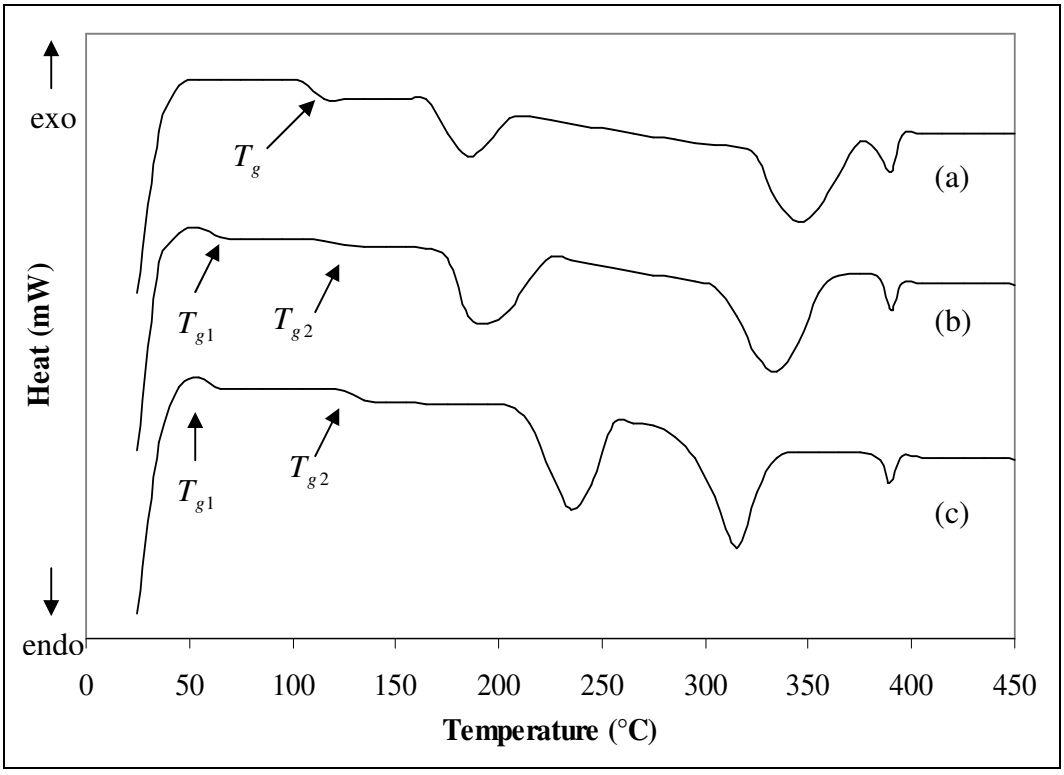

Figure 4.21: DSC thermograms of (a) PE 3, (b) PE 5 and (c) PE 9.

Designations	DSC measurements (°C)		
	T_g	T_m	T_d
PE 3	115.12	185.12	345.38, 388.01
PE 5	65.40, 125.09	192.13	335.16, 387.05
PE 9	66.23, 134.98	235.06	315.21, 386.31

Table 4.4: DSC measurements of PMMA–PVC based polymer blend electrolytes.

Initiation:

Step 1: Degrading product from PVC after combustion, which is Cl free radical.

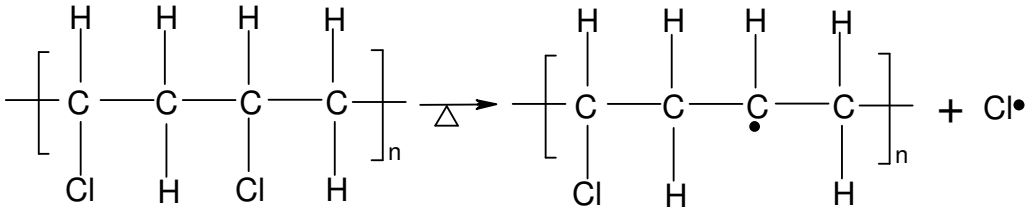

Propagation:

Step 2: Dehyrochlorination is happened where the free radical reacts with PMMA. This free radicals attack the carbon at methoxyl group due to the resonance effect.

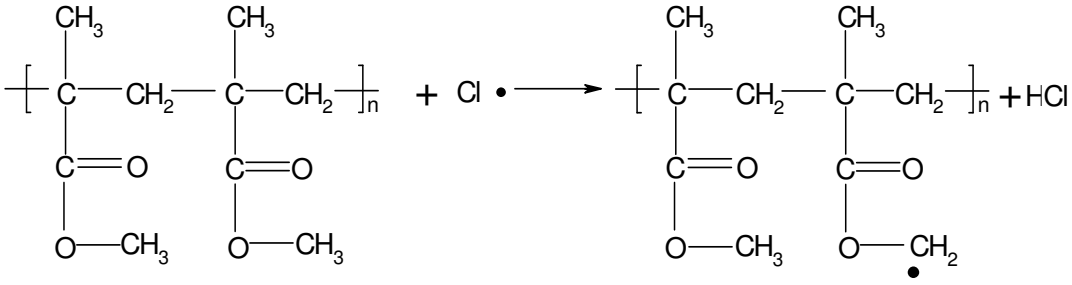

Step 3: The free radical abstracts hyrogen from PVC.

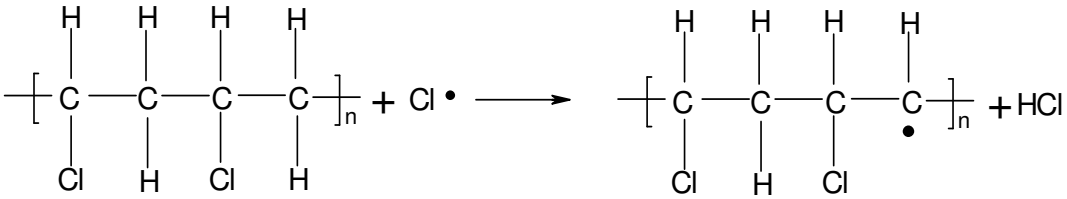

Termination:

Step 4: The product from step 3 is cross–linked with products of PMMA from step 2 PMMA

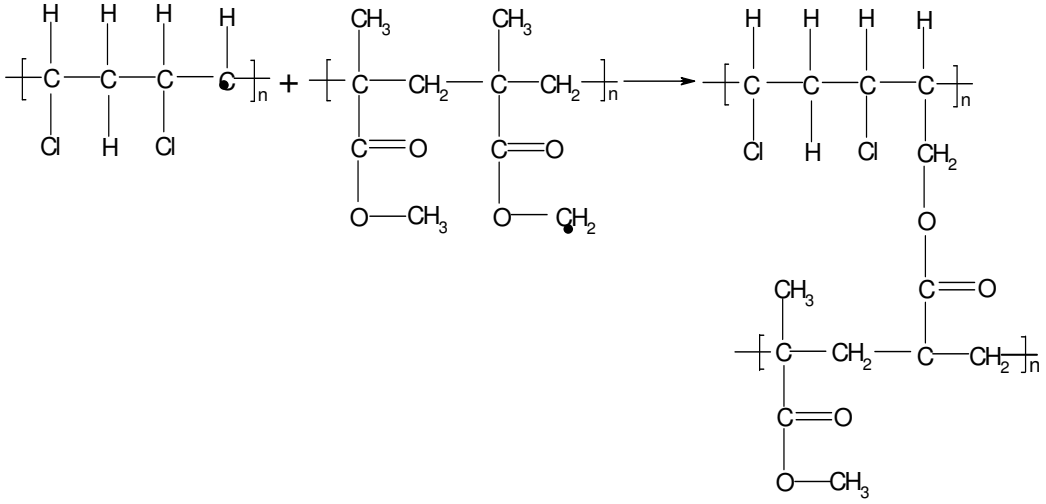

Figure 4.22: Mechanisms of cross–linking of PMMA and PVC.

4.11 TGA studies

Figures 4.23 and 4.24 depict thermogravimetric analyses of pure PMMA, pure PVC, PMMA–PVC and PMMA–PVC based polymer blend electrolytes. The weight of all the thin films remains stable up to 100 °C. It indicates that the sample has almost dried (Ramesh and Arof, 2001b). Based on the TGA curves, all the thin films have shown 3 stages, except for pure PMMA compound. The weight of all samples remains constant after the third stage, revealing the completion of decomposition. The initial weight loss of 4 % at 167 °C for pure PMMA and weight loss of 2 % at 148 °C for pure PVC sample is illustrated in Figure 4.23. However, PMMA–PVC blend has a weight loss of 2 % at 152 °C. The evaporation

of residual solvent, moisture and impurities are mainly due to fluorine. Fluorine is also the contributor for the initial weight loss, as the polymer tends to absorb moisture from its surroundings (Ramesh and Arof, 2001b). A dramatic drop in weight is observed for the second weight loss. The pure PMMA thin film looses 82 % weight at 387 °C with a residual mass of 11 %. This weight loss is attributed to the degradation of unsaturated group of PMMA as proven in DSC thermograms.

On the contrary, after complete dehydration, the second and final weight loss of PVC is 52 % at 256 °C and 6 % at 336 °C, respectively. The residual mass of 39 % has been shown at 386 °C. The second and final weight loss of PVC might be due to the volatilization of monomers, oligomers and dehydrochlorination. For PMMA–PVC blends, the baseline remains stable until 252 °C and this is followed by second and final weight losses. The second and final weight loss of 58 % at 342 °C and 13 % at 396 °C with a residue mass of 28 % was observed. It is observed that blending of PMMA with PVC enhances the thermal stability of polymers at higher decomposition temperature. The second significant weight loss may be due to the unzipping process which contributes to a reduction in molecular weight of polymer chain at high temperature. This unzipping reaction induces many degradation reactions such as random chain scission reaction, depolymerization, inter–molecular transfer reaction and intra–molecular transfer reaction whereby dimers, trimers and oligomers are produced as well as polymer fragments (Ahmad *et al*., 2007). As a result, the monomer and oligomers which chemi–adsorbed onto the polymer matrix is volatilized in this region. Dehydrochlorination of PVC might also be attributing to this mass loss. The final weight loss corresponds to the

degradation of unsaturated PMMA and PVC for PMMA–PVC polymer blends.

As shown in Figure 4.24, the first weight loss of around 11% and 4 % are obtained for PE 5 and PE 9, respectively. Beyond the first weight loss, the sample has a drastic weight loss of 56 % and 49 % for PE 5 and PE 9, respectively at about 269 °C. They are followed by a gradual fall in weight starting at 339 °C. At 389 °C, PE 5 has lost around 16 % of its weight with around 40% residual mass, whereas for PE 9, it is around 11% with 36% residual mass. However, the weight loss of the sample is remarkably low for PE 3. Based on the TGA curve, the initial weight loss of PE 3 is around 3 % followed by a modest weight loss of 29 % which starts at 279 °C until 349 °C. At 390 °C, the residual weight of PE 3 is still around 58 % with a loss of 10 %. As discussed earlier, the first weight loss is due to the evaporation of retained solvent, moisture and impurities which is mainly due to the fluorine compound from LiTFSI salt. The second weight loss is ascribed to dehyrochlorination of PVC which leads to the volatilization of monomers and oligomers. The degradation of PVC and the elimination of the degrading unsaturated functional group of PMMA are the contributors for final weight loss. In conclusion, with the increase in the decomposition temperature PE 3 shows a better thermal stability than PE 5 and PE 9 with a smaller weight loss.

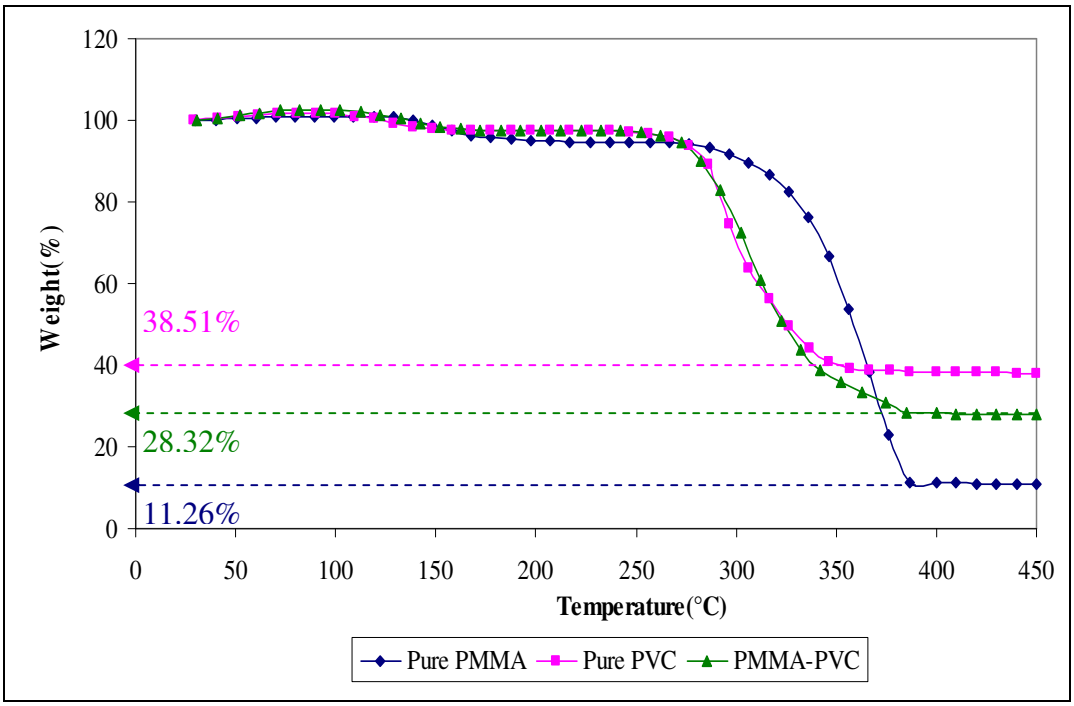

Figure 4.23: Thermogravimetric analysis of pure PMMA, pure PVC and PMMA–PVC.

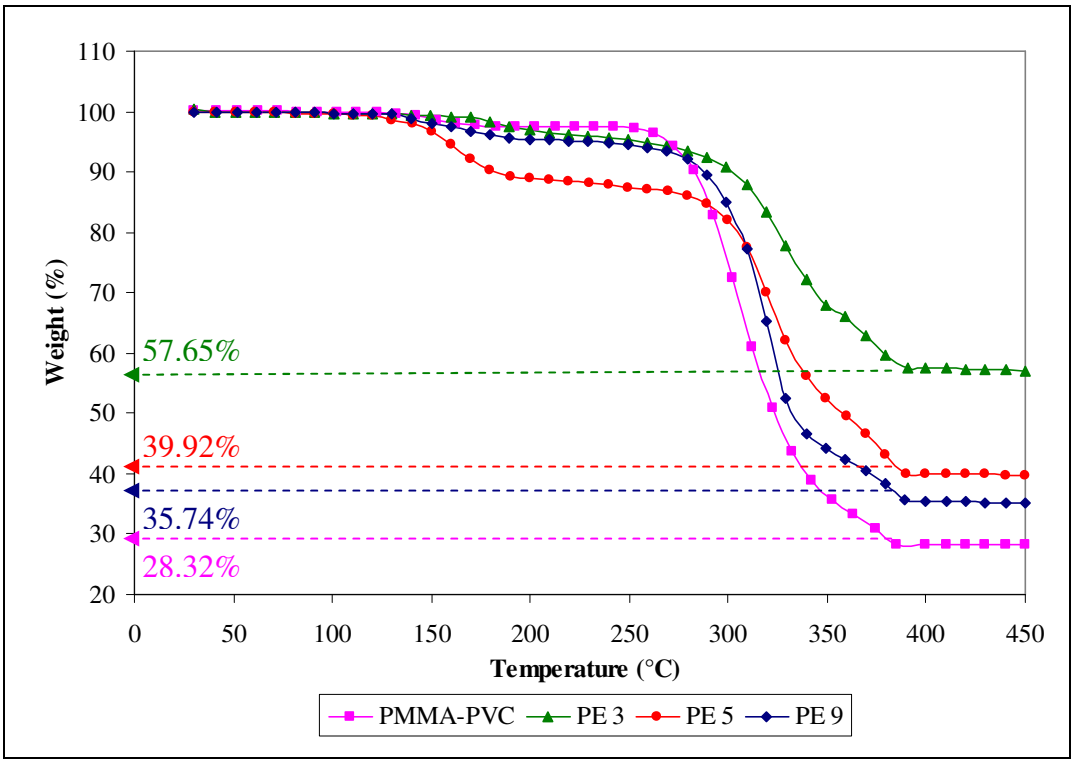

Figure 4.24: Thermogravimetric analysis of PMMA–PVC, PE 3, PE 5 and PE 9.

4.12 Amplitude Sweep

Figure 4.25 depicts the storage (G') and loss (G'') moduli as a function of imposed deformation on a logarithm scale. As shown in this figure, G' values are much greater than G'' for all the samples, implying that all the samples behave as solid. No crossover point of G' and G'' (or more commonly known as yield point or flow point) is observed for all the samples within the strain range, indicating that the transition of solid behavior to liquid behavior is absent with increasing the strain of the samples (Fonseca *et al*., 2009). General trends of all samples are observed. First, the small decrease in G' and G'' is attained and might be due to the initial deformation of samples. Thus, an almost constant range is occurred and this is usually defined as linear visco–elastic (LVE) range. In general, LVE range is the range of stability of a sample. The longer of the range, more stable of the sample is. As shown in Figure 4.25, PE 3 shows the wider stable range than PE 6. This discloses that PE 3 sample is more stable than PE 6. It still remains in high elastic properties even though longer elongation is produced.

Beyond this constant range, both of G' and G'' show an increment. They are decreased thereafter which in turn to the structural change of sample. At high strain, i.e. when the sample is more deformed, pure PMMA illustrates a sudden increases in G' and G'' and then followed by a decrement. The brief jump in G' and G'' is an evocative of enhancement of liquid properties at large change in dimensions by deformation. On the contrary, PMMA–PVC and PE 9 have same

patterns of plot. Pure PMMA shows the lowest values of G' at 0.001% of strain. However, both values are increased when PVC is introduced into the PMMA sample, inferring more solid–like behavior of PMMA–PVC polymer blends system. It is suggestive of formation of transient cross–linking between PMMA and PVC macromolecules.

The variation of composition ratio of PMMA to PVC is employed with 10 wt% of LiTFSI as a manipulated variable. At 0.001% of strain, PE 3 and PE 5 have shown abrupt increases in G' and G'' of about two orders of magnitude, whereas a gradual increase is observed for PE 9. It shows that PE 3 and PE 5 can store a larger amount of elastic energy (Fonseca *et al*., 2009). This strongly signifies the higher solid characteristic of samples and eventually higher in mechanical properties. The phenomenon arises from the self cross–linking effect between PMMA and PVC, as explained as above. Another perspective is the complexation between LiTFSI and polymer blends through hydrogen bonding. PE 5 has similar trend as PE 3, but the values of G' and G'' decrease slightly with increasing the strain. It is indicative of heterogeneous distribution of PMMA and PVC blends with increasing the PVC loadings (Ahmad *et al*., 2007). This is mainly attributed to the agglomeration of similar phase of PVC and thus ultimately leaded to formation of phase separation in the polymer matrix. Similar explanation is also applied onto the abrupt decrease in G' and G'' for PE 9 in comparing with PE 3 and PE 5. At high PVC content, PVC molecules tend to aggregate and thus interrupt the intermolecular bonding between PMMA and PVC, favoring the phase separation. Eventually, it reduces the solid characteristic of sample.

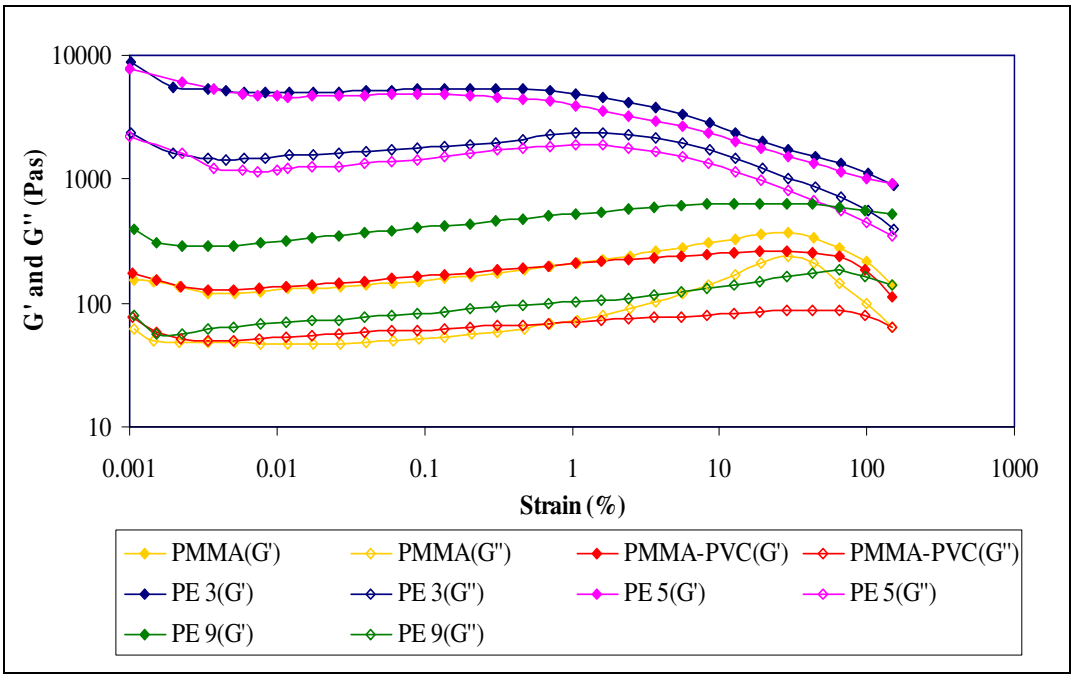

Figure 4.25: Amplitude sweeps of pure PMMA, PMMA–PVC, PE 3, PE 5 and PE 9.

4.13 Oscillatory Stress Sweep

The plot of G' and G'' versus shear stress is depicted in Figure 4.26. Solid properties of all samples are verified by showing larger amounts of G' than G'' within the range of shear stress. As expected, the flow point is absent, indicating the solid behavior of these samples. At beginning part, the gradual decrease is due to the initial disturbance on the samples when a small stress is applied. Pure PMMA shows an abrupt increase in G'' at higher shear stress, asserting the increase in the liquid nature of sample. It further indicates the decrease the elastic behavior when a large amount of stress is applied. Structural changes have been observed at high shear stress by demonstrating the decreases in G' and G''. Pure

PMMA and PMMA–PVC polymer solutions exhibit the lowest shear stress. This indicates the lowest mechanical properties of these polymer systems due to the lesser forces is required to deform the samples. Amount of shear stress is increased with the incorporation of LiTFSI. It is due to more energy is required to break the hydrogen bonding of LiTFSI and polymer matrix as hydrogen bond is the strongest covalent bond.

Among PE 3, PE 5 and PE 9, PE 3 requires the highest shear stress, while PE 9 is the lowest. It can therefore be concluded that PE 3 is a stiff material because it is difficult to rupture the transient covalent cross–linking between PMMA and PVC polymer backbones within this polymer matrix. However, stiffness of polymer systems decreases with PVC compositions. It is due to the aggregation of similar phase of PVC. As explained in section 3.1.1, this agglomeration causes the heterogeneous distribution within the polymer matrix and reduces the cross–linking effect. So, it might be divided into three regions, i.e., PMMA, PVC and combination of different ratio of PMMA–PVC polymer blends. Hence, the mechanical properties are also reduced with the presence of the heterogeneous distributions.

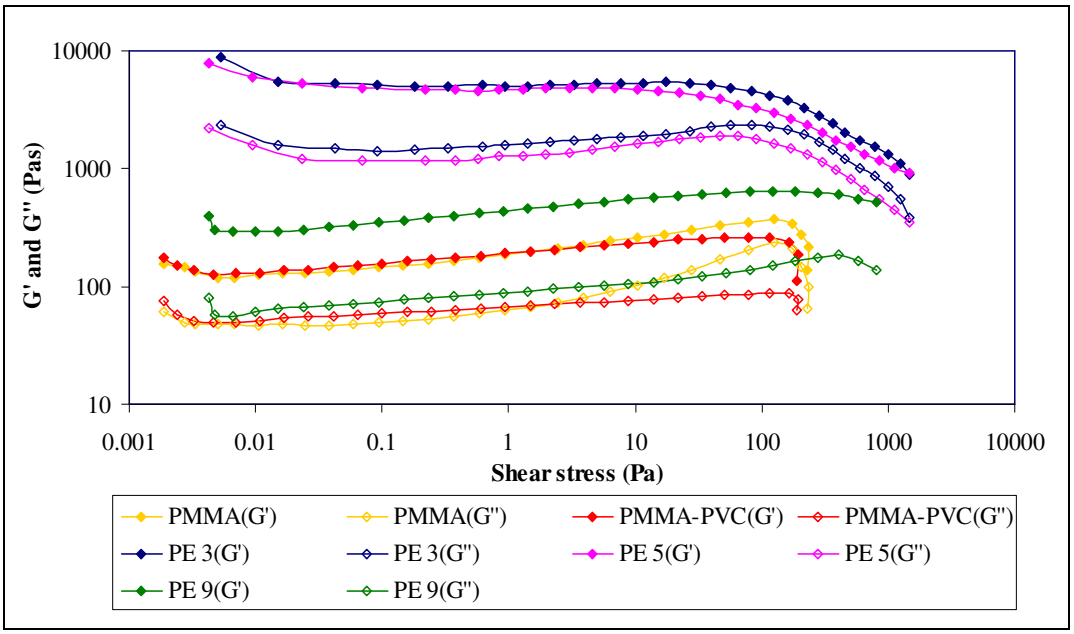

Figure 4.26: Oscillatory shear sweeps of pure PMMA, PMMA–PVC, PE 3, PE 5 and PE 9.

4.14 Oscillatory Frequency Sweep

After amplitude sweep is investigated, the frequency sweep is also performed by using the proposed strain value. Figure 4.27 illustrates the frequency sweeps of pure PMMA, PMMA–PVC, PE 3, PE 5 and PE 9 on logarithm scale. For all the samples, G'' is disappeared in this frequency regime. This denotes that the solid properties domain in the sample. Two apparent regions are observed. First, an abrupt increase in G' is occurred at low frequency whereas the frequency–independent relationship is attained at high frequency. In general, frequency is proportional to the reciprocal of time scale. The storage modulus is almost flat at high frequency and this implies the strong gel and elastic characteristic of the sample for short–term of deformation (Nicotera *et al*., 2006).

At low frequency, *G*' shows lower value. It can be concluded that the elastic properties are reduced and the long–term structural stability becomes less stable. This might be due to the longer relaxation time and therefore the polymer chain has enough time to inhibit the imposed deformation through the relaxation process (Ebagninin *et al*., 2009). The slippage of the entanglements is the main relaxation mechanism and hence it decreases the structural strength of macromolecules after a prolonged timescale. However, *G*' shows higher value at high frequency due to the declined relaxation time. The polymer chain is no longer slip past one another with this short relaxation time, and hence it reduces the segmental motion of polymer matrix. The ability of this fixed polymer chain to store the imposed energy is enhanced, leading to more elastic solid–like characteristic of polymer electrolytes.

At 0.01 $rads^{-1}$, pure PMMA shows the lowest *G*' value. It reveals that pure PMMA is the least unstable candidate for a long–term of deformation. However, the *G*' value is increased as PVC is embedded into the polymer. This strongly relates to the cross–linking effect between PMMA and PVC. However, the solid–like nature increases further with addition of LiTFSI. Among PE 3, PE 5 and PE 9, PE 3 shows the highest *G*' value and indicates the highest of its long–term structural stability. The values reduce with increasing PVC concentration. It is suggestive of the agglomeration of similar phase of PVC, which in turn to the phase separation in the polymer matrices. This phase segregation reduces the formation of transient cross–linkage. Since the cross-linking is lesser, thus the slippage of the intertwined polymer chains is more easily to be undergone,

promoting the structural change within the polymer matrix. Therefore, the polymer electrolytes will not able to store the elastic energy, which in accordance with lower value of G'.

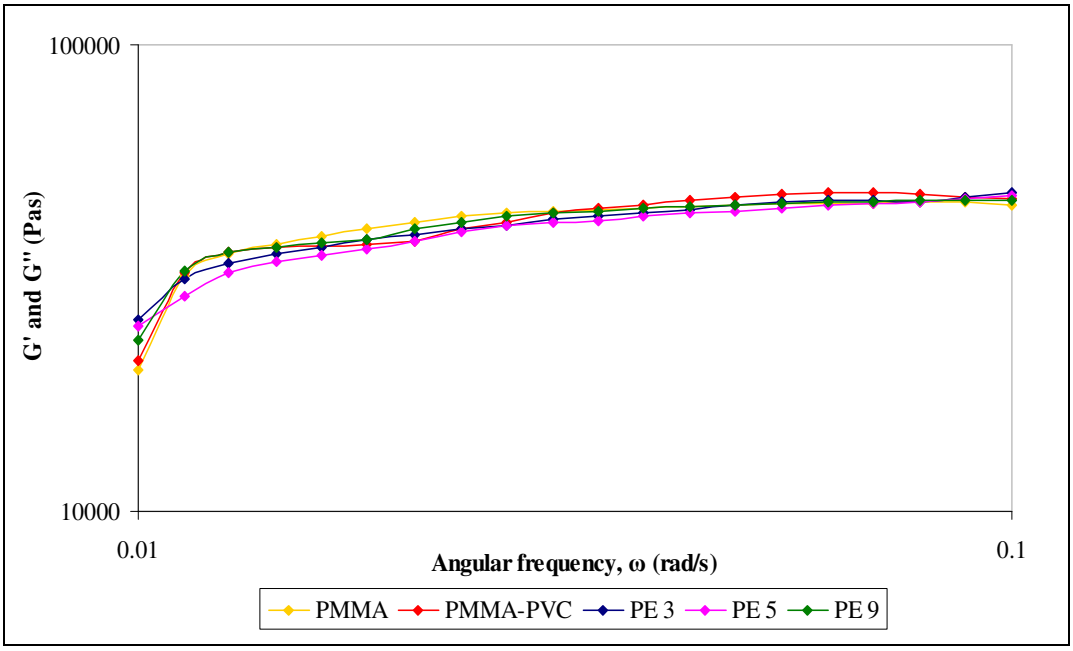

Figure 4.27: Frequency sweeps of pure PMMA, PMMA–PVC, PE 3, PE 5 and PE 9.

4.15 Viscosity Studies

Figure 4.28 illustrates the typical plot of viscosity with respect to shear rate on logarithm scale. As shown in Figure 4.28, the viscosities of all samples decrease with increasing shear rate, indicating the shear thinning properties of the samples (Ahmad *et al.*, 2005). In general, viscosity of sample is high if the particular sample exhibits a solid–like behavior when small deformation is applied. Pure PMMA solution behaves less solid–like characteristic as proven in previous

studies. So, it is expected that pure PMMA sample exhibits lower value of viscosity at low shear rate. By introducing PVC, the viscosity is increased. It is mainly attributed to the transient intercross–linking bond formation between PMMA and PVC. These cross–linkages reduce the polymeric chain mobility which in accordance with an increase in viscosity (Yang *et al*., 2008a).

On the contrary, the highest viscosity of PE 3 is further proven in this study as the storage modulus of PE 3 is the highest in the previous studies. This enhancement of viscosity arises from induction of cross–linking between PMMA and PVC and the complexation between LiTFSI and polymer blends, as discussed in previous studies. However, the viscosities of PE 5 and PE 9 are decreased at shear rate of $0.1s^{-1}$. It is indicative of aggregation of similar phase of PVC, which in turn to decreases in cross–linking effect. For pure PMMA–PVC and PE 3, the shear thinning occurs because the cross–linkage is being disrupted by the shear. On the other hand, the non–newtonian behaviors of PE 5 and PE 9 are attributed to the combination of interruption of cross–linking and break down of weak physical bonds among the PVC aggregates. At highest shear rate ($100s^{-1}$), the viscosities of PE 3, PE 5 and PE 9 are comparable. It means that the effect of PVC on viscosity is not so obvious at high rate of deformation. In other words, the viscosity is independent to PVC loadings when high shear rate is applied.

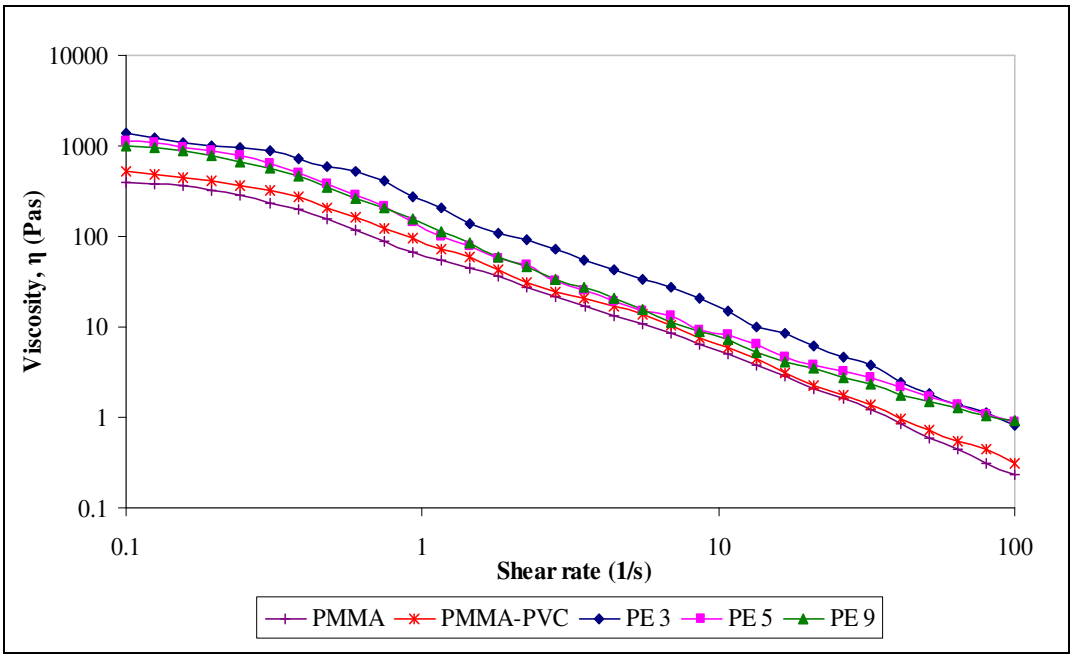

Figure 4.28: Typical viscosity curve of pure PMMA, PMMA–PVC, PE 3, PE 5 and PE 9.

4.16 Summary

The main purpose of this study is to find out the most compatible ratio of PMMA blended with PVC into the polymer electrolyte based LiTFSI system. The results obtained in ionic conductivity studies show that 70 wt% of PMMA blended with 30 wt% of PVC, denoted as PE 3, is achieved the highest ionic conductivity in the polymer blend system. In ambient temperature–ionic conductivity study, the highest ionic conductivity obtained among these samples is $(1.60\pm0.08)\times10^{-8}$ Scm^{-1}. These thin films exhibit Arrhenius behavior where the hopping mechanism is favored as shown in temperature dependence–ionic conductivity studies. According to this study, the ionic conductivity of $(3.49\pm0.01)\times10^{-8}$ Scm^{-1} is achieved at 80 °C.The dielectric behavior study is very helpful in understanding

the behavior of polymers and their blends. The dielectric studies reveal the electrode polarization effect and non–Debye properties of polymer blend electrolytes. In addition, the complexation between the PMMA, PVC and LiTFSI in the matrix polymers had been proven based on the formation of new peaks, change in intensity, shape and shift in peaks.

The XRD and SEM studies reveal the inherent amorphous properties of PE 3. Phase segregation is absent in PE 3 polymer matrix and this had been proven in SEM and DSC analyses. DSC analyses show that T_g and T_m of PE 3 are lowered whereas T_d is enhanced. This indicates the improvement of thermal properties of polymer electrolytes. By analyzing the TGA thermograms, it can be seen that PE 3 exhibits good thermal stability compared to other samples.

In the amplitude sweep and oscillatory shear sweep studies, the values of G' are much higher than G''. This indicates the solid properties of polymer electrolytes. The absence of crossover of G' and G'' indicates no behavioral transition in the samples. Pure PMMA shows the lowest mechanical properties with a smaller amount of G'. The mechanical properties of samples are improved with addition of PVC and LiTFSI by showing the higher G' values. Elastic properties of polymer electrolytes become lesser when the deformation takes place for a prolonged time at low frequency, implying the lower structural strength of polymer electrolytes. It is mainly attributed to the longer relaxation time. G'' is absent in the frequency regime and further indicates the solid behavior of samples.

The viscosity of polymer electrolytes reduces with increasing the shear rate, demonstrating the shear thinning properties. This is suggestive of disruption of cross–linkage, physical and chemical bonding in the polymer matrix. As a result, PE 3 possesses good mechanical strength without the phase separation, along with reasonable ionic conductivity.

CHAPTER 5

RESULTS AND DISCUSSION OF SECOND POLYMER BLEND ELECTROLYTES SYSTEM

5.1 AC– Impedance Studies

Figure 5.1 shows the typical Cole–Cole plots of complex impedance for SPE 6 in the temperature range of 298–353K. In low temperature range of 298–313 K, two well defined regions: a slanted spike at low frequency and a semicircle at high frequency are observed. However, the semicircle disappears beyond this temperature. It is due to random dipole orientation in the side chains of blended polymer system and induces to a non–capacitance nature (Baskaran *et al*., 2006b). The capacitance effect is characterized by polarization of immobile polymeric chain in the alternating current field. Therefore, only the resistive components in the polymer electrolytes prevail at this moment and then construct a local effective conducting pathway for ionic conduction of polymer electrolytes. As a result, migration of ions is enhanced as the electrical potential alternates between the positive and negative electrode in the alternate current field. As a conclusion, the disappearance of semi–circle region indicates the current charge carriers are ions and results an ion conduction mechanism (Rajendran *et al*., 2004).

In contrast, the semi–circle portion reveals the characteristic of a parallel combination of bulk resistance and bulk capacitance of polymer matrix. In other

words, this conduction mechanism is depending on both migration of Li^+ ion through the free volume of polymer matrix which can be represented by a resistor at low frequency whereas the polarization of immobile polymeric chain in the alternating field is represented by a capacitor at high frequency. From Figure 5.1, the R_b decreases as temperature is increased. As a result, ionic conductivity increases with increasing temperature. It is ascribed to the enhancement of thermal mobility of polymer chain in the polymer electrolyte system and rate of dissociation of LiTFSI as temperature increases. The explanation is further discussed in the temperature dependence–ionic conductivity study.

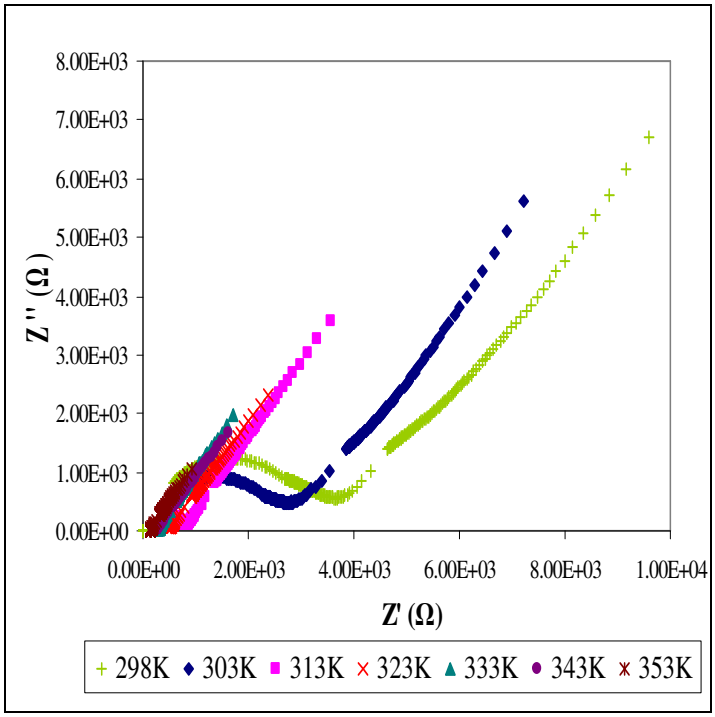

Figure 5.1: Complex impedance plot of SPE 6 in the temperature range 298–353K.

5.2 Ambient Temperature–Ionic Conductivity Studies

Figure 5.2 depicts the logarithm of ionic conductivities with respect to the amount of LiTFSI added into polymer blend electrolytes. According to the figure, SPE 6 exhibits the highest ionic conductivity of (1.11±0.09) x 10^{-6} Scm^{-1}. As expected, the ionic conductivity increases with increasing the content of LiTFSI. As the content of LiTFSI increases, the concentration of mobile charge carriers increases, thus leading to increment in ionic conductivity. In addition, the $TFSI^-$ ions tends to produce an electrostatic environment, which results in decrement of the mean hopping distance of charge carriers which increases the ionic conductivity (Baskaran *et al*., 2006b).

The ionic conductivity increases with LiTFSI concentration, to an optimum level. It is then followed up by a decrease when the LiTFSI salt is further added. The increase in ionic conductivity is due to the long Coulombic forces range that leads to re–dissociation of solvated ion pairs with increasing LiTFSI concentration. This contributes to increase in concentration of free mobile charge carriers which are available for segmental migration. Hence, the ionic conductivity is enhanced as mobility and concentration of mobile charge carriers are increased. After addition of 30 wt% LiTFSI, the maximum ionic conductivity is achieved. It is due to the concentration and mobility of charge carriers having reached an optimum limit. In addition, the optimum percolation threshold has also been reached. This gives rises to greatest extent of conductivity properties of lithium salt via formation of percolation pathways. Eventually, the highest ionic conductivity is achieved. After

this optimum limit, the ionic conductivity is decreased with increasing the LiTFSI concentration. This may be attributed to the formation of neutral ion pairs at high salt concentration. Hence, the effective number of free charge carriers which are available for transportation is reduced (Ali *et al*., 2007). At high content of LiTFSI, the retarding effect of ion cloud is more dominant rather than build–up of mobile charge carriers. This impedes mobility of charge carriers in a rigid framework and induces to a decrease in ionic conductivity (Rajendran and Uma, 2000). Other than that, the decrease in ionic conductivity is due to the conglomeration of excess LiTFSI which leads to formation of blocking phase for existing conducting paths. Thus, it hinders the mobility of charge carriers and induces to the decrement in ionic conductivity (Sharma and Sekhon, 2007).

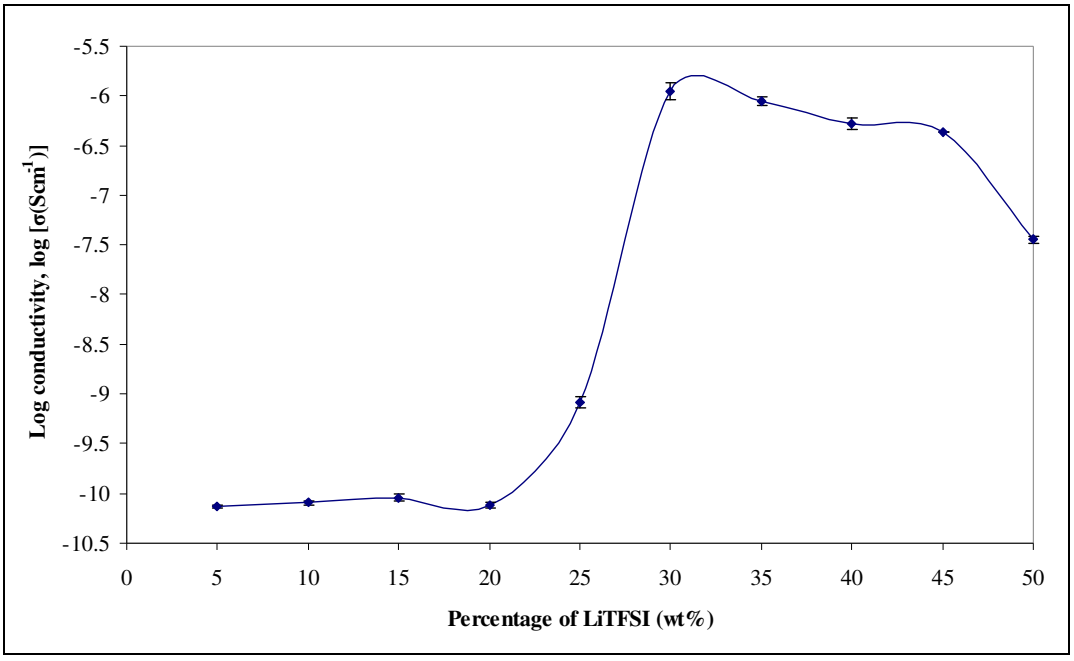

Figure 5.2: Variation of log conductivity, log σ as a function of weight percentage LiTFSI added into PMMA–PVC based polymer blend electrolytes at ambient temperature.

5.3 Temperature dependence–ionic conductivity studies

Figure 5.3 illustrates the ionic conductivity of SPE 3, SPE 6 and SPE 8 against the reciprocal absolute temperature. According to this figure, it is further proven that ionic conductivity increases with a function of temperature. As temperature increases, the expansion of polymer matrix results and thus weakens the interaction within the polymer matrix. This initiates the decoupling of Li cations from the polymer matrix. Besides, as the temperature is increased, the polymeric chain acquires faster internal modes and thus promotes the bond rotation, resulting in faster segmental mobility. Consequently, the intra–chain and inter–chain of ion hopping mechanisms are favorable, which in turn result in higher ionic conductivity (Baskaran *et al*., 2006b). At 80 °C, the ionic conductivity of SPE 6 increases by an order in magnitude, that is around (1.90±0.02) x 10^{-5} Scm^{-1}.

Since the regression values are close to unity, it implies that the variation in ionic conductivity with temperature obeys the linear relationship, which is Arrhenius relationship, as shown in Equation 4.1. In this theory, the hopping mechanism is favorable. For Arrhenius relationship, it states that the nature of transportation of charge carrier is similar with the migration in ionic crystal. Since the interaction of polar group of the blended polymers with Li cations is weaker, these charge carriers are decoupled from the segmental motion in polymer chain and tends to dissociate. Thus, it creates vacant sites or empty voids in the polymer

chain. Therefore, the ions tend to occupy these neighboring vacant sites. This transportation of charge carriers increases the ionic conductivity.

It also divulges that the polymer electrolyte is in completely amorphous phase as there is no abrupt jump in the variation of ionic conductivity with temperature (Ramesh and Arof, 2001a). From the derivation of equation above, the activation energy (E_a) which is a combination of energy required for defect migration of charge carriers and defect formation is determined. It is evaluated from the slope of the Arrhenius plot. The E_a values obtained for SPE 3, SPE 6 and SPE 8 are 0.4489 eV, 0.4427 eV and 0.4436 eV, respectively. An obvious trend could be observed from this result that is the ionic conductivity is inversely proportional to E_a. Since SPE 6 exhibits highest ionic conductivity, thus it has lowest activation energy for hopping process of the ions. This is due to the presence of completely amorphous regions in the polymer matrix which assists the transportation of charge carriers by providing larger free space for ion and segmental migration.

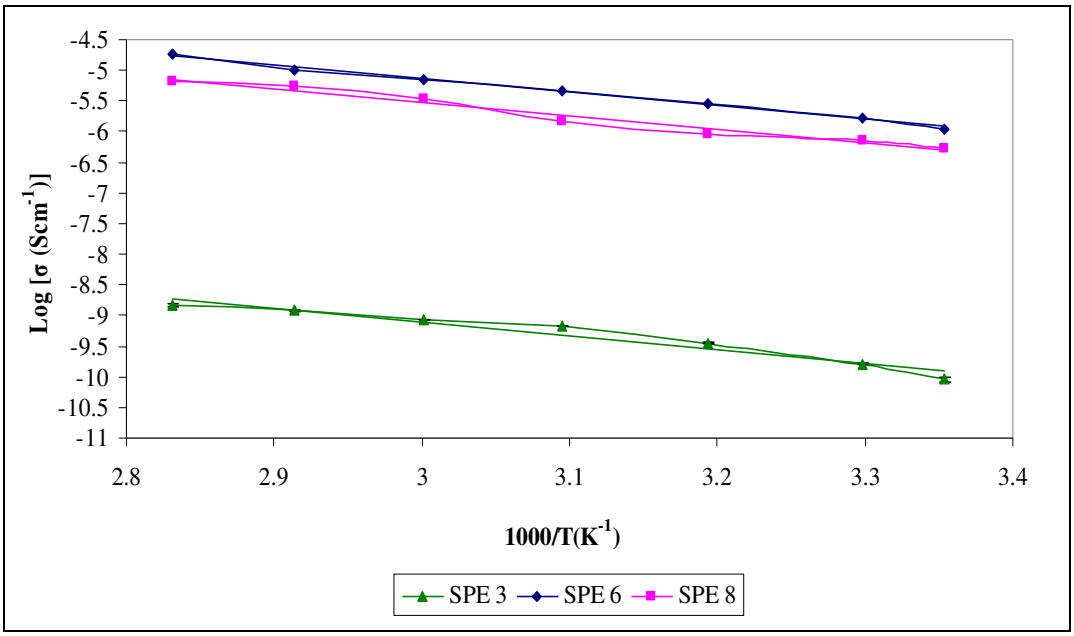

Figure 5.3: Arrhenius plot of ionic conductivity of SPE 3, SPE 6 and SPE 8.

5.4 Frequency Dependence–Ionic Conductivity Studies

Figure 5.4 depicts the frequency dependence conductivity for SPE 6 at different temperatures. The sample exhibits frequency–dependence behavior within the frequency range. As shown in Figure 5.4, the ionic conductivity increases with frequency and temperature. The low conductivity in the low frequency dispersion region is ascribed to the space charge polarization effect at the electrode–electrolyte interface, indicating the non–Debye characteristic of polymer matrix (Ramesh *et al*., 2007). It may be due to the enhancement of space charge carriers accumulated at this interface and thus the effectiveness of applied field across the sample is decreased. Thus, the density of mobile ions available for migration is reduced and this decreases the ionic conductivity (Baskaran *et al*., 20006b). In contrast, the concentration of space charge which builds up at the

electrode–electrolyte interface is lesser at high frequency and leads to an increase in mobility of charge carriers. Hence, the ionic conductivity increases with increasing frequency.

In addition, the ionic conductivity increases with temperature. As temperature increases, the hopping process of charge carriers is more favored and leads to an increase in movement of ions and eventually to an increment in ionic conductivity. It also indicates the presence of hopping mechanisms between coordinating sites, local structural relaxations and segmental migration of the polymer matrix (Baskaran *et al*., 2006b). Based on these variations, it agrees with Jonscher's universal law which is applied to all dielectric materials in the condensed phase. Jonsher had compiled the ac–conductivity in varying the frequency as shown below.

$$\sigma(\omega) = \sigma_{dc} + A\omega^{n}, 0.5 < n < 1 \qquad \text{(Equation 5.1)}$$

where $\sigma(\omega)$ is ac–impedance, σ_{dc} is the dc limit of conductivity, A is a constant at a particular temperature, n is the power law exponent. In this universal behavior, Jonsher proposes that the frequency–dependence ac–conduction mechanism is attributed to hopping process between the charge carriers in the polymer matrix (Stephan et al., 2000b).

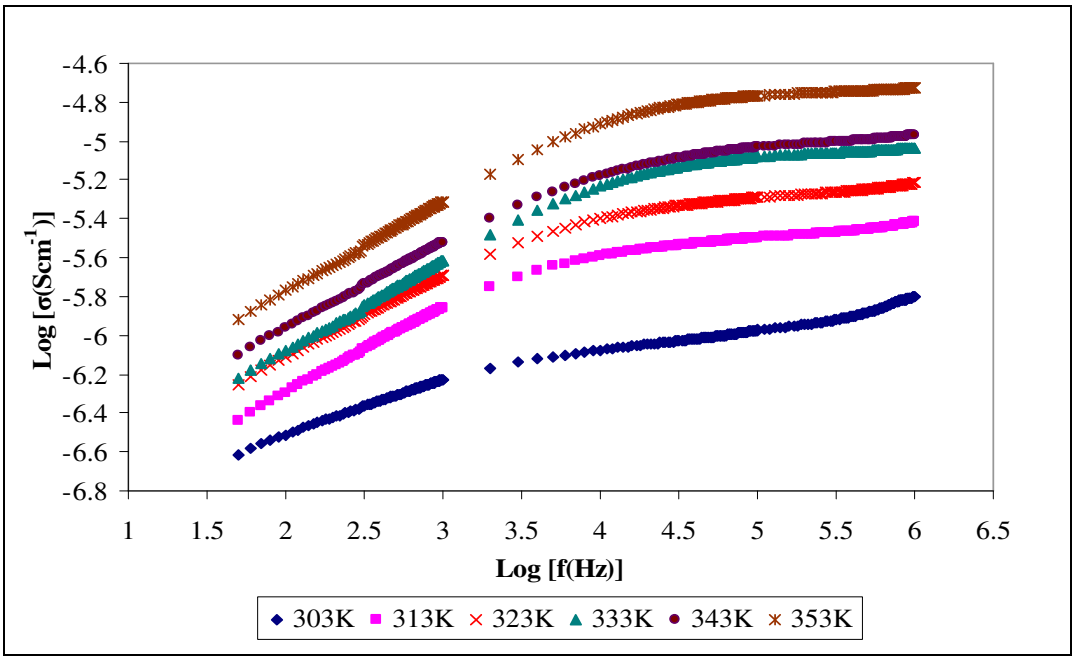

Figure 5.4: Frequency dependent conductivity for SPE 6 in the temperature range of 303–353 K.

5.5 Dielectric Relaxation Studies

Figures 5.5 and 5.6 illustrate the frequency dependence variation of real (ε') and imaginary (ε'') permittivity of the dielectric relaxation constants for SPE 6, respectively, in the temperature range of 303–353 K. Both dielectric constant and dielectric loss rise sharply towards low frequency. These observed variations in ε' and ε'' as a function of frequency are attributed to accumulation of charge at the electrode and electrolyte interface and yield a space charge region. With the presence of this polarization effect, it reveals the non–Debye type of behaviour. Moreover, it also might be due to the retention of water in the polymer matrix (Goodwin *et al.*, 1999). In contrast, ε' and ε'' decrease with increasing frequency. It is ascribed to high reversal of the external electric field at the

electrode and electrolyte interface and causes a reduction in density of charge carriers at this interface. Thus, the diffusion of excessive ions is lesser in the direction of electric field and induces the inhibition of orientation of dipoles. This leads to a decrease in polarization and then weakens the interaction of dipoles and electric field. As a consequence, ε' and ε'' decrease as frequency increases (Venkateswarlu *et al*., 2000; Kumar and Bhat, 2009).

According to both figures, ε' and ε'' increase as temperature increases. It is due to the extent of lithium salt dissociation and rate of re–dissociation of ion aggregates are increased with increasing temperature. This contributes to an increment of free mobile ions which are favorable for transportation and thus increases the density of charge carriers (Fernandez *et al*., 2008). As shown in these figures, ε' and ε'' at 353 K shown the highest value in the interval of 303–353 K and this divulges that the ionic conductivity at 353 K is the optimum value. It has been proven in the Cole–Cole plots and temperature dependence studies. The absence of polarization peaks in the figure may be attributed to the phase–separated morphology of the polymer electrolytes (Stephan *et al*., 2000b).

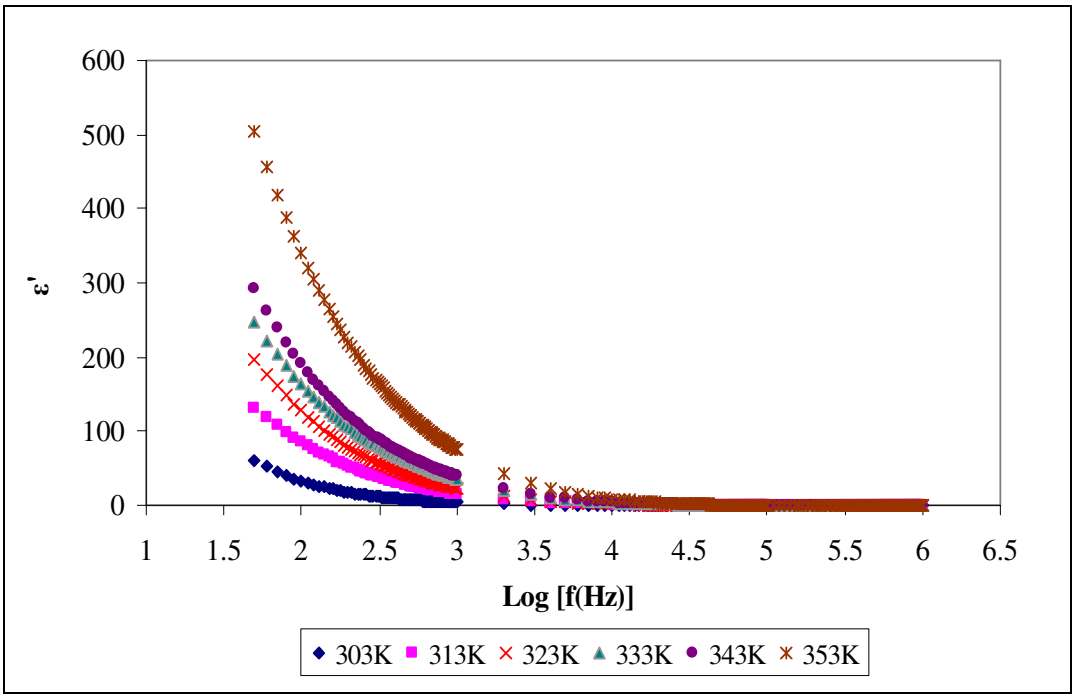

Figure 5.5: **Variation of real part of dielectric constant, ε' with respect to frequency for SPE 6 in the temperature range of 303–353 K.**

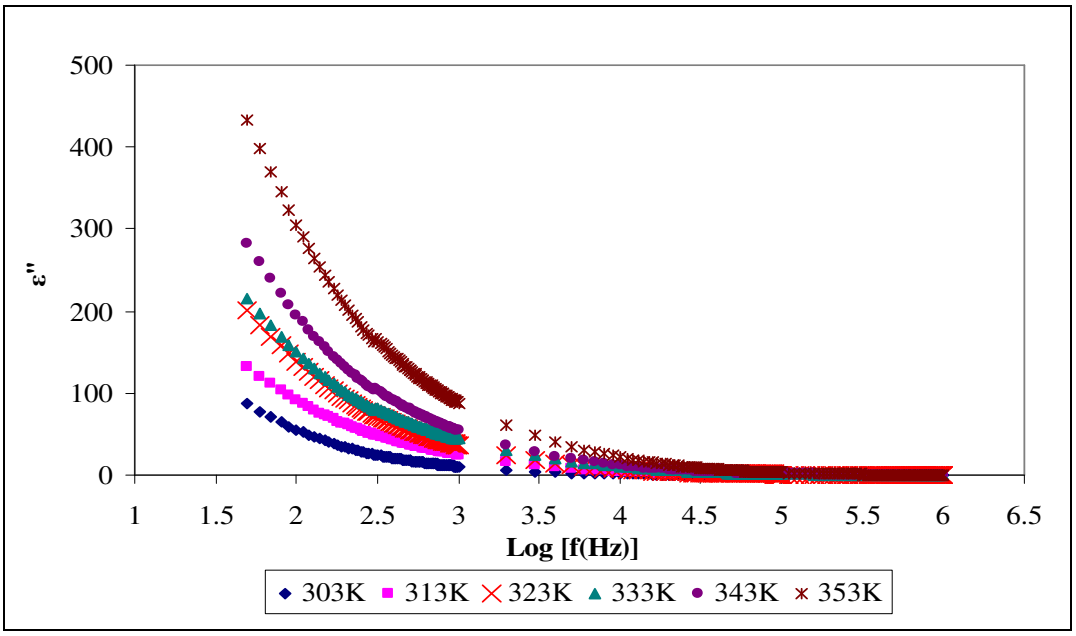

Figure 5.6: **Variation of imaginary part of dielectric constant, ε'' with respect to frequency for SPE 6 in the temperature range of 303–353 K.**

5.6 Dielectric Moduli Studies

The real ($M^{'}$) and imaginary ($M^{''}$) parts of dielectric moduli as a function of frequency for SPE 6 in the temperature range of 303–353 K are exemplified in Figures 5.7 and 5.8, respectively. At low frequency regime, both $M^{'}$ and $M^{''}$ tend to approach zero as shown in this figure. This reveals the insignificance of polarization effect at the electrode and electrolyte interface at low frequency range. A long tail is observed at low frequency regime in these figures. It implies that the capacitance associated with electrodes is higher (Kumar and Bhat, 2009). Even though well defined dispersion peaks are not observed in both of these variations, but $M^{'}$ and $M^{''}$ show obvious increment at high frequency regime. These curve peaks indicate the presence of bulk effect in the polymer matrix and polymer electrolytes are ionic conductors. The intensity of these peaks decreases with increasing temperature. It may be due to the plurality of relaxation mechanism where the time is required to accumulate charge carriers at the electrode and electrolyte interface before the field changes the direction (Ramesh and Arof, 2001a).

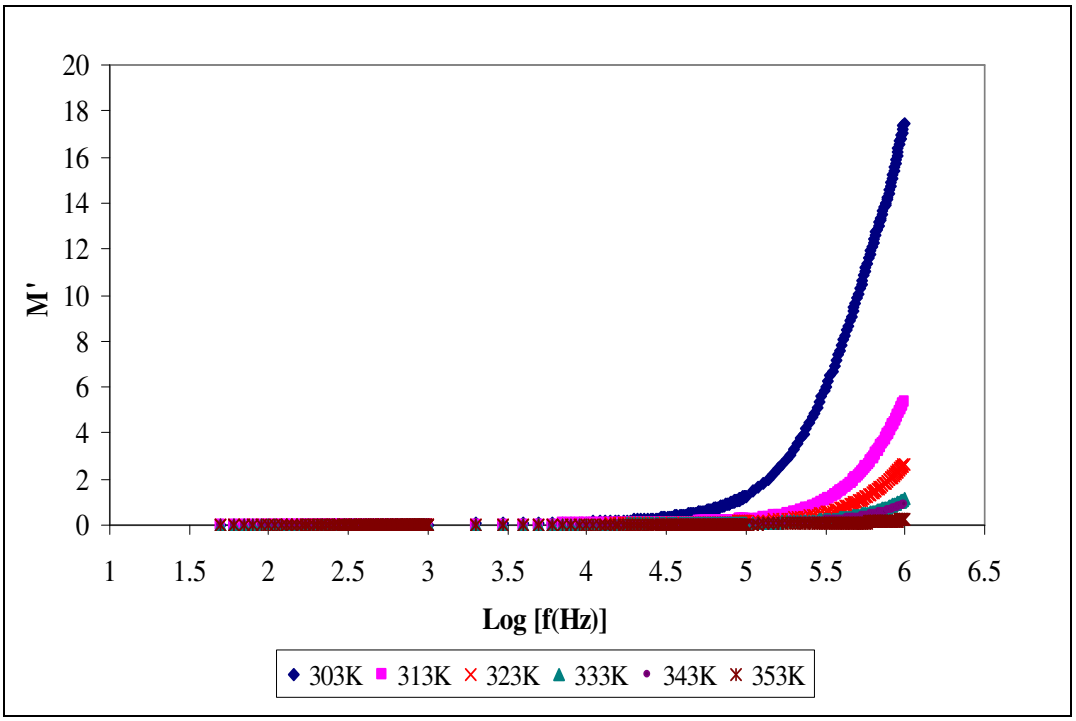

Figure 5.7: **Variation of real part of modulus, $M^{'}$ with respect to frequency for SPE 6 in the temperature range of 303–353 K.**

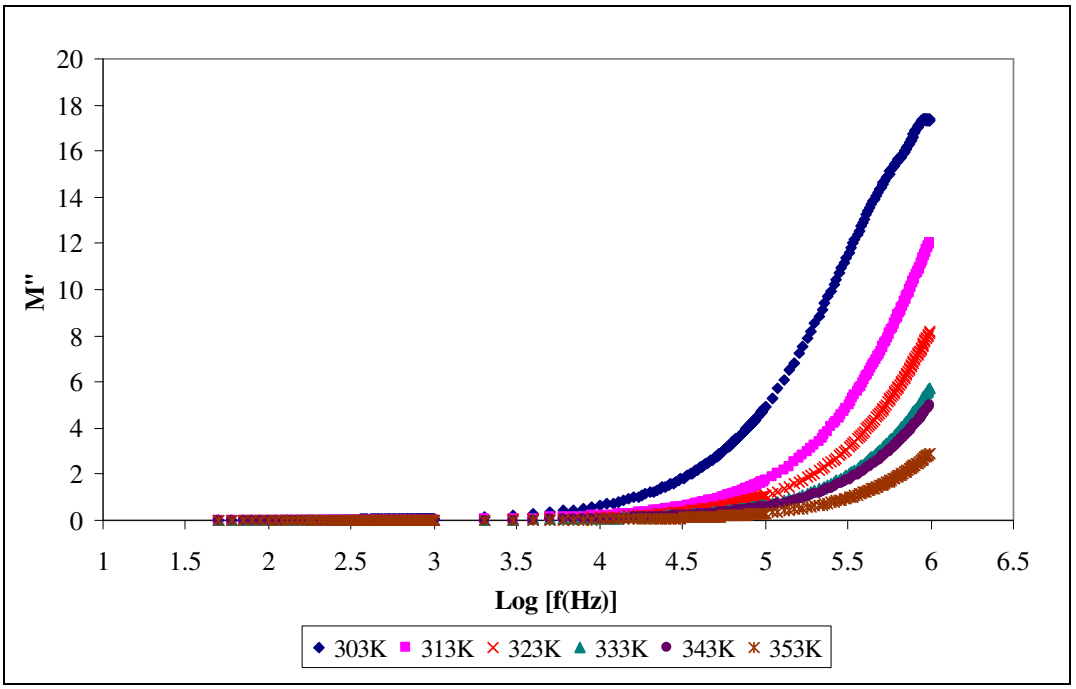

Figure 5.8: **Variation of imaginary part of modulus, $M^{''}$ with respect to frequency for SPE 6 in the temperature range of 303–353 K.**

5.7 HATR–FTIR studies

The HATR–FTIR spectra of SPE 3, SPE 6 and SPE 8 are illustrated in Figures 5.9 (a)–(c). In contrast, the comparison of HATR–FTIR spectra for PMMA–PVC, pure LiTFSI, SPE 3, SPE 6 and SPE 8 are shown in Figure 5.10. Table 5.1 shows the designations of the characteristic peaks of PMMA, PVC and LiTFSI for SPE 6 system. The HATR–FTIR spectrum of SPE 6 is further discussed as it achieves the maximum ionic conductivity in the study. There are five new peaks appearing by comparing SPE 6 with PMMA–PVC. These new peaks are assigned as combination of C–S and S–N stretching mode of LiTFSI, C–SO_2–N bonding mode of LiTFSI, SO_2 asymmetric stretching mode of LiTFSI and S–CH_3 bonding mode of LiTFSI at 791 cm^{-1}, 1327 cm^{-1}, 1349 cm^{-1}, 2845 cm^{-1} and 2997 cm^{-1}, respectively. It indicates that there is an establishment for formation of polymer salt system.

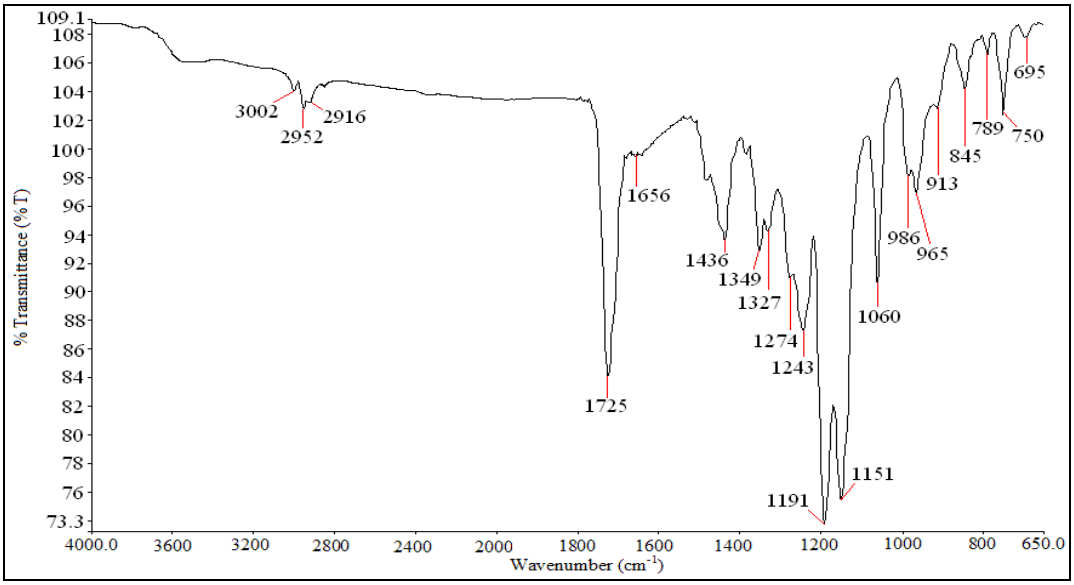

Figure 5.9 (a): HATR–FTIR spectrum of SPE 3.

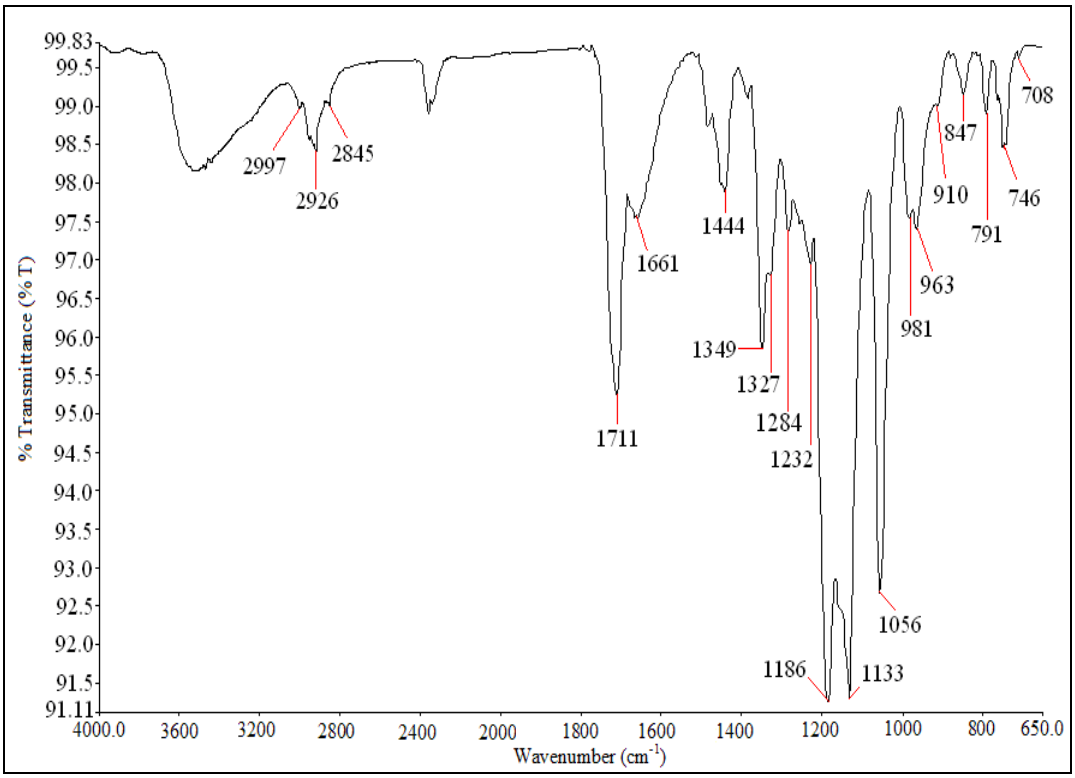

Figure 5.9 (b): HATR–FTIR spectrum of SPE 6.

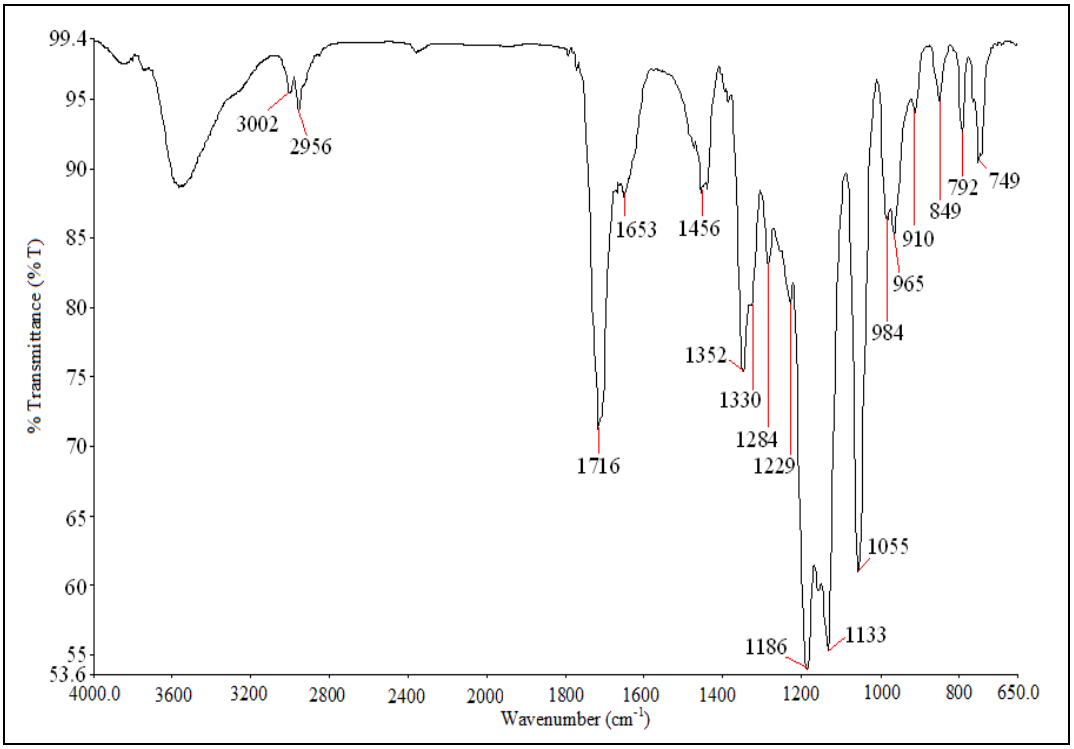

Figure 5.9 (c): HATR–FTIR spectrum of SPE 8.

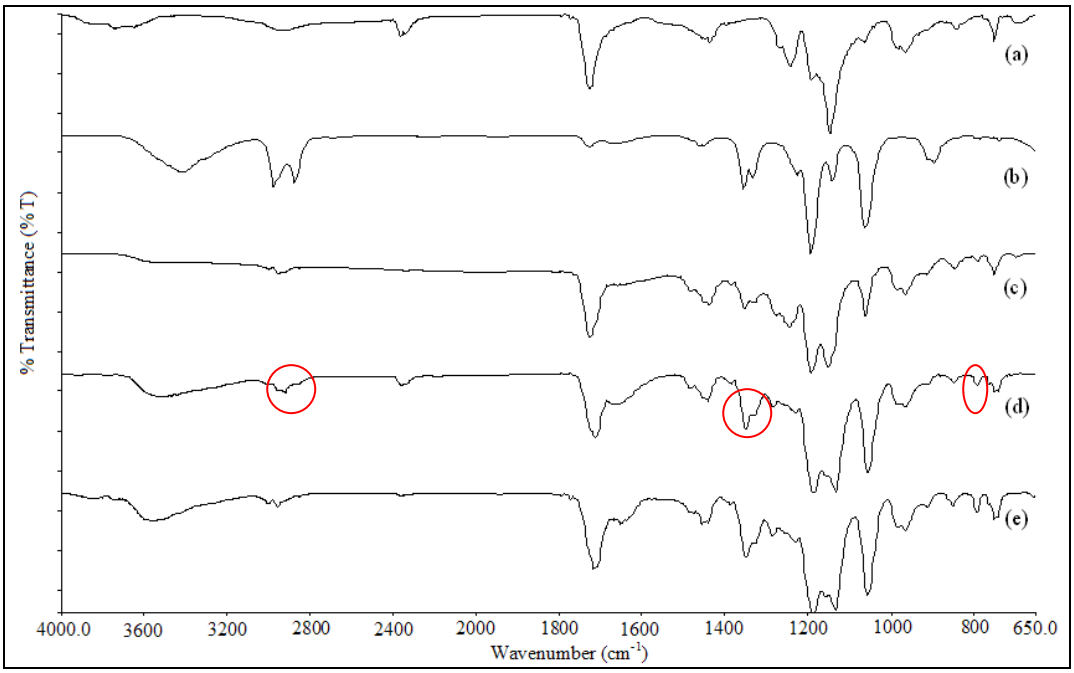

Figure 5.10: Combination of HATR–FTIR spectra for (a) PMMA–PVC, (b) pure LiTFSI, (c) SPE 3, (d) SPE 6 and (e) SPE 8.

Description vibration modes	Wavenumber (cm^{-1})	References
Cis C–H wagging mode of PVC	708	Rajendran *et al.*, 2008
Combination of CH_2 rocking of PMMA and S–N stretching of LiTFSI	746	Rajendran *et al.*, 2008; Ahmad *et al.*, 2008
Combination of C–S and S–N stretching mode of LiTFSI	791	Ahmad *et al.*, 2008
C–Cl stretching of PVC	847	Li *et al.*, 2006a
Trans C–H wagging mode of PVC	910	Achari *et al.*, 2007
Combination of C–O symmetric stretching mode in C–O–C linkage of PMMA and trans C–H wagging mode of PVC	963	Achari *et al.*, 2007
CH_2 wagging mode of PMMA	981	Rajendran *et al.*, 2002
Combination of C–H rocking mode of PVC and S–N–S asymmetric bonding mode of LiTFSI	1056	Achari *et al.*, 2007; Ahmad *et al.*, 2008
Combination of C–O asymmetric stretching mode in C–O–C linkage of PMMA and C–SO_2–N bonding mode of LiTFSI	1133	Jiang *et al.*, 2006; Ramesh and Lu, 2008
Combination of CH_2 twisting mode of	1186	Rajendran *et al.*,

PMMA and CF_3 symmetric stretching mode of LiTFSI		2004; Ahmad *et al*., 2008
CH_3 symmetric bending mode of PMMA	1232	Jiang *et al*., 2006
C–O–C symmetric stretching mode of PMMA	1284	Jiang *et al*., 2006
C–SO_2–N bonding mode of LiTFSI	1327	Ramesh and Lu, 2008
SO_2 asymmetric stretching mode of LiTFSI	1349	Ahmad *et al*., 2008
Combination of CH_3 asymmetric bending mode of PMMA and C–H stretching mode of CH_2 group of PVC	1444	Rajendran *et al*., 2004; Rajendran *et al*., 2008
C=C stretching mode of PVC	1661	Achari *et al*., 2007
C=O stretching mode of PMMA	1711	Li *et al*., 2006a
S–CH_3 bonding mode of LiTFSI	2845, 2997	Ramesh and Lu, 2008
CH_3 asymmetric stretching mode of PMMA and PVC	2926	Achari *et al*., 2007; Rajendran *et al*., 2008

Table 5.1: Assignments of vibrational modes of PMMA, PVC and LiTFSI for SPE 6 polymer matrix system.

As shown in Figure 4.9 (c), a weak peak which designated as C–H rocking mode of PVC is observed in PMMA–PVC spectrum. However, this peak is disappeared in comparison to SPE 6 spectrum. It is suggestive of overlapping with S–N–S asymmetric bonding mode of LiTFSI, indicating the interaction between polymer blends and LiTFSI. In order to prove the complexation between polymer blends and LiTFSI, the changes in intensity and changes in shape of the characteristic peak are probed further.

Besides, there is an obvious change in shape for the S–CH_3 bonding mode of LiTFSI in the region of 2979–2876 cm^{-1}. In the pure LiTFSI spectrum, it appears as two sharp peaks; however, it appears as a single peak with two small shoulders after incorporation with PMMA–PVC polymer blend matrix. It is due to

overlapping of C–H stretching mode of PMMA, C–H stretching mode of PVC and S–CH_3 bonding mode of LiTFSI. This reveals that there is a binding of PMMA, PVC and LiTFSI. Apart from that, a distinctive change of characteristic absorption in the region of 1186–1133 cm^{-1}, that is from a single peak with a small shoulder to double peaks is illustrated in Figure 5.11. In this region, 1133 cm^{-1} is assigned as combination of C–O asymmetric stretching mode in C–O–C linkage of PMMA and C–SO_2–N bonding mode of LiTFSI, whereas 1186 cm^{-1} is assigned as combination of CH_2 twisting mode of PMMA and CF_3 symmetric stretching mode of LiTFSI. The change in shape for latter peak may attributed to the occurrence of an interaction of CH_3 in PMMA and CF_3 in LiTFSI via coordination bond involving hydrogen bond of hydrogen atom of PMMA with fluorine atom of LiTFSI leading to a complexation between PMMA and LiTFSI. This discloses the interaction between PMMA and LiTFSI.

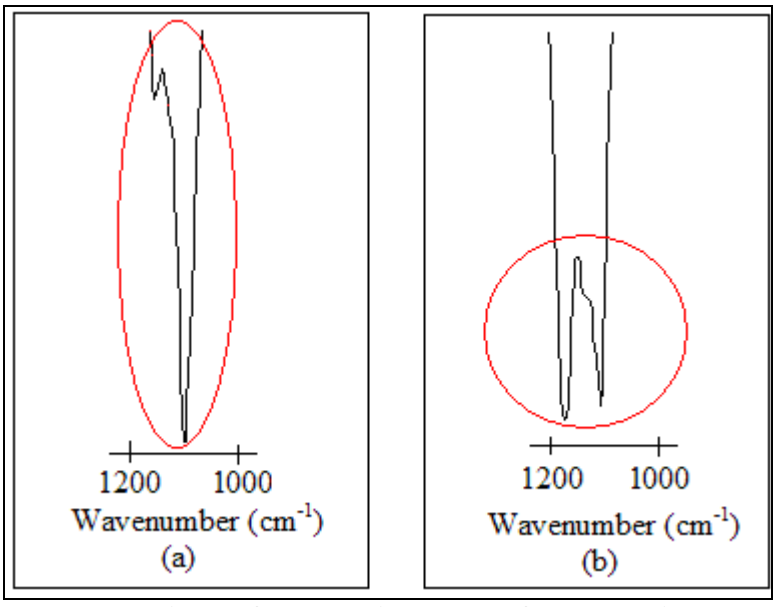

Figure 5.11: The comparison of change in shape of overlapping asymmetric O–CH_3 stretching mode of PMMA and symmetric stretching mode of CF_3 of LiTFSI in (a) PMMA–PVC and (b) SPE 6.

Upon addition of 30 wt% of LiTFSI, some characteristic peaks exhibit changes in shift. The characteristic peaks of cis C–H wagging mode of PVC, C–Cl stretching mode of PVC, CH_2 wagging mode of PMMA and C=C stretching mode of PVC are shifted from 698 cm^{-1}, 842 cm^{-1}, 983 cm^{-1} and 1684 cm^{-1} to 708 cm^{-1}, 847 cm^{-1}, 981 cm^{-1} and 1661, respectively. It divulges that there is an interaction between PMMA, PVC and LiTFSI. The CH_2 rocking mode of PMMA at 751 cm^{-1} is shifted to 746 cm^{-1} due to the overlapping with S–N stretching of LiTFSI. However, the combination of C–O symmetric stretching mode in C–O–C linkage of PMMA and trans C–H wagging mode of PVC remains unchanged at 963 cm^{-1}. Apart from that, the intensity of characteristic absorption peaks has also been changed. As exemplified in Figure 5.12, there is an observable change in intensity in C=O stretching mode of PMMA at 1711 cm^{-1}. Intensity of this sharp peak increases by 1.35 % in transmittance mode, which is from 1.90 % to 3.25 %; meanwhile it also undergoes shifting in wavenumber that is shifted from 1725 cm^{-1}. It might due to an interaction of C=O of ester in PMMA with LiTFSI via coordination bond.

Similarly, the intensity of combination of CH_3 asymmetric bending mode of PMMA and C–H stretching mode of CH_2 group of PVC at 1444 cm^{-1} is also enhanced by 0.54 % after addition of LiTFSI. It changes from 0.6 % to 1.14 %, whereas it changes from 1436 cm^{-1} to 1444 cm^{-1} in terms of shift in peak. Again, this reveals the interaction between polymer blends and LiTFSI. On the contrary, the intensity of CH_3 symmetric bending mode of PMMA is reduced by 0.80 %, which is from 1.20 % in PMMA–PVC spectrum and this peak is shifted from 1244

cm^{-1} to 1232 cm^{-1}. It signifies the coordination bonding between PVC and LiTFSI. Based on these results, it denotes the presence of complexation between PMMA, PVC and LiTFSI.

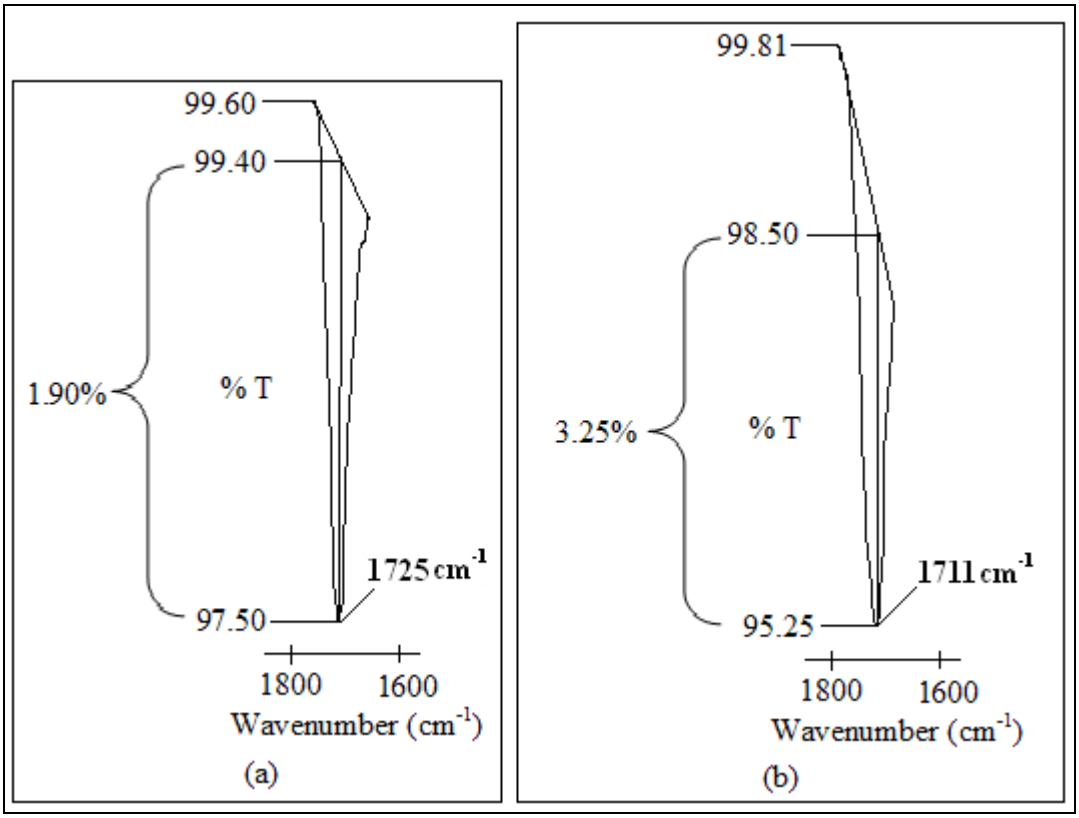

Figure 5.12: The comparison of change in intensity of C=O stretching mode of PMMA in (a) PMMA–PVC and (b) SPE 6.

All the vibrational modes of SPE 3, SPE 6 and SPE 8 have been shown in Figure 5.9 (a)–(c). However, cis C–H wagging mode of PVC is absent in SPE 8. In order to further investigate the ion aggregation, the bands in the wavenumber region of 1400–1100 cm^{-1} were explored (Ahmad *et al*., 2008). There are some obvious changes in shift at 1327 cm^{-1} and 1349 cm^{-1}. The first peak is assigned as C–SO_2–N bonding mode of LiTFSI, whereas SO_2 asymmetric stretching mode of LiTFSI is for latter peak. Both Figures 5.9 (a) and (b) show a peak at 1349 cm^{-1}

with a shoulder at 1327 cm^{-1}. However, upon further addition of LiTFSI, the peak is shifted to 1352 cm^{-1}, whereas the shoulder peak is shifted to 1330 cm^{-1}, as shown in Figure 5.9 (c). These upward shifts reveal the ion aggregation of LiTFSI, which in turn to impede the ionic transportation within the polymer matrix. In other words, reduction in ion pairing is occurred at lower frequency in SPE 3 and SPE 6.

5.8 XRD Studies

XRD analysis has been performed and their respective diffraction patterns of PMMA–PVC, pure LiTFSI, SPE 3, SPE 6 and SPE 8 are shown in Figure 5.13 (a)–(e). Sharp diffraction peaks appear at 2θ=13.6°, 15.9°, 18.6°, 18.9° and 21.4° reveals the crystalline behavior of pure LiTFSI. All these peaks pertaining to LiTFSI are absent, indicating the absence of uncomplexed excessive LiTFSI and no separate phase in the SPE 3 and SPE 6 polymer systems (Saikia and Kumar, 2004; Rajendran *et al*., 2008). Hence, it divulges that there is a complete dissolution of LiTFSI in the polymer complexes and form complexation between PMMA–PVC with LiTFSI as well as inhibits crystallization (Sivakumar *et al*., 2007). However, there is a sharp peak at 2θ=13.8° for SPE 8 and this indicates the presence of excessive LiTFSI salt precipitation. These bulky ion associations obstruct the Li^+ cations transportation and leading to decreases in ionic conductivity as demonstrated in Figure 5.14. As shown in Figure 5.12(a), two broad peaks are observed at 2θ= 15.8° and 22.3° for PMMA–PVC polymer blends,

revealing the amorphous characteristic of PMMA–PVC polymer blends. However, these peaks are shifted to 2θ value of 17.1° and 22°, 16.9° and 22.6° and 16° and 22.3° for SPE 3, SPE 6 and SPE 8, respectively upon addition of LiTFSI. This shift indicates the complexation between polymer blends and lithium salt (Sivakumar *et al*., 2006). Another evidence to prove the complexation of PMMA–PVC with LiTFSI is observed. Upon inclusion of LiTFSI, the decrease in the peak width of characteristic peaks is the apparent proof.

A discernible change in peak width and relative intensity of characteristic peaks for SPE 6 is illustrated in Figure 5.13. These apparent peaks become broader and intensity is reduced upon addition of 30 wt% of LiTFSI. Based on these observations, it reveals more amorphous region of SPE 6 than SPE 3 and SPE 8 and forms disorder arrangement in the polymer matrix. This significant disorder induces a more flexible polymer backbone and thus enhancing ionic transportation. Similarly, the peaks of SPE 3 are slightly sharper than SPE 8. This suggesting SPE 8 exhibits higher degree of amorphous as sharper of apparent peaks indicating higher degree of crystallinity (Saikia and Kumar, 2004). This result is consistent with the coherence length measurement. The coherence length of these polymer electrolytes was determined for the peak at $2\theta \approx 16°$.

From Figure 5.14, the coherence length of SPE 8 is higher than SPE 3. In general, coherent length defines as crystallite size. As the diffraction peak width is longer, the crystallite size is shorter, and hence contributing to lower crystallinity (Aravindan *et al*., 2009). Therefore, it is another evidence to prove the higher

amorphousity of SPE 8 than SPE 3. In addition, this result in good agreement with ionic conductivity at ambient temperature as illustrated in Figure 5.14. From this figure, ionic conductivity of SPE 8 is higher than SPE 3. Higher degree of amorphous of polymer matrix attributes to more disorder arrangement of polymeric chain and thus increases flexibility of polymer matrix. The flexible backbone increases the mobility and concentration of charge carrier. As a result, more voids are formed into the polymer system, promoting the ionic transportation and thus leading ultimately to highest ionic conductivity at room temperature. As discussed earlier, SPE 6 exhibits highest degree of amorphous. It is further proven in coherence length measurement by showing the shortest value. It might be due to the concentration and mobility had reached the optimum level, inferring the highest ionic conductivity of SPE 6 as illustrated in Figure 5.14.

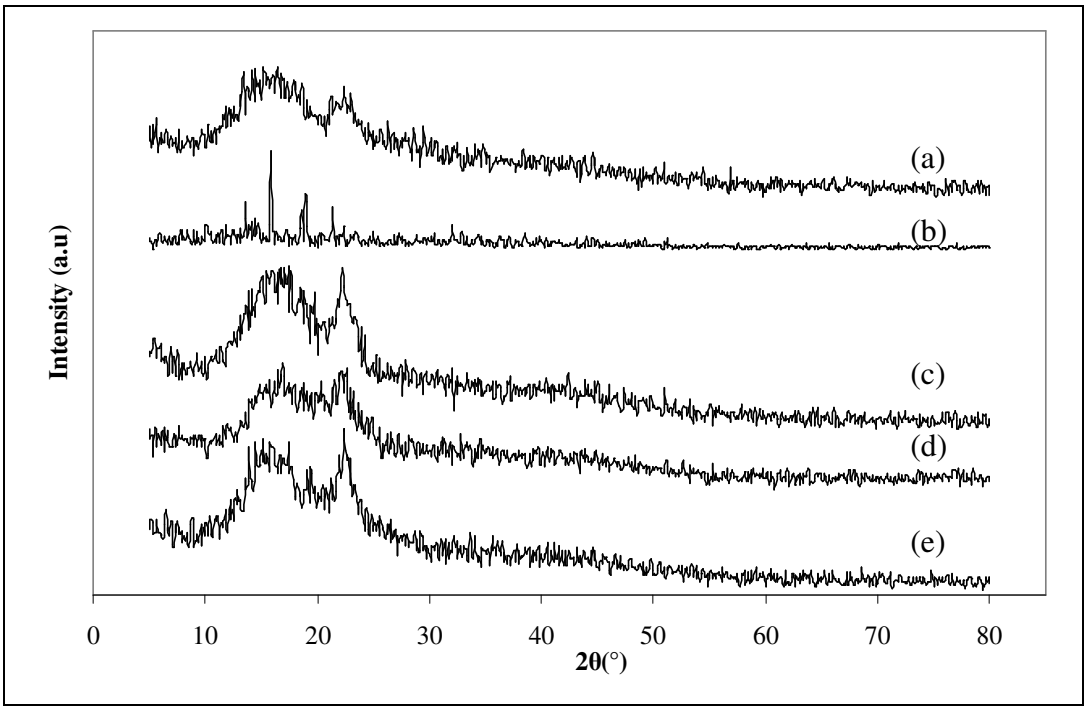

Figure 5.13: XRD patterns of (a) PMMA–PVC, (b) pure LiTFSI, (c) SPE 3, (d) SPE 6 and (e) SPE 8.

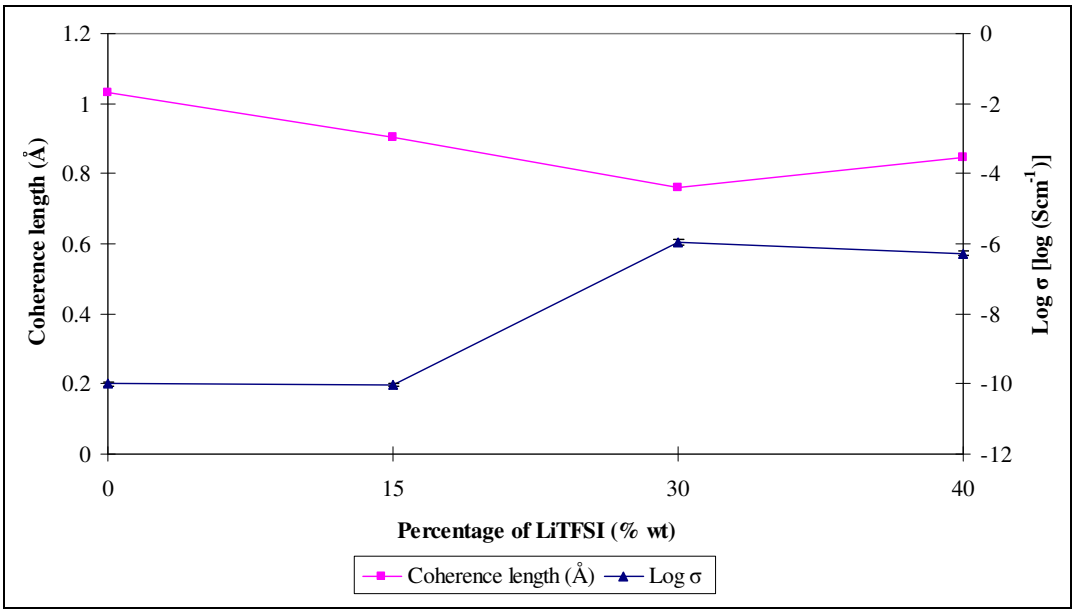

Figure 5.14: Variation of coherence length logarithm of ionic conductivity at ambient temperature with respect to different mole fraction of LiTFSI into PMMA–PVC polymer blends–based polymer electrolytes at $2\theta \approx 16°C$.

5.9 SEM Studies

Figures 5.15 (a)–(c) depict SEM images of SPE 3, SPE 6 and SPE 8 polymer electrolytes, respectively. SPE 3 membranes illustrate coarse texture, indicating that the higher crystallinity. In contrast, SPE 6 and SPE 8 polymer systems have higher amorphous region by illustrating a smooth surface onto these systems (Baskaran *et al*., 2007). Figure 5.15 (a) has shown some craters with average pore size around 1 μm. The effect of rapid volatilization of THF solvent during preparation is a contributor of this phenomenon (Rajendran *et al*., 2000a). The decrease in these craters might be due to the interaction between LiTFSI and polymer blends. An evident change in shape of pores is observed in this study.

Upon dispersion of LiTFSI, it has been changed from rectangular to spherical shape by comparing Figure 4.19 (c) with Figures 5.15 (a)–(c). This is mainly due to the disruption of LiTFSI onto polymer blends via coordination bonding between Li^+ cations with electron–rich group, such as oxygen from PMMA where the coordinating sites are C–O–C and C=O.

According to Figure 5.15 (a), the pores with size of 9–20 μm are observed. These pores are much larger than SPE 6 and SPE 8 and assigned to the coagulation of PMMA–PVC. Thus, the complexation of LiTFSI with PMMA–PVC polymer blends is lesser. Therefore, the Li^+ cations migration is unfavorable and induces to lower ionic conductivity. In addition, these aggregates are surrounded by fine streak with average size of 1 μm and suggesting the PMMA–PVC polymer blend is bounded by LiTFSI salt and thus LiTFSI salt starts to interact with PMMA–PVC. Eventually, it forms complexation with PMMA–PVC polymer blends. Similarly, some fine spherical cavities with average size of 1 μm are observed in Figure 5.15 (c), which mainly due to LiTFSI salt precipitation (Baskaran *et al*., 2007). At high LiTFSI loadings, the salts tend to exist in ion pairs rather than form complexation with PMMA–PVC polymer blends. These aggregated ions lead to more crystalline phase in this polymer electrolyte. Eventually, these crystalline regions hinder the ionic mobility in this polymer membrane. This observation is in good agreement with HATR–FTIR and XRD analyses.

On the contrary, Figure 5.15 (b) demonstrates a well distribution of pores in oval shape within similar dimension, with average size of 6 μm in the polymer

matrix. This infers the well dissolution of LiTFSI and high homogeneity of polymer electrolyte with lesser agglomerates (Fonseca *et al*., 2009). This even distribution attributed to excellent complexation between LiTFSI and PMMA–PVC, which in turn to promote the migration of ions and eventually leads to higher ionic conductivity. Generally, the main role of pores is to act as a passage for Li^+ cations during charge–discharge cycle (Uma *et al*., 2005). Higher porosity of SPE 6 is also exemplified in this figure and revealing the higher ions shipping.

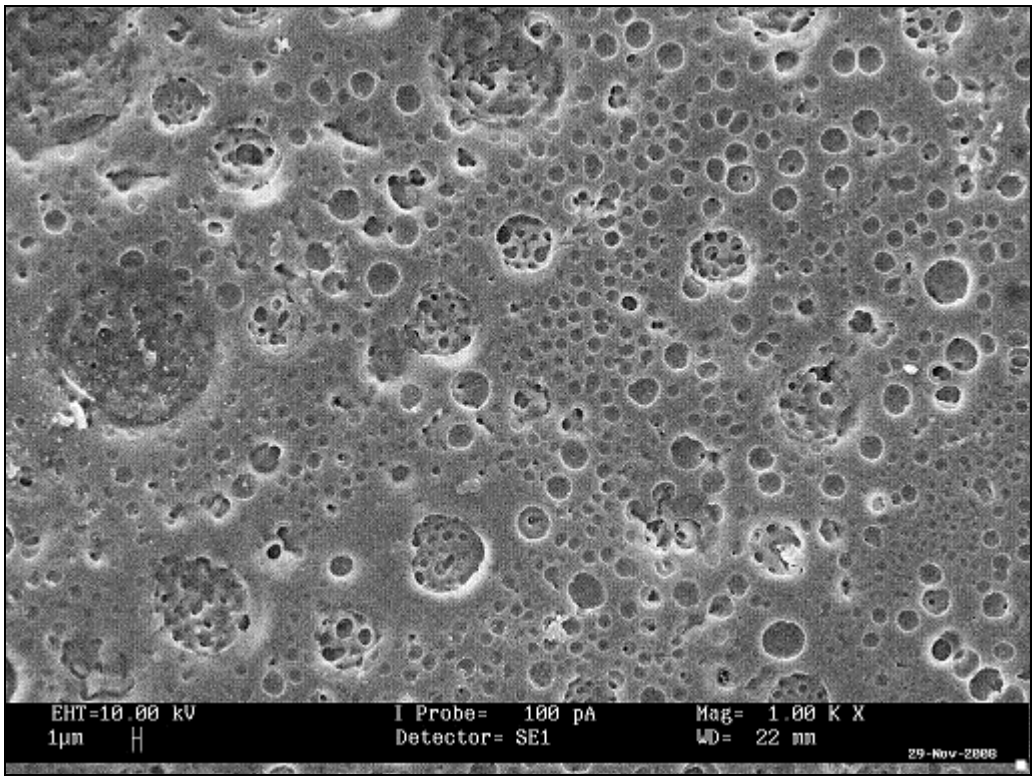

Figure 5.15 (a): SEM image of SPE 3.

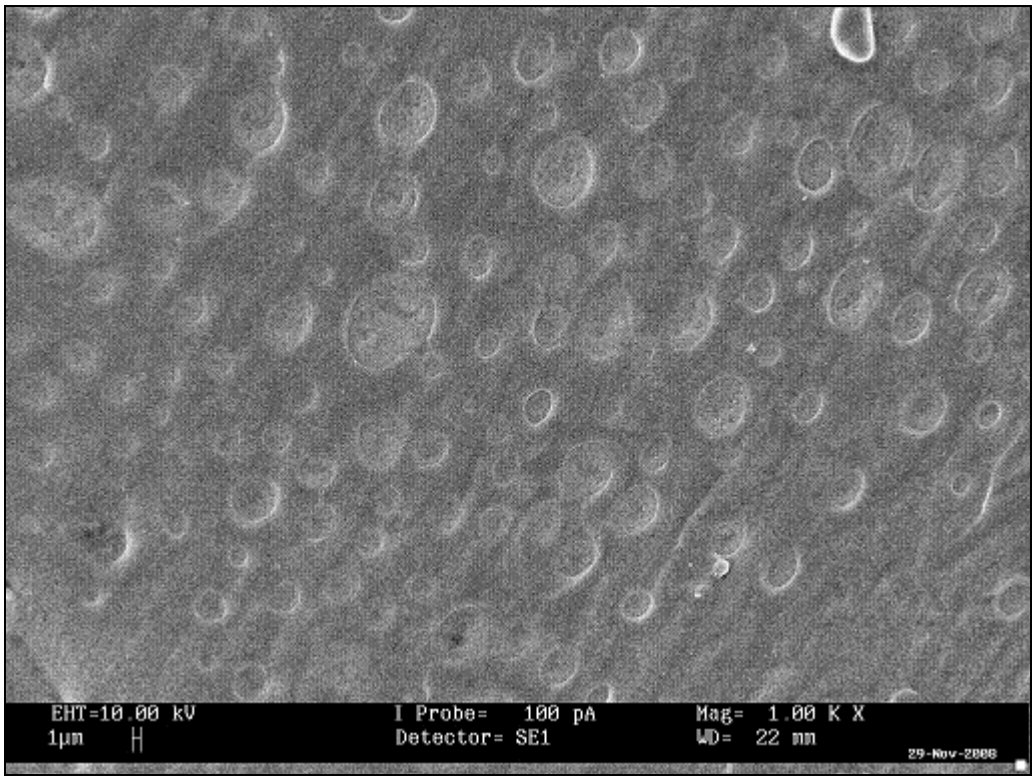

Figure 5.15 (b): SEM image of SPE 6.

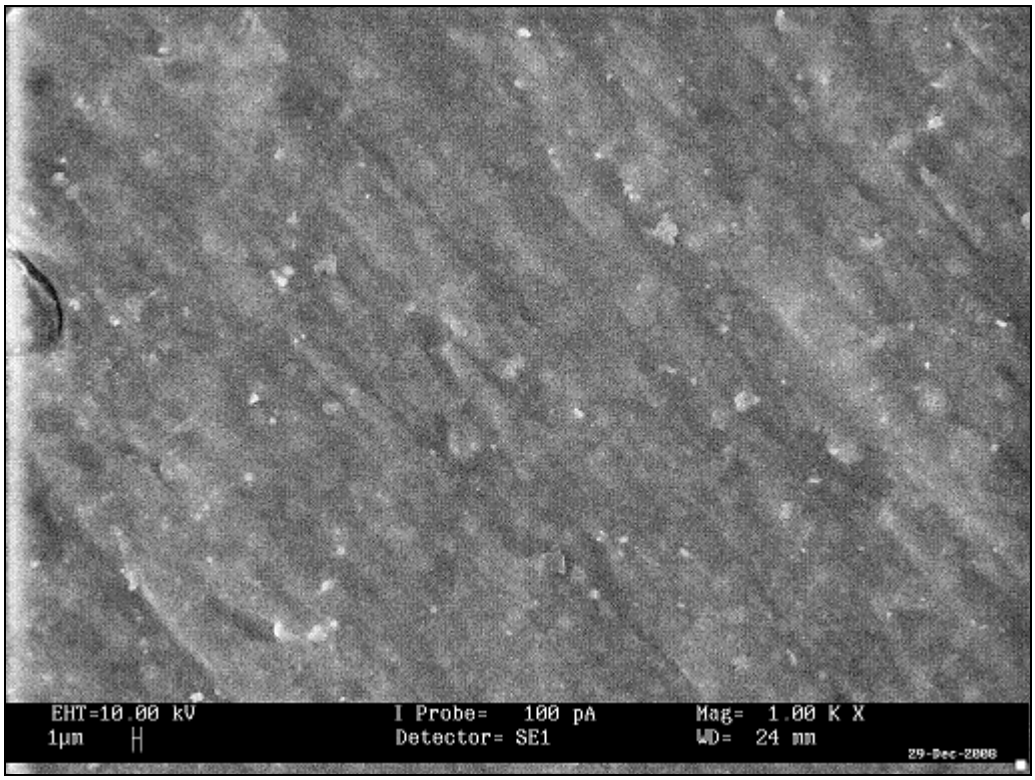

Figure 5.15 (c): SEM image of SPE 8.

5.10 DSC Studies

Only one T_g appears for all the samples indicating the homogenous samples as shown in Figure 5.16 (Ahmad *et al*., 2006b). T_g is shifted towards higher temperature upon incorporation of LiTFSI as shown in Table 5.2. This might be due to the formation of transient self cross–linking as a result of coordination between Li^+ cations with the electron–withdrawing groups, such as –O– and C=O functional groups (Li *et al*., 2006a). This binding energy increases the barrier of the polymer matrix and reduces the degree of mobility of polymer segments. Therefore, the polymer backbone becomes less flexible (Ramesh and Arof, 2001b).

As expected, T_g is decreased with increasing the LiTFSI concentration. T_g decreases from around 125 °C to 118 °C by adding more 15 wt % of LiTFSI and this result is clearly depicted in Table 5.2. Plasticizing effect of LiTFSI is the main contributor. As increases LiTFSI loadings, salts tend to exist in ion pairs or ion clusters between polymer matrix and thus lead to weaken the dipole–dipole interactions. As a result, the transient cross–linkage between polymer matrix is absent and resulting a decreases in solvation of Li^+ cations with oxygen of ester functional group from PMMA. Eventually, a softer polymer backbone is formed and resulting in enhancement of segmental motion and flexibility of polymer matrix (Baskaran *et al*., 2007). Thus, more voids are formed as the segmental mobility is increased. Therefore, Li^+ cations are easier to migrate in this polymer

matrix when the electric field is applied (Ramesh and Arof, 2001b). However, T_g is increased with addition of 40 wt% of LiTFSI. This is suggestive of increases in formation of inter–self crosslinking bonds between LiTFSI and polymer blends with excessive addition of LiTFSI, leading to higher barrier for rotation in the polymer chain and hence, flexibility of polymer chain becomes lesser by lowering degree of segmental movement in the polymer chain (Yang *et al*., 2008a).

Beyond T_g, heat flow of polymer matrix becomes stable up to above 160 °C, a distinct endothermic peak is observed and denotes as broad melting point of electrolyte, T_m. The broadening of this endothermic peak is assigned to overlapping of melting point of both PMMA and PVC. Thus, it is followed by a stable range of heat flow again over the temperature regime and then a visible sharp peak endothermic peak is obtained at above 300 °C. After that, a small endothermic peak is also observed as shown in Figure 5.16. These peaks are corresponding to decomposition temperature of polymer electrolyte, T_d. Obviously, SPE 6 exhibits highest melting temperature. This implies that the thermal properties of polymer electrolytes are enhanced with adulteration of 30 wt% of LiTFSI.

Moreover, the initial T_d is associated with dehydrochlorination of PVC which initiated by Cl free radical (Ahmad *et al*., 2007), whereas the second relatively small T_d is attributed to the degradation of unsaturated group from PMMA, such as C–O bonds and degradation of PVC (Ahmad *et al*., 2006b).

Overall, T_d is increased upon assimilation of LiTFSI due to the interaction of LiTFSI and PMMA–PVC by forming the cross–linkage between Li^+ cations and coordinating sites. Therefore, more energy is required to break the bonds and decompose the electrolytes. However, a slightly decreases in T_d at high LiTFSI loadings is illustrated. This is due to coordination of Li^+ cations with oxygen or chloride. Thus, the electron density is becoming lesser and eventually induces weaker unsaturated groups in the polymer matrices, such C–O bonds from PMMA (Wu *et al*., 2009). As a result, SPE 6 reveals the better thermal properties than SPE 3 and SPE 8 by exhibiting lowest T_g and highest T_m and T_d.

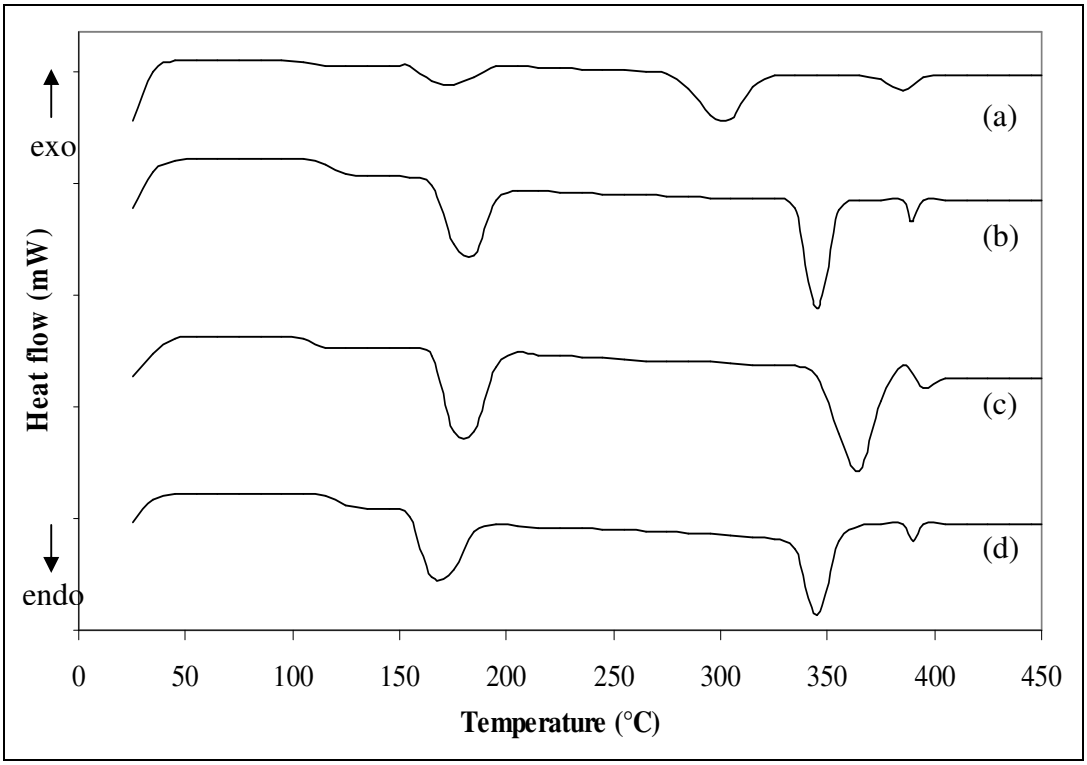

Figure 5.16: DSC thermograms of (a) PMMA–PVC, (b) SPE 3, (c) SPE 6 and (d) SPE 8.

Designations	DSC measurements		
	T_g (°C)	T_m (°C)	T_d (°C)
PMMA–PVC	105.40	175.54	305.38, 385.40
SPE 3	125.21	163.83	345.50, 389.23
SPE 6	118.16	184.50	366.20, 390.27
SPE 8	127.11	165.67	343.83,389.46

Table 5.2: DSC measurements of PMMA–PVC–LiTFSI based polymer electrolytes.

5.11 TGA Studies

According to Figure 5.17, three apparent segments are observed for all the samples. Initially, 2–4 % of weight loss is attained at 172 °C, 121 °C, 139 °C and 130 °C for PMMA–PVC, SPE 3, SPE 6 and SPE 8, respectively. This first small weight loss discloses the evaporation process of residue THF solvent and elimination of impurities which mainly due to fluorine compound from LiTFSI. Besides, dehydration of moisture is also a contributor for this phenomenon as the tendency of polymer to absorb water from surrounding is quite high.

Above this initial weight loss, it remains stable up to above 252 °C for PMMA–PVC, 269 °C for SPE 3, 288 °C for SPE 6 and 279 °C for SPE 8. At this temperature, it starts to degrade and forms second significant weight loss. The weight losses of 59 % and 35 % at 342 °C and 349 °C are obtained for PMMA–PVC and SPE 3, respectively. In contrast, 26 % mass loss is appeared at 348 °C for SPE 6. For SPE 8, weight loss at 339 °C corresponds to 30.3 % is achieved. The second significant weight loss is mainly due to the unzipping process which

contributed a reduction in molecular weight of polymer chain at high temperature. This unzipping reaction causes many degradation reactions such as random chain scission reaction, depolymerization, intra–molecular transfer reaction whereby dimer, trimers and oligomers are produced and inter–molecular transfer reaction as well as polymer fragments. As a result, the monomer and oligomers which chemi–adsorbed onto the polymer matrix is volatilized in this temperature regime (Ahmad *et al*., 2007). Besides, another attributor is the dehydrochlorination reaction from PVC, as proven in DSC thermogram.

A gradual weight loss is followed up thereafter. For PMMA–PVC and SPE 3, around 31 % and 24 % of mass losses, with residual mass of 28 % and 41 % are shown at 385 °C and 389 °C, respectively. Smaller weight losses are obtained for SPE 6 and SPE 8. SPE 6 has around 11 % weight loss at 390 °C, with residual mass of 60.35 %, whereas around 21 % of mass loss, with residual weight of 45 % at 389 °C is observed clearly for SPE 8. Above 400 °C, the baseline remains stable and hence indicates the end of the thermal decomposition of the polymer electrolytes (Fonseca *et al*., 2009). As a conclusion, SPE 6 is a promising candidate because its thermal stability is up to 288 °C and greatly preferred in lithium polymer batteries as its operating temperature is normally in the range of 40–70 °C (Stephan *et al*., 2002).

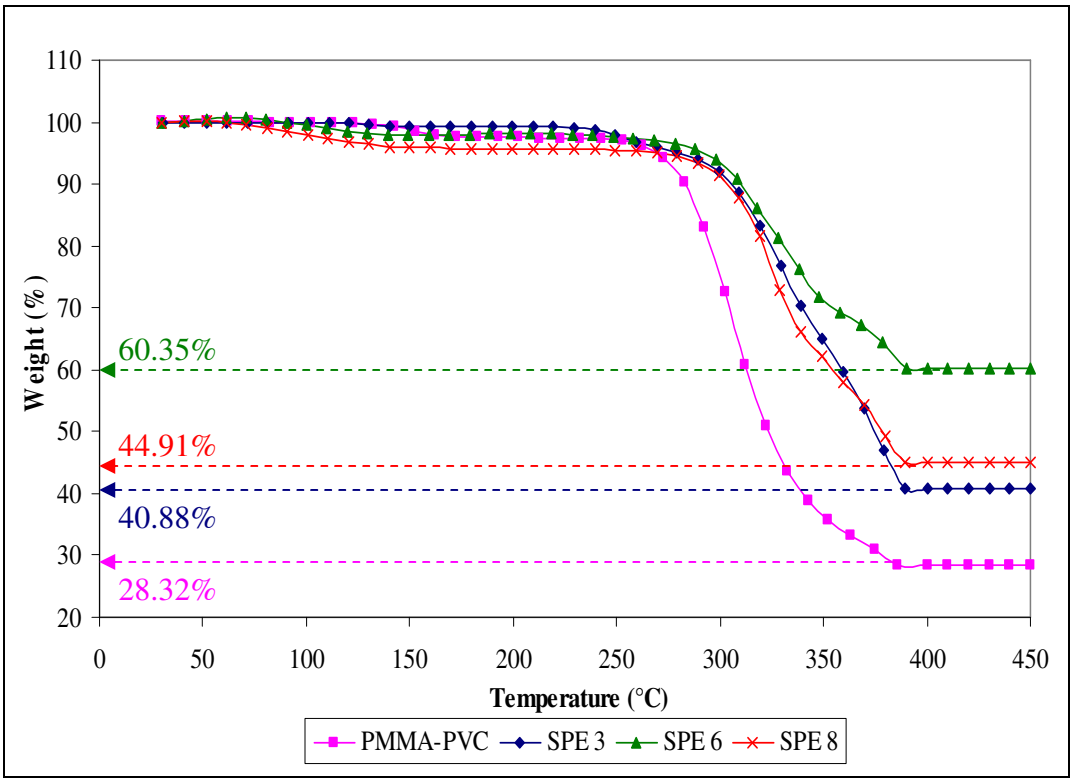

Figure 5.17: Thermogravimetric analysis of PMMA–PVC, SPE 3, SPE 6 and SPE 8.

5.12 Amplitude Sweep

Figure 5.18 shows the logarithm scale of amplitude sweep of this polymer electrolyte system. According to the figure, the yield point is absent within the strain regime and there is no behavioral transition in this polymer complex (Fonseca *et al.*, 2009). Elongation of samples is produced when stress is applied. Different evident trends are observed with addition of LiTFSI. At high strain, PMMA–PVC polymer blends shows a slow decrement. Nevertheless, the LiTFSI–based polymer electrolytes decrease rapidly at high strain. It divulges that the elastic properties decrease in favor of viscous properties at higher elongation of

sample when the stress is applied. This is attributed to the broken down of the structures of the sample once the stress is applied on the samples. All the samples show that G' values are greater than G'' within the elongation range, implying the predominant solid nature of all the samples. Upon inclusion of LiTFSI, at 0.001% strain, both G' and G'' values increases by more than an order of magnitude, indicating the solid–like medium of samples. Hydrogen bonding might be an attributor as it forms the complexation between LiTFSI and polymer blends. It can be seen that the hydrogen atom of polymer blends is readily reacted with oxygen atom of LiTFSI and contributes to the complexation. These hydrogen bonds initiate the entanglements within the polymer matrix and eventually lead to higher solid components in the samples.

The values of G' and G'' decrease with increasing the LiTFSI mass fraction. It is primarily correlated to the plasticizing effect of LiTFSI. This helps in softening the polymer backbone and thus further reduces the crystalline region of the sample. Amorphous is pre–dominant and therefore weakens the interaction between the molecular bonding of polymer matrix. Consequently, the elastic properties of polymer electrolytes are decreased at higher concentration of LiTFSI. As shown in Figure 5.18, the interval between G' and G'' of SPE 6 decreases sharply compared to SPE 3. This indicates that the viscous behavior is increased, meanwhile the solid properties is destroyed. However, for SPE 8, both values of G' and G'' are increased somewhat due to the precipitation of excessive salt in the polymer system. This agglomeration of salt increases the solid nature of polymer blends systems. Among SPE 3, SPE 6 and SPE 8, SPE 6 illustrates the widest LVE

range. It proposes that the structural stability of SPE 6 is the highest and it is difficult to be deformed.

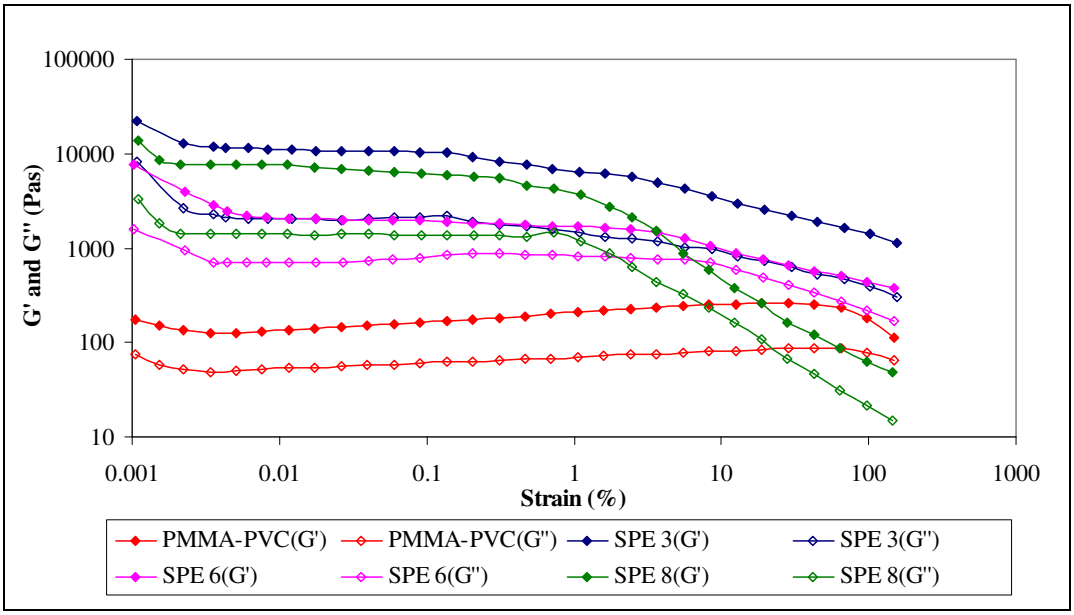

Figure 5.18: Oscillatory shear sweeps for PMMA–PVC, SPE 3, SPE 6 and SPE 8.

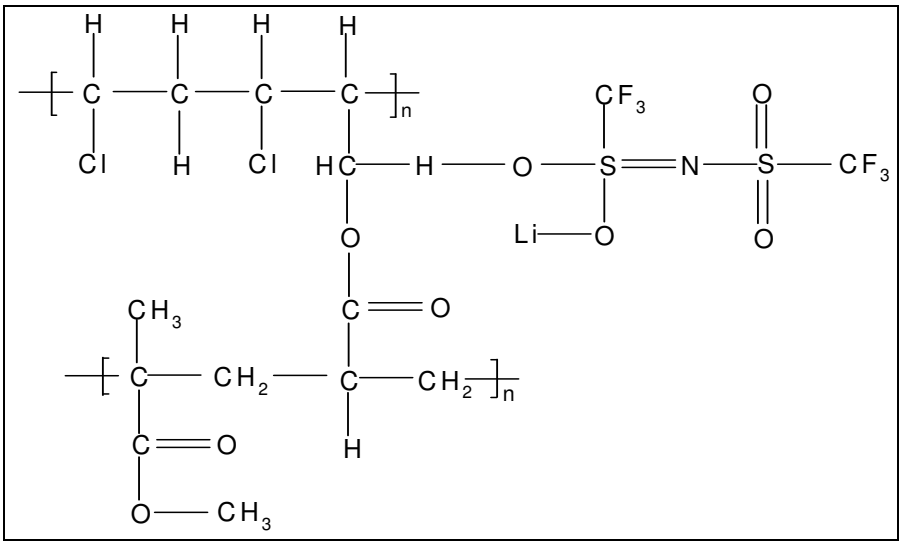

Figure 5.19: Hydrogen bonding between LiTFSI and polymer blends.

5.13 Oscillatory Stress Sweep

Figure 5.20 shows oscillatory shear sweeps of PMMA–PVC, SPE 3, SPE 6 and SPE 8 on logarithm scale. For all the samples, the values of G' are greater than G'', indicating that the solid properties domain in the polymer matrices. The crossover of G' and G'' is absent within the range of shear stress. This important feature indicates that there is no behavioral transition in the polymer electrolytes (Fonseca *et al*., 2009). G' increases with dispersion of LiTFSI due to the occurrence of complexation through the hydrogen bonding. The solid behavior of the samples is further confirmed in this oscillatory shear sweep. As explained in section 5.12, G' and G'' values decrease with incorporation of 30 wt% of LiTFSI, but, they are enhanced as 10 wt% of LiTFSI were further added in the polymer electrolyte system. This result is in good agreement with the amplitude sweep study. The first phenomenon is mainly due to the plasticizing effect, whereas the agglomeration of salt is an attributor for latter trend. An insignificant reduction in G' and G'' is observed at initial part. It is suggestive of initial interruption of the polymer structures when some forces are applied on the samples. On the other hand, the sharp decrease at the end region is attributed to the destruction of the chemical bonding between the polymeric systems.

For the initial shear stress, PMMA–PVC illustrates the lowest value. In other words, the deformation of PMMA–PVC compound can be arisen easily by applying a small amount of small forces and reveals the lowest mechanical

stability. As explained above, the solid behavior of LiTFSI–based polymer electrolytes is increased. Since the solid behavior is increased, therefore the mechanical strength is also improved with impregnation of LiTFSI. It can further been proven in this study by increasing the amount of shear stress. It is expected that more shear stress is required to deform the LiTFSI–based polymer electrolytes. SPE 3 shows higher shear stress in comparing with PMMA–PVC due to the formation of coordination bonding between LiTFSI and polymer blends. However, SPE 6 depicts lower shear stress and thereby asserting the ease distortion of this sample. It might be associated with plasticizing effect of LiTFSI. In general, the plasticizing effect assists to destroy the dipole–dipole interactions, which in turn to the enhancement of segmental motion and flexibility of polymer matrix. Therefore, less energy is needed to break the bonds in the polymer complex. In contrast, the quantity of shear stress applied on SPE 8 is higher due to the salt agglomeration and this effect compensates the plasticizing effect. The salts have a tendency to form aggregation when the salts loadings are in excess. More stress is required to break the bonds among the aggregates, and thus the mechanical stability is enhanced.

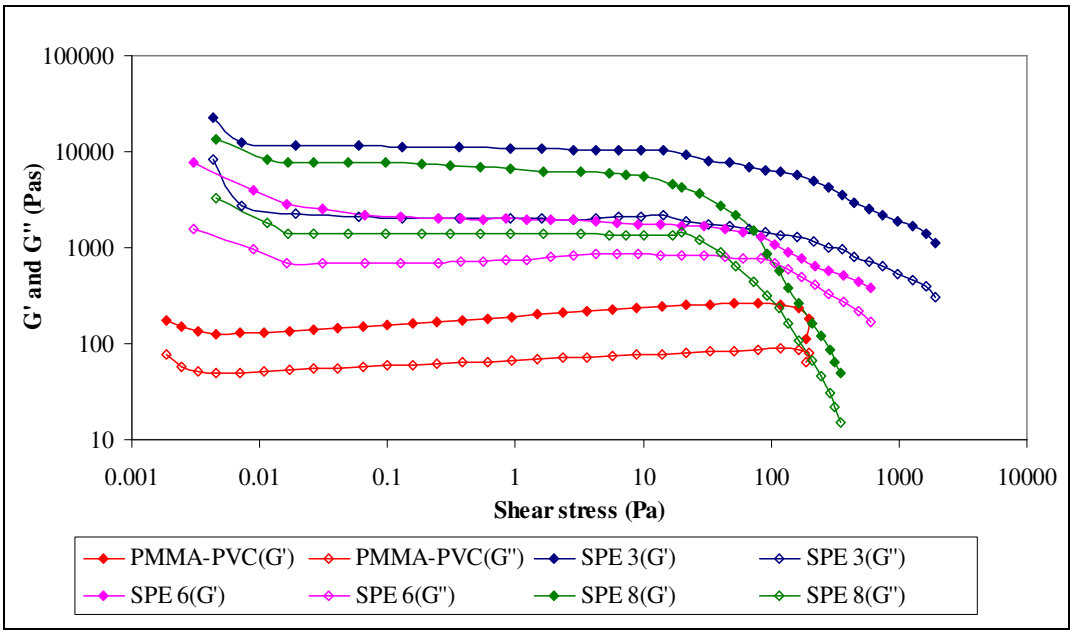

Figure 5.20: Amplitude sweeps of PMMA–PVC, SPE 3, SPE 6 and SPE 8.

5.14 Oscillatory Frequency Sweep

The frequency sweeps of PMMA–PVC, SPE 3, SPE 6 and SPE 8 are shown in Figure 5.21. The disappearance of *G*'' confirms once again the solid–like of all the samples. Again, same observations are obtained for second system in comparison to first polymer electrolyte system. Two visible regions are observed within the frequency range. *G*' exhibits frequency–dependent at low frequency, meanwhile an almost constant region is detected at high frequency. At high frequency, the value of elastic properties of polymer electrolytes is higher for short–term of deformation and it is attributed to short relaxation time. The polymer chain is unable to slip past one another and thus increases the ability of the unmoved polymer chain to store the imposed energy, leading to more elastic

properties of the sample (Ebagninin *et al*., 2009). However, the structural strength has been changed when the deformation takes place for a prolonged time. The relaxation time becomes longer and the slippage of the entanglements of the polymeric chain is available. The ability of polymer chain to store the elastic energy is reduced. As a result, the solid behavior becomes lesser at low frequency.

At the highest frequency (0.1 $rads^{-1}$), G' values of all the samples are almost the same. All the samples exhibit the same elastic energy at this frequency and indicate that the addition of LiTFSI does not bring up any effect on the structural stability at high frequency. However, the G' values are varied as the frequency is decreased. This describes the different long–term structural stability of each sample. PMMA–PVC compound manifests higher structural stability by showing the least decrease in G'. The G' values are relatively decreased upon inclusion of LiTFSI. In comparing of all LiTFSI–based polymer electrolytes, the decrease in G' values is in this order: SPE 8 > SPE 3 > SPE 6. The larger amount of G' of SPE 8 is due to the salt precipitation. The coordination bonds among the salt aggregates induce to a difficulty on the slippage process. Therefore, the elastic properties are gradually decreased. Plasticizing effect is the contributor for the lowering in G' value. As explained in previous study, the plasticizing effect of LiTFSI weakens the dipole–dipole interaction. After a long–term of deformation timeline, the LiTFSI is further weakens those physical and chemical interactions within the polymer matrix, such as the cross–linking between PMMA and PVC, promoting the mobility of polymer segments. Thus, the entanglements among the

polymer matrix are more easily to be slipped past one another and therefore reduce the elastic solid–like properties of the polymer electrolyte. In conclusion, the solid–like behavior becomes lesser at low frequency.

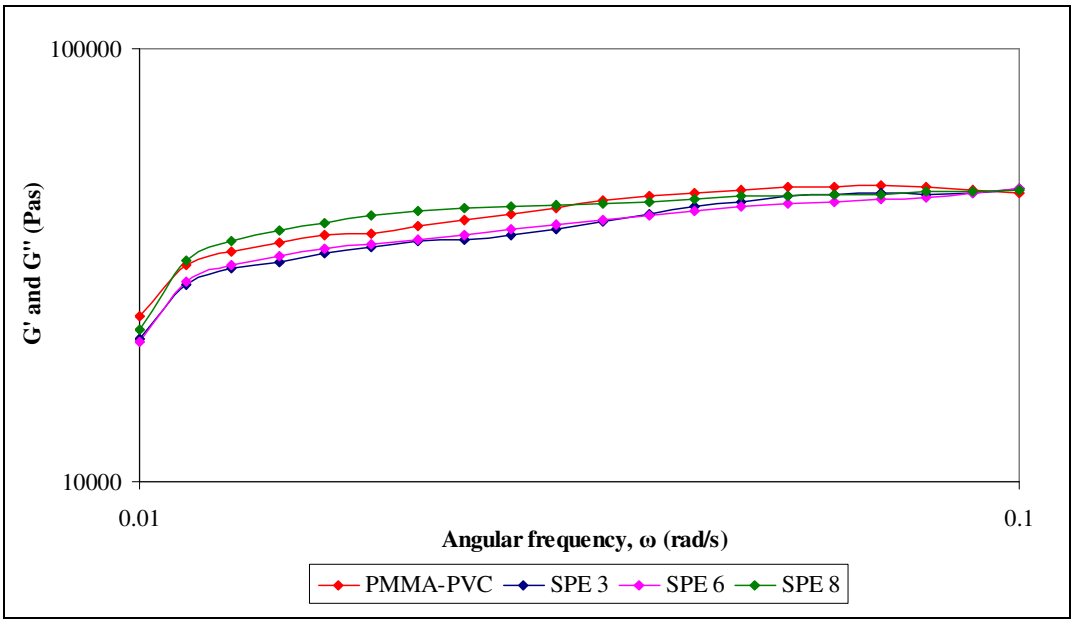

Figure 5.21: Frequency sweeps of PMMA–PVC, SPE 3, SPE 6 and SPE 8.

5.15 Viscosity Studies

The viscosity of samples as a function of shear rate is depicted in Figure 5.22. As shown in Figures 5.18 and 5.20, PMMA–PVC polymer blend has the least amount of storage modulus, divulging the lowest value of viscosity. It has been proven in Figure 5.22. By comparing all the LiTFSI–based polymer electrolytes, SPE 6 shows the lowest viscosity at $0.1s^{-1}$. It is primarily attributed to the plasticizing effect of LiTFSI. This effect softens the polymer backbone and hence increases the segmental motion of polymer blends, favoring the

disentanglements within the polymer matrix. As a result, it reduces the viscosity and hence increases the amorphous proportion which accompanied with higher ionic transportation within the polymer electrolytes. Theoretically, the viscosity of SPE 8 would be the lowest as it is embedded with higher LiTFSI compositions. However, it is higher than SPE 6 due to the salt precipitation in the polymer system. Weak physical bonds are formed among the salt aggregates and leads to a reduction of the movement of polymer chain. Hence, the viscosity is increased with formation of this network structure. SPE 3 has highest viscosity because of insufficient of the plasticizing effect.

All samples exhibit downward shift in viscosity as increases in shear rate, implying the shear thinning behavior (Ahmad *et al*., 2005). The occurrence of non–newtonian characteristic is due to the rupture of structure and bonding among the polymer matrix with increasing the shear rate. It commonly denotes as disruption of inherent self–crosslinking between PMMA and PVC. For LiTFSI–based polymer electrolytes, the hydrogen bonding between LiTFSI and polymer blends has also been destroyed. The interactions between those excessive salt aggregates are being interrupted for SPE 8 as well. The values of viscosity are almost the same at the highest shear rate of $100s^{-1}$. This suggests that the addition of LiTFSI does not possess any contribution to the viscosity when high shear is applied.

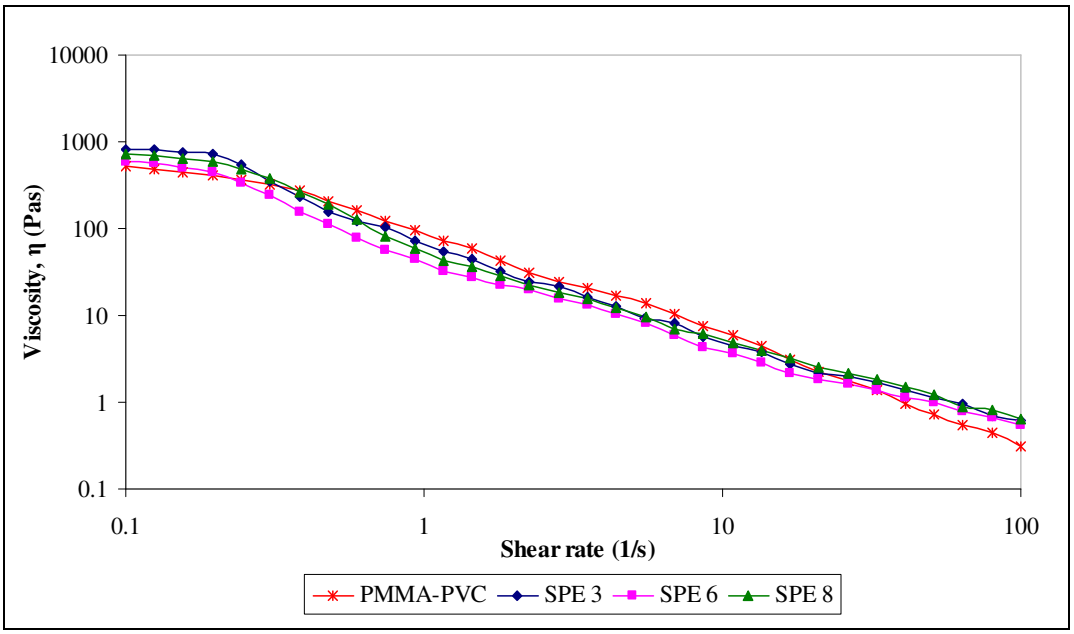

Figure 5.22: Typical viscosity curve of PMMA–PVC, SPE 3, SPE 6 and SPE 8.

5.16 Summary

PMMA–PVC polymer blends electrolytes are prepared by solution casting technique. Based on all the analyses, 70 wt % PMMA–PVC polymer blends and 30 wt % LiTFSI as dopant salt is found to be better choice as a polymer electrolyte in lithium batteries. In this present work, the highest ambient temperature–ionic conductivity of $(1.11\pm0.09)\times10^{-6}$ Scm^{-1} was achieved upon addition of 30 wt% LiTFSI salt. The temperature dependence study obeys Arrhenius rules and it obeys Jonscher's universal law for frequency dependence study. Both of these laws suggest the occurrence of hopping mechanism in the polymer matrix. In dielectric relaxation study, the polarization effect is the main contributor to increase these ε' and ε'' values at low frequency region. Only bulk effect can be observed in the

variation of $M^{'}$ and $M^{''}$ at high frequency regime. The ac–impedance and dielectric study reveals the occurrence of non–Debye characteristic of polymer electrolytes. Based on HATR–FTIR analysis, there is a complexation between PMMA, PVC and LiTFSI with the presence of new peaks, change in shift, change in intensity and change in shape.

XRD result had shown the shortest coherence length and reveals the high degree of amorphous in this polymer electrolyte. High porosity is also divulging the higher degree of ionic transportation in the polymer matrix as illustrated in SEM. From DSC and TGA measurements, an excellent thermal property of the polymer matrix is observed. From DSC analysis, T_g is lowered which produces a more flexible polymer backbone, whereas highest T_m and T_d are achieved. Thermal stability is well enhanced upon addition of 30 wt % of LiTFSI and this result is proven in TGA analysis.

Elastic properties are much higher than viscous properties within the range as shown in the amplitude sweep and oscillatory shear sweep studies. The disappearance of crossover of G' and G'' indicates the absence of behavior transition. The viscous behavior is absent in the frequency sweep and indicates the solid–like characteristic within the frequency regime. At low frequency, solid properties of polymer electrolytes reduced when the deformation takes place for a prolonged time, denoting the lower structural strength of polymer electrolytes. The viscosities of all the samples are decreased with increasing the shear rate.

CHAPTER 6

RESULTS AND DISCUSSION OF THIRD POLYMER BLEND ELECTROLYTES SYSTEM

6.1 AC–Impedance Studies

Figures 6.1 and 6.2 depict the complex impedance diagrams for IL 2, IL 5 and IL 6 at ambient temperature. In general, the electrolyte–electrode interface is regarded as capacitance and a vertical spike is observed while the capacitance is in ideal mode (Stephan *et al*., 2000b). However, a spike is inclined at an angle of 90° to the real axis as shown in Figures 6.1 and 6.2. This implies the non–idealism of capacitance properties and leads to ionic polarization at the blocking electrodes. As a consequence, a constant phase element (CPE) is present in the electrolyte–electrode interface and it is known as non–Debye nature (Venkateswarlu *et al*., 2000). The amounts of inclined slope and angle indicate the roughness of the electrolyte surface and distribution of relaxation time (Stephan *et al*., 2000b; Venkateswarlu *et al*., 2000). For this relaxation distribution, these charge carriers are accumulated at the electrode and electrolyte interface before the electric field changes the direction.

Obviously, two regions: a slanted spike at low frequency and a semicircle at high frequency are observed in Figure 1. This divulges the parallel combination

of bulk resistance (R_b) and bulk capacitance (C_p) effects of the polymeric electrolyte in the conduction process. Resistance is related to the ionic migration among the polymer matrix and represented by resistor at lower frequency, whereas the polarization of immobile polymer chain in the alternating field is represented by capacitor at higher frequency (Ramesh and Arof, 2001a). However, the semicircle portion is disappeared in Figure 2, revealing the non–capacitance behavior of the electrolytes due to random dipole orientation in the polymer side chain. Therefore, only the resistive component exists in this stage and hence generates a local effective conducting pathway for ionic transportation as the electrical potential alternates between the positive and negative electrodes in the alternate current electrical field. It can be concluded that the current charge carriers are ions which induces to the ionic conduction mechanism in the polymer electrolytes with the presence of blocking of polarization at electrode–electrolyte interface (Rajendran *et al*., 2004; Egashira *et al*., 2008).

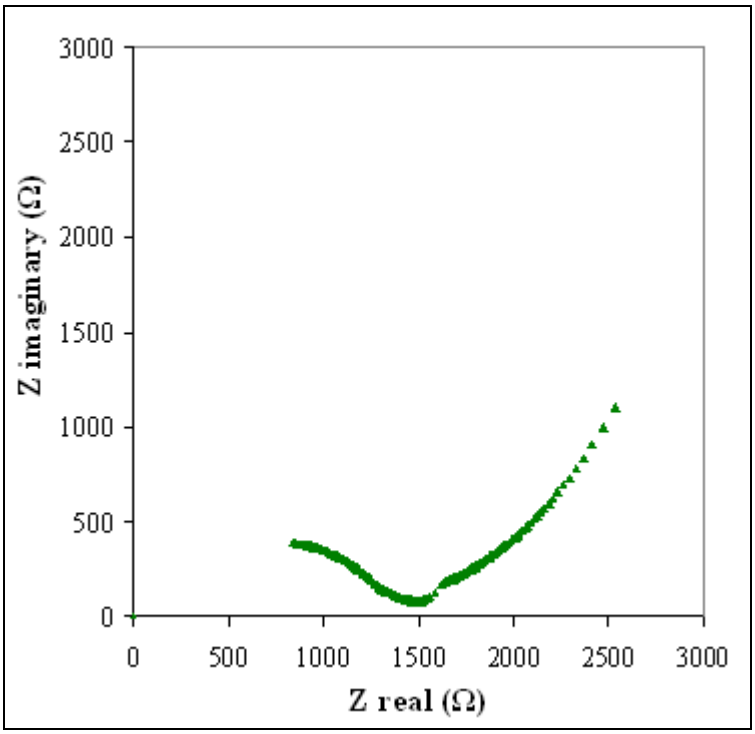

Figure 6.1: Complex impedance plot of IL 2 at ambient temperature.

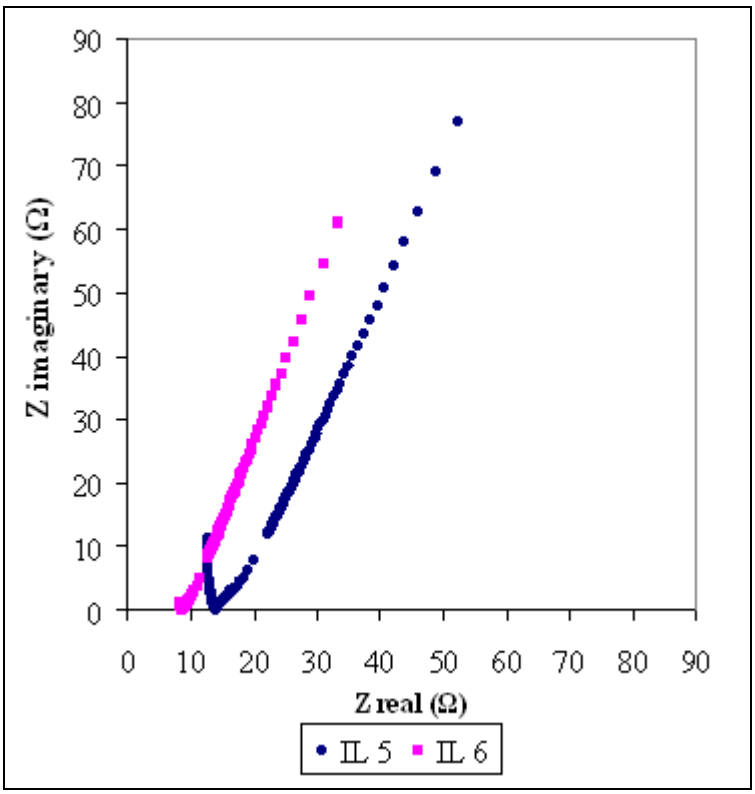

Figure 6.2: Complex impedance plot of IL 5 and IL 6 at ambient temperature.

6.2 Ambient Temperature–Ionic Conductivity Studies

Figure 6.3 shows the variation of logarithm of ionic conductivities of polymer electrolytes with respect to BmImTFSI amount at ambient temperature. The ionic conductivities of all the samples are tabulated in Table 6.1. The ionic conductivity rises further with increasing amount of BmImTFSI. It is mainly ascribed to production of large number of charge carriers as increases the BmImTFSI loadings since it provides $BmIm^+$ and $TFSI^-$ (Singh *et al*., 2008). Addition of BmImTFSI weakens the interaction within the polymer chains, reduces the solvation of Li cations by polymer matrix and hence promotes the decoupling of ions due to its high self–dissociating and ionic hopping properties (Jiang *et al*., 2006). This initiates the ion transportation from polymer segments and leads to an increase in ionic conductivity.

In general, ionic liquid has low viscosity behavior. Therefore, BmImTFSI helps to reduce the viscosity of the gel polymer electrolytes and thus decreases the crystallinity of the polymer matrix by destroying the ordered arrangement of the polymeric backbone (Singh *et al*., 2009). The reduction of crystalline regions leads to increase in amorphous degree. This provides more voids and free spaces for ion migration and thereby enhances ionic conductivity. Strong plasticizing effect also contributes to the increase in ionic conductivity (Sekhon *et al*., 2006). This effect softens the polymer backbone and enhances flexibility of polymer matrix, accelerating the polymer segmental motion and ionic transportation by providing more conducting pathways.

It can clearly be seen that the inclusion of 60 wt% of BmImTFSI (denotes as IL 6) increases the ionic conductivity by two orders of magnitude and achieves the highest ionic conductivity of $(1.64\pm0.01)\times10^{-4}$ Scm^{-1} at ambient temperature. This infers that the polymer segmental mobility and concentration of charge carriers have reached the optimum level. At this maximum concentration, the polymer electrolyte exhibits percolation theory and suggests that IL 6 has reached the maximum percolation threshold (Ramesh and Chai, 2007). The formation of percolation paths produces large number of ionic conducting pathways and increases the ionic conductivity to a greater extent. The highest ionic conductivity of IL 6 is also driven by the lower viscosity of sample with increasing the BmImTFSI loading. However, beyond the maximum value, the ionic conductivity is decreased. It is due to the agglomeration of mobile ions and hence leads to the formation of ion pairs (Singh *et al*., 2008). These ion pairs inhibit the mobility of ions and thus prevent the passage of ions in the polymer matrix. In addition, it blocks the ionically conducting pathway and it is greatly affects the ion conduction mechanism.

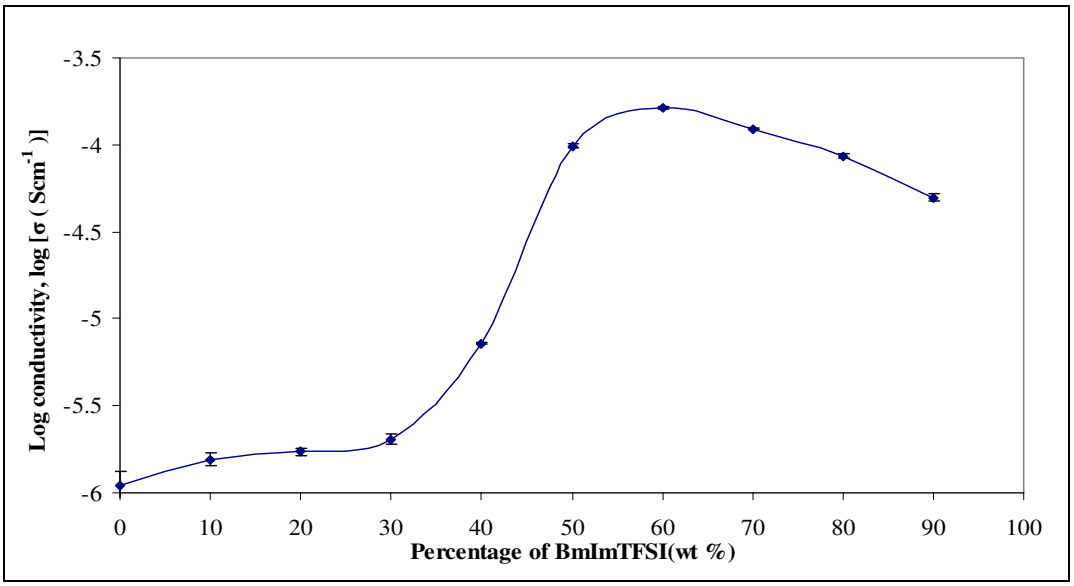

Figure 6.3: **Variation of log conductivity of ionic liquid–based gel polymer electrolytes as a function of weight percentage BmImTFSI at ambient temperature.**

Composition of (PMMA–PVC–LiTFSI):BmImTFSI (wt %)	Designations	Ionic conductivity at ambient temperature (Scm^{-1})
100:0	SPE 6	$(1.11\pm0.08)\times10^{-6}$
90:10	IL 1	$(1.56\pm0.04)\times10^{-6}$
80:20	IL 2	$(1.72\pm0.02)\times10^{-6}$
70:30	IL 3	$(2.04\pm0.03)\times10^{-6}$
60:40	IL 4	$(7.23\pm0.01)\times10^{-6}$
50:50	IL 5	$(9.82\pm0.01)\times10^{-5}$
40:60	IL 6	$(1.64\pm0.01)\times10^{-4}$
30:70	IL 7	$(1.23\pm0.01)\times10^{-4}$
20:80	IL 8	$(8.60\pm0.01)\times10^{-5}$
10:90	IL 9	$(4.99\pm0.02)\times10^{-5}$

Table 6.1: **Designations and ambient temperature–ionic conductivities of BmImTFSI based gel polymer electrolytes.**

6.3 Temperature dependence–ionic conductivity studies

Figure 6.4 shows Arrhenius plots of ionic conductivity for gel polymeric electrolytes. As expected, the ionic conductivity of the GPEs increases with

increasing the temperature. It is mainly attributed to an increase in ionic mobility, which in turn to an increase in ionic conductivity (Marcilla *et al*., 2006). The polymer expansion effect is another reason for that phenomenon. As temperature increases, it initiates the breakdown of the interaction within the polymer matrix and promotes the decoupling of ions. This facilitates the migration of ions and diminishes the ion clouds effect between the electrodes and electrolyte interface (Li *et al*., 2006a). The vibrational mode of polymer segment has sufficient energy to push against the hydrostatic pressure which is imposed by its surrounding atoms with increasing the temperature, which in turns to formation of voids. Consequently, these voids are aid to increase the segmental and ionic migrations in the polymer matrix, leading to an increase in ionic conductivity (Rajendran *et al*., 2004).

The increase in ionic conductivity is in this order: SPE 6< IL 2 < IL 5 < IL 6. As shown in Figure 6.4, IL 6 shows a modest increase in ionic conductivity from ambient temperature to 80 °C, reaching an optimum ionic conductivity of $(8.08\pm 0.01)\times10^{-4}$ Scm^{-1} at 80 °C. This reveals that the mobility and concentration of charge carriers has reached maximum level. Apparently, the ionic conductivity of IL 2 is increased slightly in comparing with ionic liquid–free polymer electrolytes. Again, it is due to the small quantity of BmImTFSI is added into the polymer electrolyte. Therefore, the evidence of plasticizing effect of ionic liquid is not so discernible. However, the ionic conductivity enhances extensively by one order of magnitude upon addition of 50 and 60 wt% BmImTFSI. It is mainly due to the significant increase in plasticizing effect, as explained in previous study.

The linear pattern is suggestive of Arrhenius relationship for all the samples as their regression values are close to unity. The Arrhenius behavior is shown in Equation 4.1. Hopping mechanism is favored in this theory, indicating the weaker interaction of polar group of the polymer backbone with Li^+ upon incorporation of BmImTFSI. Thus, it promotes the decoupling process of charge carriers from segmental motion of polymer matrix and leads to formation of vacant sites. Therefore, the neighboring ions from adjacent sites tend to occupy these vacant sites and coordinate with the polymer chain again. There is no abrupt change in the value of conductivity with respect to temperature, inferring no phase transitions within the temperature regime for all the complexes.

In order to probe the ion dynamic of polymer electrolytes further, activation energy, E_a is determined by fitting it in Arrhenius equation as shown in Equation 4.1. E_a is defined as the energy required to overcome the reorganization and reformation of the polymer chain with Li^+. E_a decreases significantly upon addition BmImTFSI and further decreases with increasing BmImTFSI mass fraction. E_a values of IL 2, IL 5 and IL 6 are 0.4386 eV, 0.2632 eV and 0.2572 eV, respectively. As discussed earlier, the addition of BmImTFSI disrupts the interaction between the polymer backbone and Li^+. Thus, it requires lesser energy to break and reform the coordination bond among the polymer matrix. As a result, the ion diffusion is favorable in the hopping process.

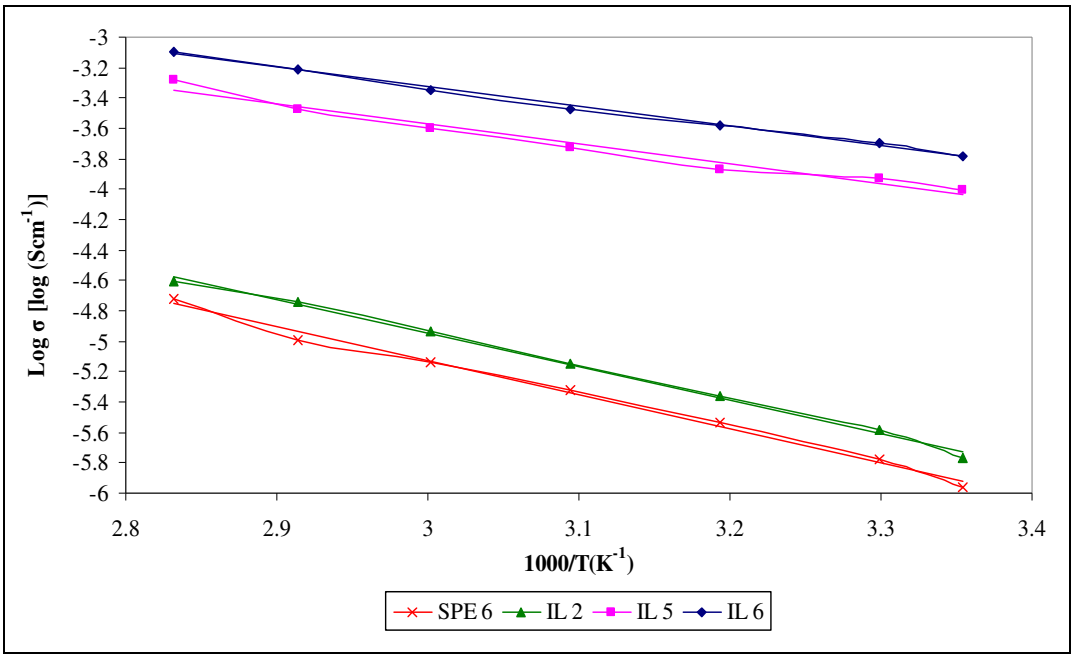

Figure 6.4: Arrhenius plot of ionic conductivity of SPE 6, IL 2, IL 5 and IL 6.

6.4 Frequency Dependence–Ionic Conductivity Studies

Figure 6.5 depicts room temperature frequency dependence–ionic conductivity of IL 6 in the temperature range of 303 K–353 K. It can clearly be observed that the spectrum is fitted to Jonscher's universal power law, as depicted in Equation 5.1. Based on this equation, it discloses that the ac conductivity is found to vary with angular frequency in all the dielectric materials (Ramesh and Arof, 2001a; Almond *et al*., 1982). Three obvious dispersion regions are observed in Figure 6.5. At low frequency, the conductivity increases sharply with frequency. It is mainly attributed to the slow periodic reversal of the applied electric field onto the sample and leads to an accumulation of charge carriers at the electrode–electrolyte interface. Polarization is further occurred at the interface and then it

leads to a decrease in concentration of mobile ions, revealing the non–Debye behavior of the polymer system (Ramesh and Arof, 2001a; Khiar *et al*., 2006).

On the other hand, the conductivity is higher at high frequency. The mobility of ions increases with frequency and asserts that the ionic hopping mechanism is favorable. As the frequency increases, the conductivity is increased, up to a maximum level. At this stage, an almost frequency–independent plateau region is observed and this implies that the conductivity is equal to the bulk ionic conductivity. Maximum mobility and concentration of charge carriers have been reached and thus contributes to the highest ionic conductivity. The conductivity is decreased abruptly thereafter due to the formation electrical double layer (EDL) on the electrode surface. As increases the frequency, the mobile ions are present in excessive mode, leading to agglomeration of ions. These aggregates form constant phase element (CPE) onto the electrode and this layer is known as EDL which acts as a blocking layer. As explained in previous study, the ionic conductivity increases with temperature and this result is in good agreement in this study as well. The conductivity increases with increasing temperature in the same frequency range. This is due to higher drift of ions upon heating up the samples. This high mobility of ions favors the ion transportation in the polymer matrix and enhances the ionic conductivity at higher temperature. However, above 3 MHz of frequency, the opposite observation is obtained. The ionic conductivity at lower temperature is higher than at higher temperature. It might be due to the ionic mobility is in extremely high mode. Hence, it helps in formation of EDL in the polymer electrolyte, leading to lesser ionic conductivity.

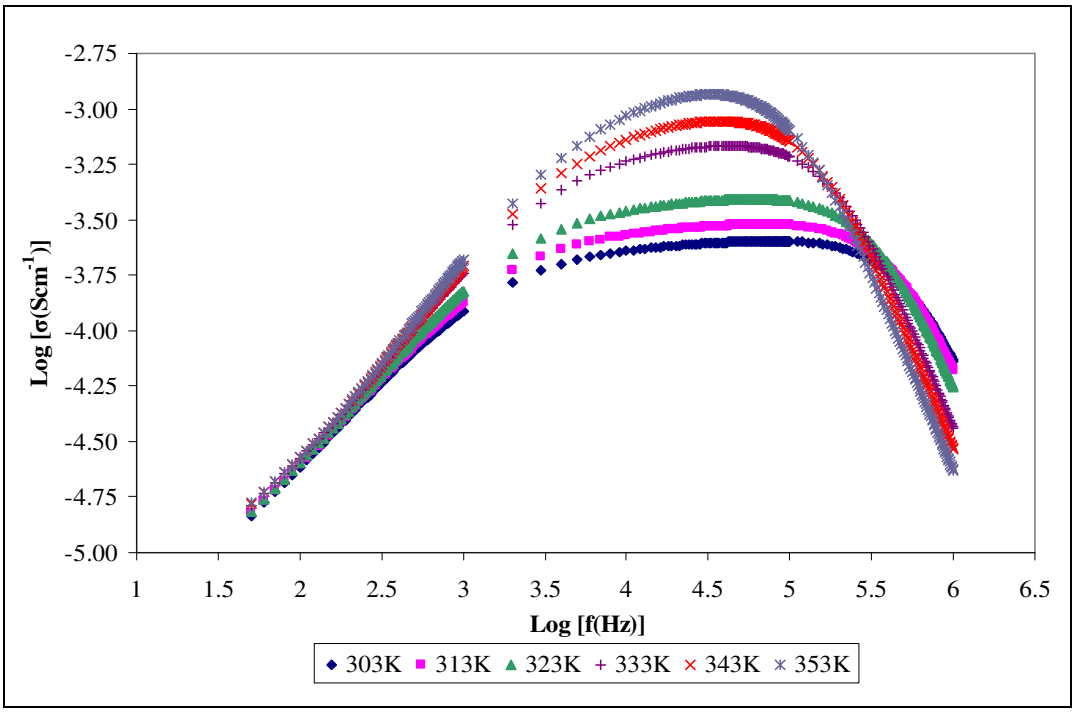

Figure 6.5: Frequency dependent conductivity for IL 6 in the temperature range of 303–353 K.

6.5 Dielectric Relaxation Studies

Frequency response of dielectric permittivity and dielectric loss of IL 6 in the temperature range are shown in Figures 6.6 and 6.7. No relaxation peaks are attained in these figures. In general, both dielectric constant and dielectric loss do not correspond to the bulk dielectric processes; however, they are mostly due to the accumulation of mobile charge at the electrode–electrolyte interface (Baskaran *et al*., 2006a). As shown in these figures, dielectric constant and dielectric loss increase tremendously at low frequency due to electrode polarization and space charge effect at the electrode–electrolyte interface. It has further confirmed the non–Debye response where more than one relaxation distribution is expressed onto

the polymer matrix when the electrical fields change the direction. For this behavior, the space charge region with respect to the frequency is explained in terms of ion diffusion (Ramesh and Arof, 2001a; Rajendran *et al*., 2004). At low frequency, the free charge carriers build up at the electrode–electrolyte interface and then associate with electrode polarization when the electrical field is applied across the sample. Retention of water in the polymer matrix might be another attributor since polymer tends to absorb moisture from surroundings (Goodwin *et al*., 1999). Moreover, time is required to accumulate the charges at the interface before the electrical field changes the direction, contributing to high values of ε''. On the contrary, both of dielectric constant and dielectric loss are decreased at high frequency. It is mainly due to the fast occurrence of periodic reversal of electric field and consequently, it causes the absence of excess ion diffusion in the electric field direction. This decreases the charge density which accumulates at the interface and polarization effect further (Ramesh and Arof, 2001a; Rajendran *et al*., 2004; Egashira *et al*., 2008).

The dielectric permittivity and dielectric loss also increases with temperature due to the increase in concentration of free ions. As explained in section 6.3, the increase in temperature shields cation–anion interaction in ionic liquid, which in turn to the ion dissociation from ionic liquid compounds. It also increases the degree of re–dissociation process of ion pairs, asserting the increase in concentration of free charge carriers at the interface. The high dielectric constant inhibits the ion aggregates and ion clusters in the polymer matrix further (Eliasson *et al*., 2000). It can be concluded that the higher value of IL 6 at 353 K is

due to the higher charge carrier density at the electrode–electrolyte interface, leading to the increase in the equivalent capacitance (Baskaran *et al*., 2006a).

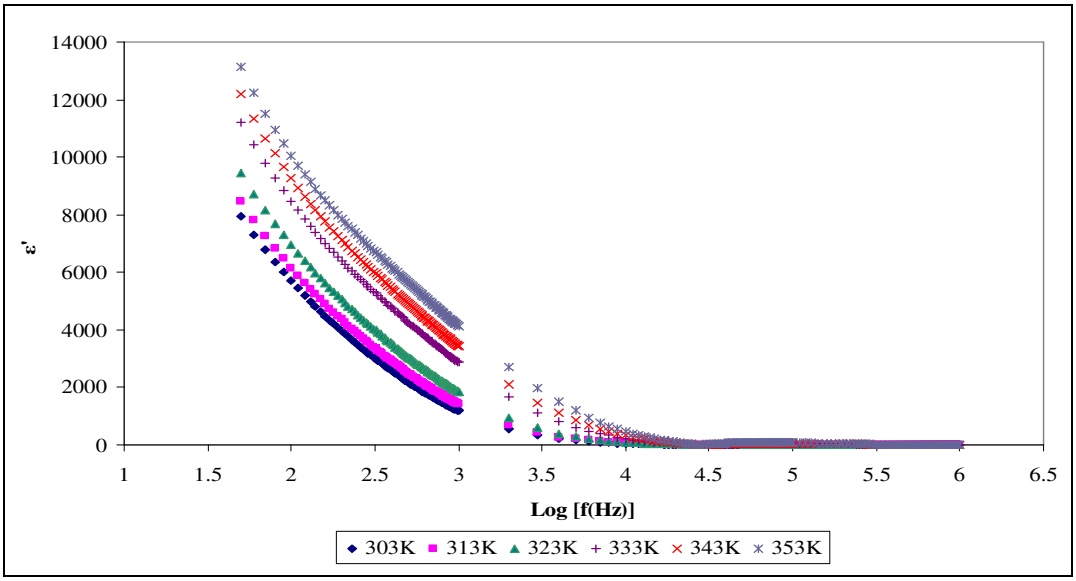

Figure 6.6: Typical plot of the variation of real part of dielectric constant (ε') with frequency for IL 6 in the temperature range of 303–353 K.

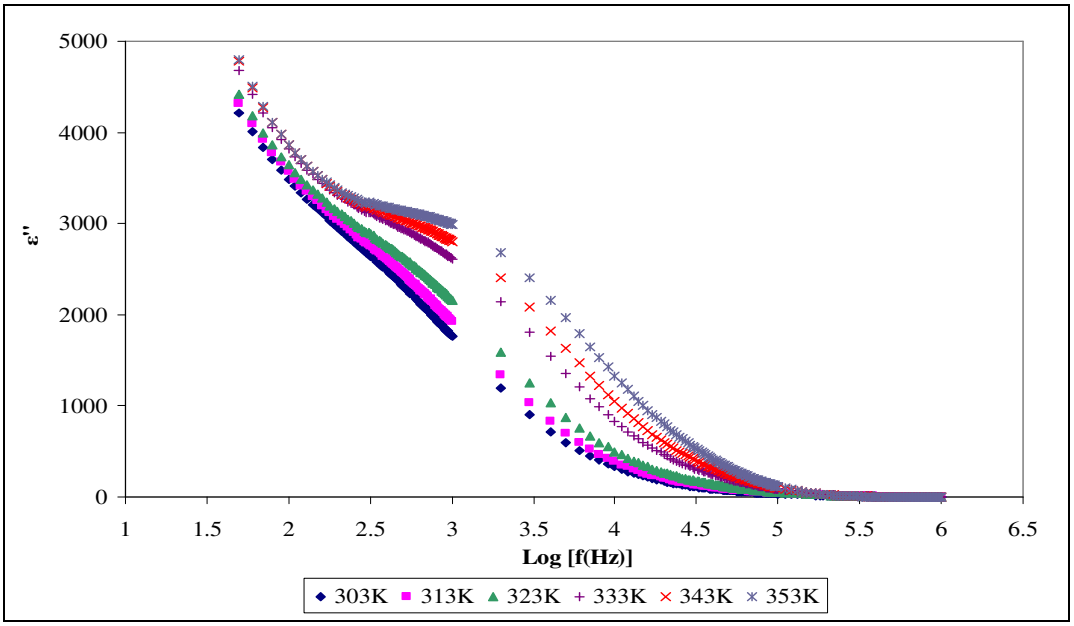

Figure 6.7: Typical plot of the variation of imaginary part of dielectric constant (ε'') with frequency for IL 6 in the temperature range of 303–353 K.

6.6 Dielectric Moduli Studies

Dielectric modulus study is another alternative approach to investigate the bulk dielectric response by suppressing the electrode polarization effect (Shastry and Rao, 1991). Figures 6.8 and 6.9 depict the variation of real ($M^{'}$) and imaginary ($M^{''}$) parts of dielectric moduli as a function of frequency. Although the relaxation peaks are absent in these figures, however, there is an abrupt increase is observed at higher frequency end. At low frequency regime, both of $M^{'}$ and $M^{''}$ tend towards zero. This long tail indicates the suppression of electrical double layer effect at the electrode–electrolyte interface (Ramesh and Arof, 2001a; Shastry and Rao, 1991). It is mainly due to high capacitance values with the electrode in the polymer electrolyte system (Ramesh and Chai, 2007; Suthanthiraraj *et al*., 2009). In other words, dielectric moduli formalism facilitates the processes of identification and separation of polarization effect from the bulk relaxation phenomenon in the polymer electrolyte. An apparent observation is observed in Figure 6.8. For real part of dielectric modulus, all the curves demonstrate superposition features in the temperature regime at high frequency and thus disclose that the modulus spectral formalisms exhibit temperature–independent properties, revealing the excellent electrochemical stability of IL 6 (Suthanthiraraj *et al*., 2009). However, the spectral are completely superimposable in the high frequency region for imaginary part of dielectric modulus.

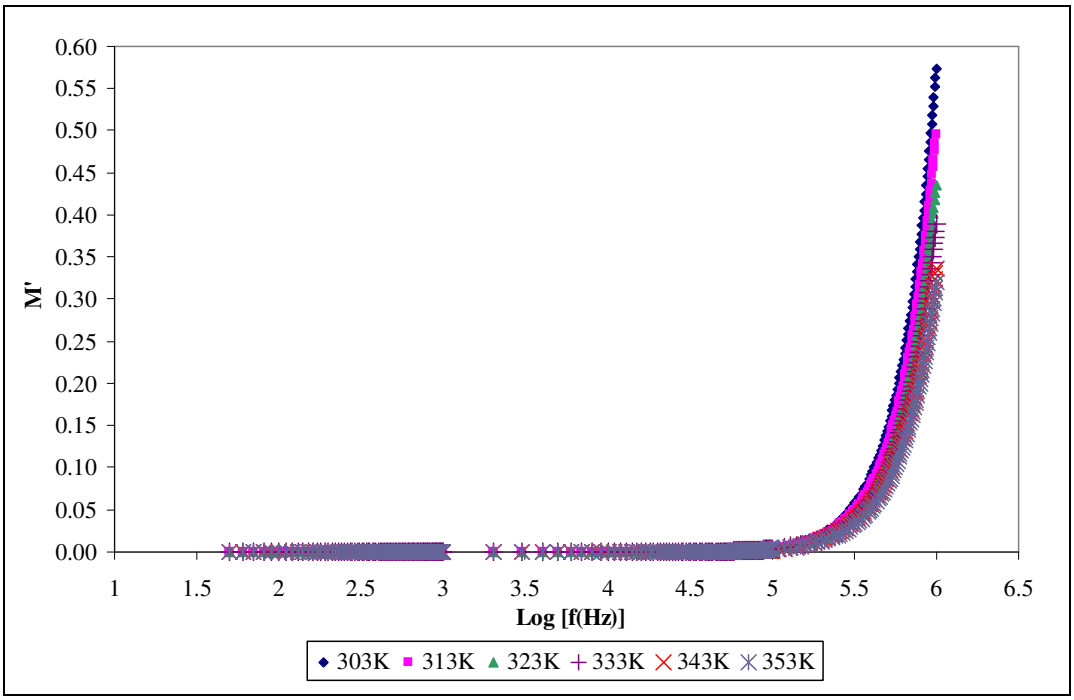

Figure 6.8: **Variation of real modulus ($M^{'}$) as a function of frequency for IL 6 in the temperature range of 303–353 K.**

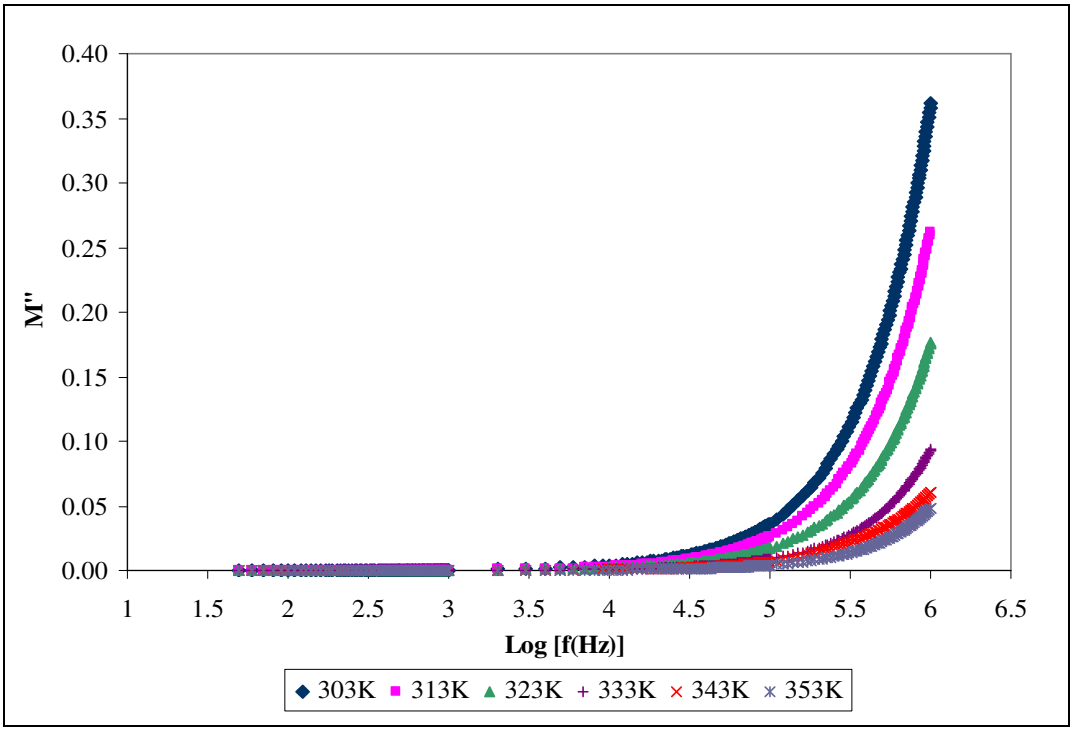

Figure 6.9: **Variation of imaginary modulus ($M^{''}$) as a function of frequency for IL 6 in the temperature range of 303–353 K.**

6.7 HATR–FTIR studies

Typical plots of HATR–FTIR spectra for pure BmImTFSI, IL 2, IL 5 and IL 6 and their combinations are shown in Figures 6.10 (a)–(d) and 6.11, respectively. Table 6.2 shows the assignments of the vibrational modes of polymer, doping salt and ionic liquid for IL 6. The descriptions of vibrational modes of IL 6 would be discussed in details as it achieves the highest ionic conductivity among all the samples.

Inclusion of 60 wt% BmImTFSI yields eight new peaks, by comparing SPE 6 with IL 6. This indicates the interaction between BmImTFSI and polymer matrix. These peaks are assigned as CF_3 symmetric bending mode at 761 cm^{-1}, N–H stretching mode at 1226 cm^{-1} and 3583 cm^{-1}, CH_3 symmetric stretching mode at 1461 cm^{-1}, C–C and C–N bending mode at 1574, CH_2 stretching mode at 2963 cm^{-1} and C–H vibrational mode for cyclic $BmIm^+$ at 3121 cm^{-1} and 3157 cm^{-1}, as highlighted in Figure 6.11 (e). The presence of C–H vibrational modes for cyclic $BmIm^+$ indicates the interaction between O^- from PMMA and BmImTFSI and hence accelerates the ion dissociation. A weak peak which assigned as C–Cl stretching mode of PVC is shifted from 847 cm^{-1} to 845 cm^{-1} and the intensity of peak increases from 0.5 % to 27.14 % in transmittance mode, indicating the interaction of PVC and BmImTFSI. C=C stretching mode of PVC shifts from 1661 cm^{-1} to 1631 cm^{-1} and implies the complexation between PVC and BmImTFSI .

Similar observation is observed at 789 cm^{-1} which assigned as combination of C–S and S–N stretching mode of LiTFSI and BmImTFSI. It shifts from 791 cm^{-1} and the intensity of peak enhances by 30.93 % in transmittance mode, which is from 0.5 % to 31.43 %. Upon addition of 60 wt% BmImTFSI, the characteristic peak which assigned as S–N–S asymmetric stretching mode of LiTFSI and BmImTFSI exhibits downward shift, from 1056 cm^{-1} to 1055 cm^{-1}. In term of peak intensity, it increases by 41.89 % in transmittance mode, from 5.25 % to 47.14 %. The characteristic peaks at 1330 cm^{-1} and 1346 cm^{-1} are assigned as C–SO_2–N bonding mode of LiTFSI and BmImTFSI and SO_2 asymmetric stretching mode of LiTFSI and BmImTFSI, respectively. The first characteristic peak shifts upward, from 1327 cm^{-1} to 1330 cm^{-1}. In contrast, the downward shift is shown for latter peak, from 1349 cm^{-1} to 1346 cm^{-1}. In addition to the change in shift, it also depicts a noticeable change in shape. It changes from a medium sharp peak with a shoulder to two new weak peaks. These changes in shift, changes in shape and changes in intensity have divulged the interaction between LiTFSI and BmImTFSI despite they have same anions. Another evidence to prove the interaction between PVC, LiTFSI and BmImTFSI is observed at 740 cm^{-1}. This characteristic peak is assigned as combination of CH_2 rocking mode of PVC and S–N stretching mode of LiTFSI and is shifted from 746 cm^{-1} by comparing Figures 6.11 (a) and (c).

As shown in Figure 5.9 (c), SPE 6 shows a shoulder peak at 1232 cm^{-1} which denoted as CH_3 symmetric bending mode of PMMA. However, it is disappeared in the IL 6 spectrum. It is due to the overlapping with N–H stretching mode of BmImTFSI which located at 1226 cm^{-1}. This indicates the interaction

between PMMA and BmImTFSI. Moreover, the interaction between PMMA and BmImTFSI is also being proven in the Figures 6.11 (a) and (c). Both characteristic peaks at 966 cm^{-1} and 988 cm^{-1} exhibit upward shifts from 963 cm^{-1} and 981 cm^{-1}, respectively. At 1281 cm^{-1}, the intensity of C–O–C symmetric stretching peak increases by 7.97 % in transmittance mode, from 0.6 % to 8.57 %. The wavenumber shifts from 1284 cm^{-1} to 1281 cm^{-1} with addition of 60 wt% of BmImTFSI. This reveals the interaction between O^- and $BmIm^+$ which leads to the ionic transportation by breaking the coordination bond and then reforming the bonds. Another proof to verify the ion transportation is observed at 1725 cm^{-1}. As shown in Figure 6.12, the peak intensity is increased greatly, from 3.14 % to 56.43 % in transmittance mode. It is assigned as C=O stretching mode and it shifts from 1711 cm^{-1} to 1725 cm^{-1}. The increase in intensity discloses that the interaction between O^- and $BmIm^+$ accelerating the dissociation of BmImTFSI. The intensity of this peak increases with amount of BmImTFSI by comparing Figures 6.11 (a), (b) and (c). It indicates that more interaction of O^- with $BmIm^+$ are formed with increasing the BmImTFSI loading and thus the ion hopping mechanism is favorable, which in turn to high ionic conductivity for IL 6. This result is in agreement with ionic conductivity studies.

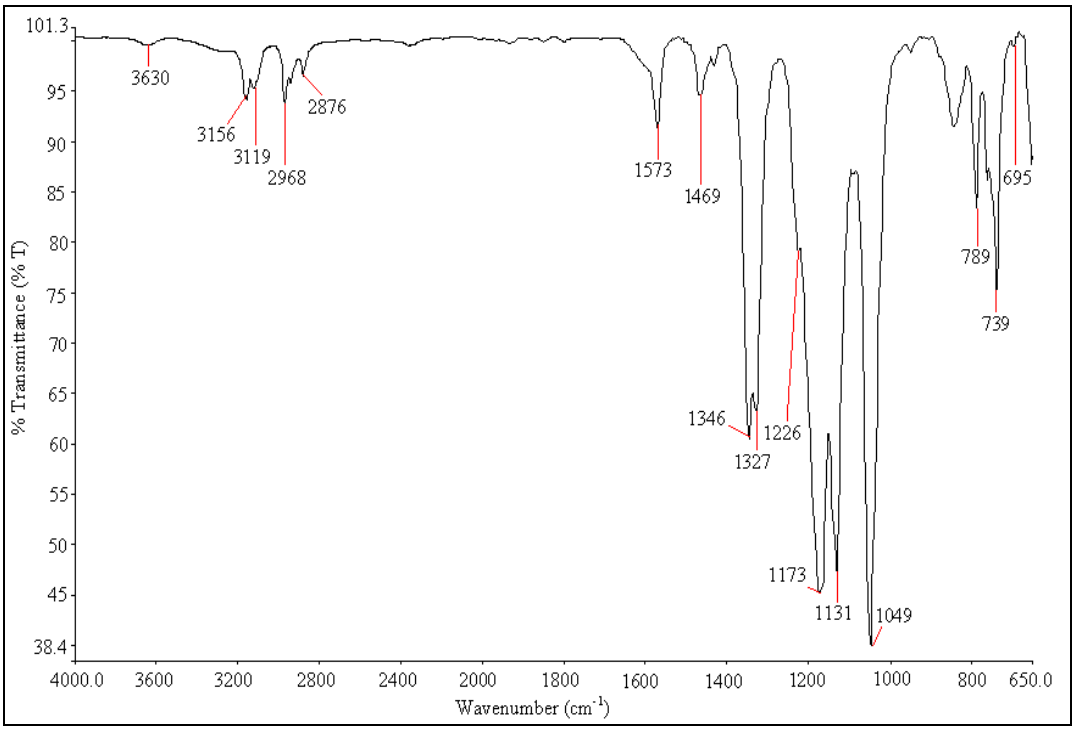

Figure 6.10 (a): HATR-FTIR spectrum of pure BmImTFSI.

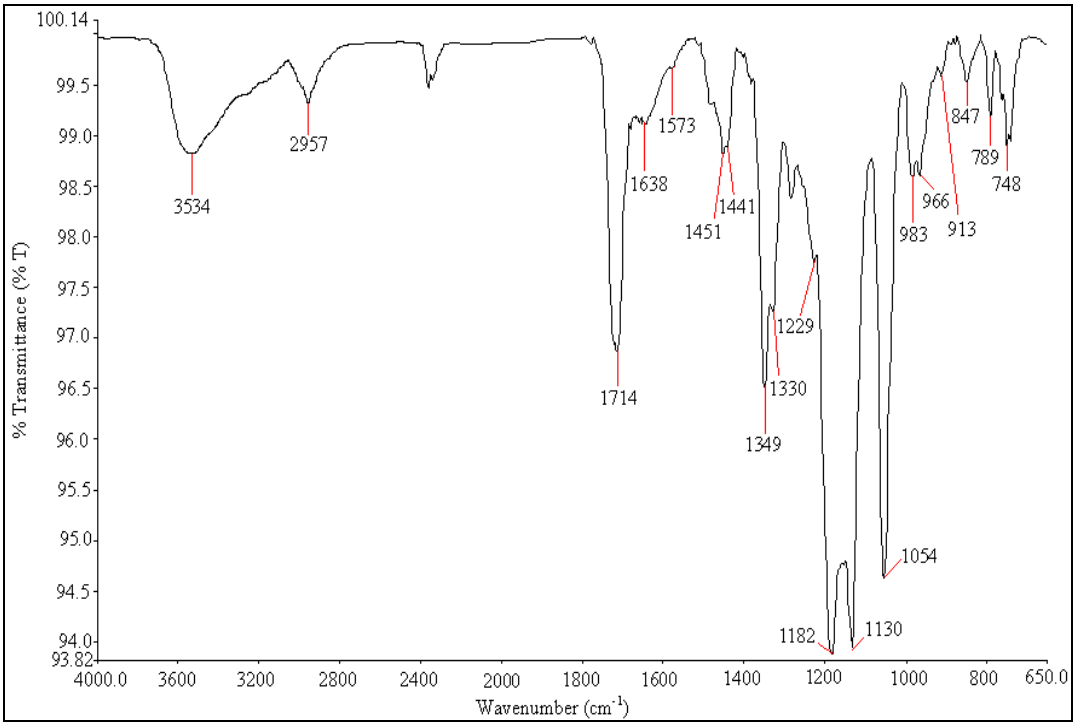

Figure 6.10 (b): HATR–FTIR spectrum of IL 2.

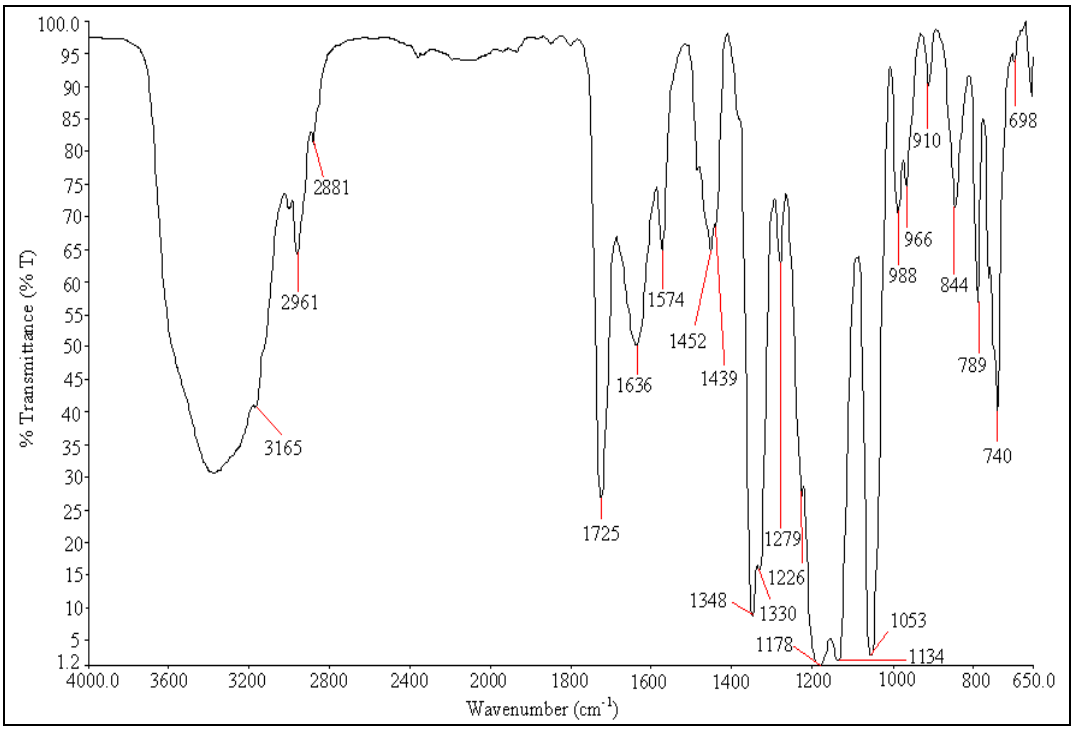

Figure 6.10 (c): HATR–FTIR spectrum of IL 5.

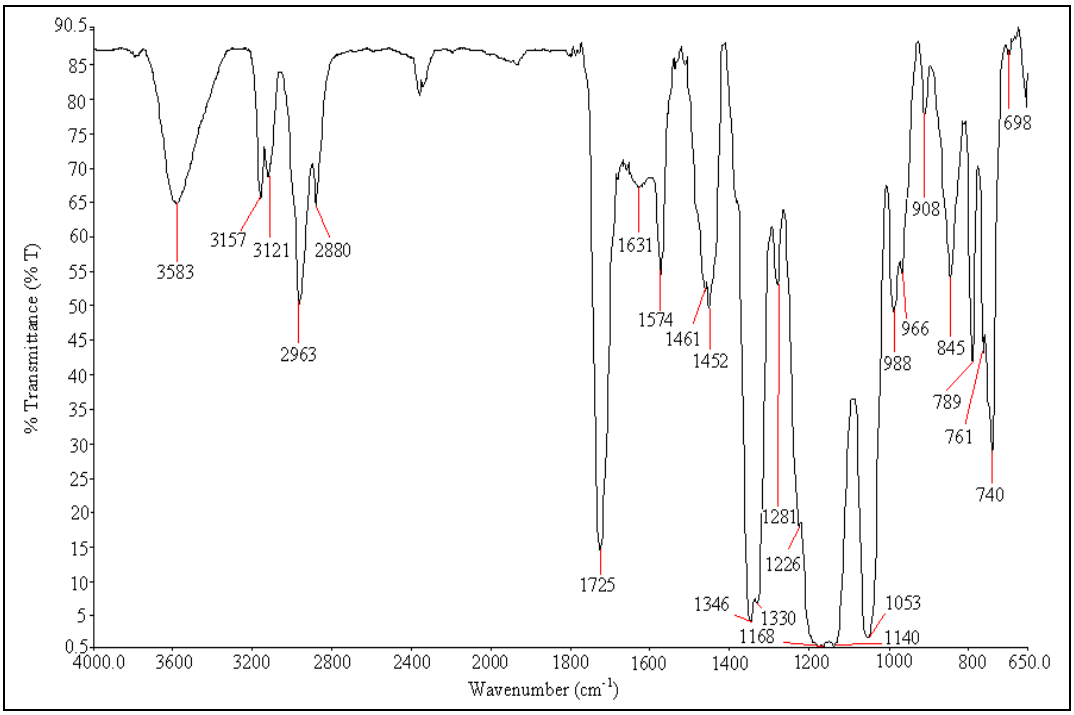

Figure 6.10 (d): HATR–FTIR spectrum of IL 6.

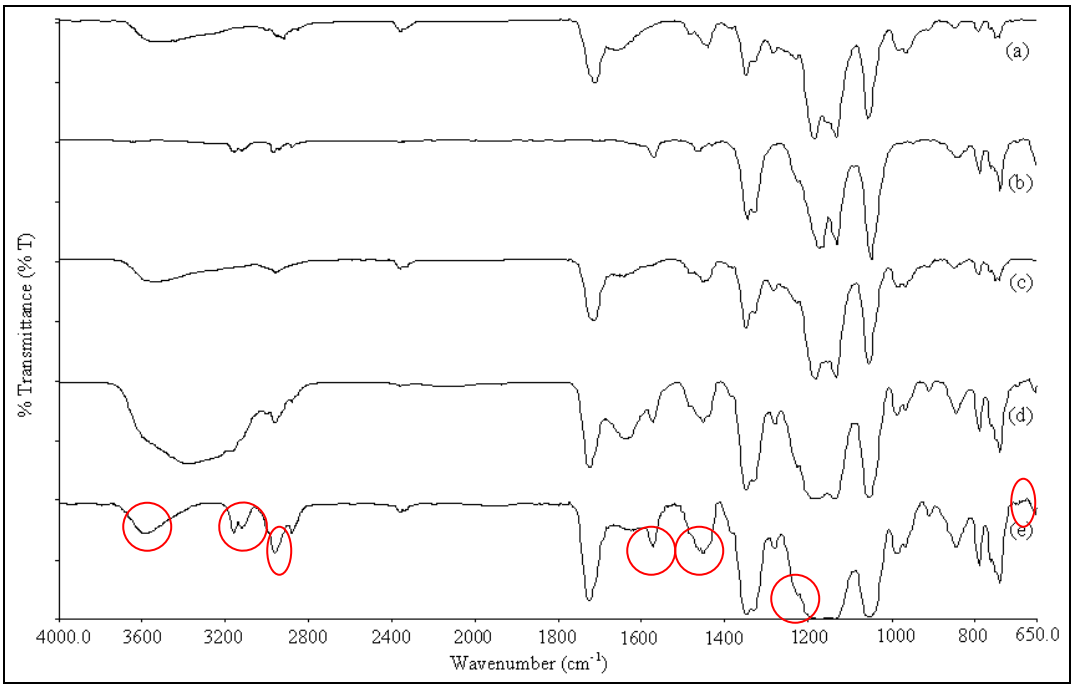

Figure 6.11: Combination of HATR–FTIR spectra for (a) SPE 6, (b) pure BmImTFSI, (c) IL 2, (d) IL 5 and (e) IL 6.

Descriptions of vibration modes	Wavenumber (cm^{-1})	References
Combination of cis C–H wagging mode of PVC and C–H vibrational mode for cyclic $BmIm^+$ of BmImTFSI	698	Rajendran *et al.*, 2008; Jiang et al., 2006
Combination of CH_2 rocking mode of PVC and S–N stretching mode of LiTFSI	740	Rajendran *et al.*, 2008; Ahmad *et al.*, 2008
CF_3 symmetric bending mode of BmImTFSI	761	Bazito *et al.*, 2007
Combination of C–S and S–N stretching mode of LiTFSI and BmImTFSI	789	Ahmad *et al.*, 2008
C–Cl stretching mode of PVC	845	Li *et al.*, 2006a
Trans C–H wagging mode of PVC	908	Achari *et al.*, 2007
C–O symmetric stretching mode in C–O–C linkage of PMMA	966	Achari *et al.*, 2007
CH_2 wagging mode of PMMA	988	Rajendran *et al.*, 2002
S–N–S asymmetric stretching mode of LiTFSI and BmImTFSI	1053	Achari *et al.*, 2007; Ahmad *et al.*, 2008
Combination of C–O–C asymmetric stretching mode of PMMA, C–SO_2–N	1140	Jiang *et al.*, 2006; Ramesh and Lu,

bonding mode of LiTFSI and BmImTFSI		2008
Combination of CH_2 twisting mode of PMMA, CF_3 symmetric stretching mode of LiTFSI and C–H vibrational mode for cyclic $BmIm^+$ of BmImTFSI	1168	Rajendran *et al*., 2004; Ahmad *et al*., 2008; Jiang et al., 2006
N–H stretching mode of BmImTFSI	1226	Bazito *et al*., 2007
C–O–C symmetric stretching mode of PMMA	1281	Jiang *et al*., 2006
C–SO_2–N bonding mode of LiTFSI and BmImTFSI	1330	Ramesh and Lu, 2008
SO_2 asymmetric stretching mode of LiTFSI and BmImTFSI	1346	Ahmad *et al*., 2008
Combination of CH_3 asymmetric bending mode of PMMA, C–H stretching mode of CH_2 group of PVC	1452	Rajendran *et al*., 2004; Rajendran *et al*., 2008
CH_3 symmetric stretching mode of BmImTFSI	1461	Jiang *et al*., 2006
C–C and C–N bending mode of BmImTFSI	1574	Jiang *et al*., 2006
C=C stretching mode of PVC	1631	Achari *et al*., 2007
C=O stretching mode of PMMA	1725	Li *et al*., 2006a
S–CH_3 bonding mode of LiTFSI and BmImTFSI	2880	Ramesh and Lu, 2008
CH_2 stretching mode of BmImTFSI	2963	Jiang *et al*., 2006
C–H vibrational mode for cyclic $BmIm^+$ of BmImTFSI	3121, 3157	Jiang *et al*., 2006
N–H stretching mode of BmImTFSI	3583	Jiang *et al*., 2006

Table 6.2: Assignments of vibrational modes of PMMA, PVC, LiTFSI and BmImTFSI for IL 6.

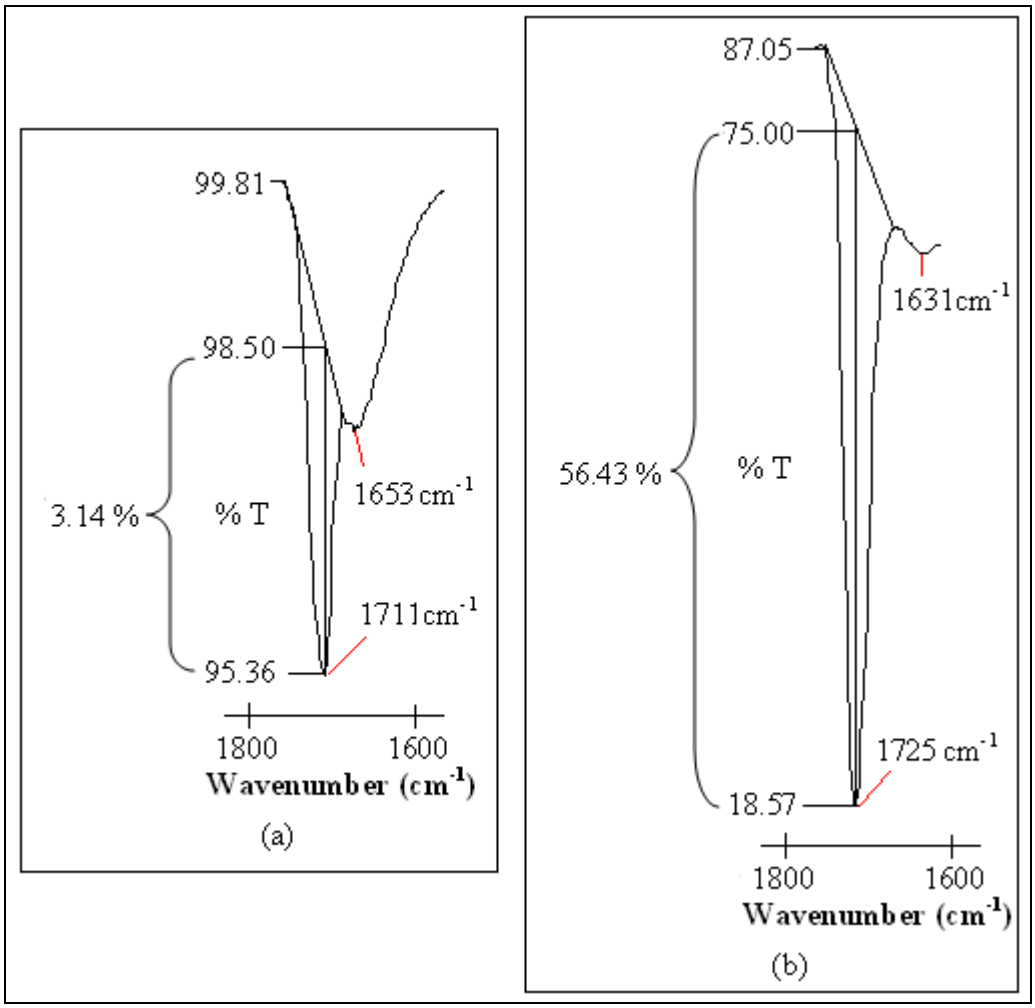

Figure 6.12: The comparison of change in intensity of C=O stretching bonding mode of PMMA in (a) SPE 6 and (b) IL 6.

The weak peak at 698 cm^{-1} is assigned as cis wagging mode of PVC and it is shifted from 708 cm^{-1}. The intensity of peak increases obviously and it is due to the overlapping of C–H vibrational mode for cyclic $BmIm^+$ of BmImTFSI. An apparent change in shape is observed in Figure 6.13. The first peak represents combination of C–O–C asymmetric stretching mode of PMMA, C–SO_2–N bonding mode of LiTFSI and BmImTFSI, whereas second peak is assigned as combination of CH_2 twisting mode of PMMA and CF_3 symmetric stretching mode of LiTFSI. The first peak shifts from 1133 cm^{-1} to 1140 cm^{-1}, whereas it shifts

from 1186 cm^{-1} to 1168 cm^{-1} for latter peak. Regarding to the change in shape, two sharp peaks have been changed to two new broad bands. It is mainly due to the overlapping of C–H vibrational mode for cyclic $BmIm^+$ with polymer matrix and induces to interaction of BmImTFSI with PMMA and LiTFSI. This indicates the complexation between PMMA, LiTFSI and BmImTFSI and consequently, produces the ionic migration within the polymer matrix.

In order to investigate the ion aggregation further, the bands in the wavelength region of 1400 cm^{-1}–1100 cm^{-1} are explored. The remarkable downward shift is obtained with increasing the BmImTFSI loading. The peak shifts from 1186 cm^{-1} (SPE 6) to 1182 cm^{-1} (IL 2), 1178 cm^{-1} (IL 5) and 1168 cm^{-1} (IL 6). It reveals the high CF_3^- aggregations and it leads to lesser agglomeration of cations which in accordance with higher ionic conductivity. The downward shift is also observed for SO_2 asymmetric stretching of LiTFSI and BmImTFSI. It shifts from 1349 cm^{-1} for (IL 2) to 1348 cm^{-1} (IL 5) and 1346 cm^{-1} (IL 6). This infers the high SO_2^- aggregation. Again, it contributes to higher ionic conductivity with lower frequency. The lowest peak intensity of IL 6 at 1168 cm^{-1} is another evidence to prove the highest ionic conductivity of the sample. The intensity of this characteristic peak is reduced substantially as increases the BmImTFSI amount, attributing to the lower viscosity of the sample. In general, lower viscosity would forms lesser entanglements and hence requires less energy to break the coordination bonds. As a result, the peak intensity is reduced. It can clearly seen that IL 6 has lowest viscosity and thus it forms more conducting pathways by producing lesser entanglements among the polymer matrix which results in higher

ionic conductivity.

Comparing IL 2 with IL 6, four peaks are absent and they are combination of cis C–H wagging mode of PVC and C–H vibrational mode for cyclic $BmIm^+$ of BmImTFSI, S–CH_3 bonding mode of LiTFSI and BmImTFSI and C–H vibrational mode for cyclic $BmIm^+$ of BmImTFSI (two peaks are obtained for this vibrational mode). On the other hands, IL 5 exhibits all the vibrational modes, except C–H vibrational mode for cyclic $BmIm^+$ of BmImTFSI at 3121 cm^{-1} and N–H stretching mode of BmImTFSI at 3583 cm^{-1}. The disappearance of characteristic peaks is suggestive of the small amount of ionic liquid added into the polymer system. The absent of C–H vibrational mode for cyclic $BmIm^+$ reveals lesser interaction between O^- and $BmIm^+$ and contributes to the lower ion hopping process which in accordance with lower ionic conductivity.

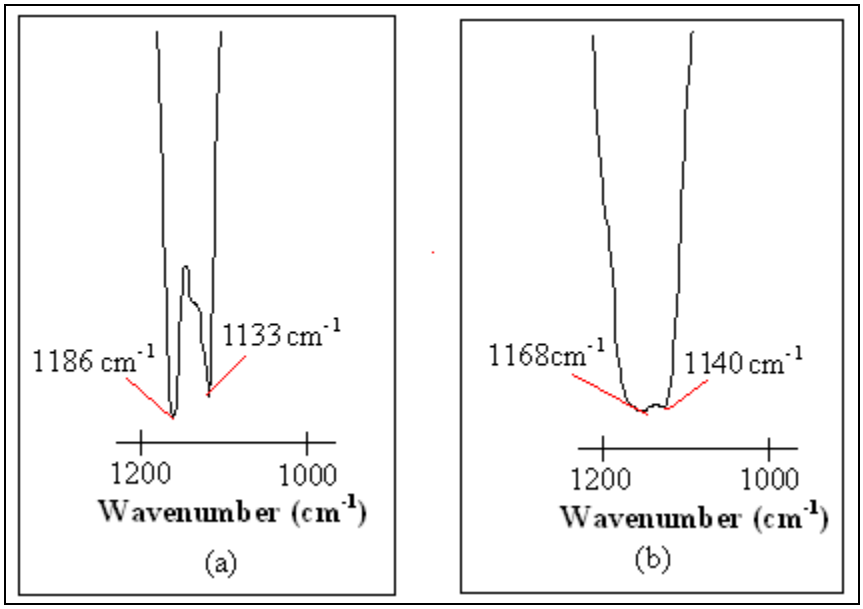

Figure 6.13: The comparison of change in shape of vibrational modes in (a) SPE 6 and (b) IL 6 in the wavenumber range of 1200–1000 cm^{-1}.

6.8 XRD Studies

XRD analysis has been performed, and their respective diffraction patterns of SPE 6, IL 2, IL 5 and IL 6 are shown in Figures 6.14 (a)–(d). Obviously, two broad peaks are present for SPE 6 and IL 2 at Bragg angle of 2θ=16° and 22.6°, revealing the amorphous behavior of polymer electrolytes. IL 2 does not show any rapid change in shift and it is primarily attributed to the smaller amount of BmImTFSI added into the polymer matrix. As a result, the visible change in crystallographic organization in the polymer matrix is barely observed. Nevertheless, it shifts to 2θ=13° and 18.5° upon further addition of BmImTFSI and implies the weaker bonding within polymer matrix, accelerating the formation of complexation between polymer blends and BmImTFSI (Singh *et al*., 2008).

Change in intensity of the peaks is an indicative amorphous characteristic of polymer electrolytes. Addition of 2 wt% of BmImTFSI does not show any appreciable effect on the change in intensity of peaks. Again, this is due to the insufficient amount to dislocate the polymer network and thus results an insignificant increase in amorphous degree among the polymer backbone. In contrast, the amorphous region increases greatly upon addition of 50 and 60 wt% of BmImTFSI as the intensity reduces drastically. In other word, inclusion of 50 and 60 wt% of BmImTFSI is remarkably disturbed the ordered arrangement of polymer matrix, decreasing the crystallinity. IL 5 is still showing two broad peaks. However, IL 6 illustrates a change of peak shape and it changes to a new broad peak with a shoulder. The decrease in relative intensity for IL 6 is higher than IL 5

and this indicates the higher amorphous characteristic of IL 6. Higher amorphous proportion facilitates the ion mobility and provides more flexible backbone, and thereby gives rise to ionic conductivity. This result is in good agreement with ionic conductivity studies.

It is further proven in coherent length study. In principle, coherent length defines as crystallite size of polymer electrolytes. Based on Debye–Scherrer equation, the broader of the diffraction peak width, the shorter of crystallite size is. Hence, it contributes to lower crystallinity and higher ionic conductivity (Ramesh and Chai, 2007). As illustrated in Figure 6.15, the coherent length decreases with increasing the BmImTFSI amount. The disordered arrangement of polymer matrix is occurred with incorporation of ionic liquid, leading to construction of amorphous region. This aids to enhance the segmental motion and flexibility of polymer backbone. Hence, it results an increment of the ionic transportation in accordance with the higher ionic conductivity.

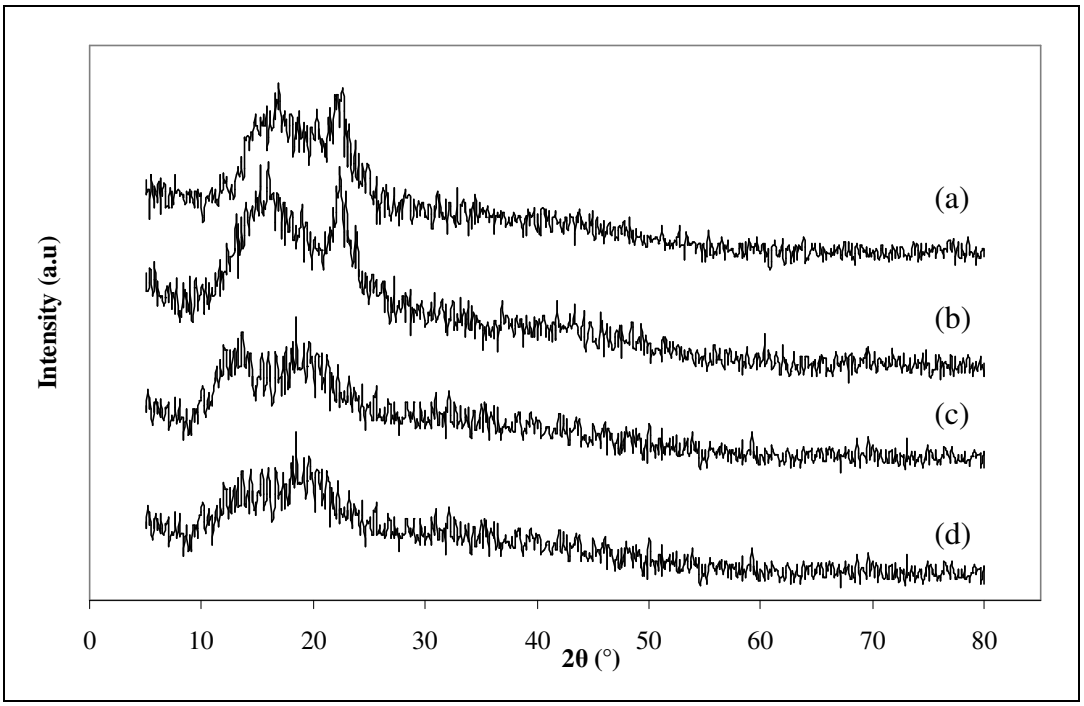

Figure 6.14: XRD patterns of (a) SPE 6, (b) IL 2, (c) IL 5 and (d) IL 6.

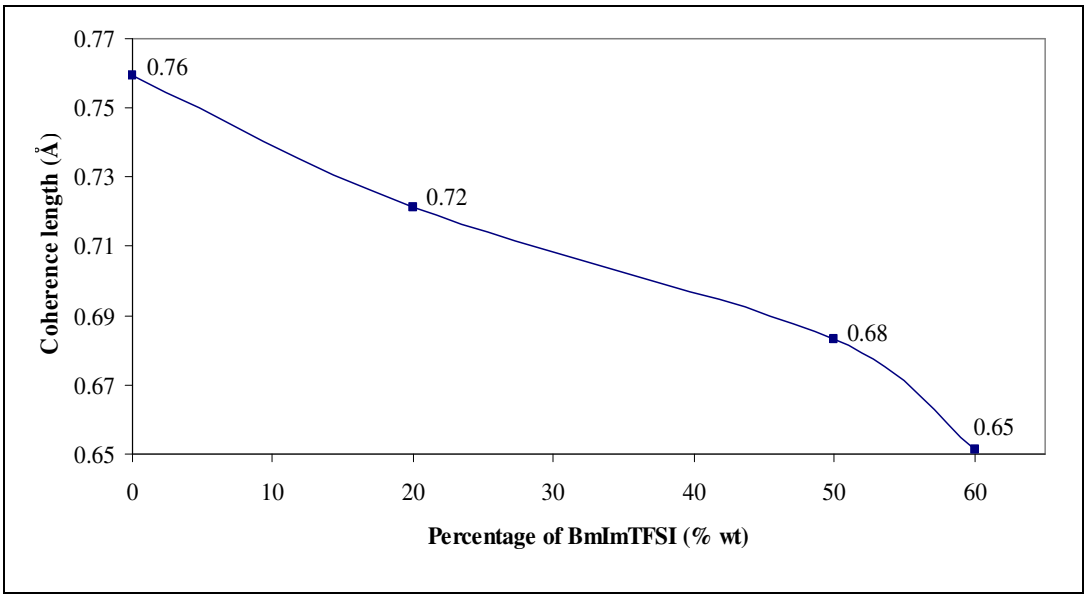

Figure 6.15: Variation of coherence length at ambient temperature with respect to different mole fraction of BmImTFSI into PMMA–PVC–LiTFSI based gel polymer electrolytes at $2\theta \approx 16°C$.

6.9 SEM Studies

Figures 6.16 (a)–(c) depict SEM images for all GPEs. The presence of white spherulites is mainly attributed to the entrapments of ionic liquid which are being retained in the polymer matrix. This induces to formation of the entanglements between ionic liquid and polymer network. Smooth appearance is obtained by adding BmImTFSI. This strongly discloses the presence of amorphous nature of GPEs. These entanglements enhance the segmental motion of polymer backbone by weakening the interaction between polymer chains and Li cations. Thus, this produces flexible polymer backbone and facilitates the ionic transfer among the polymer network. Consequently, it does not impede ionic conductivity.

Amount of entrapments is rising up with increasing BmImTFSI loadings as depicted in Figures 6.16 (b)–(c). The least entrapment in IL 2 implies the least amorphous degree of polymer matrix. The amount of ionic liquid is insufficient to interrupt the crystallinity nature of the polymer matrix to a greater extent and eventually, it inhibits the ionic transportation among the polymer electrolyte. IL 6 has more distribution of ionic liquid entrapments and tends to aggregate in comparing with IL 5. These aggregations weaken the coordination bonds of polymer matrix and Li cations and form more flexible polymer backbone with enhanced plasticizing effect. Hence, it favors the ionic hopping mechanism which in accordance with higher ionic conductivity. Some blackish cavities are formed on the surface morphology of IL 6 as highlighted in Figure 6.16 (c). This is

suggestive of ionic migration effect by providing the continuous conducting pathway within the entrapments.

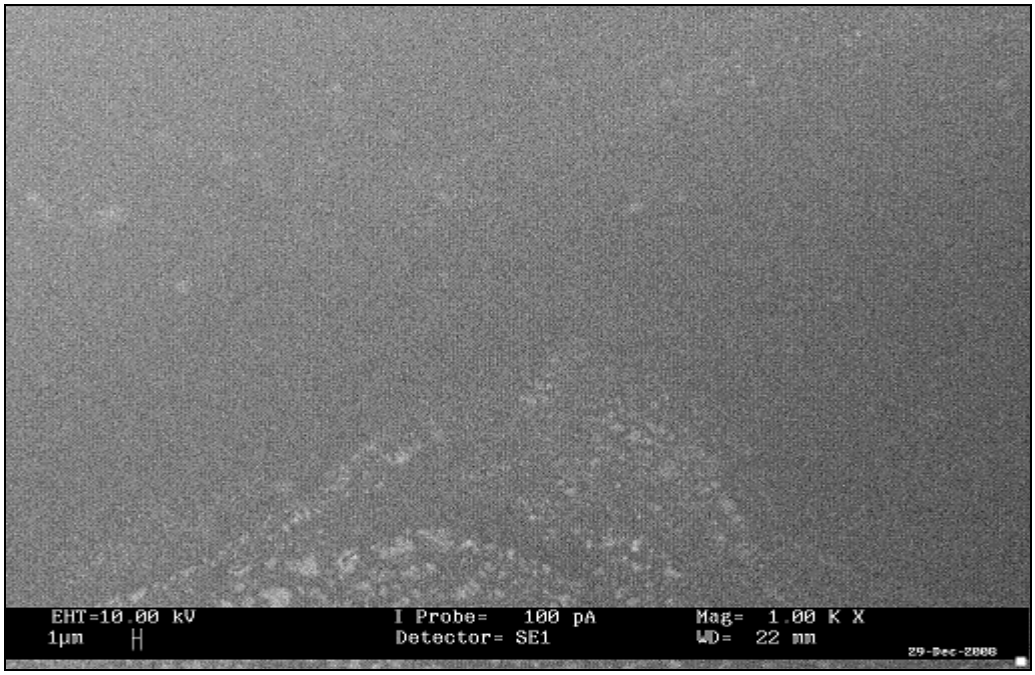

Figure 6.16 (a): SEM image of IL 2.

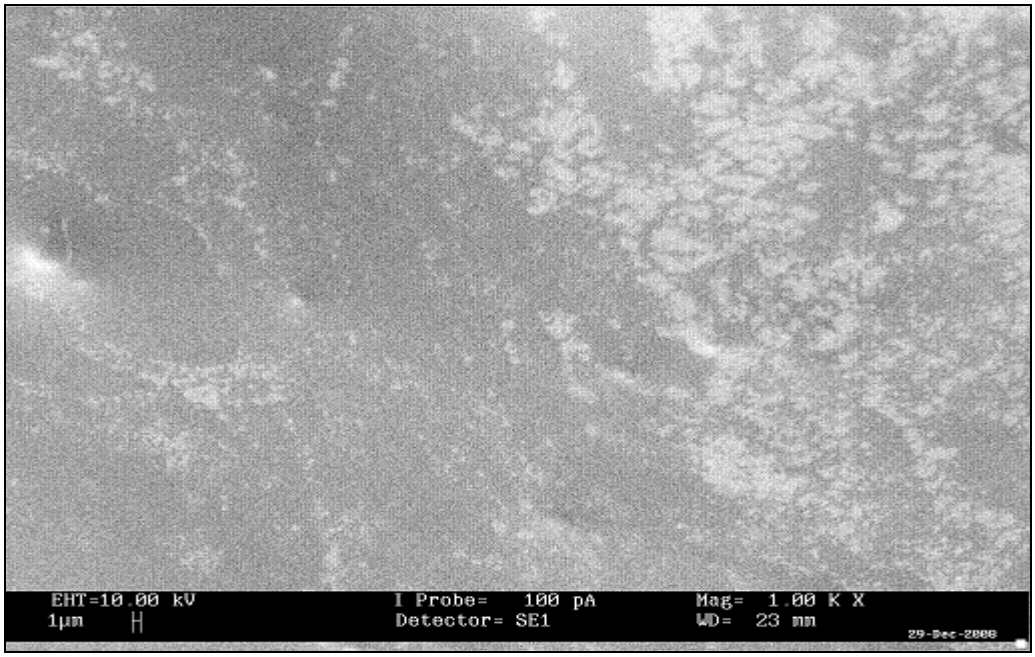

Figure 6.16 (b): SEM image of IL 5.

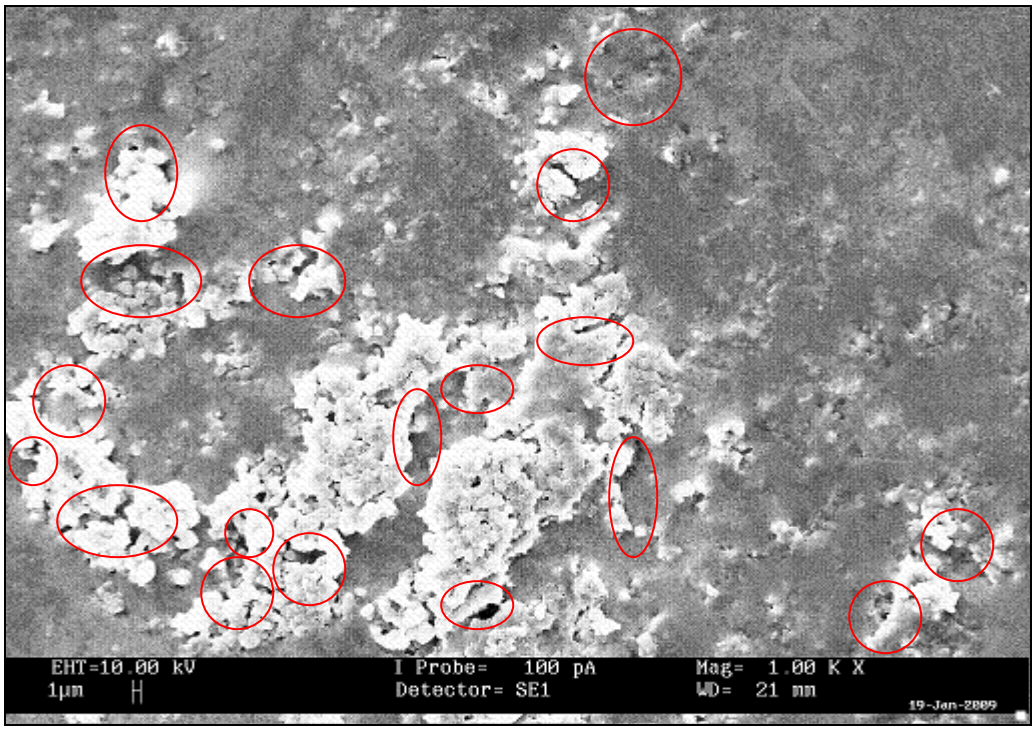

Figure 6.16 (c): SEM image of IL 6.

6.10 DSC Studies

Figure 6.17 illustrates DSC profiles of GPEs, meanwhile all the DSC measurements are tabulated in Table 6.3. Same trends of all DSC traces of GPEs are clearly observed. A small drop in heat flow from exothermic reaction to endothermic reaction is initially observed and it is commonly known as glass transition glass transition temperature (T_g). Thus, heat flow of polymer matrix decreases monotonically, up to above 157 °C, and follows by a weak endothermic peak which known as melting point of the polymer electrolytes, T_m . Two consecutive peaks are observed thereafter and they are defined as decomposition temperatures of polymer electrolytes, T_d . The first endothermic decomposition

peak is corresponding to the dehydrochlorination of PVC, as explained in section 4.10 (Ahmad *et al*., 2007). The second endothermic peak is originated from the degradation of unsaturated group of PMMA such as carbonyl functional group and decomposition of PVC (Ahmad *et al*., 2006b).

A single T_g implies the homogenous and amorphous behavior of GPEs (Ahmad *et al*., 2006a). As expected, T_g is lowered down by incorporating with ionic liquid and further shifted to downward with increasing the mass fraction of BmImTFSI. The major contributor is the plasticizing effect of ionic liquid. The plasticizing effect weakens the dipole–dipole interactions and thus disrupts the transient cross–linkage bonds among polymer matrix. As a result, the solvation of Li^+ cations with oxygen of ester functional group from PMMA is enormously decreased. Therefore, inclusion of BmImTFSI ionic liquid softens the polymer backbone, enhances the segmental motion and hence increases flexibility of the polymer chains (Baskaran *et al*., 2007).

T_g decreases from 118 °C, 115 °C, 114 °C to 112 °C, correspondingly from free–ionic liquid (SPE 6), 20 wt%(IL 2), 50 wt% (IL 5) to 60 wt% (IL 6) of BmImTFSI. Plasticizing effect is more clearly evidenced by increasing ionic liquid loadings further. Another perspective is the weakening of the interactions among the gel polymer electrolytes upon dispersion of ionic liquid. This promotes the decoupling of ions from the polymer segmental motion and improves ionic

transportation (Cheng *et al*., 2007). It can therefore be conferred that the ionic conductivity enhances with increasing BmImTFSI loadings.

T_m exhibits downward shift by adding BmImTFSI as shown in Figure 6.17. The melting point of electrolytes reduces from 184 °C, 161 °C, 158 °C to 157 °C with respect to SPE 6, IL 2, IL 5 and IL 6. Apparently, the endothermic meting peaks become more asymmetric and broad peaks, showing the decrease in crystalline degree or increase in amorphous region of the electrolytes (Pandey *et al*., 2009). The amorphous nature of polymer electrolytes accelerates the segmental mobility and ionic motions in the electrolytes, attributing to the increased ionic conductivity as mentioned above. Lower T_m evolves with smaller peak area (or lower of heat of fusion) is illustrated with increases in the mass fraction of ionic liquid. The increase in amorphous proportion within the polymer electrolytes with increasing the amount of BmImTFSI is further proven. As explained above, this deterioration of arrangement in polymer matrix facilitates the formation of flexible backbone and improves the ion hopping process by providing more voids for ion transportation. This result is proven in XRD and SEM analyses.

An opposite feature is obtained for T_d. The decomposition temperatures are shifted upward upon inclusion of BmImTFSI. The first decomposition temperature increases substantially, from 366 °C (SPE 6), 370 °C (IL 2), 373 °C (IL 5) to 376 °C (IL 6), whereas the second decomposition temperature lies within the range of 390 °C (SPE 6), 398 (IL 2) and 399 °C (IL 5 and IL 6). Based on all

the DSC results, it concludes that IL 6 is a promising candidate as gel polymer electrolyte in electrochemical devices since it achieves the highest decomposition temperature.

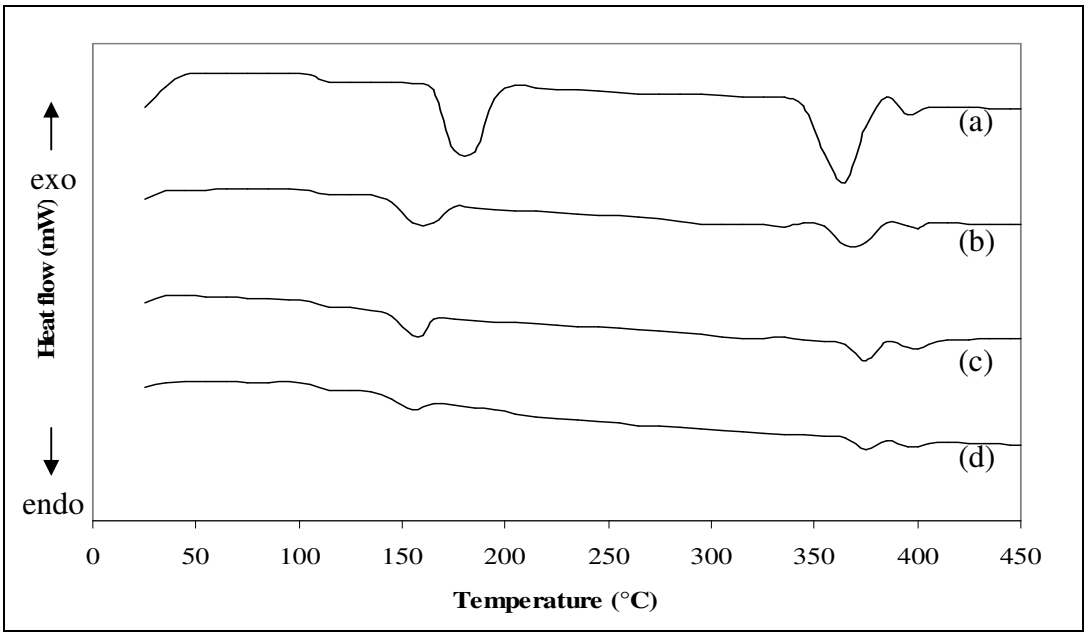

Figure 6.17: DSC thermograms of (a) SPE 6, (b) IL 2, (c) IL 5 and (d) IL 6.

Designations	DSC measurements		
	T_g (°C)	T_m (°C)	T_d (°C)
SPE 6	118.16	184.50	366.20, 390.27
IL 2	115.20	160.83	370.42, 398.14
IL 5	113.80	158.40	373.20, 398.90
IL 6	112.50	157.30	375.66, 399.40

Table 6.3: DSC profiles of PMMA–PVC–LiTFSI based gel polymer electrolytes and their designations.

6.11 TGA Studies

TGA study is further carried out in order to examine thermal properties of GPEs. Figure 6.18 divulges the TGA thermograms of SPE 6, IL 2, IL 5 and IL 6. Three stages are clearly observed for all the degradation curves. Around 3 % of first weight loss is obtained for SPE 6, up to 139 °C. However, the mass loss shows a significant rise and 5% of weight loss is observed for IL 2, IL 5 and IL 6 in the temperature range from 137 °C to 140 °C. The first weight loss is ascribed to the evaporation of THF solvent and elimination of impurities especially fluorine compound (Stephan *et al*., 2002). Since polymers and LiTFSI are hygroscopic compounds, thus dehydration of entrapped moisture is also another attributor for this weight loss. Upon addition of BmImTFSI, the increase in weight loss indicates more impurities are being trapped in LiTFSI and BmImTFSI. In addition, gel–like electrolytes has higher absorption and retention of solvent and moisture abilities.

Beyond the first mass loss, a stable weight is followed up in the thermal range. Second and third weight losses are evaluated thereafter. The unzipping process is the major contributor for second weight loss in the temperature regime. This process causes many degradation reactions such as random chain scission reaction, depolymerization, intra–molecular transfer reaction whereby dimer, trimers and oligomers are produced and inter–molecular transfer reaction as well as polymer fragments. As a result, the monomer and oligomers which chemi–adsorbed onto the polymer matrix are volatilized in this temperature regime. This induces to a decrease in the weight loss (Ahmad *et al*., 2007). Exclusion of HCl

compounds from the dehydrochlorination reaction is another factor, as proven in DSC thermograms. SPE 6 has mass loss of 26 %, starting from 288 °C to 348 °C, whereas for IL 2, the weight loss is found to be decreased by 5 %, starting from 235 °C until 345°C. In contrast, IL 5 has weight loss of 13 % in the temperature range of 260 °C and 350 °C, meanwhile weight loss of IL 6 is around 17 % whereby the degradation temperature starts from 255 °C to 355 °C.

A consecutive gradual mass loss is displayed after the second weight loss. This particular weight loss is related to the degradation of unsaturated groups of PMMA such as C–O and –O– and decomposition of PVC, as verified in DSC study. The BmImTFSI–free polymer electrolyte shows the weight loss of 11 % at 390 °C, with residual mass of around 60 %. Around 21 % and 13 % of weight losses are attained for IL 2 and IL 5, with residual mass of 62 % and 64 %, at 385 °C and 390 °C, respectively. On the contrary, IL 6 demonstrates around 12 % of weight loss at 385 °C with a residual mass of 66 %. The presence of stable mass after third stage implies the complete decomposition of electrolytes. Among all the electrolytes, IL 6 exhibits excellent thermal stability (stable up to 255 °C) and concludes that it is an excellent candidate as GPE.

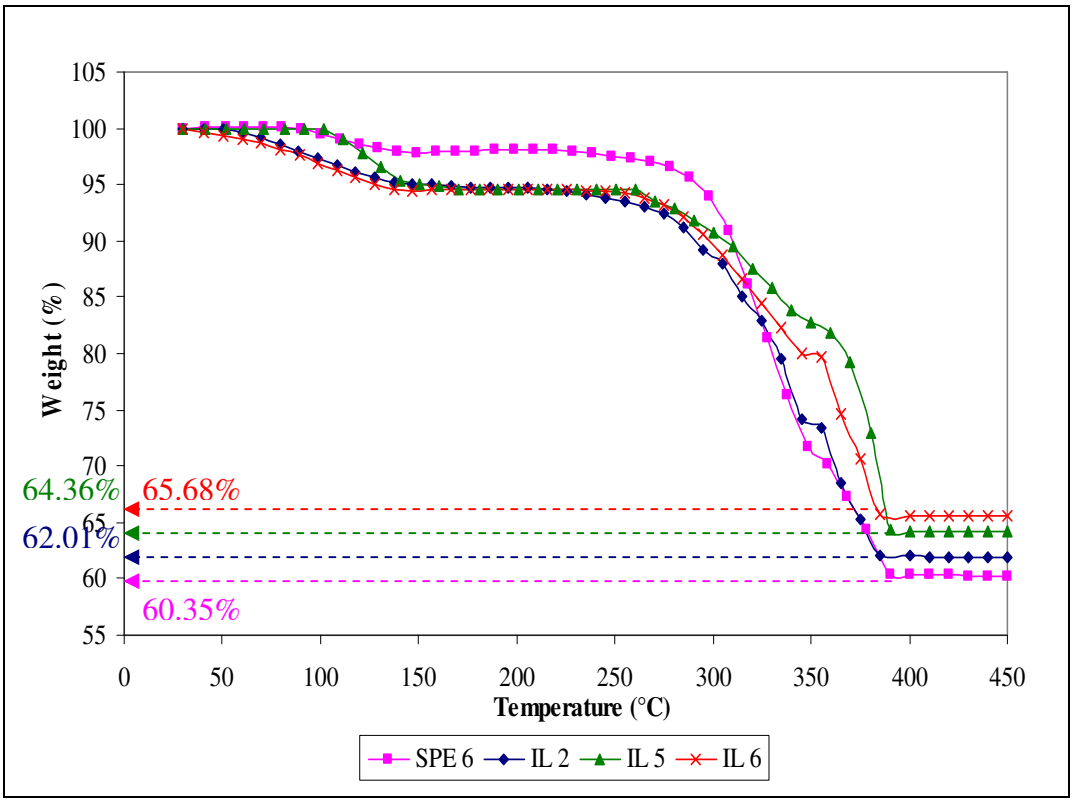

Figure 6.18: Thermogravimetric analysis of SPE 6 and ionic liquid–based gel polymer electrolytes.

.

6.12 Amplitude Sweep

Figure 6.19 shows a typical plot of G' and G'' moduli as a function of strain for GPEs with different proportion of ionic liquid on logarithm scale. The values of G' are much greater than G'' for all the samples over the range of strain. This indicates the solid properties of all the samples within the range (Li *et al.*, 2006b). For all the samples, the crossover point of G' and G'' (usually known as yield point or flow point) is not appeared, implying the absence of behavioral transition of the sample upon the applied shear (Fonseca *et al.*, 2009). Similar

trends are observed for all the samples. Three distinct regions are attained within the range. In the first region, initial gradual decreases in G' and G'' is observed due to the initial deformation of the polymer system. It is then followed up by a constant range which known as LVE range. This LVE range is defined as the stability range of the sample. Beyond this range, the values of G' and G'' decrease again due to the breakdown of the structures of polymer matrix with larger deformation, resulting the reduction of mechanical properties of polymer electrolytes.

Upon addition of ionic liquid, the values of G' and G'' are decreased. It suggest that the ionic liquid favors to weaken the interactions between the polymer matrices by forming the hydrogen bonding of TFSI anions with polymer blends, as shown in Figure 6.20. At 0.001 % of strain, SPE 6 and IL 2 exhibit comparable G' and G'' values. It is mainly attributed to the lesser amount of ionic liquid and therefore the effect is not so apparent. These values decrease further with increasing BmImTFSI content. It confirms the interruption of the transient coordination bonds within the polymer matrix as increase in BmImTFSI concentration, asserting the lower mechanical stability of polymeric system.

Another perspective is the plasticizing effect of ionic liquid. This effect softens the polymer backbone and thus weakens the interactions between the polymer systems. Even though the mechanical properties of polymer electrolytes are lower, however, it still discloses the elastic behavior of samples. The gel appearance of samples possesses advantage in electrochemical device designing

for providing a good contact between electrode and electrolyte (Reiter *et al*., 2006). As shown in Figure 6.19, LVE range increases with BmImTFSI loadings. This indicates that the stability of polymer electrolytes increases with ionic liquid compositions. Since IL 6 illustrates the widest LVE range, thus it can be concluded that IL 6 is the most stable polymer electrolyte.

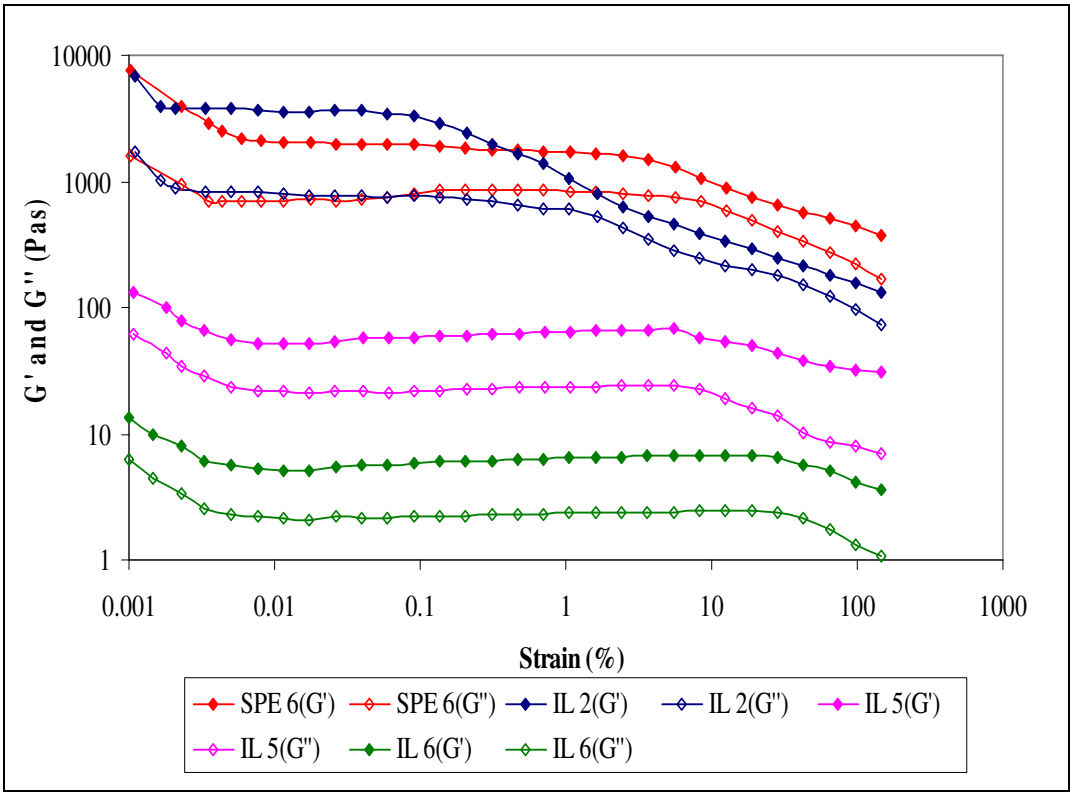

Figure 6.19: Amplitude sweeps of SPE 6 and ionic liquid–based gel polymer electrolytes.

.

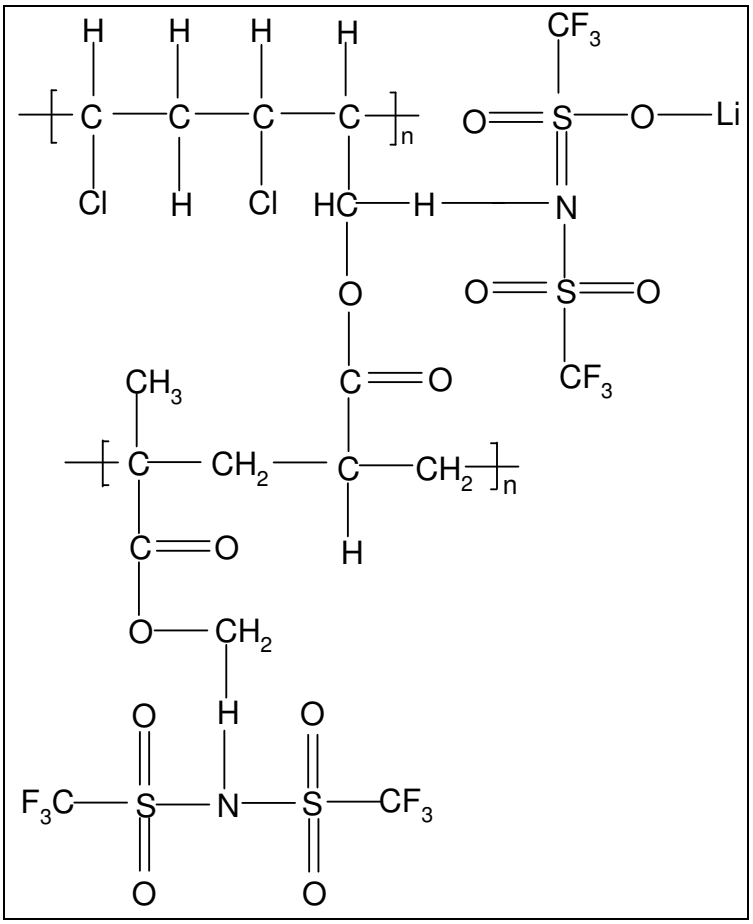

Figure 6.20: The interaction between TFSI anions from BmImTFSI and polymer matrix through formation of hydrogen bonding.

6.13 Oscillatory Stress Sweep

Figure 6.21 depicts the variation of G' and G'' as a function of shear stress on logarithm scale. The values of G' are higher than G'' in the range and this discloses the gel–like behavior of the samples (Li *et al*., 2006b). The crossover of G' and G'' is absent in all the samples, signifying that there is no behavioral transition in the polymer electrolytes within the range (Fonseca *et al*., 2009). Again, the same pattern of plots is observed. IL 2 manifests the highest value of

shear stress in comparing of all the ionic liquid–based GPEs. IL 2 requires more stress for deformation and thus discloses the higher mechanical stability of IL 2. It is suggestive of insufficient amount of ionic liquid to break the interactive bonds within polymer electrolytes.

As shown in Figure 6.21, the starting shear stress of IL 6 is the lowest and this implies that IL 6 sample has the lowest mechanical properties of the sample with lowest viscosity. It is in good agreement in previous section. This strongly correlated to the interruption of coordination bonds within polymer matrix by BmImTFSI, as explained in previous studies. The weakening of the bonds reveals the lower values of G' and G'' with the presence of plasticizing effect. In other words, the physical and chemical bonds within the polymer matrix is more easily to be deformed with increasing the ionic liquid mass fraction as ionic liquid weakens the entanglements in the polymer electrolyte system. At high shear stress, there is an abrupt decrease in G' and G'' for IL 2. This decrement divulges the unstable properties of IL 2 at high shear stress. Although the mechanical integrity of IL 6 is the lowest, however, it shows higher stability at high deformation by demonstrating the small changes in G' and G''.

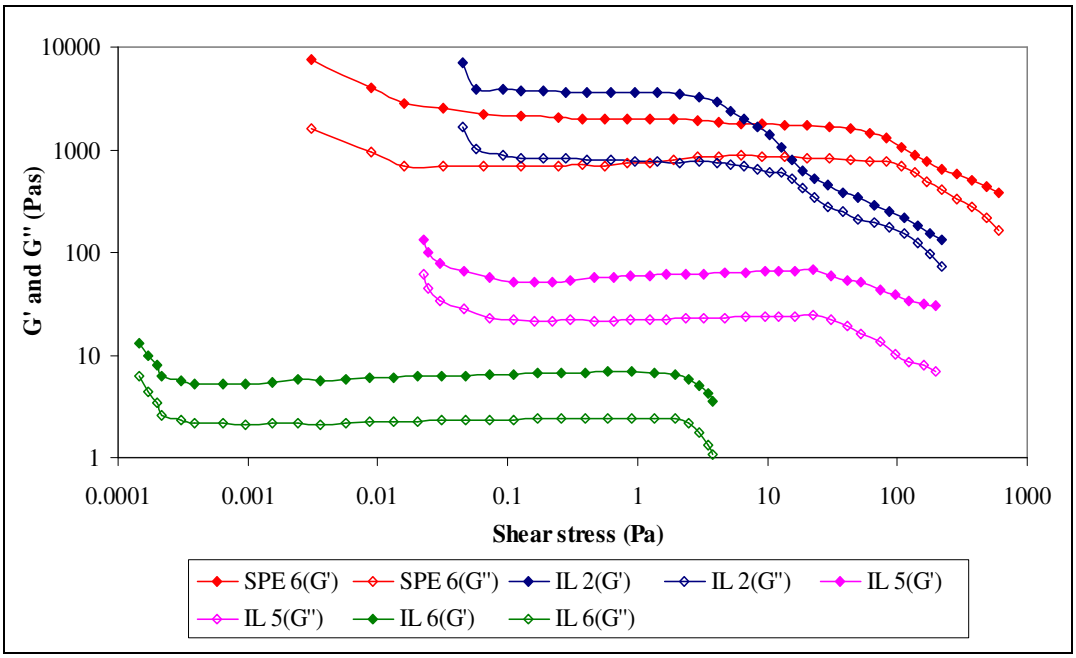

Figure 6.21: Oscillatory shear sweeps of SPE 6 and ionic liquid–based gel polymer electrolytes.

6.14 Oscillatory Frequency Sweep

Figure 6.22 shows the logarithm of storage modulus with respect to frequency. The absence of *G''* within the frequency regime is the main feature of this study. This characteristic reveals the gel nature of ionic liquid–based GPEs. As shown in Figure 6.22, *G'* is frequency dependent. At low frequency, the deformation of samples takes place for longer time and *G'* shows the lower value. This is mainly attributed to the longer relaxation time whereby the polymer chain have enough time to prevent the externally imposed deformation by relaxing to an energetically more favorable state (Ebagninin *et al.*, 2009). The slippage of the entanglements of the entwined polymer chains contributes to the relaxation process, leading to the increase in segmental motion. Consequently, it reduces the

solid properties of polymer electrolytes and hence indicates the lower structural stability at low frequency. However, the structural stability of polymer electrolytes at low frequency can be improved by adding ionic liquid.

As shown in Figure 6.22, the value of *G'* increases with impregnation of BmImTFSI. It is suggestive of formation of hydrogen bonding of TFSI anions with the polymer chain, which in turn to the difficulty of slippage of the entanglements or cross–linkage in the polymer matrix as hydrogen bond is well known as strongest covalent bond. As a result, the elastic properties of polymer electrolytes decline slowly. On the other hand, the value of *G'* is increased with an upward shift in frequency. This indicates the excellent stability of polymer electrolytes at shorter time scale of deformation, arising from the decrease in relaxation time. At this stage, the polymer chain is no longer slip past one another and therefore the entanglements within the polymer matrix act like fixed network junctions (Ebagninin *et al*., 2009). This temporary polymer network favors to store the temporarily imposed energy and eventually increases the elastic properties. At higher frequency range, the almost flat region implies the strong gel behavior of the polymer electrolytes (Nicotera *et al*., 2006). Since the *G'* values for ionic liquid–free polymer electrolytes and CPEs are similar, thus it can be concluded that addition of ionic liquid does not possesses any effect on the structural stability at high frequency when the deformation takes places for shorter time.

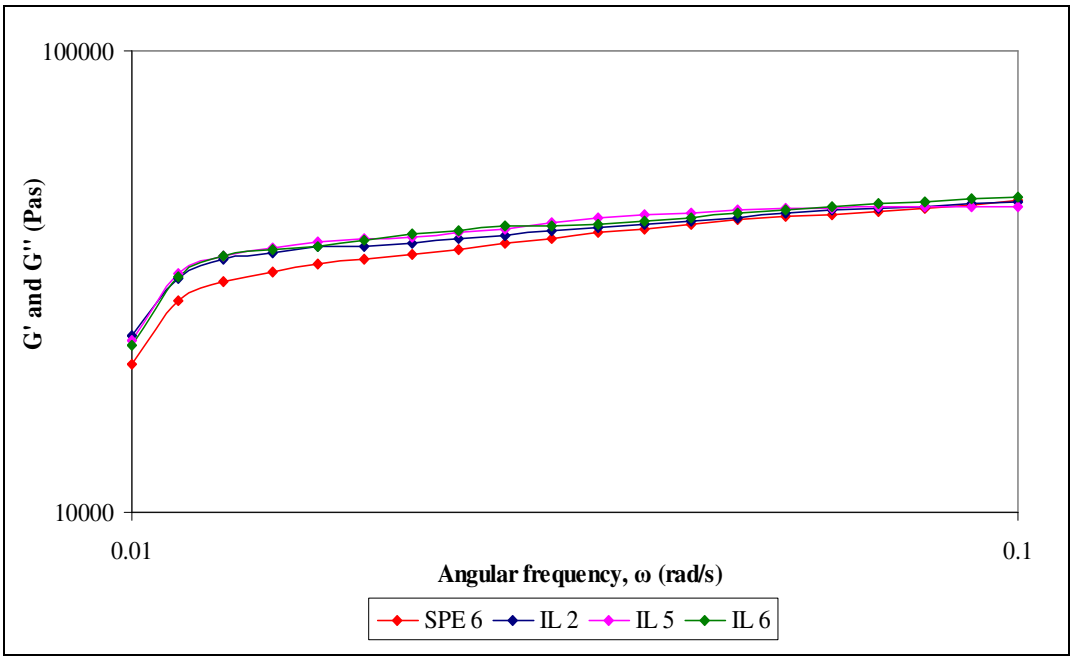

Figure 6.22: Frequency sweeps of SPE 6 and ionic liquid–based gel polymer electrolytes.

6.15 Viscosity studies

The comparison of viscosity of polymer electrolytes with or without ionic liquid as a function of shear rate is depicted in Figure 6.23. As can be seen, the viscosity follows a linear relationship with respect to the shear rate, revealing the non–newtonian properties of the polymer electrolytes. Under shear, the viscosity becomes lesser and it is a typical shear thinning behavior (Ahmad *et al*., 2005). At low shear rate, the sample still remains its solid–like behavior with a high viscosity value when the deformation is lesser. On the other hand, the viscosity is decreased at high shear rate. It is due to the disturbance and breakdown of the interactive bonds in the complex by applying the shear on the polymer electrolyte. Another important feature is observed at high shear rate, i.e. the analogous of the viscosity

and shear thinning rate of all the polymer electrolytes. It arises from the preferential orientation of the entanglements of polymer electrolyte parallel to flow direction (Ahmad *et al*., 2005).

Since ionic liquid is a low viscosity material, thus it is expected that the ionic liquid–based gel polymer electrolytes have lower viscosity. At 0.1 s^{-1} of shear rate, the viscosity of GPEs is declined upon addition of BmImTFSI, as shown in Figure 6.23. The viscosity decreases further with increasing BmImTFSI loadings due to its plasticizing effect. The entanglements of polymer matrix such transient cross–linkage can be disordered easily as ionic liquid favors to weaken the physical and chemical interactions within the polymer system. In general, the low viscosity of polymer electrolyte enhances the ionic hopping process by providing more amorphous region. As a result, IL 6 achieves the highest ionic conductivity as it has the lowest viscosity in comparison to IL 2 and IL 5.

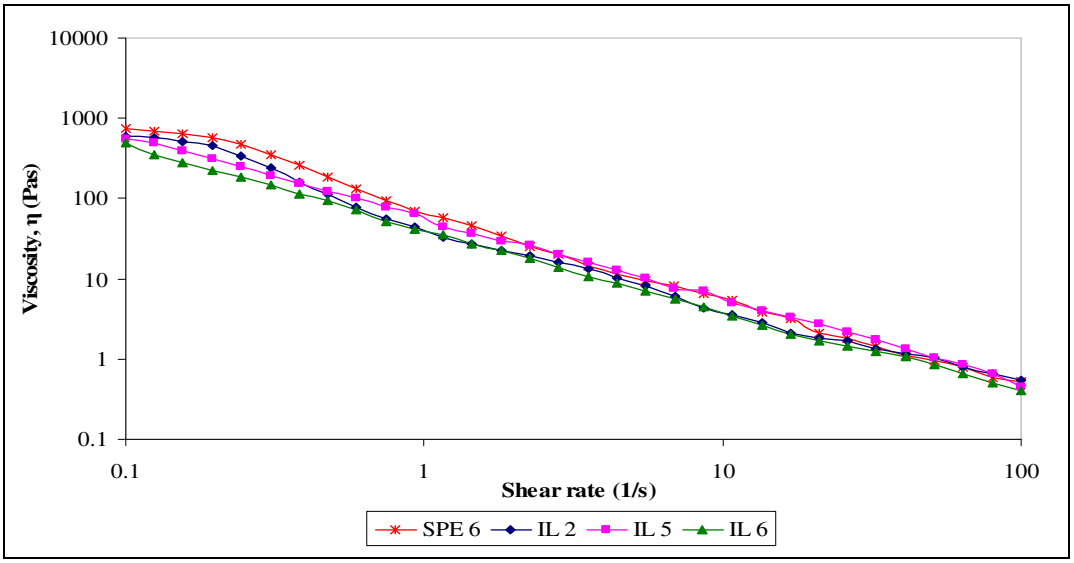

Figure 6.23: Typical viscosity curve of SPE 6 and ionic liquid–based gel polymer electrolytes.

6.16 Summary

BmImTFSI–based gel polymer electrolytes are prepared by solution casting technique. The highest ionic conductivity of $(1.64\pm0.01)\times10^{-4}$ Scm^{-1} is achieved upon addition of 60 wt% of BmImTFSI. In temperature dependence–ionic conductivity study, all samples exhibit Arrhenius type within the temperature regime and favor the ion hopping mechanism at elevated temperature. According to this study, the maximum ionic conductivity of $(8.08\pm0.01)\times10^{-4}$ Scm^{-1} is achieved at 80 °C. Polarization effect is observed in frequency dependence–ionic conductivity study. Both the dielectric constants rise enormously with decreasing the frequency. It is related to the accumulation of charge carriers at the electrode–electrolyte interface. Dielectric moduli studies are further investigated by suppressing the electrode polarization effect. Upon inclusion of ionic liquid, the changes in intensity, changes in shift and changes in shape divulge the complexation between PMMA, PVC, LiTFSI and BmImTFSI, as proven in HATR–FTIR spectra.

On the other hand, XRD study proves the pre–dominant amorphous region in the polymer electrolytes and this is in good agreement with coherent length study. The morphology of SEM shows the higher amorphous degree with doping of BmImTFSI. DSC and TGA studies imply the improved thermal stabilities polymer electrolytes upon addition of ionic liquid. Decreases in T_g and T_m values reflect the enhancement of flexibility and amorphous degree of polymer electrolytes, respectively. Excellent thermal properties of polymer electrolytes are

obtained by showing a insignificant decrease in weight loss of polymer electrolytes upon heating to 450 °C.

In amplitude sweep and oscillatory shear sweep tests, it is found out that the values of storage modulus (G') are much higher than loss modulus (G''). This indicates the elastic behavior of these samples. No behavioral transition of samples is observed in the tests. Linear visco–elastic range (LVE) of samples becomes wider with increasing the content of ionic liquid. The long–term structural stability is enhanced upon addition of ionic liquid. In the frequency sweep test, the absence of G'' further confirmed the solid properties of samples. In the viscosity curve, the viscosity decreases as increases in shear rate due to the structural changes. The zero–shear viscosities are reduced with inclusion of ionic liquid.

CHAPTER 7

RESULTS AND DISCUSSION OF FOURTH POLYMER BLEND ELECTROLYTES SYSTEM

7.1 Ambient Temperature–Ionic Conductivity Studies

Conductivity data for composite gel polymer electrolytes containing different weight ratios of SiO_2 are presented in Figure 7.1 and Table 7.1. The ionic conductivity increases with SiO_2 loadings, up to 8 wt%. However, above this quantity, the ionic conductivity is decreased slightly. Ionic conductivity increases with amount of SiO_2. This is mainly attributed to higher degree of amorphous in the polymer system. It increases the defects concentration along the SiO_2 particles interface (Saikia and Kumar, 2005). In principle, fumed silica is a hydrophilic compound and prefers to form silanol (Si–OH) bonding on the surface of silicon atom of fumed silica. Formation of hydrogen bonding between SiO_2 grains is favorable with the presence of Si–OH bond, leading to the formation of three–dimensional network when sufficient amount of SiO_2 is embedded into the polymer matrix. Therefore, it imparts high viscosity of polymer electrolytes with addition of SiO_2 (Ahmad *et al*., 2005). However, the TFSI anions which originated from LiTFSI and BmImTFSI interrupt the hydrogen bonding among aggregates via formation of hydrogen bonding of N atoms from TFSI anion with H from the Si–OH bond, as shown in Figure 7.2. The interaction between TFSI anions and SiO_2 reduces the solvation of Li^+ and $BmIm^+$ from LiTFSI and BmImTFSI

respectively, decreasing the viscosity. Therefore, this interaction is readily to dissociate the coordination bond and then promote the ionic transportation within the polymer matrix, which in accordance with high ionic conductivity. The addition of filler inhibits the degree of polymer segmental mobility with formation of nano–particles boundaries. Since the polymer chains can only be arranged to ordered arrangement in order to yield the crystalline structure through segmental movement, hence it increases the amorphous region with restricted polymer segmental mobility (Xie *et al*., 2004).

As shown in Figure 7.1, CPE 4 achieves the highest ionic conductivity of $(4.11\pm0.01)\times10^{-3}$ Scm^{-1} by adding 8 wt% of SiO_2. This value is increased by one order in magnitude compared to SiO_2–free based gel polymer electrolyte (or denoted as IL 6). It can therefore be concluded that the concentration and mobility of charge carriers have reached the optimum level at this composition. The highest ionic conductivity is suggestive of the superior distribution of anions at the filler–ionic liquid interface (Ahmad & Agnihotry 2009). The highest ionic conductivity is also closely related to the formation of nano–sized filler grain boundaries. The nano–particles become more and more packed and initiate the formation of grain boundary with increasing the SiO_2 concentration, which results an additional ionic hopping mechanism. In this theory, it postulates that nano–SiO_2 particles interact with BmImTFSI ionic liquid and form the double layer (also known as space charge layer) through hydrogen bonding. These interfacial layers are claimed as source of electrical field. The distance of inter–particles is decreased as increases SiO_2 loadings and these space charge layers are tend to overlap with each other. At

high SiO_2 filler content, the particles are getting closer to contact with their neighbors and assist to form a continuous interpenetrating of silica grains in the inter–particles region (Osinska *et al*., 2009). As a consequence, a fast and favorable ionic conduction pathway is produced in this region, as demonstrated in Figure 7.3.

Beyond 8 wt% of SiO_2, the volume filling effect dominates over the preferential path of Li^+ when a vast weight fraction of SiO_2 was added into the polymer electrolytes. The ionic motion is hindered with excessive SiO_2 weight composition and contributes to the decreased ionic conductivity for CPE 5 (Ahmad *et al*, 2009). At sufficient large SiO_2 concentration, the decrease in ionic conductivity is also due to the formation of ion aggregates, leading to formation of thick interfacial layer within the grain boundary. Such blocking effect impedes the ionic transportation within the polymer matrix by affecting the effective conducting pathway (Mei *et al*., 2008). Another perspective is the presence of ion association and then leads to formation of neutral ion pairs. The formation of neutral ion pairs decreases the density of free mobile ions and no contribution on the ionic conduction, decreasing the ionic conductivity (Ali *et al*., 2007). Kumar *et al.* (2007) suggest that the viscosity is increased upon inclusion of large mass fraction of SiO_2. It is mainly attributed to the formation of inter–chain and self cross–linking and hence decreases the polymeric chain segmental motion. As a consequence, it hinders the migration of Li^+ ions along the polymer chain which results in the decrement of the conductivity (Kumar *et al*., 2007).

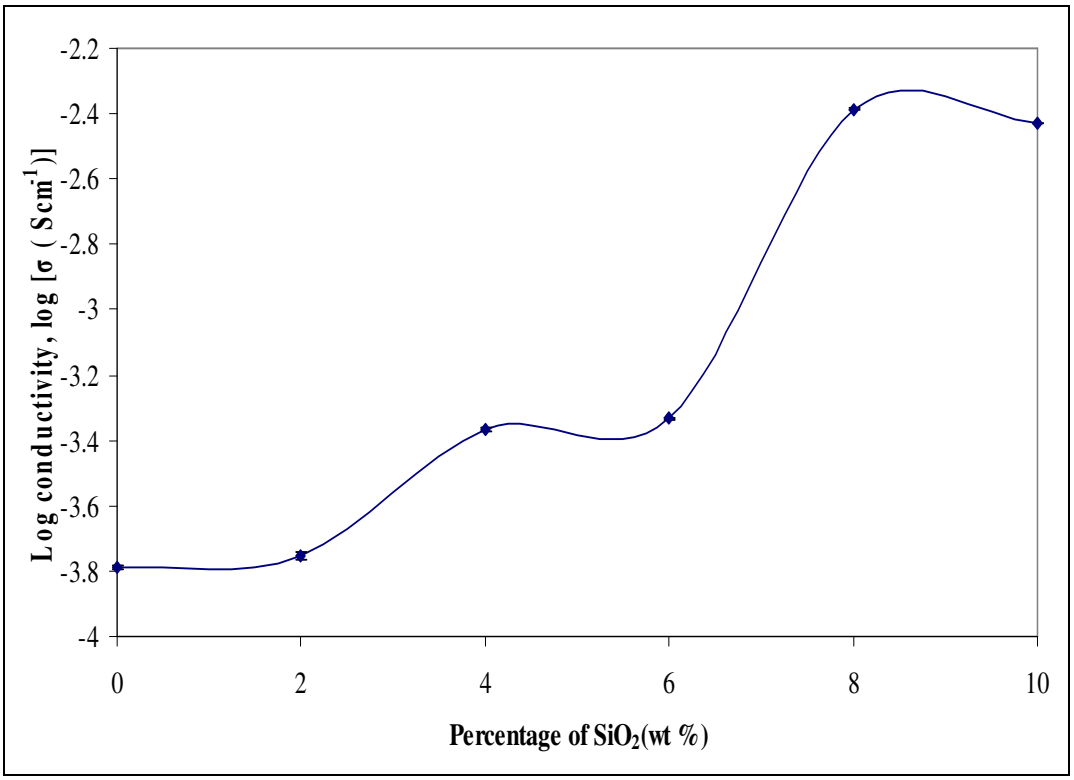

Figure 7.1: **Variation of log conductivity, log σ of nano–sized SiO_2 based composite polymer electrolytes as a function of weight percentage SiO_2 at ambient temperature.**

Composition of (PMMA–PVC–LiTFSI–BmImTFSI):SiO_2 (wt %)	Designations	Ionic conductivity at ambient temperature (Scm^{-1})
100:0	CPE 0	$(1.64\pm0.01)\times10^{-4}$
98:2	CPE 1	$(1.76\pm0.01)\times10^{-4}$
96:4	CPE 2	$(4.28\pm0.01)\times10^{-4}$
94:6	CPE 3	$(4.65\pm0.01)\times10^{-4}$
92:8	CPE 4	$(4.11\pm0.01)\times10^{-3}$
90:10	CPE 5	$(3.73\pm0.01)\times10^{-3}$

Table 7.1: **Ionic conductivities of nano–sized SiO_2 based composite polymer electrolytes and their designations.**

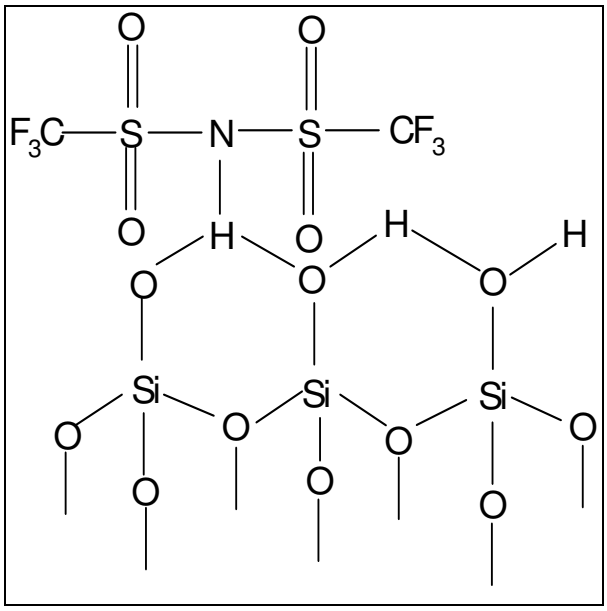

Figure 7.2: Formation of hydrogen bonding between TFSI anions and SiO_2.

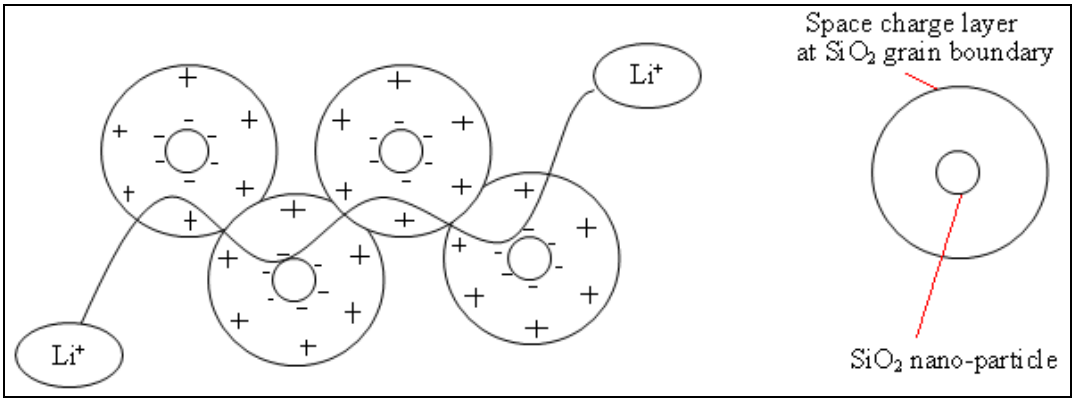

Figure 7.3: Model representation of an effective ionic conducting pathway through the space charge layer of the neighboring SiO_2 grains at the boundaries.

7.2 Temperature Dependence–Ionic Conductivity Studies

Arrhenius plots of ionic conductivity for nano–composite gel polymeric electrolytes are shown in Figure 7.4. Ionic conductivity of CPEs increases with temperature due to the enhancement in ionic mobility (Marcilla *et al*., 2006). By

heating up, the ions have greater freedom of movement and hence favor the ionic transportation in the polymer matrix, which in turn to rise in ionic conductivity (Marcilla *et al*., 2006). In addition, the vibrational mode of the polymer segment is increased and it tends to push against the hydrostatic pressure which is imposed by its surrounding atoms with increasing the temperature. Consequently, voids are formed and these empty spaces aid to increase the segmental and ionic motion in the polymer matrix, which in turns to an increase in ionic conductivity (Rajendran *et al*., 2004).

There is no abrupt change in ionic conductivity for all the samples within the temperature regime. It implies that these samples do not undergo any phase transitions. Among all the samples, IL 6 is expected to exhibit the lowest ionic conductivity. For CPE 1, the ionic conductivity is lower because the amount of fumed silica is insufficient to provide conducting pathway. However, the ionic conductivity increases significantly by embedding SiO_2 further. The explanation is discussed in previous study. As shown in Figure 7.4, CPE 4 achieves the maximum ionic conductivity of (8.26±0.02) $mScm^{-1}$ at 80 °C.

All the samples exhibit Arrhenius behavior as their regression values are close to unity, indicating the ionic hopping mechanism. As discussed earlier, three–dimensional polymer network is formed in the polymer matrix. It tends to weaken the interaction of polar group of the polymer backbone with Li^+. Thus, it promotes the decoupling process of charge carriers from polymer segmental

motion and contributes to formation of vacant sites. As a result, the ions from adjacent sites tend to occupy these neighboring voids and re–coordinate with the polymer backbone.

E_a decreases by incorporating with SiO_2 and it exhibits downshift with further dispersed of SiO_2. CPE 1 shows E_a value of 0.2423 eV, while E_a value of CPE 3 is 0.1780 eV. CPE 4 depicts the lowest E_a value that is around 0.1102 eV. As explained, filler promotes the dissociation of ions via formation of three–dimensional polymer network. Hence, lesser energy is required to break and reform the coordination bond, favoring the ion hopping mechanism. It can therefore be concluded that increase in SiO_2 amount facilitates dissociation of ions and reflects the enhancement of ion transportation, contributing to higher ionic conductivity.

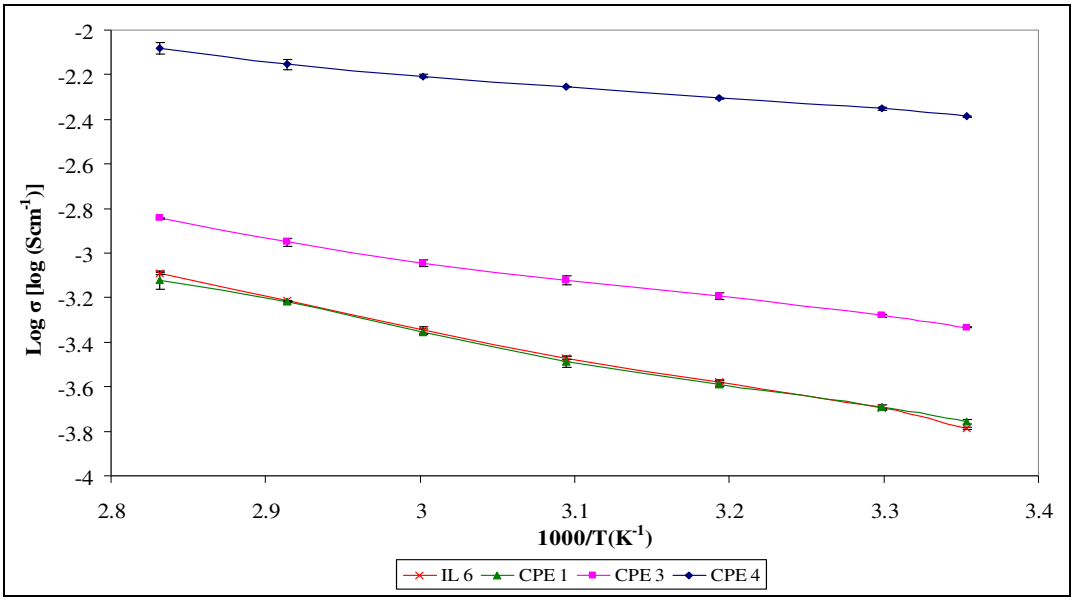

Figure 7.4: Arrhenius plot of ionic conductivity of IL 6, CPE 1, CPE 3 and CPE 4.

7.3 Frequency Dependence–Ionic Conductivity Studies

Three distinct regions are discerned in Figure 7.5. First, the conductivity rises sharply with increasing frequency. In the low frequency region, the conductivity is lower due to its slow periodic reversal of electric field. It therefore induces to the accumulation of charge carriers at the electrode–electrolyte interface and thus decreases the density of free mobile ions which available for ion hopping mechanism. This phenomenon is known as interfacial impedance effect or space charge polarization effect, revealing non–Debye behavior (Ramesh *et al*., 2007). At higher frequency, the rise in conductivity implies that the ionic hopping mechanism obeys Jonsher's universal power law, as shown in Equation 5.1. According to this power law, the ionic hopping mechanism is favorable.

Frequency–independent plateau region is attained thereafter. This signifies that the conductivity is equal to the bulk conductivity of polymer electrolytes (Venkateswarlu *et al*., 2007). The conductivity is decreased sequentially in third phase. It is evocative of the formation of electrical double layer. The TFSI anions travel much faster due to high periodic reversal of applied electric field and lead to rapid interaction of TFSI anions with SiO_2 through hydrogen bonding. These high interactions are associated with the formation of thick interfacial layer between the grain boundaries and decreased the ionic conductivity. The formation of electrical double layer is also attributed to adsorption of complex aggregates of the constituents in the polymer matrix (Sengwa *et al*., 2009).

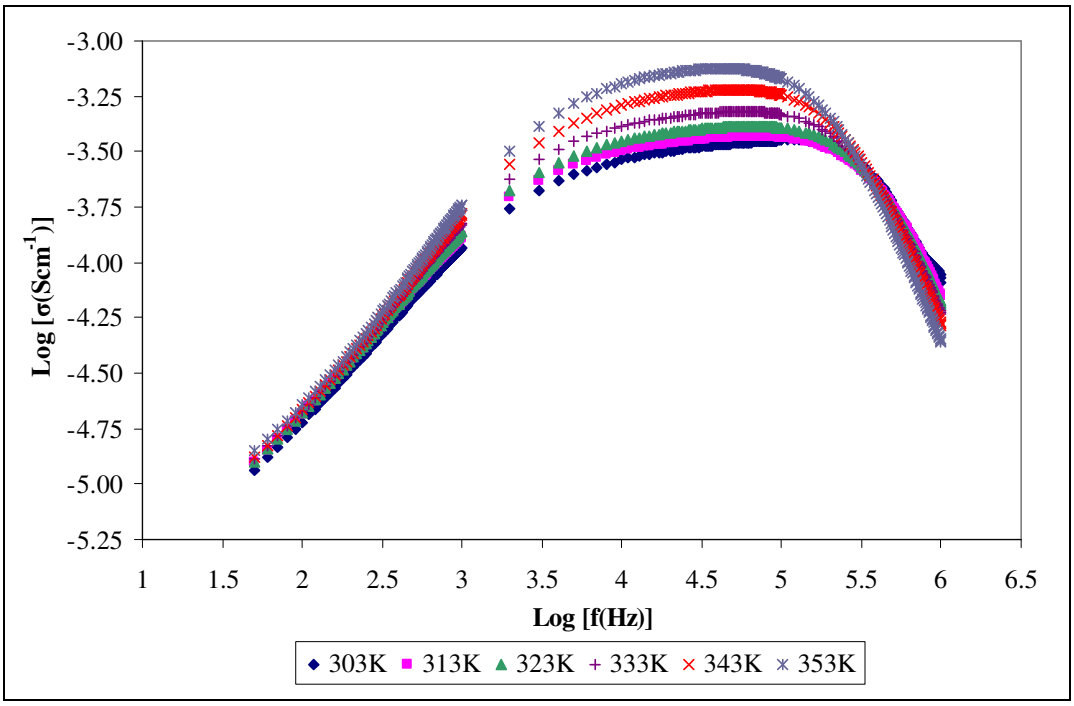

Figure 7.5: Frequency dependent conductivity for CPE 4 in the temperature range of 303–353 K.

7.4 Dielectric Relaxation Studies

The variation of dielectric constant (ε') and dielectric loss (ε'') with respect to frequency are depicted in Figures 7.6 and 7.7, respectively. No noticeable relaxation peak is discovered within the frequency regime in both figures. Both real and imaginary parts of dielectric constants increase significantly at low frequency. This arises from the electrode polarization and space charge effects, which contributes to localization of charge carriers. It is further proven the occurrence of non–Debye characteristic. In this behavior, the space charge region as a function of frequency is explained in terms of ion diffusion. Ions travel much slower due to the slower periodic reversal of the applied electric field. It can

therefore be seen that the free mobile ions tend to build up at the electrolyte–electrode interface and then initiate the polarization, forming space charge region at the interface (Baskaran *et al*., 2006a; Khiar *et al*., 2006; Ramesh *et al*., 2007).

On the other hand, the values of both dielectric permittivity and dielectric loss are much lower at high frequency. It is mainly attributed to the fast periodic reversal of the electric field, which results the absence of ion diffusion in the direction of electric field. Consequently, it decreases the ionic polarization and leads to the decrement of both dielectric constants at high frequency (Baskaran *et al*., 2006a; Ramesh *et al*., 2007). Higher ε' value is obtained at high temperature due to high salt dissociation. This prevents the ions association and readily to perform re–dissociation of ion aggregation with increasing temperature. This implies that the higher amounts of charge carrier is gathered at the space charge region and thereby increased in the equivalent capacitance (Baskaran *et al*., 2006a).

Large apparent values of ε'' are observed at low frequency. It infers that free charge carriers require some relaxation times to build up the space charge region at the electrolyte–electrode interface before the field changes the direction of electric field (Baskaran *et al*., 2006a). Moreover, ε'' increases with temperature. As temperature is increased, the thermal movement of free charge carriers is improved. So, the accumulation of ions is easy to be happened. Again, another attributor is the high degree of salt dissociation and re–dissociation of ion aggregates.

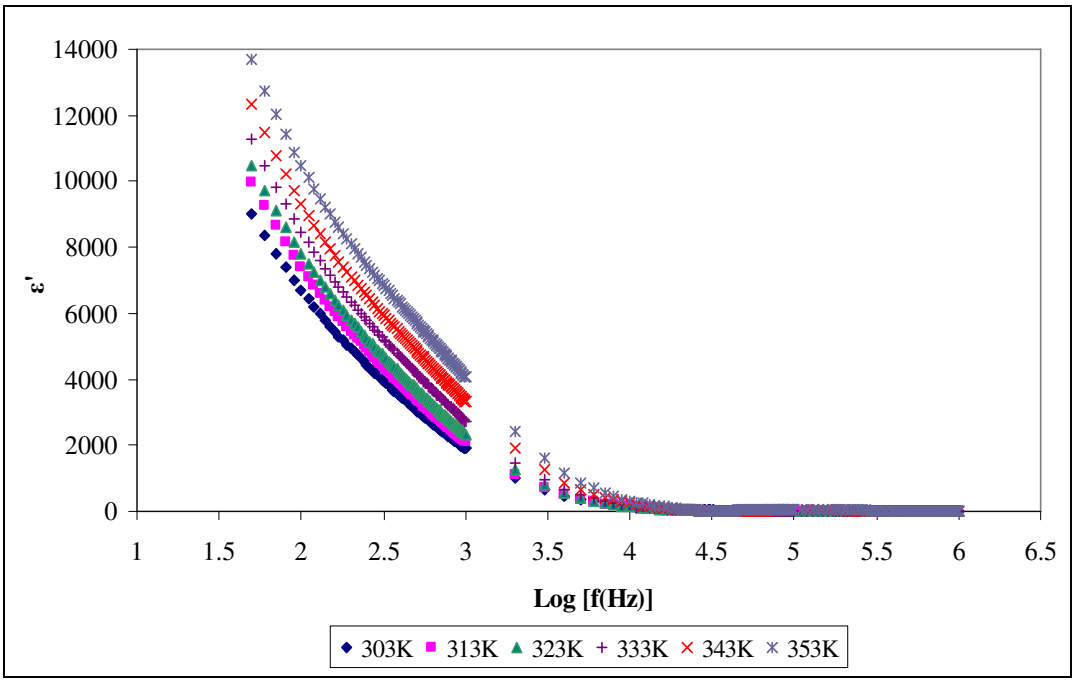

Figure 7.6: **Typical plot of the variation of real part of dielectric constant (ε') with frequency for CPE 4 in the temperature range of 303–353 K.**

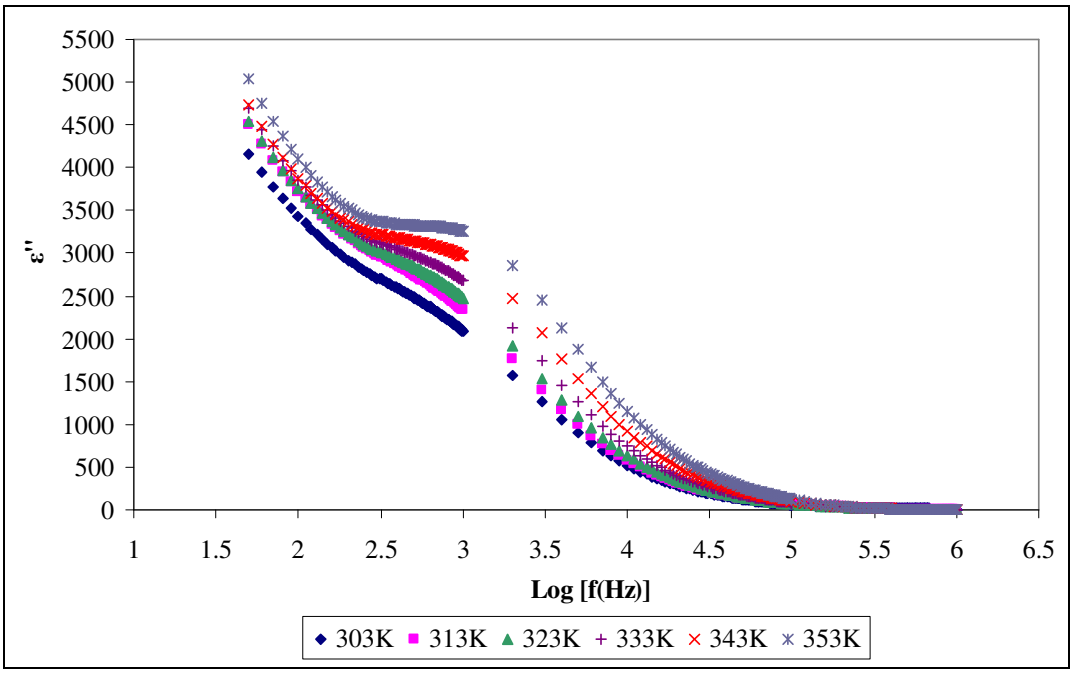

Figure 7.7: **Typical plot of the variation of imaginary part of dielectric constant (ε'') with frequency for CPE 4 in the temperature range of 303–353 K.**

7.5 Dielectric Moduli Studies

The dielectric modulus parameter is well known to represent the bulk dielectric behavior of the polymer electrolytes because of the elimination of polarization effect (Ramesh *et al*., 2007). Real ($M^{'}$) and imaginary ($M^{''}$) parts of dielectric moduli as a function of frequency are shown in Figures 7.8 and 7.9, respectively. These values approach to zero at low frequency and signify the suppression of electrode polarization effect. The long tail denotes the large extent of capacitance associated with electrodes (Ramesh *et al*., 2007). An obvious observation is examined for real part of dielectric modulus at high frequency. The dielectric modulus response shows the superposition characteristic in the same temperature range. This implies the temperature–independent of real dielectric modulus of CPE 4 at high frequency and suggests that CPE 4 exhibits excellent electrochemical stability (Suthanthiraraj *et al*., 2009). Even though well–defined relaxation peak is not observed in both figures; however it shows the intense increase at high frequency region. The curve peaks indicate the bulk effect in the polymer matrix and further infer that the polymer electrolytes are in ionic conducting mechanism. The intensity of these peaks decreases with increasing temperature due to the plurality of relaxation mechanism.

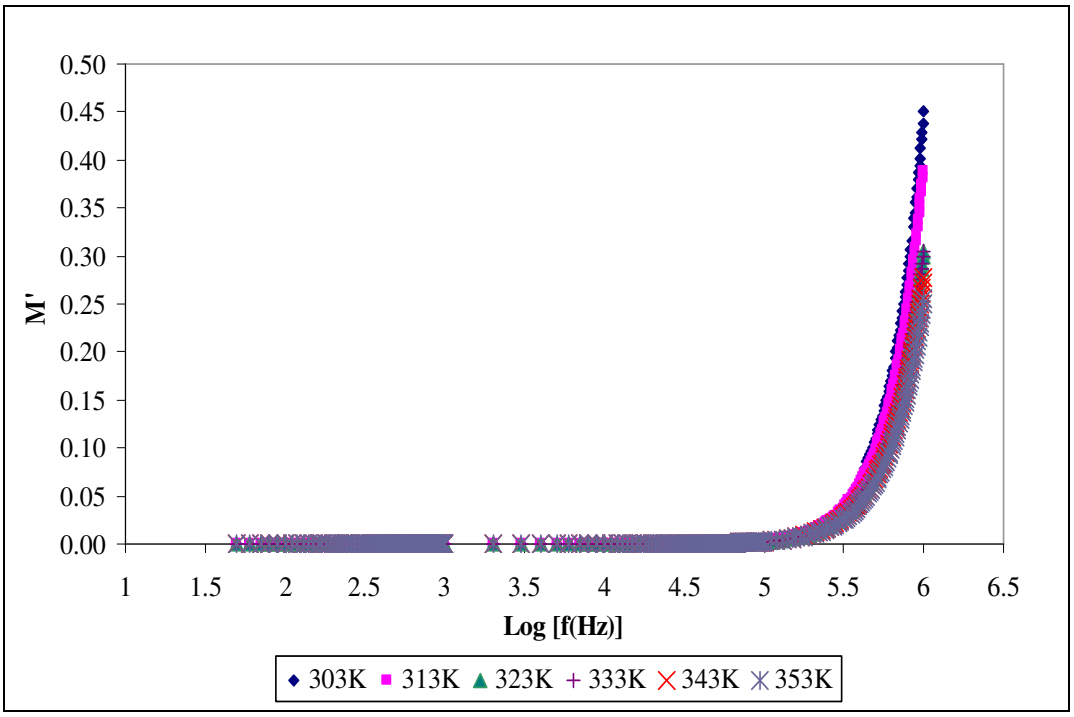

Figure 7.8: **Variation of real modulus ($M^{'}$) as a function of frequency for CPE 4 in the temperature range of 303–353 K.**

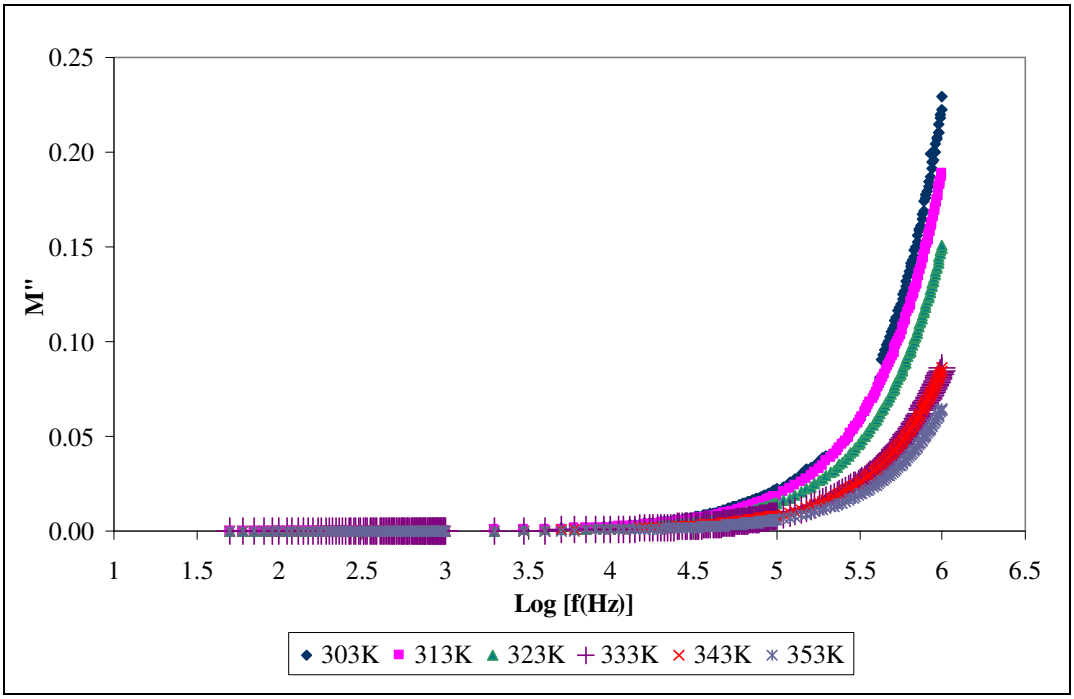

Figure 7.9: **Variation of imaginary modulus ($M^{''}$) as a function of frequency for CPE 4 in the temperature range of 303–353 K.**

7.6 HATR–FTIR studies

HATR–FTIR spectra of pure SiO_2, CPE 1, CPE 3 and CPE 4 are shown in Figure 7.10(a)–(d). The combination of HATR–FTIR spectra of IL 6, pure SiO_2, CPE 1, CPE 3 and CPE 4 is depicted in Figure 7.11. The HATR–FTIR spectrum of CPE 4 is discussed in details as it achieves maximum ionic conductivity. All of the descriptions of the vibrational modes for this polymer electrolyte are tabulated in Table 7.2. The changes in shift, changes in shape and changes in intensity are examined in order to confirm the complex mode between SiO_2 and polymer matrix. Regarding to the changes in shift, most of the vibrational modes manifest downward shifts. The characteristic peaks at 963 cm^{-1} and 985 cm^{-1} are defined as C–O symmetric stretching mode in C–O–C linkage of PMMA and CH_2 wagging mode of PMMA, respectively. For first peak, it shifts from 966 cm^{-1} to 963 cm^{-1}, whereas it is shifted from 988 cm^{-1} for latter peak, asserting the interaction between PMMA and SiO_2. An apparent shift is also observed. The combination of CH_3 asymmetric bending mode of PMMA and C–H stretching mode of CH_2 group of PVC shifts from 1452 cm^{-1} to 1436 cm^{-1} and thereby indicates the establishment of interaction of PMMA, PVC and SiO_2.

As explained in ac–impedance studies, the interaction between BmImTFSI and SiO_2 filler disrupts the hydrogen bonding among SiO_2 aggregates and this is being verified in the study. CH_3 symmetric stretching mode of BmImTFSI and CH_2 stretching mode of BmImTFSI shift from 1461 cm^{-1} to 1441 cm^{-1} and 2963 cm^{-1} to 2952 cm^{-1}, respectively. C–H vibrational modes for cyclic $BmIm^+$ of

BmImTFSI at 3119 cm^{-1} and 3156 cm^{-1} are shifted from 3121 cm^{-1} and 3157 cm^{-1}, respectively. The shift of S–CH_3 bonding mode of TFSI anions from 2880 cm^{-1} to 2851 cm^{-1} divulges the interaction between SiO_2 and $TFSI^-$. Pure SiO_2 illustrates a broad and sharp peak at 3448 cm^{-1} and it is assigned as O–H stretching vibrations of surface hydroxyl group of SiO_2. However, it is disappeared in CPE 4 spectrum. It might be due to the overlapping with N–H stretching mode of BmImTFSI which located at 3583 cm^{-1}, leading to a formation of a new broad band at 3620 cm^{-1} in CPE 4 spectrum. This is reminiscent of the hydrogen bonding between N atom of TFSI anions and Si–OH of surface hydroxyl group of fumed silica, as shown in Figure 7.2. On the other hand, the characteristic peak at 700 cm^{-1} which assigned as combination of cis wagging mode of PVC and C–H vibrational mode for cyclic $BmIm^+$ is shifted upward, from 698 cm^{-1} to 700 cm^{-1}.

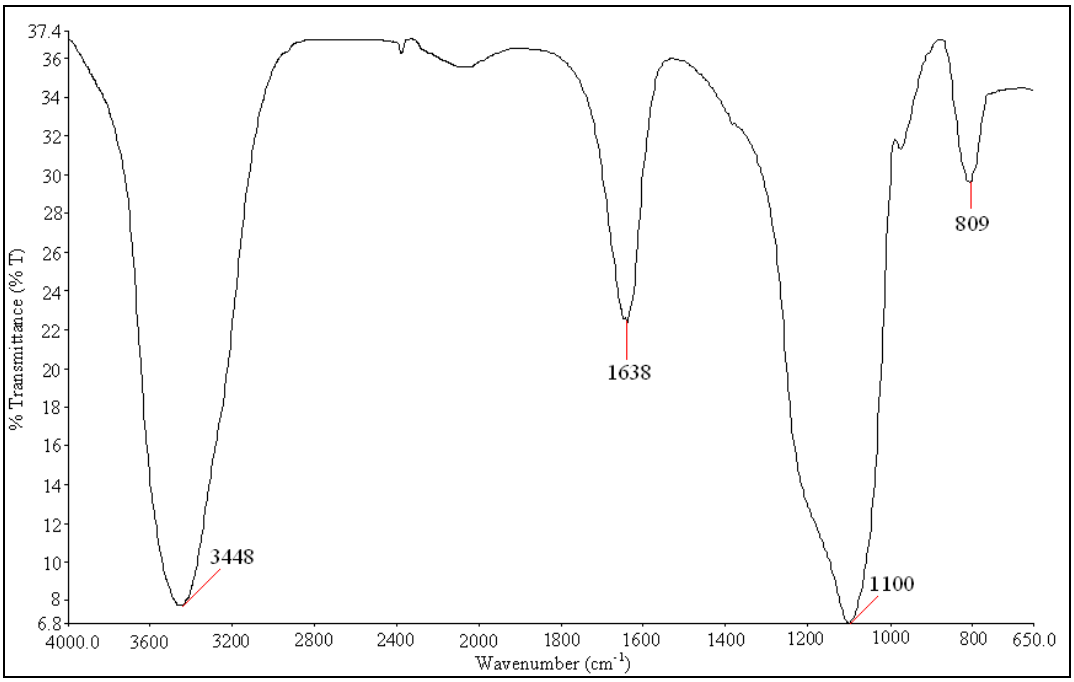

Figure 7.10 (a): HATR–FTIR spectrum of pure SiO_2.

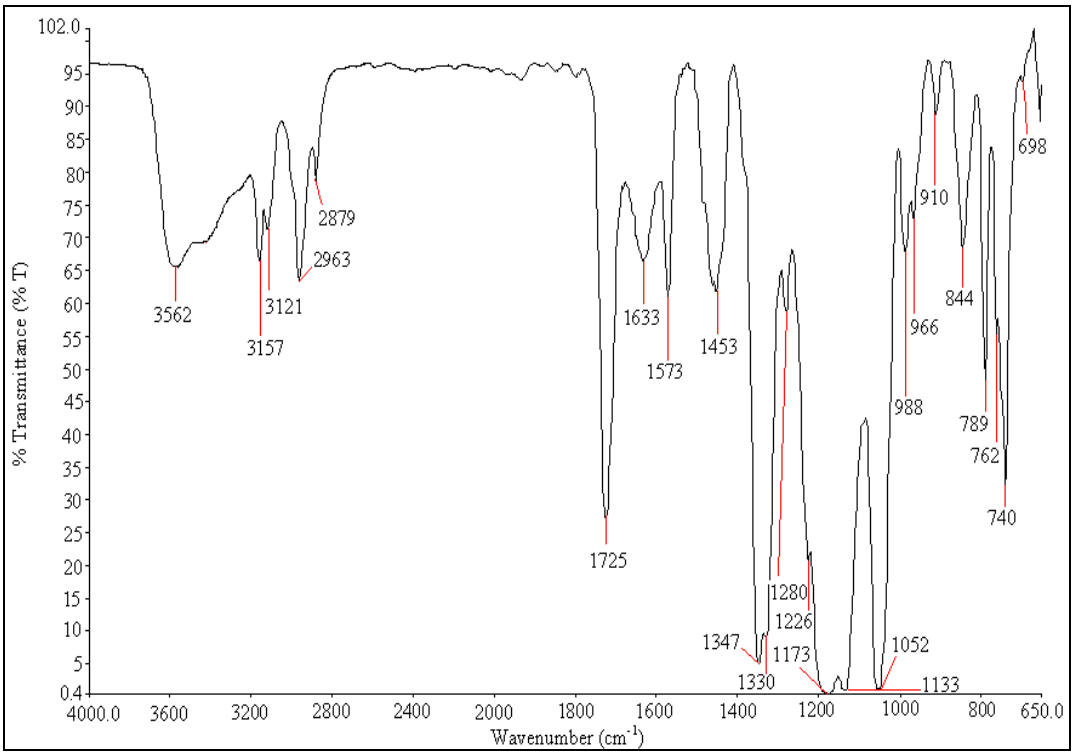

Figure 7.10 (b): HATR–FTIR spectrum of CPE 1.

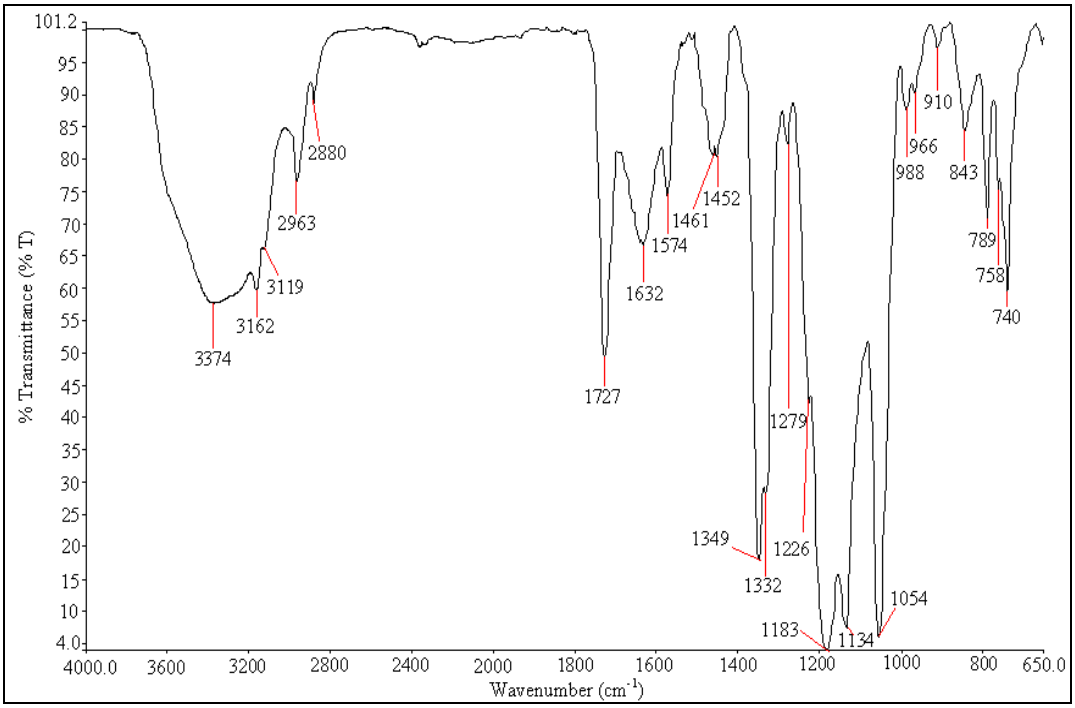

Figure 7.10 (c): HATR–FTIR spectrum of CPE 3.

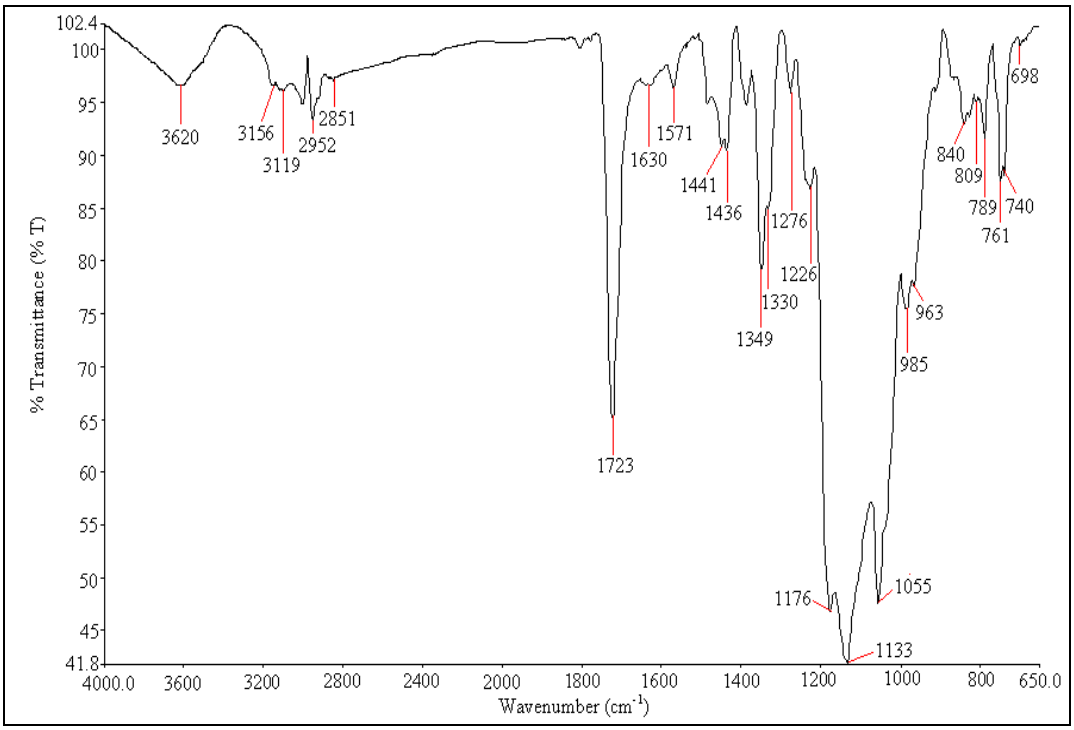

Figure 7.10 (d): HATR–FTIR spectrum of CPE 4.

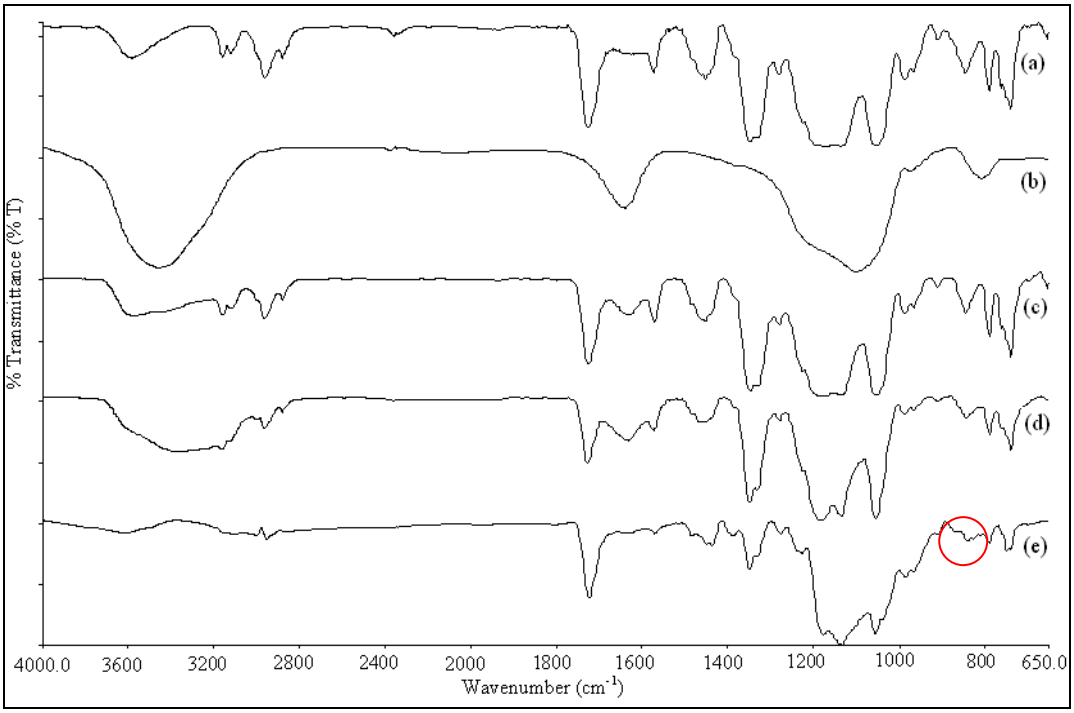

Figure 7.11: Combination of HATR–FTIR spectra for (a) IL 6, (b) pure SiO_2, (c) CPE 1, (d) CPE 3 and (e) CPE 4.

Descriptions of vibration modes	Wavenumber (cm^{-1})	Reference
Combination of cis C–H wagging mode of PVC and C–H vibrational mode for cyclic $BmIm^+$ of BmImTFSI	698	Achari *et al*., 2007; Jiang *et al*., 2006
Combination of CH_2 rocking mode of PVC and S–N stretching mode of LiTFSI	740	Ahmad *et al*., 2008; Rajendran *et al*., 2008
CF_3 symmetric bending mode of BmImTFSI	761	Bazito *et al*., 2007
Combination of C–S and S–N stretching mode of LiTFSI and BmImTFSI	789	Ahmad *et al*., 2008
Characteristic peak of SiO_2	809	Ramesh and Lu, 2008
C–Cl stretching mode of PVC	840	Rajendran *et al*, 2008
Trans C–H wagging mode of PVC		Achari *et al*., 2007
C–O symmetric stretching mode in C–O–C linkage of PMMA	963	Achari *et al*., 2007
CH_2 wagging mode of PMMA	985	Rajendran *et al*, 2002
S–N–S asymmetric stretching mode of LiTFSI and BmImTFSI	1055	Ahmad *et al*., 2008
Combination of C–O–C asymmetric stretching mode of PMMA, C–SO_2–N bonding mode of LiTFSI and BmImTFSI and Si–O–Si of SO_2	1133	Jiang *et al*., 2006; Ramesh and Lu, 2008
Combination of CH_2 twisting mode of PMMA, CF_3 symmetric stretching mode of LiTFSI and C–H vibrational mode for cyclic $BmIm^+$ of BmImTFSI	1176	Achari *et al*., 2007; Ahmad *et al*., 2008; Jiang *et al*., 2006
N–H stretching mode of BmImTFSI	1226	Bazito *et al*., 2007
C–O–C symmetric stretching mode of PMMA	1276	Jiang *et al*., 2006
C–SO_2 –N bonding mode of LiTFSI and BmImTFSI	1330	Ramesh and Lu, 2008
SO_2 asymmetric stretching mode of LiTFSI and BmImTFSI	1349	Ahmad *et al*., 2008
Combination of CH_3 asymmetric bending mode of PMMA, C–H stretching mode of CH_2 group of PVC	1436	Rajendran *et al*, 2008
CH_3 symmetric stretching mode of BmImTFSI	1441	Jiang *et al*., 2006

C–C and C–N bending mode of BmImTFSI	1571	Jiang *et al*., 2006
Combination of C=C stretching mode of PVC and O–H deformation vibrations of surface hydroxyl group of SiO_2	1630	Achari *et al*., 2007
C=O stretching mode of PMMA	1723	Li *et al*., 2006a
S–CH_3 bonding mode of LiTFSI and BmImTFSI	2851	Ramesh and Lu, 2008
CH_2 stretching mode of BmImTFSI	2952	Jiang *et al*., 2006
C–H vibrational mode for cyclic $BmIm^+$ of BmImTFSI	3119, 3156	Jiang *et al*., 2006
Combination of N–H stretching mode of BmImTFSI and O–H stretching vibrations of surface hydroxyl group of SiO_2	3620	Jiang *et al*., 2006

Table 7.2: Assignments of vibrational modes of PMMA, PVC, LiTFSI, BmImTFSI and SiO_2 for CPE 4.

Figure 7.12 illustrates the evidence of change in intensity of C=O stretching mode of PMMA. The intensity of peak reduces by 23.25 %, from 56.43 % to 33.18 %, in transmittance mode. In addition, it shifts downward slightly, that is from 1725 cm^{-1} to 1723 cm^{-1}. Similar observation is attained for C–O–C symmetric stretching mode at 1276 cm^{-1}. This characteristic peak is shifted from 1281 cm^{-1} to 1276 cm^{-1} and its intensity is decreased by 3.57 % in transmittance mode, from 8.57 % to 5 %. This signifies the interaction of PMMA with SiO_2 and thereby initiates the ion transportation by decoupling the Li^+ from the coordination bond with C=O of PMMA. Visible changes in intensity are noticed at 1055 cm^{-1} and 1571 cm^{-1}. First peak is assigned as S–N–S asymmetric stretching mode of LiTFSI and BmImTFSI. In terms of peak intensity, it decreases by 30.32 % in transmittance mode, from 47.14 % to 16.82 %. It has also been shifted from 1053 cm^{-1}. These changes further reveal the hydrogen bonding between N atoms of TFSI anions and Si–OH on the surface of nano–sized filler. Combination of C–C

and C–N bending mode of BmImTFSI shifts from 1574 cm^{-1} to 1571 cm^{-1}. Around 15.06 % of decrease in intensity is attained and it is shifted from 16.42 % to 1.36 %, in transmittance mode. Even though the wavenumber of combination of C–S and S–N stretching mode of LiTFSI and BmImTFSI still remains at 789 cm^{-1}, however, the peak intensity reduces by 22.59 %, from 27.14 % to 4.55 % in transmittance mode.

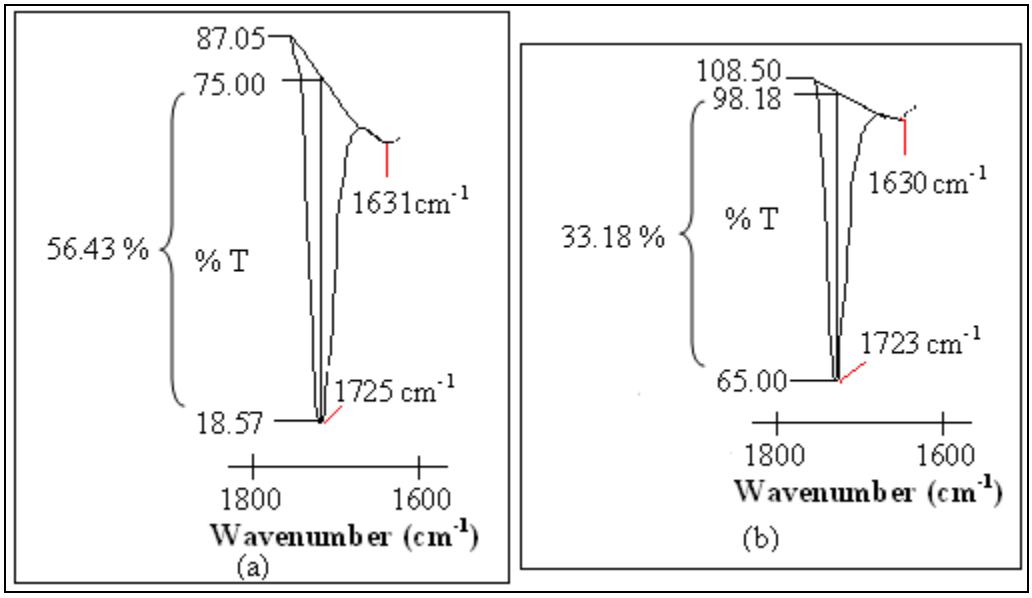

Figure 7.12: The comparison of change in intensity of C=O stretching mode of PMMA in (a) IL 6and (b) CPE 4.

Some facts of changes in shape have been shown in comparing IL 6 and CPE 4. The assignment for the characteristic peak at 738 cm^{-1} is combination of CH_2 rocking mode of PVC and S–N stretching of LiTFSI. On the other hand, the CF_3 symmetric bending mode of BmImTFSI is placed at 748 cm^{-1}. Both of these peaks demonstrate downward shifts. The first peak shifts from 740 cm^{-1}, whereas 761 cm^{-1} is for latter peak. These two peaks possess some obvious changes in shape that is from a sharp peak with shoulder to two weak peaks, revealing the

interaction between PVC, LiTFSI, BmImTFSI and SiO_2. C–Cl stretching mode of PVC is not only shifted from 845 cm^{-1} to 840 cm^{-1}, but it also has been changed from a sharp peak to a weak peak. A new resolved peak is appeared at 809 cm^{-1} and assigned as characteristic peak of SiO_2, as highlighted in Figure 7.11 (c). A noticeable change is observed for C=C stretching mode of PVC at the wavenumber of 1630 cm^{-1}. A medium sharp peak has been changed to a less intense broad band. It might be due to the overlapping effect of O–H deformation vibrations of surface hydroxyl group of SiO_2 with this stretching mode. This broad band is further implied the lower crystallinity of sample with addition of 8 wt% of SiO_2 as a broad peak is an indicative of low crystalline structure of polymer electrolyte (Suthanthiraraj *et al*., 2009).

The bands in the wavenumber range of 1400 cm^{-1}–1100 cm^{-1} are explored in order to investigate the ion aggregation further. Two important peaks are obtained in the region of 1200 cm^{-1}–1100 cm^{-1}. The first peak is assigned as combination of C–O–C asymmetric stretching mode of PMMA, C–SO_2–N bonding mode of LiTFSI and BmImTFSI at 1133 cm^{-1}, whereas combination of CH_2 twisting mode of PMMA, CF_3 symmetric stretching mode of LiTFSI and C–H vibrational mode for cyclic $BmIm^+$ of BmImTFSI is assigned at 1176 cm^{-1}. The downward shift of first peak from 1140 cm^{-1} to 1133 cm^{-1}, might be due to the contribution of Si–O–Si bonding of SiO_2 at 1100 cm^{-1}. This indicates that the TFSI anions favor to interact with silica and thus promote the decoupling of Li^+ and $BmIm^+$ from doping salt and ionic liquid. Eventually, it induces to higher ionic conductivity. On the other hand, the second peak exhibits upward shift from 1168

cm^{-1} to 1176 cm^{-1}. Based on these two peaks, the obvious change in shape is obtained as shown in Figure 7.13. This figure illustrates that a broad band is changed to two sharp peaks.

The HATR–FTIR spectra of CPE 1, CPE 3 and CPE 4 are compared in order to prove the highest ionic conductivity of CPE 4. At 809 cm^{-1}, the characteristic peak of SiO_2 is absent in CPE 3 and CPE 4 spectrum. Two weak peaks should be shown in the region 1500 cm^{-1}–1400 cm^{-1}. However, there is only a peak has been shown in this range for CPE 1. The peak which designated as combination of CH_3 asymmetric bending mode of PMMA, C–H stretching mode of CH_2 group of PVC is absent. On the other hand, a weak peak which assigned as combination of cis C–H wagging mode of PVC and C–H vibrational mode for cyclic $BmIm^+$ of BmImTFSI is also absent in CPE 3 spectrum. Other assignments are present in both spectra. As shown in Figure 7.11, the intensity of peak is increased as increases amount of SiO_2 by comparing CPE 1, CPE 3 and CPE 4. This suggests the formation of grain boundaries between the aggregates with excessive SiO_2 nano–particles and contributes to higher polarity of the polymer matrix. It can therefore be seen that higher bond energy is obtained and hence forms more intense absorption peak in this region.

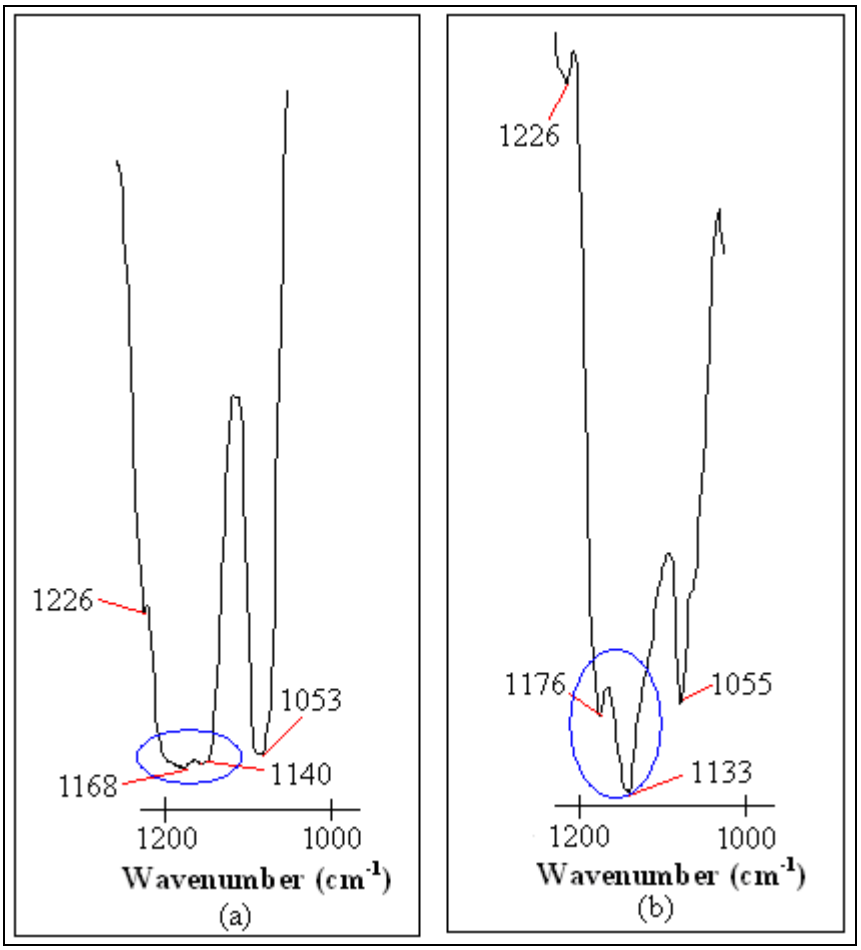

Figure 7.13: The comparison of change in shape of the vibrational modes in the wavenumber region of 1200 cm^{-1}–1000 cm^{-1} for (a) IL 6 and (b) CPE 4.

Viscosity is another attributor for the increase in ionic conductivity for CPE 4, as explained in ac–impedance study. This factor can be proven in HATR–FTIR study in the wavenumber region of 1400 cm^{-1}–1100 cm^{-1}. Two peaks are observed in this range. First peak at 1330 cm^{-1} is assigned as C–SO_2–N bonding mode of LiTFSI and BmImTFSI, whereas SO_2 asymmetric stretching mode of LiTFSI and BmImTFSI is for the characteristic peak at 1349 cm^{-1}. The wavenumber for first peak remains the same, however, the latter peak shifts from 1346 cm^{-1} to 1349 cm^{-1}, asserting the TFSI anions with SiO_2. As shown in Figure

7.11, the intensity of peak decreases with increasing SiO_2 concentration. It can therefore be concluded that CPE 4 has lowest viscosity. As increases the composition of SiO_2, the interaction between BmImTFSI and polymer matrix becomes lesser as the interaction between BmImTFSI and SiO_2 is more favorable. As a result, the entanglements within polymer matrix are lesser and lead to lower viscosity of polymer electrolytes.

7.7 XRD Studies

XRD analysis has been performed, and their respective diffraction patterns of IL 6, CPE 1, CPE 3 and CPE 4 are shown in Figures 7.14 (a)–(d). Apparently, the change in shape is observed, from a broad peak with a shoulder to a new broad peak upon inclusion of SiO_2, as shown in Figure 7.14. The disappearance of shoulder is insinuative of an increase in amorphous behavior of polymer electrolytes, which is primarily due to the formation of polymeric network. It deteriorates the ordered arrangement of polymer matrix, promotes the segmental mobility of polymer chain and favors the ionic transportation as discussed in ionic conductivity studies. The peak is slightly shifted upon dispersion of SiO_2. The broad peak at Bragg angle of $2\theta=18.5°$ is shifted to $2\theta=18°$, indicating the complexation between the SiO_2 and polymer matrix (Kumar *et al*., 2007). Another noticeable observation is obtained for CPE 3 and CPE 4. The peak of CPE 4 is much broader than CPE 3 infers that the CPE 4 has higher amorphous behavior than CPE 3, ultimately leads to improvement of the ion diffusivity in accordance

with higher ionic conductivity.

In addition, coherent length study is carried out to examine the crystallite size in the polymer matrix. Based on Debye–Scherrer equation, the broader the diffraction peak width, the shorter of crystallite size is, contributing to the lower crystallinity in the polymer matrix (Aravindan *et al*., 2009). Therefore, the coherent length decreases with increasing SiO_2 amount, as illustrated in Figure 7.15. As explained above, inclusion of SiO_2 forms three–dimensional network among aggregates and contributes to the distortion of the arrangement of polymer matrix. Hence, it leads to development of amorphous region. In general, the segmental mobility and flexibility of polymer backbone are enhanced in amorphous phase and this promotes ionic transportation, reflecting the higher ionic conductivity.

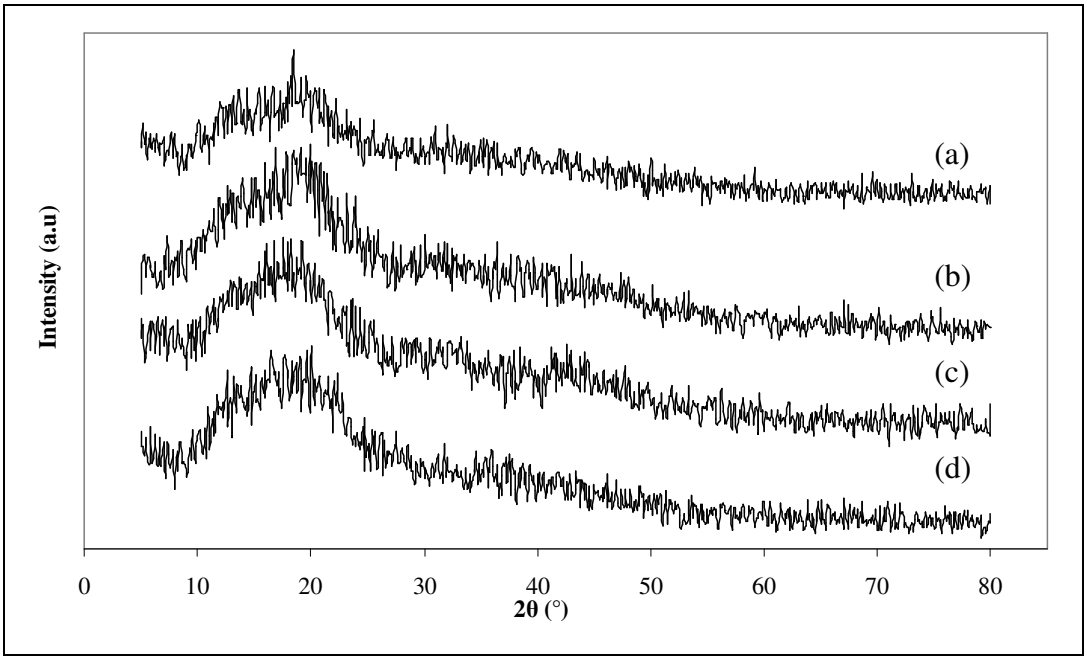

Figure 7.14: XRD patterns of (a) IL 6, (b) CPE 1, (c) CPE 3 and (d) CPE 4.

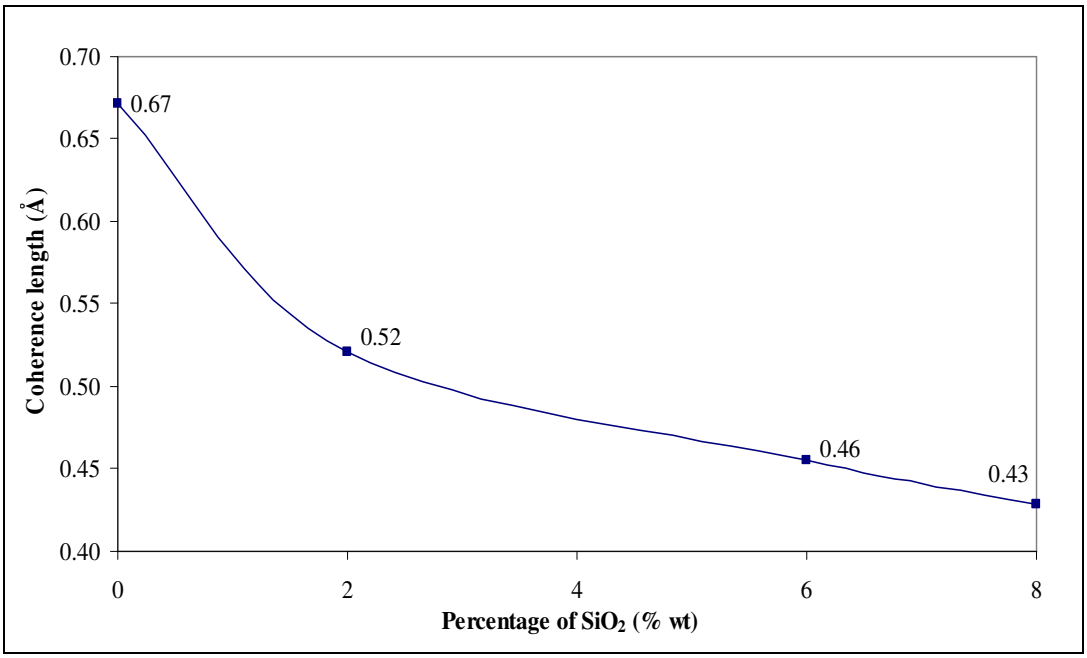

Figure 7.15: Variation of coherence length at ambient temperature with respect to different mole fraction of SiO_2 in the nano–composite polymer electrolytes at $2\theta \approx 18°C$.

7.8 SEM Studies

The morphologies of all CPEs are illustrated in Figure 7.16 (a)–(c). Indeed, the morphology of polymer electrolytes is totally altered upon addition of SiO_2. The spherulites in the IL 6 are suddenly disappeared and the appearances of CPEs are being transformed into a wavy type surface morphology. This wavy type appearance reveals the pre–dominant amorphous region in the polymer electrolytes by destroying the crystallinity portion among the polymer matrix, along with further disruption of interaction among the polymer side chain. The blackish cavities infer the presence of ion transfer in the polymer electrolytes, as shown in Figures 7.16 (a)–(c). As discussed earlier, the occurrence of black cavity is an

evidence for ionic transportation in the polymer matrix. Comparing CPE 1 and CPE 3, CPE 3 has more black cavities than CPE 1. Therefore, it could be concluded that the ion hopping mechanism of CPE 3 is more favorable than CPE 1. It is mainly due to SiO_2 is in excess mode for CPE 3 and hence promotes the ionic migration in the nano–composite polymer electrolyte. In contrast, the ion mobility of CPE 1 does not reaches the desired level as little amount of SiO_2 is added into the polymer electrolyte.

Some fine and tiny white sphericals are obtained in Figure 7.16 (c) is evocative of the dispersion of SiO_2 nano–particles. The diameter of the sphericals is within the range of 0.1 μm instead of nano–sized. This reveals the aggregations among the nano–sized particles via hydrogen bonding on the surface of silica atoms. Figure 7.16 (c) shows that the size of cavities is also distinctively increased. Typically, it might be due to the formation of three–dimensional network as a result of the hydrogen bonding among aggregates. This creates some entrapments within polymer matrix. So, large volumes of filler and gel electrolytes are being entrapped in the cavities and hence, it accounts for the highest ionic conductivity by enhancing the ionic migration among the polymer matrix.

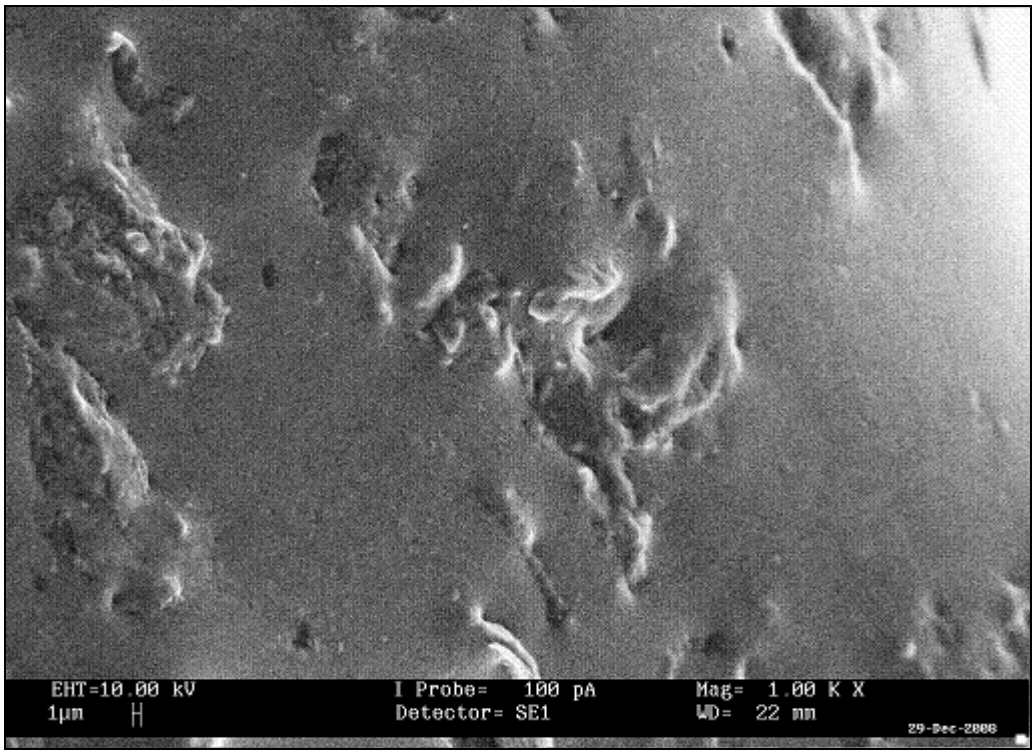

Figure 7.16 (a): SEM images of CPE 1.

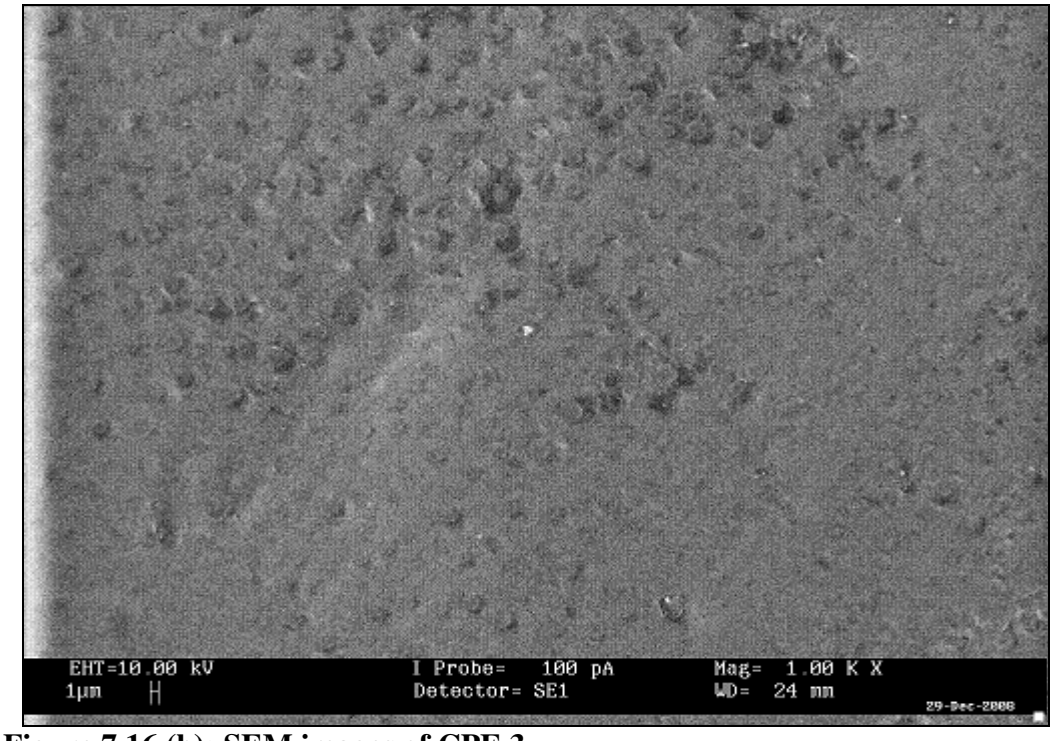

Figure 7.16 (b): SEM images of CPE 3.

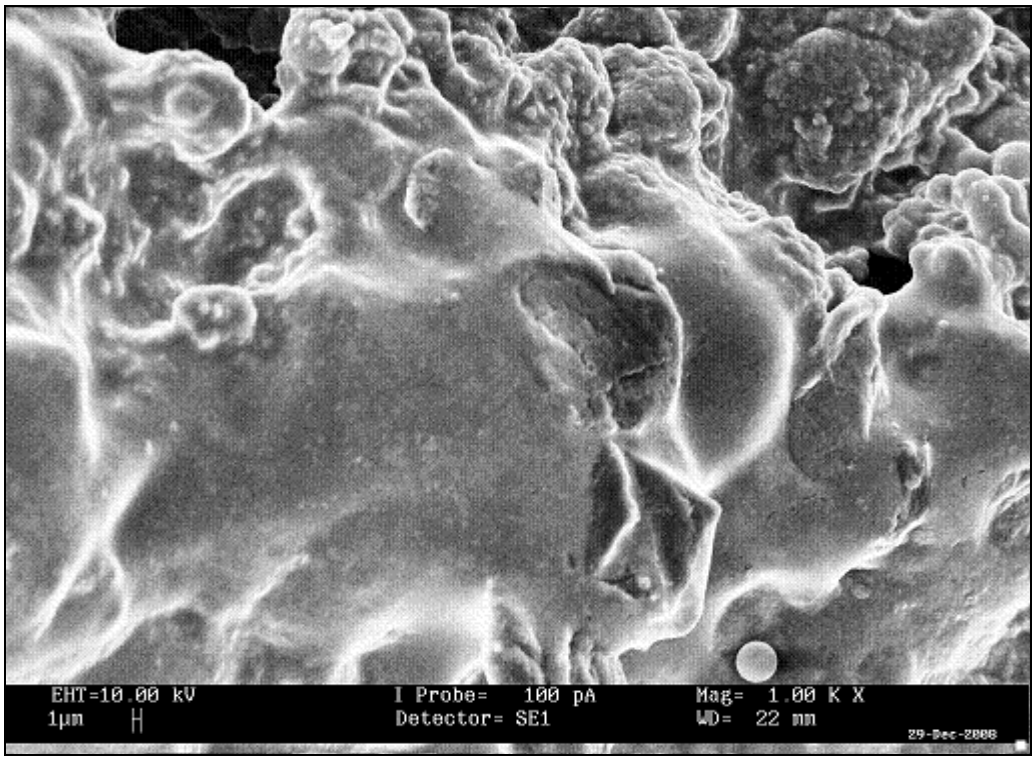

Figure 7.16 (c): SEM images of CPE 4.

7.9 DSC Studies

DSC traces of all the CPEs samples are depicted in Figure 7.17 and tabulated in Table 7.3. Same trends of all DSC profiles are clearly observed. Initially, a small change in heat flow from exothermic reaction to endothermic reaction and it is commonly assigned as glass transition temperature (T_g). A gradual decrease in heat flow of polymer matrix is tagged along, up to above 151 °C. A weak endothermic peak is then observed and it is known as melting point of the polymer electrolytes, T_m. Two consecutive peaks are observed thereafter and they are defined as decomposition temperatures of polymer electrolytes, T_d. The

first endothermic decomposition peak is originated from the dehydrochlorination of PVC, as explained in section 4.10 (Ahmad *et al*., 2006b). On the other hand, the second endothermic peak is ascribed to the breakdown of unsaturated group of PMMA such as carbonyl functional group and degradation of PVC (Ahmad *et al*., 2006a).

A slight downward shift in T_g from 112 °C for IL 6 to 109 °C for CPE 4 reveals that the amorphous proportion increases with the mass fraction of fumed silica. The shift towards lower temperature indicates the softening effect in the polymer matrix and thus enhances the segmental motion of polymer backbone (Ramesh and Arof, 2001b). This suggests that the formation of three–dimensional network among aggregates has interrupted the coordination bond in the polymer matrix and formed more flexible polymer backbone. It can therefore be seen that the ionic migration is enhanced after impregnation of SiO_2 by weakening the coordination bonding within the polymer matrix.

T_m also exhibits same feature as T_g . As quantity of SiO_2 increases, it is further decreased. T_m decreases from 157 °C (IL 6) to 152 °C (CPE 4) as shown in Figure 7.17. Indeed, more asymmetric endothermic meting peaks are being depicted in the DSC thermogram. This divulges the decrease in crystalline degree or increase in amorphous region of both polymer electrolytes (Pandey *et al*., 2009). The amorphous nature of polymer electrolytes accelerates the segmental mobility and ionic transportation in the electrolytes, which results high ionic conductivity.

Lower T_m evolves with smaller peak area (or known as lower of heat of fusion) is illustrated with increasing the mass fraction of fumed silica. This further indicates the increase in amorphous proportion in polymer electrolytes. As explained, formation of three–dimensional network disrupts the ordered arrangement within polymer matrix and forms more flexible backbone and voids within the polymer matrix. As a result, it improves the ion hopping process. This result is in good agreement with XRD and SEM analyses.

Two endothermic decomposition peaks are sequentially observed. An apparent characteristic is obtained for T_d : the decomposition temperatures shift upward upon enclosure of SiO_2. A gradual increase from 376 °C for SiO_2–free polymer electrolyte to 379 °C for CPE 4 is obtained for first decomposition temperature. Nevertheless, a smaller deviation of second decomposition temperature is further achieved, that is from 399 °C (without SiO_2 dispersion) until 400 °C (CPE 1, CPE 3 and CPE 4). Upon inclusion of SiO_2, the decomposition temperatures are increased. It is mainly ascribed to the formation of hydrogen bonding among its aggregates via chemi–adsorptions of Si–OH on the hydroxyl surface of silica atoms from SiO_2. Development of network is more preferred when the sufficient amount of SiO_2 is thoroughly dispersed the polymer matrix. So, it requires more energy to break the hydrogen bonds within the polymeric network. The highest decomposition temperatures of CPE 4 imply that the thermal property of the polymer matrix is increased. Therefore, CPE 4 is the better choice as composite polymer electrolyte.

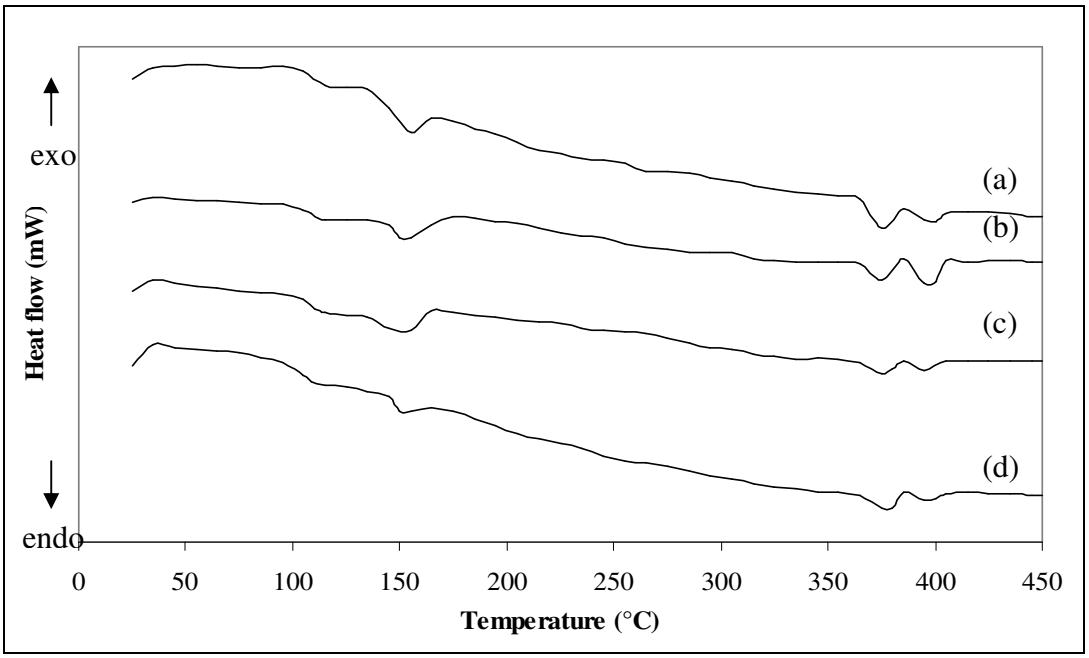

Figure 7.17: DSC thermograms of (a) IL 6, (b) CPE 1, (c) CPE 3 and (d) CPE 4.

Designations	DSC measurements		
	T_g (°C)	T_m (°C)	T_d (°C)
IL 6	112.50	157.30	375.66, 399.40
CPE 1	111.50	154.60	377.40, 399.80
CPE 3	110.40	153.80	378.10, 399.80
CPE 4	109.50	151.90	379.20, 399.90

Table 7.3: DSC profiles of PMMA–PVC–LiTFSI–BmImTFSI based nano–composite polymer electrolytes.

7.10 TGA Studies

TGA thermograms are shown in Figure 7.18, three stages are clearly observed for the degradation curves. Initial weight loss of 5 % at 137 °C, 3 % at 146 °C, 5 % at 166 °C and 1% at 178 °C are observed for IL 6, CPE 1, CPE 3 and CPE 4, respectively. The initial weight loss is generally ascribed to the evaporation of THF solvent, elimination of impurities especially fluorine compound and

dehydration of entrapped moisture (Stephan *et al*., 2002). Beyond the first mass loss, it follows by a constant weight. After that, second and third weight losses exist in the TGA thermogram. Second weight loss is mostly attributed to the unzipping process in the temperature regime. This process initiates many degradation reactions such as random chain scission reaction, depolymerization, intra–molecular transfer reaction and inter–molecular transfer reaction as well as polymer fragments. Therefore, volatilization of the monomer and oligomers which chemi–adsorbed onto the polymer matrix is occurred in this temperature regime. Eventually, the weight loss is significantly decreased (Ahmad *et al*., 2007). Elimination of HCl compounds from the dehydrochlorination reaction is another contributor, as proven in DSC thermograms. Around 17 % of second mass loss is observed for IL 6, starting from 255 °C to 355 °C, however, this respective weight loss decreases further by dispersing nano–sized SiO_2. CPE 1 and CPE 3 exhibit the mass losses of 14 % and 15 % with correspond of theirs' temperature ranges of 274 °C–384 °C and 284 °C–364 °C. Excellent thermal stability is revealed by CPE 4, 13 % of weight loss is observed, whereby the degradation temperature starts from 277 °C and end up at 357 °C.

After second weight loss, a gradual mass loss is observed thereafter. This particular weight loss is related to degradation of unsaturated groups of PMMA and decomposition of PVC, as verified in DSC analysis. In this stage, IL 6 displays around 12 % of weight loss at 385 °C with a residual mass of 66 %, weight losses of CPEs decreases enormously by incorporating fumed silica. CPE 1 and CPE 3 reveal 12 % and 7 % of mass losses, along with 71 % and 73 % residue

at 384 °C, respectively. Nevertheless, CPE 4 illustrates around 7 % weight loss with residual mass of 79 % at 387 °C. This might be due to inclusion of high amount of fumed silica in the polymer matrix. It leads to tight bonding within the polymer segments. Therefore, less volatilization is occurred (Rajendran *et al*., 2002). A complete decomposition of all the electrolytes has been verified by showing a stable mass thereafter. Among all the polymer electrolytes, CPE 4 discloses the excellent thermal stability, where the stability is up to 277 °C.

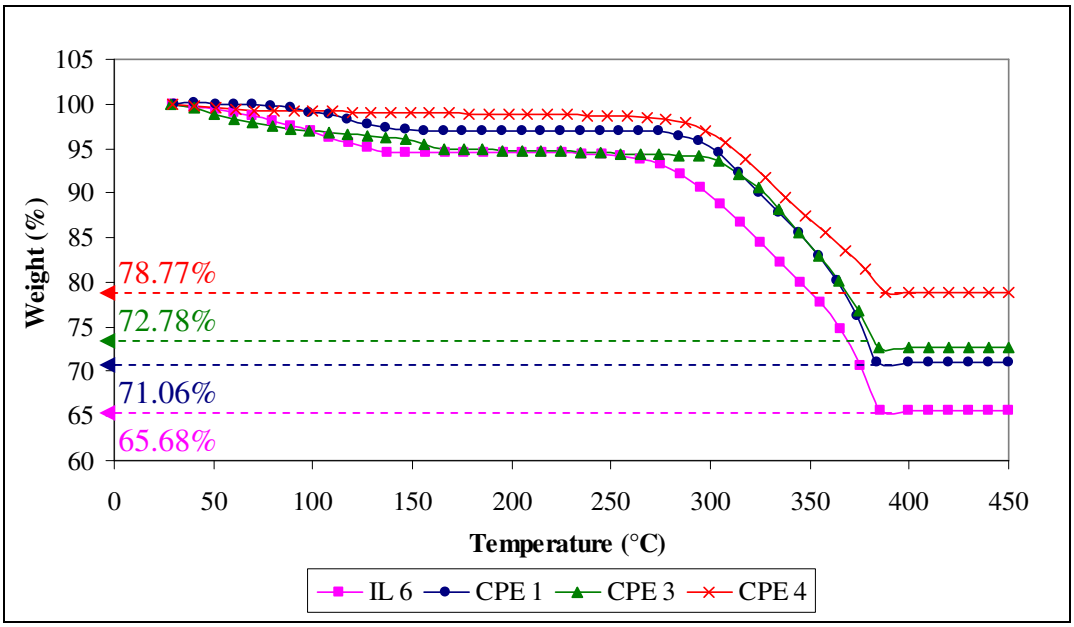

Figure 7.18: Thermogravimetric analysis of IL 6, CPE 1, CPE 3 and CPE 4.

7.11 Amplitude Sweep

The amplitude sweeps of IL 6 and SiO_2–based gel polymer electrolytes are shown in Figure 7.19, on logarithm scale. For all the samples, the G' values are higher than G'' in the strain regime, inferring the solid properties of all the

samples. The absence of crossover point of G' and G'' denotes that the behavioral transition of the polymer electrolytes did not occurs within the range (Fonseca *et al*., 2009). The trend of plots is similar as the previous polymer system. First, slight decreases in G' and G'' are observed for initial deformation. It thus followed by a constant LVE range, and eventually, the abrupt decrease is attained at high imposed deformation. As can be seen, CPE 1 shows the narrowest LVE range among all the composite polymer electrolytes, indicating the least stable of the sample.

At 0.001 % of strain, the values of G' and G'' are substantially increased upon addition of fumed silica. It is suggestive of establishment of three–dimensional network among the SiO_2 particles due to the formation of silanol (Si–OH) linkages on the surface of silicon atom of SiO_2 through Van der waals attractive force and hydrogen bonding as it is a hydrophilic compound (Ahmad et al., 2005; Ahmad et al., 2006a; Li *et al*., 2006b). As a theoretical result, more physical reticulate structures would be formed as increases in SiO_2 composition, which results the increment of G' and G'' values. However, the result is against the theory.

This observation might be due to the formation of space charge layers as a result of repulsion forces between the SiO_2 particles. At high SiO_2 content, these space charge layers induce to the longer distances between the SiO_2 grains and further weaken the physical networks. Additionally, the network is also destroyed with the inclusion of ionic liquid. As shown in Figure 7.19, the TFSI anions prefer

to form hydrogen bond with the network between SiO_2 grains and thus weaken the interaction among the aggregates. Among all the composite polymer electrolytes, CPE 4 exhibits the lowest values of G' and G'', inferring the lowest viscosity of CPE 4.

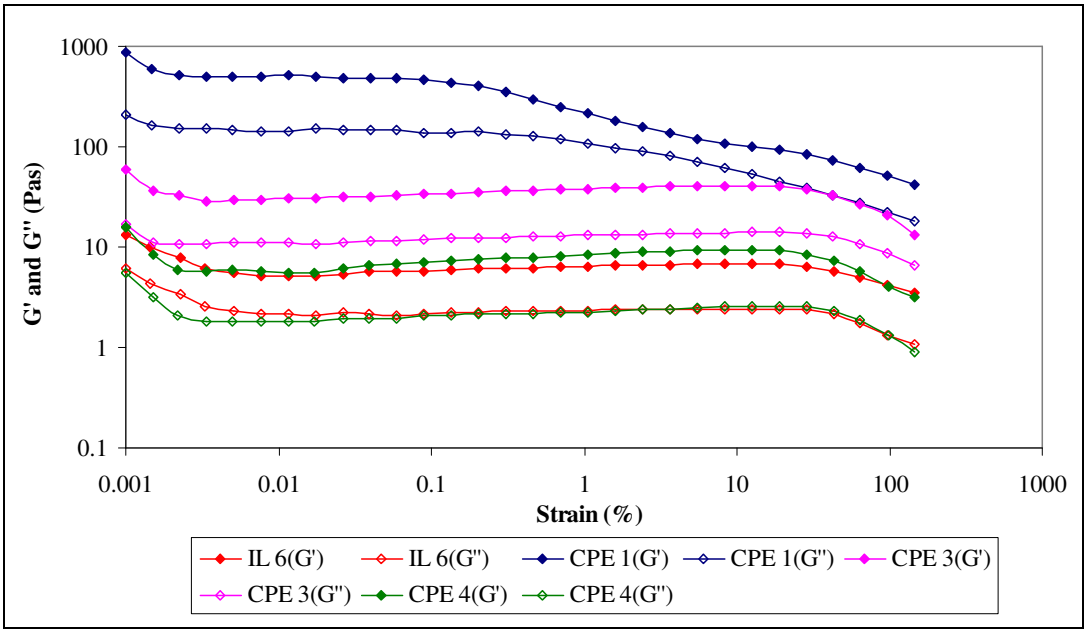

Figure 7.19: Amplitude sweeps of IL 6 and SiO_2–based gel polymer electrolytes.

7.12 Oscillatory Stress Sweep

The oscillatory shear curves of IL 6 and SiO_2–based gel polymer electrolytes are exemplified in Figure 7.20, on logarithm scale. The higher values of G' than G'' proposes the solid nature of the samples within the range of shear stress (Li *et al.*, 2006b). The behavioral transition is not being occurred as the flow point is absent in all the samples (Fonseca *et al.*, 2009). Three distinct stages are

observed and the trend of plots is discussed in previous section. Upon incorporation of SiO_2, the polymer electrolytes normally use larger shear stress to disrupt the bonds and linkages due to the formation of three–dimensional network. As proven in the figure, CPE 1 and CPE 3 are not easily to be distorted as they need high shear stress to rupture the polymeric systems. The main attributor of this observation is the silanol linkages among the silica particles and it favors the three–dimensional network in the complex. As a result, more energy is required to destroy this entanglement.

Among all the CPEs, the increase sequence in the required amount of shear stress for the initial deformation is in this order: CPE 4 < CPE 3 < CPE 1. The apparent decrease in initial shear stress is attained as increases the SiO_2 loadings. Excessive nano–SiO_2 particles cause the repulsion among the aggregates and hence weaken the interactions within the polymer matrix further, which in turn to the lower values of G' and G''. In addition, CPE 1 imparts lower stability at high shear stress by showing the rapid decreases in G' and G''. In contrast, CPE 3 and CPE 4 exhibit higher stability even though they depict lower values of both moduli. Therefore, the solid–like behavior of polymer electrolytes can be improved by doping more SiO_2 concentration at high deformation.

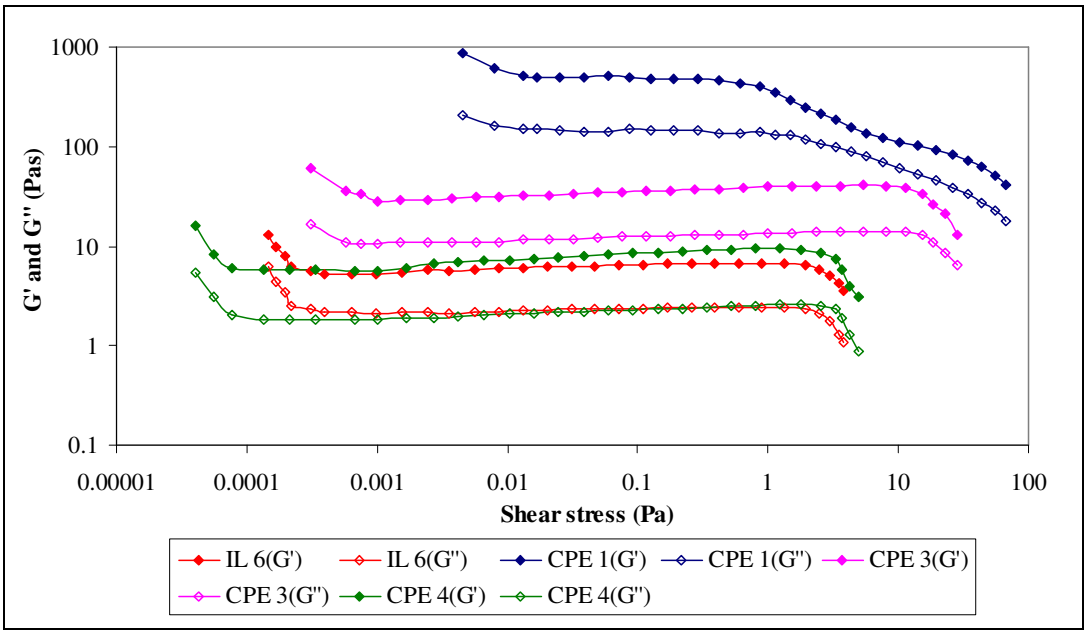

Figure 7.20: Oscillatory shear sweeps of IL 6 and SiO_2–based gel polymer electrolytes.

7.13 Oscillatory Frequency Sweep

The typical frequency sweeps of IL 6 and SiO_2–based gel polymer electrolytes are shown in Figure 7.21. The absence of *G*'' profile confirms once again the elastic solid–like properties of CPEs in the frequency range. The effect of incorporation with SiO_2 is not apparently observed as the *G*' values are almost the same in the frequency regime. It might be due to the low doping amount of SiO_2 and it induces to the futile effect on the structural stability of polymer electrolytes. For IL 6 and all CPEs, there is an abrupt decrease in *G*' at low frequency, as illustrated in Figure 7.21. When the deformation occurs for longer time at low frequency, the relaxation time becomes longer and contributes to the slippage of entanglements. This slippage reduces the ability for storing the

imposed energy and hence decreases the solid behavior of sample, indicating the low structural stability of the polymer system at low frequency.

In contrast, at higher frequency, the structural stability of polymer electrolytes is improved as the high value of *G*' is shown in Figure 7.21. Again, it is primarily attributed to the low relaxation time and then leads to insufficient time for slippage mechanism. Therefore, the structural strength of polymer electrolytes at high frequency is better than at low frequency. Since all the plots show the comparable values within the range, it can therefore be concluded that the addition of SiO_2 is not a promising candidate to improve the stability of polymer electrolytes.

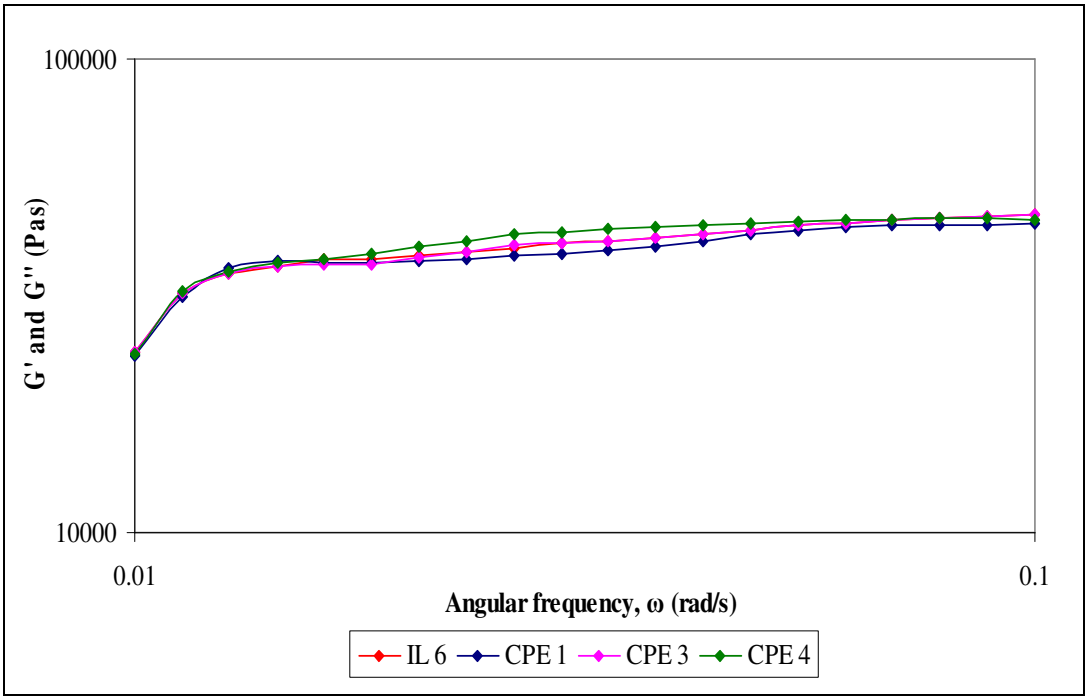

Figure 7.21: Frequency sweeps of IL 6 and SiO_2–based gel polymer electrolytes.

7.14 Viscosity Studies

Figure 7.22 shows the typical viscosity profile as a function of shear rate with various mass fractions of fumed silica. Non–newtonian nature has been shown in IL 6 and CPEs as the viscosity exhibits the linear relationship with respect to shear rate (Ahmad *et al*., 2005). When the sample is less deformed, the value of viscosity is still high at lower shear rate. This is due to the initial deformation and the sample still maintains its elastic properties by forming the polymer network among the aggregates via silanol linkage. However, the viscosity decreases monotonically with increasing the shear rate, revealing the shear thinning properties. It is because the network among the SiO_2 particles is destroyed by shear. At high shear rate, the viscosity and shear thinning rate for IL 6 and CPEs are quite similar due to the preferential orientation of the silanol linkage parallel to the flow direction (Ahmad *et al*., 2005).

In principle, the viscosity of sample should be increases with shear rate due to the formation of three–dimensional network among the aggregates through the silanol linkage, as explained in previous amplitude sweep and oscillatory shear sweep studies. However, at low shear rate (0.1 s^{-1}), the viscosity is reduced upon addition of fumed silica. The perspective on this result is because of the presence of ionic liquid. The ionic liquid contributes the plasticizing effect and thus weakens the intertwined network linkages among the aggregates. The viscosity of CPEs decreases with increasing the content of SiO_2. At high SiO_2 composition, SiO_2 nano–particles are in excess mode. Excessive SiO_2 causes the repulsion

forces between the aggregates and therefore weakens the interaction between three–dimensional networks by producing longer distance between the aggregates. As a result, CPEs imparts lower viscosity.

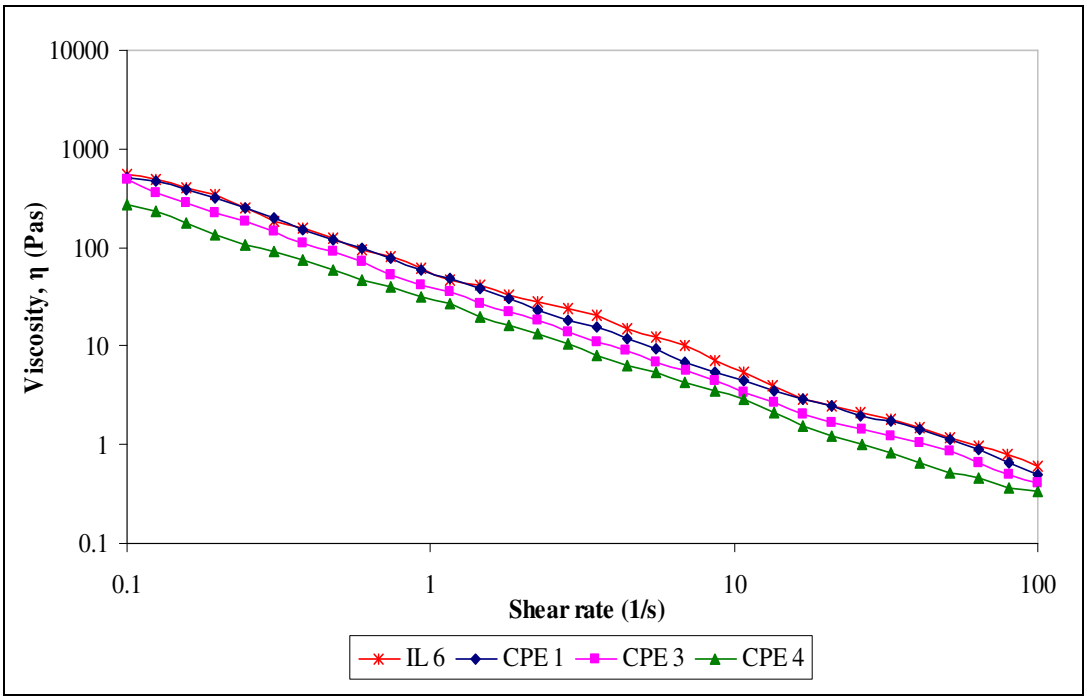

Figure 7.22: Typical viscosity curve of IL 6 and SiO_2–based gel polymer electrolytes.

7.15 Summary

Nano–composite polymer electrolytes with different ratio of fumed silica were prepared by solution casting technique. Among all the samples, CPE 4 (8 wt% of SiO_2) is a feasible candidate. Maximum ionic conductivity of $(4.11\pm0.01)\times10^{-3}$ Scm^{-1} is achieved by CPE 4 due to the formation of an effective conducting pathway between the grain boundaries. The conductivity increases

with frequency, up to an optimum level. Beyond this region, the decrease in conductivity is perceived. At low frequency, slow periodic reversal causes the accumulation of ions and hence decreases the ion transport in the polymer matrix which in accordance with lower conductivity. Both of dielectric permittivity and dielectric loss decrease with frequency. Electrode polarization due to the accumulation of ions is the main attributor. There is no ion diffusion in the direction of electric field at high frequency due to the fast periodic reversal of electric field. In order to study the bulk dielectric response of polymer electrolytes, the dielectric modulus which mask the polarization effect is investigated. No evident relaxation peak is observed in both real and imaginary parts of dielectric moduli. HATR–FTIR study is employed to study the structural of polymer electrolytes and thus verified the complexation between fumed silica and polymer blends.

In temperature dependence–ionic conductivity studies, CPE 4 achieves the highest ionic conductivity of (8.26±0.02) $mScm^{-1}$ at 80 °C with stability up to 277 °C. CPEs exhibit Arrhenius behavior within the temperature range. Arrhenius relationship reflects the ion hopping mechanism at elevated temperature. On the other hand, XRD and coherent length studies prove the highest amorphous region of the CPE 4. Enhancement in amorphous proportion and ionic mobility in the polymer matrices are further proven in the SEM morphologies. DSC and TGA studies imply the improved thermal stability nano–composite polymer electrolytes as increases in filler loadings. Decrease in T_g and T_m implies the enhancement of

flexibility and amorphous degree of polymer electrolytes, respectively. Significant decrease in weight loss indicates the excellent thermal properties of composite polymer electrolytes upon heating to 450 °C.

The elastic solid–like properties of CPEs have been found out in the amplitude sweep and oscillatory shear sweep studies, as the value of G' is higher than G''. In amplitude sweep, both of G' and G'' decrease with fumed silica composition, revealing the gel–like appearance of polymer electrolytes with low mechanical stability. The samples still remain in gel–like behavior due to the strong plasticizing effect of ionic liquid. LVE range becomes wider with increasing fumed silica content and indicates the better stability of these polymer electrolytes. In addition, the low mechanical properties of the samples are also shown in oscillatory shear sweep by showing the lower value of starting point of shear stress. In frequency sweep, G'' is absent and further implies the solid nature of CPEs. At low frequency, G' shows lower value due to the longer relaxation time, which in turn to the slippage of the polymer chain. Therefore, the structural stability is reduced at low frequency. In contrast, the structural stability is improved at the short–term of deformation. It is mainly attributed to the declined relaxation time. Shear–thinning properties of CPEs were observed in viscosity curve with respect to the shear rate. Under shear, the viscosity is decreased due to interruption of the weak physical and chemical bonds within the polymer matrix.

7.16 Summary of Four Systems on Room Temperature–Ionic Conductivity Study

Figure 7.23 shows the comparisons of the ionic conductivity for the highest ionic conducting samples in the polymer blend electrolyte system at room temperature. As explained in sections 3.2.1 and 3.2.2, 10 wt% of LiTFSI is fixed in first system, whereas the ratio of PMMA–PVC polymer blends to salt is varied in second system. Based on the results obtained in Chapter 4, the highest ionic conductivity of 1.60×10^{-8} Scm^{-1} is reached in the first system. On the contrary, inclusion of 30 wt% of LiTFSI achieves the maximum ionic conductivity of 1.11×10^{-6} Scm^{-1}, as explained in Chapter 5. By comparing first system with second system, the ionic conductivity increases with the mass fraction of lithium salt. It is mainly ascribed to the increase in the amount of charge carriers (Li^+) by doping LiTFSI further. Therefore, it promotes more ionic hopping mechanism within the polymer matrix and then raises the ionic conductivity.

In third polymer blend electrolyte system, the ionic conductivity increases drastically upon adulteration of BmImTFSI ionic liquid. Strong plasticizing effect of ionic liquid is the main attributor. This effect would soften the polymer backbone and thus enhance the segmental mobility of polymeric chain, favoring the ionic transportation which in accordance with high ionic conductivity. Doping of ionic liquid also weakens the interaction with the polymer matrix and initiates the decoupling of ions by reducing the solvation of Li^+. As a result, the ionic migration is favored due to its high self–dissociating behavior. The ionic

conductivity increases by one order of magnitude upon addition of 8 wt% of fumed silica onto third system. The ionic conductivity of 4.11 $mScm^{-1}$ is achieved. The enhancement of ionic conductivity is suggestive of formation of nano–sized filler grain boundary. A continuous interpenetrating conducting pathway between the silica grains in the inter–particles region is generated as the particles are getting closer to each other. This assists in ionic hopping mechanism and hence leads to the high ionic conductivity.

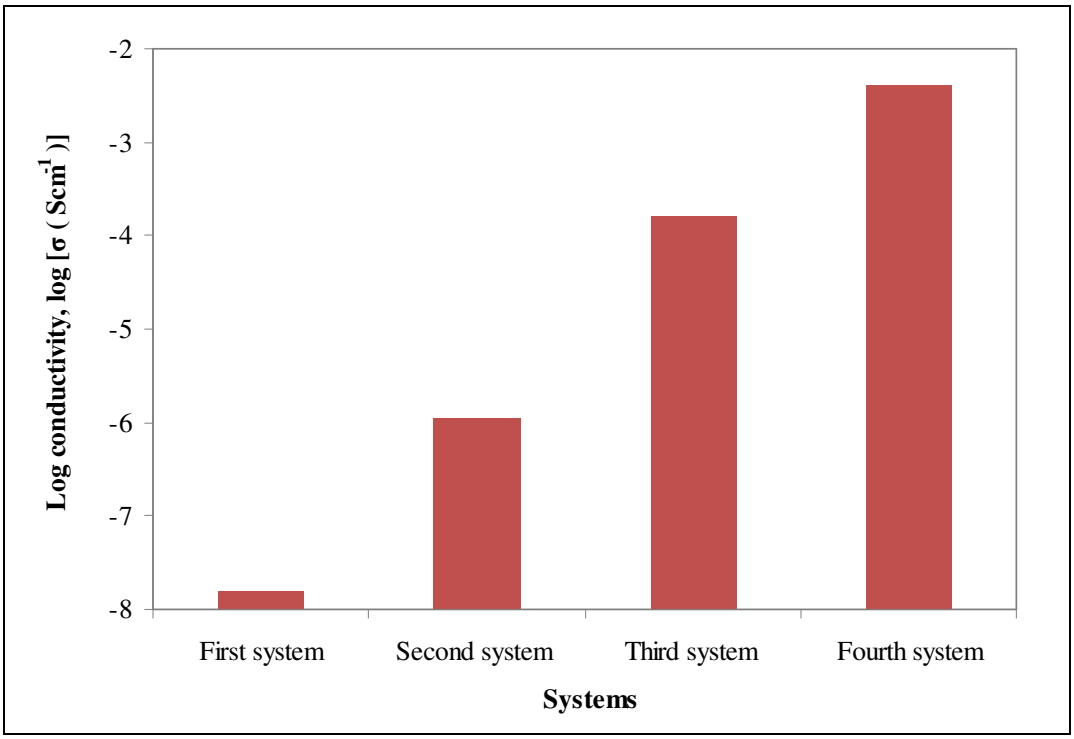

Figure 7.23: Variation of log conductivity, log σ of the highest ionic conducting samples in the particular system at ambient temperature.

CHAPTER 8

CONCLUSION

Four polymer electrolyte systems were prepared by solution casting technique. PMMA and PVC were used as host polymers with LiTFSI as doping salt. Additives such as BmImTFSI ionic liquid and nano–sized inorganic filler, SiO_2 were employed. PMMA (70 wt%) blended with PVC (30 wt%) based polymer electrolyte was a promising candidate. The highest ionic conductivity obtained was 1.60×10^{-8} Scm^{-1} at ambient temperature. Maximum ionic conductivity of 1.11×10^{-6} Scm^{-1} was achieved at room temperature with addition of 30 wt% LiTFSI salt. Ionic liquid was incorporated in this polymer blend electrolytes to improve the ionic conductivity. The ambient temperature–ionic conductivity of gel polymer electrolytes enhanced to a maximum value of 1.64×10^{-4} Scm^{-1} upon addition of 60 wt% BmImTFSI. The ionic conductivity increased by two orders of magnitude. The dispersion of 8 wt% of SiO_2 (denoted as CPE 4) was achieved the highest ionic conductivity of 4.11 $mScm^{-1}$ at room temperature.

The ionic conductivities of all the samples increased with temperature. It disclosed the Arrhenius behavior and thus further indicated the ion hopping mechanism. The dielectric behavior was analyzed using dielectric permittivity and dielectric modulus of the samples. In frequency dependence study, it obeyed Jonscher's universal law and further proven the hopping process between the

charge carriers in the polymer matrix. Non–Debye characteristic was divulged in dielectric relaxation study. In order to study the bulk dielectric response of polymer electrolytes, the dielectric modulus which masks the polarization effect was investigated. In addition, horizontal attenuated total reflectance–Fourier Transform infrared (HATR–FTIR) spectroscopy indicated the complexation of the materials in the polymer electrolytes based on the changes in peak shifting, intensity, shape and formation of new peaks.

X–ray diffraction (XRD) studies implied the higher degree of amorphous nature of the polymer electrolytes by reducing the intensity of characteristic peaks. The higher amorphous region is further verified in coherence length study. SEM is used to investigate the morphology of the samples. By analyzing the SEM images, the higher porosity revealed the improved ionic migration in the sample. Entrapments of ionic liquid into the polymer matrix were verified through the images. DSC studies inferred the improved thermal properties of samples. TGA asserted the excellent thermal stability of the polymer electrolyte where their stability is up to 200 °C. Rheological studies revealed the solid and elastic properties through amplitude sweep and oscillatory shear sweep studies, as the values of G' are much higher than G''. Elastic property of polymer electrolytes became lesser when the deformation takes place for a prolonged time at low frequency. In the typical viscosity curves, shear–thinning properties of samples were observed. CPE 4 is a promising candidate as polymer electrolyte and is greatly preferred in lithium ion polymer batteries as it shows the excellent thermal stability, where the stability is up to 277 °C.

For further study, liquid crystal will be added as additive into this polymer blend electrolytes in order to improve the ionic conductivity and overall performances. Doping of liquid crystal will lead to the formation of liquid crystal polymer electrolytes. In addition, ionic liquid and nano–sized filler would be synthesized and then used as additives in the polymer blend electrolytes. The comparisons between synthesized and commercial additives would be made. The fabrication of lithium ion rechargeable battery will also be done by using the highest ionic conducting sample. The overall electrical and electrochemical performances of the cell will be studied and analyzed in various aspects such as the cost effectiveness of the cell, charge capacity, discharge capacity and Coulombic efficiency. The results will be validated with commercial polymer battery.

LIST OF REFERENCES

Achari, V.B., Reddy, T.J.R., Sharma, A.K. & Rao, V.V.R.N. (2007). Electrical, optical, and structural characterization of polymer blend (PVC/PMMA) electrolyte films. *Ionics*, 13, 349–354.

Adebahr, J., Byrne, N., Forsyth, M., MacFarlane, D.R. & Jacobsson, P. (2003). Enhancement of ion dynamics in PMMA–based gels with addition of TiO_2 nano–particles. *Electrochimica Acta*, 48, 2099–2103.

Ahmad, S., Ahmad, S. & Agnihotry S.A. (2005). Nanocomposite electrolytes with fumed silica in poly(methyl methacrylate): thermal, rheological and conductivity studies. *Journal of Power Sources*, 140, 151–156.

Ahmad, S., Bohidar, H.B., Ahmad, S. & Agnihotry, S.A. (2006a). Role of fumed silica on ion conduction and rheology in nanocomposite polymeric electrolytes. *Polymer*, 47, 3583–3590.

Ahmad, S., Saxena, T.K., Ahmad, S. & Agnihotry, S. A. (2006b). The effect of nanosized TiO_2 addition on poly(methylmethacrylate) based polymer electrolytes. *Journal of Power Sources*, 159, 205–209.

Ahmad, S., Deepa, M. & Agnihotry, S.A. (2008). Effect of salts on the fumed silica–based composite polymer electrolytes. *Solar Energy Materials and Solar Cells*, 92, 184–189.

Ahmad, S. & Agnihotry, S.A. (2009). Effect of nano γ–Al_2O_3 addition on ion dynamics in polymer electrolytes. *Current Applied Physics*, 9, 108–114.

Ahmad, Z., Al–Awadi, N.A. & Al–Sagheer, F. (2007). Morphology, thermal stability and visco–elastic properties of polystyrene–poly(vinyl chloride) blends. *Polymer Degradation and Stability*, 92, 1025–1033.

Ali, A.M.M., Yahya, M.Z.A., Bahron, H., Subban, R.H.Y., Harun, M.K. and Atan, I. (2007). Impedance studies on plasticized PMMA–LiX [X: $CF_3SO_3^-$, $N(CF_3SO_2)^{2-}$] polymer electrolytes. *Materials Letters*, 61, 2026–2029.

Almond, D.P., West, A.R. & Grant, R. J. (1982). Temperature dependence of the A.C. conductivity of Na β–alumina. *Solid State Communications*, 44, 1277–1280.

Arof, A.K. and Ramesh, S. (2000). Electrical conductivity studies of poly(vinylchloride) based electrolytes with double salt system. *Solid State Ionics*, 136–137, 1197–1200.

Aravindan, V., Lakshmi, C. & Vickraman, P. (2009). Investigations on Na^+ ion conducting polyvinylidenefluoride–co–hexafluoropropylene / poly ethylmethacrylate blend polymer electrolytes. Current Applied Physics, 9, 1106–1111.

Barsoukov, E. & Macdonald, J.R. (2005a). Fundamentals of Impedance Spectroscopy. Impedance Spectroscopy Theory, Experiment, and Applications. 2nd Edition (pp. 1–26). New Jersey: John Wiley and Sons.

Barsoukov, E. & Macdonald, J.R. (2005b). Fundamentals of Impedance Spectroscopy. Impedance Spectroscopy Theory, Experiment, and Applications. 2nd Edition (pp. 28–128). New Jersey: John Wiley and Sons.

Baskaran, R., Selvasekarapandian, S., Kuwata, N., Kawamura, J. & Hattori T. (2006a). Ac impedance, DSC and FT–IR investigations on (x)PVAc–(1–x)PVdF blends with $LiClO_4$. *Materials Chemistry and Physics*, 98, 55–61.

Baskaran, R., Selvasekarapandian, S., Kuwata, N., Kawamura, J. & Hattori, T. (2006b). Conductivity and thermal studies of blend polymer electrolytes based on PVAc–PMMA. *Solid State Ionics*, 177, 2679–2682.

Baskaran, R., Selvasekarapandian, S., Kuwata, N., Kawamura, J. & Hattori, T. (2007). Structure, thermal and transport properties of PVAc–$LiClO_4$ solid polymer electrolytes. *Journal of Physics and Chemistry of Solids*, 68, 407–412.

Bazito, F.F.C., Silveira, L.T., Torresi, R.M. & Torresi, S.I.C. (2007). Spectroelectrochemical study of a soluble derivative of poly(aniline) in a room temperature ionic liquid. *Electrochimica Acta*, 53, 1217–1224.

Braun, D., Cherdron, H., Rehahn, M., Ritter, H. & Voit, B. (2005a). Introduction. *Polymer Synthesis: Theory and Practice*. (pp. 1–37). Berlin: Springer.

Braun, D., Cherdron, H., Rehahn, M., Ritter, H. & Voit, B. (2005b). Modification of Macromolecular Substances. *Polymer Synthesis: Theory and Practice*. (pp. 362–367). Berlin: Springer.

Braun, D., Cherdron, H., Rehahn, M., Ritter, H. & Voit, B. (2005c). Methods and Techniques for Synthesis, Characterization, Processing, and Modification of Polymers. *Polymer Synthesis: Theory and Practice*. (pp. 39–156). Berlin: Springer.

Cheng, H., Zhu, C., Huang, B., Lu, M. & Yang, Y. (2007). Synthesis and electrochemical characterization of PEO–based polymer electrolytes with room temperature ionic liquids. *Electrochimica Acta*, 52, 5789–5794.

Choi, N.S. & Park, J.K. (2001). New polymer electrolytes based on PVC/PMMA blend for plastic lithium–ion batteries. *Electrochimica Acta*, 46, 1453–1459.

Deepa, M., Sharma, N., Agnihotry, S.A., Singh, S., Lal, T. & Chandra, R. (2002). Conductivity and viscosity of liquid and gel electrolytes based on $LiClO_4$, $LiN(CF_3SO_2)_2$ and PMMA. *Solid State Ionics*, 152–153, 253–258.

Durairaj, R. Ramesh, S., Mallik, S., Seman, A. & Ekere, N. (2009). Rheological characterisation and printing performance of Sn/Ag/Cu solder pastes. Materials and Design, 30, 3812–3818.

Ebagninin, K.W., Benchabane, A. & Bekkour, K.J. (2009). Rheological characterization of poly(ethylene oxide) solutions of different molecular weights. *Journal of Colloid Interface Science*, doi: 10.1016/j.jcis.2009.03014.

Egashira, M., Todo, H., Yoshimoto, N. & Morita, M. (2008). Lithium ion conduction in ionic liquid–based gel polymer electrolyte. *Journal of Power Sources*, 178, 729–735.

Eliasson, H., Albinsson, I. & Mellander, B.E. (2000). Conductivity and dielectric properties of $AgCF_3SO_3$–PPG. *Materials Research Bulletin*, 35, 1053–1065.

Endo, K. (2002). Synthesis and structures of poly(vinyl chloride). *Progress in Polymer Science*, 27, 2021–2054.

Fernandez, M.E., Diosa, J.E. & Vargas, R.A. (2008). Impedance spectroscopy studies of the polymer electrolyte based on poly(vinyl alcohol)–(NaI + 4AgI)–H_2O. *Microelectronics Journal*, 39, 1344–1346.

Fonseca, C.G., Basaglia, R.M.F., Brant, M.C., Matencio, T. & Domingues, R.Z. (2009). Study of the rheological behavior of an anode slurry and the microstructural properties of anode functional film obtained by spray coating. *Powder Technology*, 192, 352–358.

Fu, Y.B., Ma, X.H., Yang, Q.H. & Zong, X.F. (2003). The effect of fumed silica on the interfacial stability in the polymer gel electrolyte. *Materials Letters*, 57, 1759–1764.

Ganesan, S., Muthuraaman, B., Mathew, V., Madhavan, J., Maruthamuthu, P. & Suthanthiraraj, S.A. (2008). Performance of a new polymer electrolyte incorporated with diphenylamine in nanocrystalline dye–sensitized solar cell. *Solar Energy Materials and Solar Cells*, 92, 1718–1722.

Gray, F.M. (1991a). Polymer Electrolytes–Based Devices. *Solid polymer electrolytes: Fundamentals of technological applications*. (pp. 1–30). United Kingdom: Wiley–VCH.

Gray, F.M. (1991b). Aspects of Conductivity in Polymer Electrolytes. *Solid polymer electrolytes: Fundamentals of technological applications*. (pp. 83–91). United Kingdom: Wiley–VCH.

Gray, F.M. (1991c). Transport Properties: Effects of Dynamic Disorder. *Solid polymer electrolytes: Fundamentals of technological applications*. (pp. 149–179). United Kingdom: Wiley–VCH.

Gray, F.M. (1997a). What are Polymer Electrolytes? *Polymer Electrolyte*. (pp. 1–30). Cambridge: The Royal Society of Chemistry.

Gray, F.M. (1997b). What Materials are suitable as Polymer electrolyte? *Polymer Electrolyte*. (pp. 31–78). Cambridge: The Royal Society of Chemistry.

Gray, F.M. (1997c). What is the Structure of a Polymer Electrolytes? In: *Polymer Electrolyte*. (pp. 83–93). Cambridge: The Royal Society of Chemistry.

Goodwin, A.A., Atkinson, J.R., Hay, J.N. & Mercer, F.W. (1999). Dielectric relaxation behaviour of fluorinated aromatic poly(ether)s and poly(ether ketone)s, *Polymer*, 40, 1515–1524.

Han, H.S., Kang, H.R., Kim, S.W. & Kim, H.T. (2002). Phase separated polymer electrolyte based on poly(vinyl chloride)/poly(ethyl methacrylate) blend. *Journal of Power Sources*, 112, 461–468.

Ikeda, Y., Kohjiya, S., Nishimoto, A. & Watanabe, M. (1998). High ionic conductivity of new polymer electrolytes based on high molecular weight polyether comb polymers. *Electrochimica Acta*, 43, 1177–1184.

Jain, N., Kumar, A., Chauhan, S. & Chauhan, S. M. S. (2005). Chemical and biochemical transformations in ionic liquids. *Tetrahedron*, 61, 1015–1060.

Jiang, J., Gao, D., Li, Z. & Su, G. (2006). Gel polymer electrolytes prepared by in situ polymerization of vinyl monomers in room–temperature ionic liquids. *Reactive and Functional Polymers*, 66, 1141–1148.

Joel, R. F. (2003a). Additives, Blends, and Composites. *Polymer Science and Technology*. 2nd Edition (pp. 283–317). U.S.: Prentice Hall.

Kang, X. (2004). Nonaqueous Liquid Electrolytes for Lithium–Based Rechargeable Batteries. *Chemical Reviews*, 104, 4303–4417.

Kavanagh, G.M. & Murphy, S.B.R. (1998). Rheological characterization of polymer gels. Programme Polymer Science, 23, 533–562.

Kerr, J. (2002). Grafted Polyelectrolyte Membranes for Lithium Batteries and Fuel Cells. URL: http://www.osti.gov/bridge/servlets/purl/836037–Nla6kp/native. Accessed on 11st January 2010.

Khiar, A.S.A., Puteh, R. & Arof, A.K. (2006). Conductivity studies of a chitosan–based polymer electrolyte. *Physica B*, 373, 23–27.

Kim, H.S., Kum, K.S., Cho, W. & Hee, W.R. (2003). Electrochemical and physical properties of composite polymer electrolyte of poly(methyl methacrylate) and poly(ethylene glycol diacrylate), *Journal of Power Sources*, 124, 221–224.

Kim, K.S., Park, S.Y., Choi, S. & Lee, H. (2006). Ionic liquid–polymer gel electrolytes based on morpholinium salt and PVdF(HFP) copolymer. *Journal of Power Sources*, 155, 385–390.

Kuila, T., Acharya, H., Srivastava, S.K., Samantaray, B.K. & Kureti, S. (2007). Enhancing the ionic conductivity of PEO based plasticized composite polymer electrolyte by $LaMnO_3$ nanofiller, *Materials Science and Engineering B*, 137, 217–224.

Kumar, R., Subramania, A., Sundaram, N.T.K., Kumar, G.V. & Baskaran, I. (2007). Effect of MgO nanoparticles on ionic conductivity and electrochemical properties of nanocomposite polymer electrolyte. *Journal of Membrane Science*, 300, 104–110.

Kumar, M.S. & Bhat, D.K. (2009). Polyvinyl alcohol–polystyrene sulphonic acid blend electrolyte for supercapacitor application. *Physica B*, 404, 1143–1147.

Kumar, G.G., Kim, P., Kim, A.R., Nahm, K.S. & Elizabeth, R.N. (2009). Structural, thermal and ion transport studies of different particle size nanocomposite fillers incorporated PVdF–HFP hybrid membranes. *Materials Chemistry and Physics*, 115, 40–46.

Li, Z., Liu, H., Liu, Y., He, P., Li, J., Zheng, L., J. Li et al. (2005). Effect of methylsisesquioxane filler on the properties of ionic liquid based polymer electrolyte. *Polymer*, 46, 7578–7584.

Li, W., Yuan, M. & Yang, M. (2006a). Dual–phase polymer electrolyte with enhanced phase compatibility based on Poly(MMA–g–PVC)/PMMA. *European Polymer Journal,* 42, 1396–1402.

Li, Y., Yerian, J.A., Khan, S.A., Fedkiw, P.S. (2006b). Crosslinkable fumed silica–based nanocomposite electrolytes for rechargeable lithium batteries. *Journal of Power Sources*, 161, 1288–1296.

Malcolm & Stevens, P. (1999a). Chemical structure and polymer morphology. *Polymer Chemistry: An Introduction*. 3rd Edition. (pp. 61–15). New York: Oxford University Press, Inc.

Malcolm, Stevens, P. (1999b). Evaluation, Characterization, and Analysis of Polymers. *Polymer Chemistry: An Introduction*. 3rd Edition. (pp. 129–160). New York: Oxford University Press, Inc.

Marcilla, R., Alcaide, F., Sardon, H., Pomposo, J.A., Gonzalo, C.P. & Mecerreyes, D. (2006). Tailor–made polymer electrolytes based upon ionic liquids and their application in all–phase electrochromic devices. *Electrochemistry Communications*, 8, 482–488.

Mei, A., Wang, X.L., Feng, Y.C., Zhao, S.J., Li, G.J., Geng, H.X., Lin, Y.H. & Nan, C.W. (2008). Enhanced ionic transport in lithium lanthanum titanium oxide solid state electrolyte by introducing silica. *Solid State Ionics*, 179, 2255–2259.

Nicotera, I., Coppola, L., Oliviero, C., Castriota, M. & Cazzanelli, E. (2006). Investigation of ionic conduction and mechanical properties of PMMA–PVdF blend–based polymer electrolytes. *Solid State Ionics*, 177, 581–588.

Pandey, G. P. & Hashmi, S. A. (2009). Experimental investigations of an ionic–liquid–based, magnesium ion conducting, polymer gel electrolyte. *Journal of Power Sources*, 187, 627–634.

Osinska, M., Walkowiak, M., Zalewska, A. & Jesionowski, T. (2009). Study of the role of ceramic filler in composite gel electrolytes based on microporous polymer membranes. *Journal of Membrane Science*, 326, 582–588.

Raghavana, P., Zhao, X., Manuel, J., Chauhan, G.S., Ahn, J.H., Ryub, H.S., Ahn, H.J., Kim, K.W., Nah, C. et al. (2009). Electrochemical performance of electrospun poly(vinylidene fluoride–co–hexafluoropropylene)–based nanocomposite polymer electrolytes incorporating ceramic fillers and room temperature ionic liquid. *Electrochimica Acta*, doi:10.1016/j.electacta.2009.05.025.

Rajendran, S. & Uma, T. (2000). Lithium ion conduction in PVC–$LiBF_4$ electrolytes gelled with PMMA. *Journal of Power Sources*, 88, 282–285.

Rajendran, S., Uma, T. & Mahalingam T. (2000). Conductivity studies on PVC±PMMA±$LiAsF_6$±DBP polymer blend electrolyte. *European Polymer Journal*, 36, 2617–2620.

Rajendran, S., Mahendran, O. & Kannan, R. (2002). Characterisation of [$(1-x)$ PMMA–x PVdF] polymer blend electrolyte with Li^+ ion. Fuel, 81, 1077–1081.

Rajendran, S., Sivakumar, M. & Subadevi, R. (2004). Investigations on the effect of the various plasticizers in PVA–PMMA solid polymer blend electrolytes. *Materials Letter*, 58, 641–649.

Rajendran, S., Prabhu, M.R. & Rani, M.U. (2008). Ionic conduction in poly(vinyl chloride)/poly(ethyl methacrylate)–based polymer blend electrolytes complexed with different lithium salts. *Journal of Power Sources*, 180, 880–883.

Ramesh, S. & Arof, A.K. (2001a). Ionic conductivity studies of plasticized poly(vinyl chloride) polymer electrolytes. *Materials Science and Engeneering B*, 85, 11–15.

Ramesh, S. & Arof, A.K. (2001b). Structural, thermal and electrochemical cell characteristics of poly(vinyl chloride)–based polymer electrolytes. *Journal of Power Sources*, 99, 41–47.

Ramesh, S. & Chai, M.F. (2007). Conductivity, dielectric behavior and FTIR studies of high molecular weight poly(vinyl chloride)–lithium triflate polymer electrolytes. *Materials Science and Engineering B*, 139, 240–245.

Ramesh, S., Yuen, T.F. & Shen, C.J. (2007). Conductivity and FTIR studies on PEO–LiX [X: $CF_3SO_3^-$, SO_4^{2-}] polymer electrolytes. *Spectrochimica Acta Part A*, 69, 670–675.

Ramesh, S. & Lu, S.C. (2008). Effect of nanosized silica in poly(methyl methacrylate)–lithium bis(trifluoromethanesulfonyl)imide based polymer electrolytes. *Journal of Power Sources*, 185, 1439–1443.

Ramesh. S. & Ng, K.Y. (2009). Characterization of polymer electrolytes based on high molecular weight PVC and Li_2SO_4, *Current Applied Physics*, 9, 329–332.

Ramesh, S. & Wen, L.C. (2009). Investigation on the effects of addition of SiO_2 nanoparticles on ionic conductivity, FTIR, and thermal properties of nanocomposite PMMA–$LiCF_3SO_3$–SiO_2. *Ionics*, 16, 255–262.

Reiter, J., Vondrak, J. Michalek, J. & Micka, Z. (2006). Ternary polymer electrolytes with 1–methylimidazole based ionic liquids and aprotic solvents. *Electrochimica Acta*, 52, 1398–1408.

Saikia, D. & Kumar, A. (2004). Ionic conduction in P(VDF–HFP)/PVDF–(PC + DEC)–$LiClO_4$ polymer gel electrolytes. *Electrochimica Acta*, 49, 2581–2589.

Saikia, D. & Kumar, A. (2005). Ionic transport in P(VDF–HFP)–PMMA–$LiCF_3SO_3$–(PC + DEC)–SiO_2 composite gel polymer electrolyte. *European Polymer Journal*, 41, 563–568.

Sekhon, S.S., Krishnan, P., Singh, B., Yamada, K. & Kim, C.S. (2006). Proton conducting membrane containing room temperature ionic liquid. *Electrochimica Acta*, 52, 1639–1644.

Selvasekarapandian, S., Baskaran, R., Kamishima, O., Kawamura, J. & Hattori, T. (2006). Laser Raman and FTIR studies on Li^+ interaction in PVAc–$LiClO_4$ polymer electrolytes. *Spectrochimica Acta Part A: Molecular and Biomolecular Spectroscopy*, 65, 1234–1240.

Sengwa, R.J., Choudhary, S. & Sankhla, S. (2009). Dielectric spectroscopy of hydrophilic polymers–montmorillonite clay nancomposite aqueous colloidal suspension. *Colloids and Surfaces A: Physicochemical Engineering Aspects*, 336, 79–87.

Sharma, J.P. & Sekhon, S.S. (2007). Nanodispersed polymer gel electrolytes: Conductivity modification with the addition of PMMA and fumed silica. *Solid State Ionics*, 178, 439–445.

Shastry, M.C.R. & Rao K.J. (1991). Ac conductivity and dielectric relaxation studies in AgI–based fast ion conducting glasses. *Solid State Ionics*, 44, 187–198.

Shin, J.H., Henderson, W.A. & Passerini, S. (2003). Ionic liquids to the rescue? Overcoming the ionic conductivity limitations of polymer electrolytes. *Electrochemistry Communications*, 5, 1016–1020.

Singh, P.K., Kim, K.W., Park, N.G. & Rhee, H.W. (2008). Mesoporous nanocrystalline TiO_2 electrode with ionic liquid–based solid polymer electrolyte for dye–sensitized solar cell application. *Synthetic Metals*, 158, 590–593.

Singh, P.K., Kim, K.W. & Rhee, H.W. (2009). Development and characterization of ionic liquid doped solid polymer electrolyte membranes for better efficiency. *Synthetic Metals*, 159, 1538–1541.

Sivakumar, M., Subadevi, R., Rajendran, S., Wu, N.L. & Lee, J.Y. (2006). Electrochemical studies on [(1−*x*)PVA–*x*PMMA] solid polymer blend electrolytes complexed with $LiBF_4$, *Materials Chemistry and Physics*, 97, 330–336.

Sivakumar, M., Subadevi, R., Rajendran, S., Wu, H.C. & Wu, N.L. (2007). Compositional effect of PVdF–PEMA blend gel polymer electrolytes for lithium polymer batteries. *European Polymer Journal*, 43, 4466–4473.

Sirisopanaporn, C., Fernicola, A. & Scrosati, B. (2009). New, ionic liquid–based membranes for lithium battery application. *Journal of Power Sources*, 186, 490–495.

Smart, L. & Moore, E. A. (2005a). Defects and Non–Stoichiometry. *Solid State Chemistry: An introduction.* (pp. 175–238). New York: Taylor & Francis.

Smart, L. & Moore, E. A. (2005b). Physical Methods for Characterizing Solids. *Solid State Chemistry: An introduction.* (pp. 175–238). New York: Taylor & Francis.

Stephan, A.M., Kumar, T. P., Renganathan, N. G., Pitchumani, S., Thirunakaran, R. & Muniyandi, N. (2000a). Ionic conductivity and FT–IR studies on plasticized PVC/PMMA blend polymer electrolytes. *Journal of Power Sources*, 89, 80–87.

Stephan, A.M., Renganathan, N.G., Kumar, T.P., Thirunakaran, R., Pitchumani, S., Shrisudersan, J., Muniyandi, N., et al. (2000b). Ionic conductivity studies on plasticized PVC/PMMA blend polymer electrolyte containing $LiBF_4$ and $LiCF_3SO_3$. *Solid State Ionics*, 130, 123–132.

Stephan, A.M., Saito, Y., Muniyandi, N., Renganathan, N.G., Kalyanasundaram, S. & Elizabeth, R.N. (2002). Preparation and characterization of PVC/PMMA blend polymer electrolytes complexed with $LiN(CF_3SO_2)_2$. *Solid State Ionics*, 148, 467–473.

Srinivasa, R., Raghavan, Michael, W.R., Peter, S.F. & Saad, A.K. (1998). Composite Polymer Electrolytes Based on Poly(ethylene glycol) and Hydrophobic Fumed Silica: Dynamic Rheology and Microstructure, *Chemistry Materials, 10,* 244–251.

Suthanthiraraj, S.A., Sheeba, D.J. & Paul, B.J. (2009). Impact of ethylene carbonate on ion transport characteristics of PVdF–$AgCF_3SO_3$ polymer electrolyte system. *Materials Research Bulletin*, 44, 1534–1539.

The A to Z of materials. (2002). *Silica–Fumed Silica (Silicon Dioxide)*. URL: http://www.azom.com/details.asp?ArticleID=1386. Accessed on 10th Jan 2010.

Tobishima, S. & Yamaji, A. (1984). Ethylene carbonate–propylene carbonate mixed electrolytes for lithium batteries. *Electrochimica Acta*, 29, 267–271.

Uma, T., Mahalingam, T. & Stimming, U. (2005). Conductivity studies on poly(methyl methacrylate)–Li_2SO_4 polymer electrolyte systems. *Materials Chemistry and Physics*, 90, 245–249.

Venkateswarlu, M, Reddy, K.N., Rambabu, B., Satyanarayana, N. (2000). A.c. conductivity and dielectric studies of silver–based fast ion conducting glass system. *Solid State Ionics*, 127, 177–184.

Vioux, A., Viau, L., Volland, S., Bideau J.L., Chimie, C.R. (2009). Use of ionic liquid in sol–gel; ionogels and applications. doi: 10.1016/j.crci.2009.07.002.

West, A.R. (1999a). Electrical Properties. *Basic Solid State Chemistry*. (pp. 321–361). West Sussex: John Wiley & Sons.

West, A.R. (1999b). Crystallography and Diffraction Techniques. *Basic Solid State Chemistry*. (pp. 125–165). West Sussex: John Wiley & Sons.

Wu, F., Feng, T., Bai, Y., Wu, C., Ye, L. & Feng, Z. (2009). Preparation and characterization of solid polymer electrolytes based on PHEMO and PVDF–HFP. *Solid State Ionics*, 180, 677–680.

Xie, J., Duan, R.G., Han, Y. & Kerr, J.B. (2004). Morphology, rheological and electrochemical studies of poly(ethylene oxide) electrolytes containing fumed silica nanoparticles. *Solid State Ionics*, 175, 755–758.

Xu, J.J. & Ye, H. (2005). Polymer gel electrolytes based on oligomeric polyether/cross–linked PMMA blends prepared via in situ polymerization. *Electrochemistry Communications*, 7, 829–835.

Yang, Y., Zhou, C.H., Xu, S., Hu, H., Chen, B. L., Zhang, J., Wu, S.J., Liu, W., Zhao, X. Z., et al. (2008a). Improved stability of quasi–solid–state dye sensitized solar cell based on poly(ethylene oxide)–poly(vinylidene fluoride) polymer–blend electrolytes. *Journal of Power Sources*, 185, 1492–1498.

Yang, J.M., Wang, Z.W., Yang, C.C. (2008b). Modification and characterization of semi–crystalline poly(vinyl alcohol) with interpenetrating poly(acrylic

acid) by UV radiation method for alkaline solid polymer electrolytes membrane. *Journal of Membrane Science*, 322, 74–80.

Yu, B., Zhou, F., Wang, C. & Liu, W. (2007). A novel gel polymer electrolyte based on poly ionic liquid 1–ethyl 3–(2–methacryloyloxy ethyl) imidazolium iodide. *European Polymer Journal*, 43, 2699–2707.

LIST OF PUBLICATION

1. S. Ramesh, **Chiam-Wen Liew** and K.Ramesh, "Evaluation and investigation on the effect of ionic liquid onto PMMA-PVC gel polymer blend electrolytes", **Journal of Non-Crystalline Solids** (2011) in press. (*ISI/SCOPUS Cited Publication*).

2. S. Ramesh, **Chiam-Wen Liew**, Ezra Morris and R.Durairaj, "Effect of PVC on ionic conductivity, crystallographic structural, morphological and thermal characterizations in PMMA–PVC blend-based polymer electrolytes", **Thermochimica Acta** 511 (2010) 140-146. (*ISI/SCOPUS Cited Publication*).

3. S. Ramesh and **Liew Chiam Wen,** ***"Investigation on the effects of addition of SiO_2 nanoparticles on ionic conductivity, FTIR, and thermal properties of nanocomposite PMMA- $LiCF_3SO_3$- SiO_2",*** **Ionics** 16 (2010) 255-262 (*ISI/SCOPUS Cited Publication*).

4. S. Ramesh, **Chiam-Wen Liew**, K. Ramesh and A. K. Arof, *"Electrical, Structural and Morphological Studies on Thermoplastic Corn Starch based Polymer Electrolytes Doped with Low Viscosity Ionic Liquid",* **18th Conference on Solid State Ionics**, Warsaw, Poland, 3rd – 8th July 2011 (Accepted for presentation)..

5. **Chiam-Wen Liew**, S. Ramesh, K. Ramesh and A. K. Arof, *"Preparation and Characterization of Lithium Ion Conducting Ionic Liquid–based Biodegradable Corn Starch Polymer Electrolytes",* **International Conference on Materials for Advanced Technologies**, Suntec, Singapore, 26th June –1st July 2011 (Accepted for presentation).

6. **Chiam-Wen Liew**, S. Ramesh and R. Durairaj, *"Impact of Low Viscosity Ionic Liquid on PMMA–PVC–LiTFSI Polymer Electrolytes Based on Ac–impedance, Dielectric Behavior and HATR–FTIR Characteristics",* **International Conference on Materials for Advanced Technologies**, Suntec, Singapore, 26th June –1st July 2011 (Accepted for presentation).

7. S. Ramesh, **Chiam Wen Liew** and O. K. Lee, *"Investigations on the effect of plasticizer in plasticized PVC-Li_2SO_4 polymer electrolyte based on AC-Impedance, Dielectric behavior and FTIR Studies",* **Asianalysis X**, Kuala Lumpur, Malaysia, 11th – 13th August 2009**.**

8. S. Ramesh and **Chiam-Wen Liew**, *"Dielectric and FTIR studies on blending of [xPMMA-(1-x)PVC] with LiTFSI",* **17th Conference on Solid State Ionics**, Toronto, Canada, 28th June – 3rd July 2009.

APPENDIX A

In order to determine the ionic conductivity of the polymer electrolyte, the bulk resistance, R_b of the polymer electrolyte must be determined first. In this determination, both Z axes must draw in equal scale as a minimum requirement. R_b is determined by the interception of real part of the complex impedance plot. It means that the resistance was calculated by extrapolation of the arc region to its lower frequency to Z real axis, as shown as below. The R_b value obtained in this figure is 1.25×10^{-5} Ω.

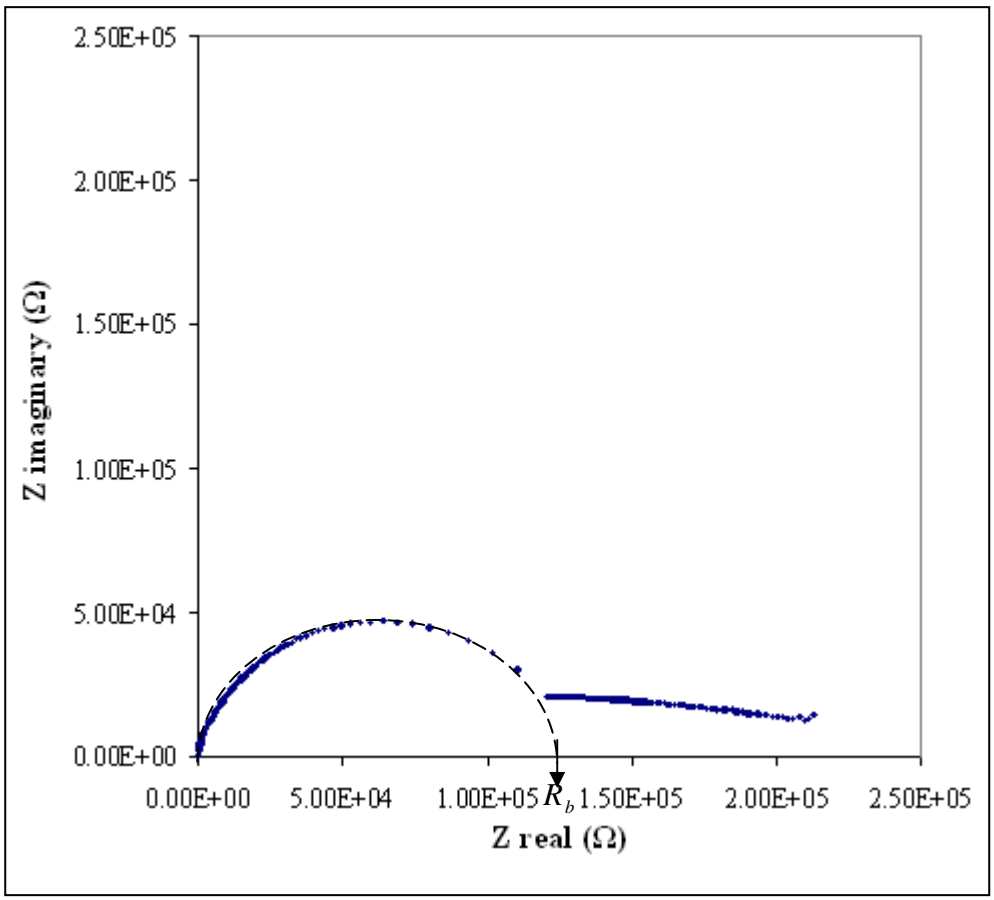

Figure 4.1: Typical Cole-Cole plot for PE 3 at ambient temperature.

APPENDIX B

The change in intensity of the peak in the HATR–FTIR spectrum was observed and determined. The figure below is shown the calculation for the changes in intensity of C=O stretching mode of PMMA.

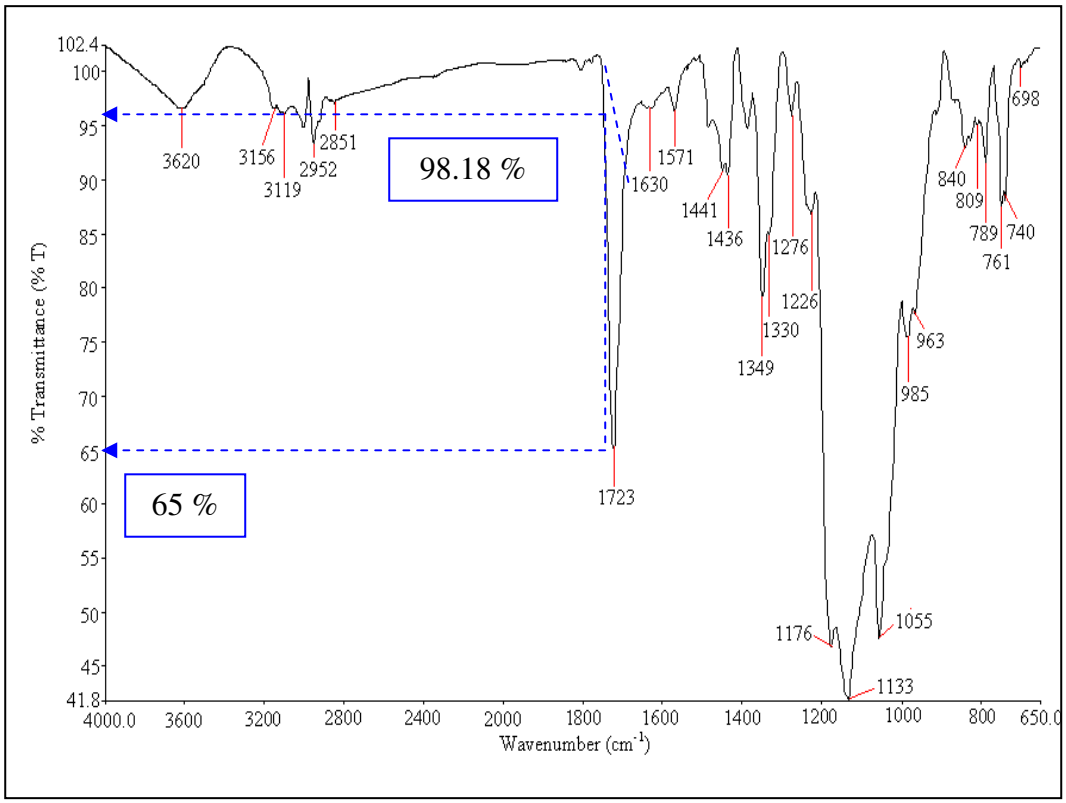

Figure 7.10 (d): HATR–FTIR spectrum of CPE 4.

From figure above, the transmittance percentage of baseline of the peak at 1723 cm^{-1} is 98.18 %, while the transmittance percentage of the peak is 65 %.

Intensity (%) = baseline transmittance – peak transmittance

= 98.18 % –65 %

= 33.18 %

Thus, the intensity of the peak at 1723 cm^{-1} is 33.18 %.